UNIVERSIDAD COMPLUTENSE DE MADRID

FACULTAD DE CIENCIAS FÍSICAS

Departamento de Física de la Tierra, Astronomía y Astrofísica I

(Geofísica y Meteorología)

TESIS DOCTORAL

Analysis of tropopause variability in observations and in an idealized model

Análisis de la variabilidad de la tropopausa en observaciones y en un modelo idealizado

MEMORIA PARA OPTAR AL GRADO DE DOCTOR

PRESENTADA POR

Jesús Ángel Barroso Pellico

Director

Pablo Zurita Gotor

Madrid, 2018

Universidad Complutense de Madrid
Facultad de Ciencias Físicas
Departamento de Física de la Tierra, Astronomía y Astrofísica I
(Geofísica y Meteorología)

Analysis of tropopause variability in observations and in an idealized model

Análisis de la variabilidad de la tropopausa en observaciones y en un modelo idealizado

Memoria para optar al grado de doctor presentada por
Jesús Ángel Barroso Pellico

Director: Pablo Zurita Gotor

Contents

Summary

Introduction

The focus of this thesis is the study of the extratropical tropopause. The tropopause is a distinctive feature of the vertical structure of the atmosphere, separating two regions, troposphere and stratosphere, with very different dynamical and chemical characteristics. The abrupt change in air properties found when moving from one layer to another serves as the basis for a wide variety of definitions. The first and most widely used definition is the thermal tropopause, based on the discontinuity in the lapse-rate. The dynamical tropopause is based on the discontinuity in the isentropic potential vorticity. Chemical definitions are also possible, based on the discontinuity in the concentration of tracer gases above and below the tropopause. The greatest variability in tropopause height is found in midlatitudes in synoptic scales, associated with the potential vorticity anomalies caused by the eddies at levels close to the tropopause. Seasonal variability, of lesser amplitude, has the form of a single wave in midlatitudes of both hemispheres and in the southern polar latitudes -where the cycle is inverted with respect to midlatitudes, while some regions of the Arctic exhibit a double-wave seasonal cycle. Previous studies attributed this interhemispheric asymmetry to the different strength of the residual circulation in both hemispheres, due to the different land-sea distributions. The tropopause has been traditionally explained as the transition from a stratospheric temperature profile in radiative equilibrium to a dynamically adjusted profile in the troposphere. Radiative-convective models seem to work well for the tropical regions, while in the extratropics it is less clear which dynamical mechanism adjusts the troposphere. Several possibilities, such as dry and moist baroclinic equilibration, have been proposed.

Objectives

The goal of this thesis is to improve our understanding of the processes that drive the variability of the tropopause, aiming to find some connection with baroclinic adjustment. This includes:

- Studying the characteristics of the Upper-Troposphere/Lower-Stratosphere region and testing the ability of the thermal definition to differentiate between the physical characteristics of the stratospheric and the tropospheric air masses.

▪ Analyzing the variability of the zonal-mean tropopause in seasonal and intraseasonal time scales. The former represents forced variability, while the latter is essentially associated to internal atmospheric variability.

▪ Using an idealized model with simplified physics to simulate the forcings that drive tropopause variability. Idealized models allow us to study the dynamics in isolation from the complications associated with physical parameterizations.

Data

Data from three different sources have been used in this thesis to improve the statistical robustness of the conclusions. Radiosonde data are the most widely used dataset for tropopause determination due to their high vertical resolution. Their sparse nature and temporal inhomogeneties, however, make them less suitable for studies of variability; in this thesis, a worldwide database, IGRA, with over 1500 sounding sites, is used. The hole left by the radiosonde data is filled with the reanalyzed data, distributed in a regular grid and extending for several years, although at the cost of a lower vertical resolution. Two reanalyses, NCEP/NCAR Reanalysis-1 and ERA-Interim are used in this thesis. An idealized model is also used to aid the interpretation of the observational results. The idealized model consists of a numerical model solving the primitive equations in a simplified physical framework (dry atmosphere forced by Newtonian relaxation to a prescribed equilibrium temperature and damped using simple linear Rayleigh friction over the boundary layer). The model setup includes a realistic stratosphere and a tropospheric seasonal cycle.

Methodology

The tropopause level is determined using the method proposed by Reichler, based on the thermal definition. Variables are interpolated to Tropopause-Based coordinates to analyze the Upper-Troposphere/Lower-stratosphere layer; this system of coordinates places the origin at the tropopause level, hence preventing the blurring effect of averaging a discontinuity that moves over time. Tropopause variability is studied by applying Principal Component Analysis to the intraseasonal tropopause anomalies, defined as differences from the daily climatology, after eliminating low-frequency variability by means of a Lanczos filter. Eliassen-Palm fluxes are used to study the dynamical evolution of the dominant modes of variability.

Results

The main findings of this thesis are the following:

▪ The critical lapse rate of the traditional thermal tropopause definition is near-optimal for separating the characteristics of the stratospheric and tropospheric air masses. Analysis of lapse rate histograms in the Upper-Troposphere and Lower-Stratosphere reveals minimum occurrence near 2K km^{-1}, separating the lapse rate distributions in both layers.

▪ Two new definitions are proposed based on the maximum curvature of the potential temperature profile and on the Brunt-Väisäla frequency (normalized by potential temperature). These definitions work reasonably well and have the advantage, compared to the traditional definition, of not being based on empirical thresholds.

▪ The seasonal cycle of the zonal-mean tropopause has a double-wave structure in the Arctic but a single wave structure in the Antarctic. Analysis of the terms in the thermodynamic equation suggests that this is due to strong eddy heat flux convergence over the polar cap in the northern lower stratosphere during late winter, which leads to a sinking of the tropopause in spring. In summer, the tropopause is higher due to the absence of eddy heating in the lower stratosphere and to the effect of moist processes in the troposphere.

▪ Intraseasonal tropopause variability is dominated by changes in the eddies and in the polar vortex intensity. Anomalous wave breaking by both planetary and synoptic waves at levels close to the tropopause induce dipolar potential vorticity anomalies there, which displace the midlatitude tropopause. Changes in the strength of the polar vortex drive the rising or sinking of the polar tropopause.

Conclusions

The main conclusions of this thesis may be summarized as follows:

▪ A lapse rate of 2K km^{-1} represents an optimal threshold for the thermal definition of the tropopause, as it provides the greatest separation between the stratosphere and the troposphere.

▪ The tropopause may be defined in terms of the discontinuity between the troposphere and the stratosphere by maximizing the curvature of the vertical potential temperature profile or the buoyancy frequency. These definitions are not specific to the present-day climate, so they may be applied to very different models, glacial periods, etc.

- Variability of the zonal-mean tropopause is mainly driving by changes in the polar vortex and in eddy activity for both seasonal and intraseasonal scales.

Resumen

Introducción

Esta tesis doctoral está enfocada al estudio de la tropopausa extratropical. La tropopausa es un rasgo muy aparente de la estructura vertical de la atmósfera que separa dos regiones de muy distintas características físicas y químicas: la troposfera y la estratosfera. El brusco cambio que se observa en los perfiles cuando se pasa de los valores típicos de una a los de la otra sirve de base a una amplia variedad de definiciones para la tropopausa. La primera que se estableció, y la más utilizada, es la tropopausa térmica, basa en la discontinuidad en el gradiente vertical de temperatura. La tropopausa dinámica se define a partir de la discontinuidad en la vorticidad potencial isentrópica. Varias definiciones químicas se han dado también basadas en la discontinuidad en la abundancia de gases traza por encima y por debajo de la tropopausa. La mayor variabilidad de la tropopausa ocurre en las latitudes medias y en las escalas sinópticas, relacionada con las anomalías de vorticidad potencial ocasionadas por las perturbaciones de dicha escala. La variabilidad estacional, de menor amplitud, tiene forma de onda en latitudes medias y en áreas polares meridionales -en éstas, el ciclo está invertido respecto a las latitudes medias-, mientras que algunas regiones del Ártico presentan una onda doble. Los estudios disponibles apuntan a que la asimetría interhemisférica podría estar relacionada con la diferente intensidad de la circulación residual, asociada a la diferente distribución de océanos y continentes en ambos hemisferios. La existencia de la tropopausa se ha explicado como la zona de transición entre el perfil de temperatura en equilibrio radiativo de la estratosfera y el perfil ajustado dinámicamente de la troposfera. Los modelos radiativo-convectivos parecen funcionar razonablemente bien en los trópicos, mientras que en los extratrópicos no está claro cuál es el mecanismo dinámico que ajusta el perfil tropoféricos. Se han propuesto varias posibilidades, como un ajuste baroclínico o bien seco o bien húmedo.

Objetivos

El principal objetivo de esta tesis es entender mejor los procesos que determinan el nivel de la tropopausa, intentando encontrar alguna relación con el ajuste baroclínico. Para ello, se busca:

▪ Analizar las características de la alta troposfera/baja estratosfera y comprobar la capacidad de la definición térmica para diferenciar entre las características físicas del aire estratosférico y el troposférico.

▪ Estudiar la variabilidad de la tropopausa promediada zonalmente en la escala estacional e intra-estacional; la primera se puede considerar como variabilidad forzada, mientras que la segunda es intrínsecamente interna.

▪ Utilizar un modelo idealizado para simular los factores que modifican el nivel de la tropopausa. Este tipo de modelos simplifican la dinámica pero reteniendo las propiedades básicas del fluido.

Datos

En esta tesis se han empleado datos de tres fuentes distintas, con el fin de mejorar la robustez estadística de los resultados. Los datos de radiosondeo son los más usado para el estudio de la tropopausa por su gran resolución vertical. Sin embargo, estos datos son dispersos por naturaleza, pues muchas estaciones de radiosondeo están concentradas en las mismas áreas, mientras que otras regiones apenas disponen de alguna; además, existen muchos saltos e inhomogeneidades temporales que no los hacen aptos para un estudio de variabilidad. En esta tesis se utiliza la base de datos IGRA, que contiene datos de más de 1500 estaciones. Para llenar este hueco, en esta tesis se usan datos de renálisis, que están distribuidos en un malla uniforme a lo largo de varios años. En concreto, se usan datos del reanálisis 1 de NCEP/NCAR y el renálisis ERA-Interim. Además, se usa un modelo idealizado para estudiar la validez de las conclusiones extraídas de las observaciones. Este modelo es un modelo numérico que resuelve las ecuaciones primitivas pero donde se establece que la temperatura tienda a un estado de equilibrio prescrito usando un esquema de enfriamiento newtoniano; además, la fricción es simulada con un amortiguamiento de Rayleigh. En esta tesis, la temperatura de equilibrio prescrita incluye una estratosfera realista y el ciclo estacional de la troposfera.

Metodología

El nivel de la tropopausa es calculado usando el método propuesto por Reichler, basado en la definición térmica. Las variables son interpoladas a coordenadas basadas en la tropopausa para estudiar la región que la rodea. Este sistema de coordenadas coloca el origen en el propio nivel de la tropopausa, de modo que se evita el suavizamiento que se produce alrededor de una discontinuidad al promediar. La variabilidad presente en los datos es extraída a través de un análisis de componentes principales de las anomalías intra-estacionales, definidas como la diferencia respecto a la climatología diaria. Para eliminar variabilidad de baja se

usa un filtro de Lanczos. El contexto dinámico en el que se producen los modos es evaluado a través del estudio de las anomalías en el flujo de Eliassen-Palm.

Resultados.

Los principales resultados de esta tesis son los siguientes:

▪ El valor crítico usado habitualmente para la tropopausa térmica es el que mejor separa la troposfera de la estratosfera. El análisis de la baja estratosfera/alta troposfera revela que dicho valor constituye el mínimo entre los gradientes verticales de temperatura de la troposfera y la estratosfera.

▪ Se establecen dos nuevas definiciones de la tropopausa, basadas en el nivel de máxima curvatura del perfil de temperatura potencial y de la frecuencia de Brunt-Väisäla divida por la temperatura potencial. Estos dos criterios funcionan razonablemente bien para los datos utilizados en esta tesis.

▪ El ciclo estacional de la tropopausa promediada zonalmente tiene forma de doble onda en el ártico, pero de onda simple en la Antártida. El análisis de los términos de la ecuación de calor demuestra que esto se debe a la fuerte convergencia de flujos de calor *eddy* sobre en la baja estratosfera polar norte al final del invierno. En verano, la tropopausa está más alta debido a la ausencia de calentamiento por los *eddies* en la baja estratosfera y los procesos húmedos que tienen lugar en la troposfera.

▪ La variabilidad intra-estacional está dominada por los efectos causados por los *eddies* y por la intensidad del vórtice polar. Por un lado, las anomalías en la ruptura de ondas sinópticas y planetarias inducen un dipolo de anomalías de vorticidad potencial en el nivel de la tropopausa que modifican su altura. Por otro lado, las variaciones en el vórtice polar producen el ascenso o descenso de la tropopausa polar.

Conclusiones

Las principales conclusiones de esta tesis se pueden resumir en los siguientes puntos:

▪ El gradiente vertical de 2K km^{-1} es el óptimo para definir la tropopausa térmica de modo que separe adecuadamente la estratosfera de la troposfera.

▪ La tropopausa puede ser definida a partir de las características que presenta la discontinuidad entre la estratosfera y la troposfera; en particular, usando la curvatura del perfil de temperatura potencial o la frecuencia de flotabilidad. Estas definiciones no están limitas a

valores extraídos del clima actual, por lo que pueden ser aplicadas a modelos, períodos glaciales,..., y en general climas distintos al actual.

- La variabilidad de la tropopausa promediada zonalmente está causada por el vórtice polar y la actividad de los *eddies* tanto en la escala estacional como en la intraestacional.

List of abbreviations

AO: Arctic Oscillation.

BD: Brewer-Dobson.

Cae: Commission for Aerology of the World Meteorological Organization.

COSMIC: Constellation Observing System for Meteorology, Ionosphere and Climate.

DJF: December, January and February.

ECMWF: European Centre for Medium-Range Weather Forecasts.

EOF: Empirical Orthogonal Function.

EP: Eliassen-Palm.

ERA: European Re-Analysis.

GCM: General Circulation Model.

GFDL: Geophysical Fluid Dynamics Laboratory.

GPS: Global Positioning System.

GPSRO: Global Positioning System Radio Occultation.

HS94: Held-Suarez setup of the idealized model.

IGRA: Integrated Global Radiosonde Archive.

JJA: June, July and August.

JFV: Jucker-Fueglistaler-Vallis setup of the idealized model.

LS: Lower-Stratosphere.

NCAR: National Center for Atmospheric Research.

NCDC: National Climatic Data Center.

NCEP: National Center for Environmental Predictions.

NOAA: National Oceanic and Atmospheric Administration.

NH: Northern Hemisphere.

PCA: Principal Component Analysis.

PC: Principal Component.

PJO: Polar-Night Jet Oscillation.

PV: potential vorticity.

PVU: potential vorticity units.

SH: Southern Hemisphere.

SLB: Sea-Level Based coordinate.

STE: Stratosphere-Troposphere Exchange.

TB: Tropopause Based coordinate.

TIL: Tropopause Inversion Layer.

TTL: Tropical Tropopause Layer.

UT: Upper-Troposphere.

UTC: Universal Time Coordinate.

UTLS: Upper-Troposphere and Lower Stratosphere.

WMO: World Meteorological Organization.

1. Introduction

The tropopause is one of the most prominent features of the atmospheric structure, playing a fundamental role both as a dynamical boundary between an active troposphere with short response times and a much quieter stratosphere and as a material boundary between the well-mixed troposphere and the stratified stratosphere. Despite this important role, there is no unique, fundamental way to define the tropopause but several empirical criteria based on properties known to experience a steep change when moving from the troposphere to the stratosphere, such as lapse rate (WMO, 1957), potential vorticity (Reed, 1955; Hoinka, 1998), or tracer abundance (Bethan *et al.*, 1996). Lacking a fundamental definition for the tropopause, some ambiguity may arise when studying the determination and/or variability of the tropopause, as the relative importance of the processes involved might depend on the framework used.

The determination of the mean tropopause is a classical problem in general circulation theory. The simplest model regards the tropopause as the boundary between a radiative-equilibrium stratosphere and a troposphere in some form of dynamical equilibrium, typically convective or baroclinic (Held, 1982; Lindzen, 1993). Although highly idealized, this model can explain the change in lapse rate (between dynamically adjusted and radiative-equilibrium

values), potential vorticity (assuming eddies greatly homogenize potential vorticity in the troposphere), and chemical species (owing to the enhanced static stability and weak mixing in the stratosphere) across the tropopause. The main limitation of this model is that the assumption of a stratosphere in radiative equilibrium is not well satisfied, as it is known that the polar stratosphere, especially in winter, is far from radiative equilibrium because of the dynamical warming by the residual circulation (Holton *et al.*, 1995), which is expected to influence tropopause height (Appenzeller *et al.*, 1996; Thuburn and Craig, 2000; Birner, 2010). To close the problem, additional assumptions must be made about the tropospheric dynamical equilibrium, for which different dynamical arguments have been proposed. These closures generally fall in two categories: some are based on dry eddy equilibration theories like baroclinic adjustment (Held, 1982; Schneider, 2004; Bordi *et al.*, 2004), while others are based on moist convection (Juckes, 2000; Wu and Pauluis, 2014).

The seasonal evolution of the extratropical tropopause is characterized by rising in summer associated with the warming of the tropospheric column and sinking in winter due to cooling (Hoinka, 1998). In the Polar Regions, however, the tropopause is higher in winter, especially in the South Pole, and lower in summer (Zängl and Hoinka, 2001), which has been associated with the cold temperatures of the Polar Vortex (Zängl, 2002). Nonetheless, there is an asymmetry between the seasonal cycles in both hemispheres, as the polar tropopause in the Northern Hemisphere is higher in summer, which may be attributed to enhanced radiative cooling (Wong and Wang, 2000). The northern seasonal cycle also presents smaller amplitude, which has been associated with higher eddy activity in the lower stratosphere during winter (Appenzeller *et al.*, 1996; Wong and Wang, 2000; Zängl, 2002).

In intraseasonal scales, previous observational studies have sought a connection between changes in eddy activity and in *zonal-mean* tropopause height, assuming that in short time scales the eddy fluxes drive the tropopause away from equilibrium during baroclinic life cycles (Dell'Aquila *et al.*, 2006; Son *et al.*, 2007). Superimposed to this zonal-mean structure, at any given time the extratropical tropopause height exhibits pronounced zonal variability along latitude circles, with low (high) tropopauses associated with cyclonic (anticyclonic) circulations. This may be understood from a potential vorticity (PV) perspective (Hoskins *et al.*, 1985; Wirth, 2001), as the tropopause essentially represents a

boundary between high PV air in the stratosphere and low PV air in the troposphere. Thus, upper-level cyclonic anomalies are inextricably associated with intrusions of stratospheric air into the troposphere.

In the next sections of this chapter we review some aspects of the tropopause and its variability of special relevance for this thesis.

1.1 Properties of the tropopause.

The tropopause is a distinctive feature of the vertical structure of the lower atmosphere. Hence, it is not surprising that it was soon detected when the first upper-air measurements became available, although its existence was not fully accepted until some time later (Hoinka, 1997). While there were some sporadic attempts at measuring the characteristics of the mid- to upper-atmosphere during the 18th and 19th centuries, real soundings did not get started until the final years of the 19th century, when the "aerological science", dedicated to the measurement and the study of the upper-atmosphere was founded. Still, systematic measurements were not possible at that time, but soundings were obtained mainly in Paris, by Teisserenc de Bort, and in Berlin, by Richard Assman. In 1902 they both presented evidences of an isothermal layer starting at around 8 to 12km height, followed by an increase in temperature at higher altitudes. As this discovery was based on only two locations relatively close to one another, it was unclear whether this was a local feature or a global characteristic of the atmosphere, so many expeditions were launched in the subsequent years to investigate the characteristics of the –at the time- upper atmosphere. Systematic measurements also started in North America in 1904. From all these observations it was clear that the isothermal layer was real and a ubiquitous feature of the atmosphere. Teisserenc de Bort proposed the name "stratosphere" for the layer extending over the isothermal region, where the temperature increases with height, and "troposphere" for the layer under it. Shortly after, Hawke proposed the term "tropopause" for the layer separating both, and by 1918 this term was already included in the Meteorological Glossary.

1.1.1 Definitions of the tropopause.

1.1.1.1 Thermal tropopause.

One year after the word "tropopause" was defined, Dines (1919) proposed a rule for identifying the level at which the tropopause occurs, which is very similar to the thermal criterion used today. The rule was to locate the tropopause at the level where the isothermal gradient starts when the stratosphere begins with an inversion. If there is an abrupt change in the lapse rate to a value below 2K km^{-1}, but no inversion, then the tropopause should lie at the abrupt transition. Finally, if no abrupt change or inversion is present, the tropopause should be located at the base of the first 1-kilometer layer where the temperature difference between the base and the top is 2K or less, provided no other 1-kilometer layer above it has a temperature difference over 2K. This set of rules is interesting, as it shows that there is a great variety of situations for the transition between the troposphere and the stratosphere, so that it is very difficult to establish a general rule for tropopause identification. At the same time, it indicates that an inversion in the vertical gradient of temperature is apparent in the individual temperature profiles in many cases. This is what has been much more recently called the Tropopause Inversion Layer (TIL). Lastly, it indicates that in many cases the temperature lapse rate changes abruptly from its tropospheric value to 2K km^{-1} instead of decreasing gradually, although there are also cases with no clear separation in the vertical gradient of both layers.

The Commission for Aerology (CAe) of the World Meteorological Organization (WMO) established a standard proceeding for determining the tropopause level in his first session, held between August and September, 1953, following the rules by Dines. Then, in 1957, a method for obtaining operationally the tropopause level in sounding profiles was finally adopted "in the light of the experience gained in the meantime" (WMO, 1957). The definition is as follows:

"(a) The first tropopause is defined as the lowest level at which the lapse rate decreases to 2°C/km or less, provided also the average lapse rate between this level and all higher levels within 2 km does not exceed 2°C/km .

(b) If above the first tropopause the average lapse rate between any level and all higher

levels within 1 km exceeds 3° C/km, then a second tropopause is defined by the same criterion as under (a). This tropopause may be either within or above the 1 km layer."

This is the standard definition used today and it is usually known as the "thermal tropopause". Part (a) involves the lapse rate descends from the tropospheric values to lower values, and that this descend keeps along a sufficiently wide layer as to not be mistaken with the common upper-troposphere inversions. Part (b) involves the transition from the troposphere to the stratosphere may not occur in one place, but in successive levels, giving rise to the concept of multiple tropopauses (Schmauss, 1909), as will be explained later. This definition was later used in other datasets apart from the radiosonde data giving reliable results (Hoerling *et al.*, 1991; Hoinka, 1998; Randel *et al.*, 2000). As shown in Fig. 1.1, the tropopause so defined is quite zonally symmetric with only slightly perturbations in the Northern Hemisphere (NH), where the tropopause tend to be higher in the west coast of the continents and lower in their east coast, hence is characterized by a wavelike pattern of zonal wavenumbers between 1 to 3 (Hoinka, 1998), and a minimum over Greenland that forms part of more extended minimum to north of Canada associated with the Polar Vortex (Zängl and Hoinka, 2001). As for the meridional structure, the tropopause is higher in the Tropics, with typical values of 120-130hPa and steep gradients in the subtropics, leading to a lower extratropical tropopause, characterized by pressures between 200 and 300hPa, the latter being the typical pressure at the polar regions.

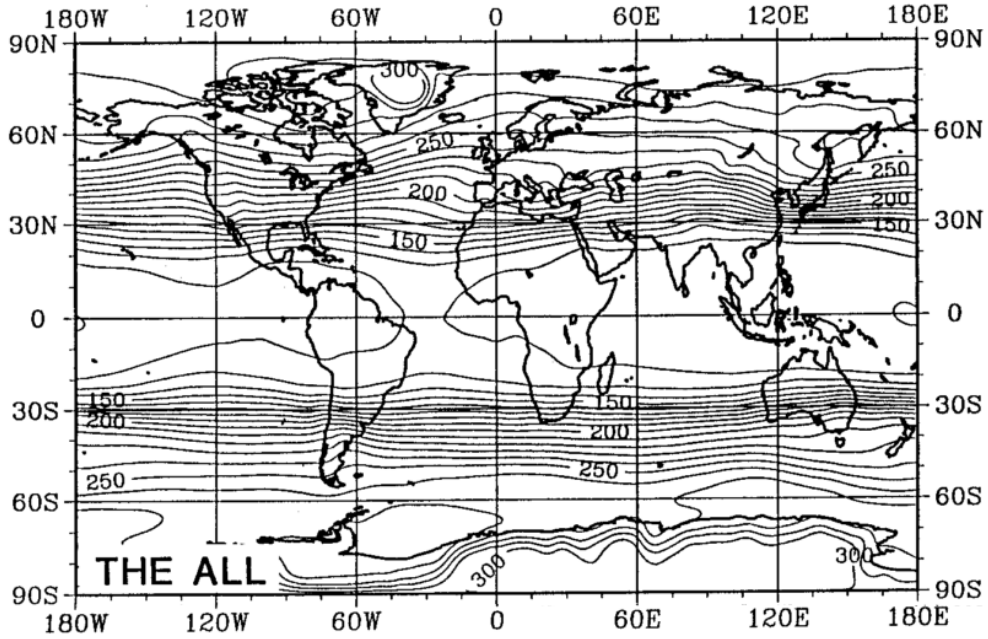

Fig. 1.1 Mean pressure of the global thermal tropopause (1979–93; 12:00 UTC) (adapted from Hoinka, 1998)

1.1.1.2 Dynamical tropopause.

A new definition of the tropopause was proposed by the WMO (WMO, 1986), after the discovery of stratospheric air intrusions to low levels of the atmosphere using isentropic analysis of the frontal areas (Reed, 1955). In these situations, the thermal definition of the tropopause may become useless, as the contrast between the tropospheric and the stratospheric stratifications disappears in the upper-levels of the frontal area (see Fig. 1.2). Still, there is a discontinuity in the relative vorticity at both sides of the geostrophic jet that can be used to define the boundary between the troposphere and the stratosphere. Given that potential vorticity is conserved in isentropic coordinates (in an adiabatic and inviscid flow), a tropopause defined from this magnitude is also conserved in the same terms, hence it behaves as a quasi-material surface, in correspondence with the observations (Sawyers, 1954). Note that the dynamical definition of the tropopause corresponds to a zero-order discontinuity for the potential vorticity profile while the thermal tropopause varies from areas and times when it is a zero-order discontinuity in the lapse-rate profiles to others where it can be a continuous transition zone (see Fig. 1.3).

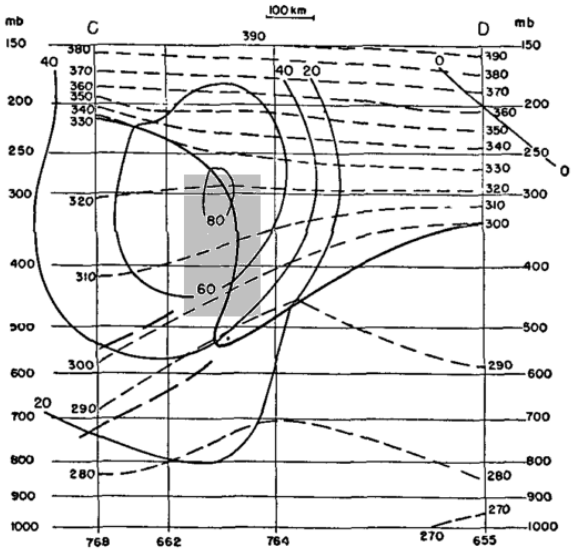

Fig. 1.2 Cross-section of a frontal area on 14 December 1953 developing in the United States. Thin solid lines give geostrophic wind speed (m s^{-1}) normal to section, dashed lines are insentropes and thick solid line represents the tropopause. In the shaded region, there is not contrast between the tropospheric and the stratospheric stratifications (reproduced from Reed, 1955).

The potential or Ertel's vorticity in isentropic coordinates is defined by:

$$P_\theta = -g\left(\zeta_\theta + f\right)\left(\frac{\partial P}{\partial \theta}\right)^{-1}$$

where $\zeta_\theta$is the relative vorticity and f is the Coriolis parameter. The method consists on finding the first isentropic level at which P_θ exceeds some threshold value, and then interpolate to pressure coordinates to obtain

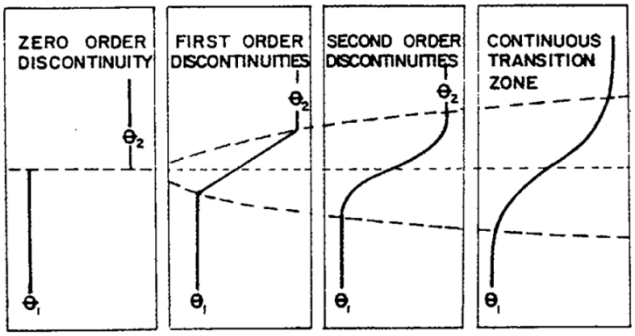

Fig. 1.3 Discontinuities of increasing order as approximations to a continuous transition zone (reproduced from Hoinka, 1997).

the tropopause pressure. The threshold value is chosen to match the climatological zonal-mean value of the thermal tropopause (WMO, 1986). The critical potential vorticity value was established by the WMO to be 1.6PVU (1PVU=$1{\cdot}10^{-6}$ K m^2 kg^{-1} s^{-1}), but other studies suggest a range of values between 2 to 3.5PVU (a detailed discussion can be found in Hoinka, 1998). According to Gettelman *et al.* (2011), this value can be deduced from the planetary approximation of the potential vorticity, this is, neglecting the relative-vorticity term, so that $P_\theta \approx f\theta\, N^2/\rho\, g$, N^2 being the Brunt-Väisäla frequency, $N^2 = (g/\theta)(\partial\,\theta/\partial\, z)$ and ρ the density. As the thermal tropopause is defined by a lapse rate of 2K km^{-1} and using a typical tropopause temperature in midlatitudes of 220K, this gives an approximate value for N^2 at the tropopause of around $3.6{\cdot}10^{-4}$ s^{-2}. Hence, introducing typical values in midlatitudes for the Coriolis parameter and the potential temperature and density at the tropopause (10^{-4} s^{-1} the former and 320K and 0.35kg m^{-3} the latter), the potential vorticity of the tropopause corresponds to a value of 3.35PVU.

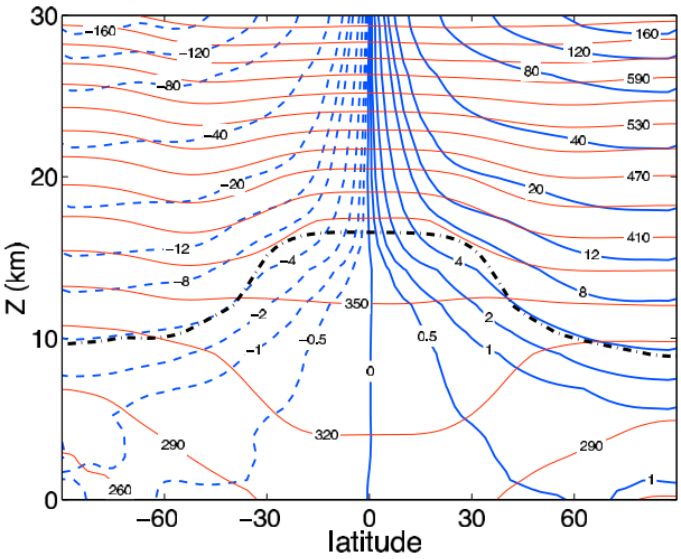

Fig. 1.4 The observed annual mean isentropes (red solid lines), potential vorticity (blue dashed lines) and tropopause level(black dash-dotted line) (reproduced from Vallis, 2005).

As shown in Fig. 1.4, the potential vorticity goes to zero in the equator due to the Coriolis parameter, so that the dynamical definition of the tropopause cannot be used in the equatorial areas -some authors resorts to a combination of dynamical tropopause in the extratropics and thermal tropopause in the Tropics.

The climatological dynamical tropopause is shown in Fig. 1.5. The tropopause so-obtained is almost identical to the thermal tropopause except in the polar areas, where it is higher. While the averaged dynamical tropopause is in good agreement with the averaged thermal tropopause, some differences may arise in areas with high values of relative vorticity, where the planetary approximation does not hold; hence, the dynamical tropopause determined with a particular P_θ value will be in general different from the thermal tropopause

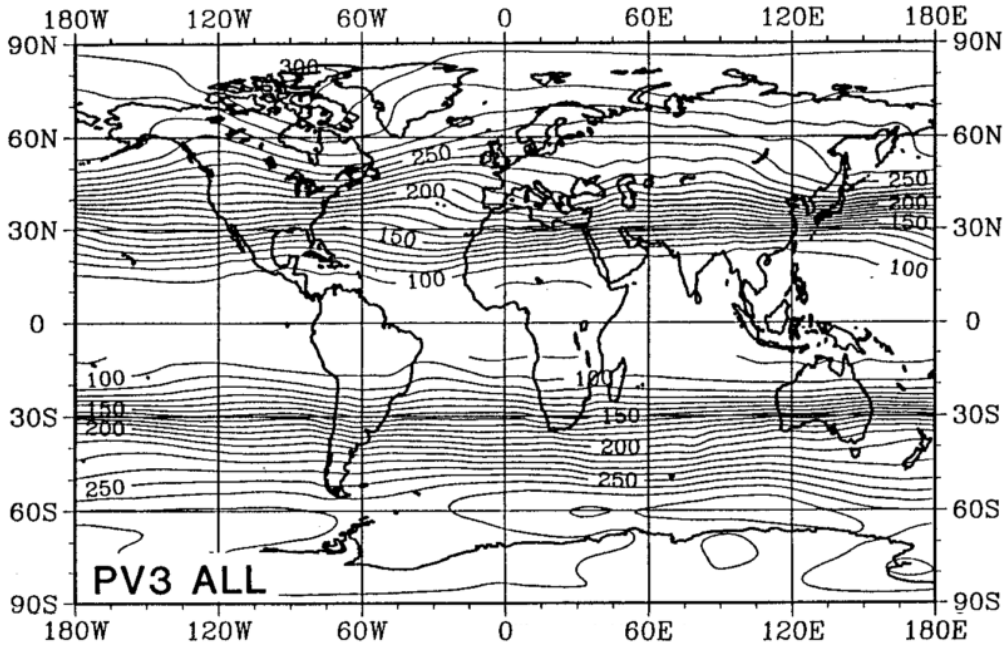

Fig. 1.5 As in Fig. 1, but for the dynamical tropopause with a 3.5PVU (see text for details) (reproduced from Hoinka, 1998).

over the intense cyclones and anticyclones (Wirth, 2000). In particular, for the Northern Hemisphere, cyclonic circulation will have a dynamical tropopause lower than the thermal tropopause, and vice versa in the anticyclonic circulations.

It should be noted that the determination of the dynamical tropopause, that takes into account not only the thermal stratification but also the three-dimensional structure of the atmospheric motions (Hoinka, 1998), requires the knowing of the wind components along the isentropic surfaces. Hence, it cannot be obtained from single vertical profiles as the thermal tropopause. The dynamical tropopause has been then widely used in analysed or reanalysed data and in models. Due to the sparse nature of the radiosonde datasets, it is difficult to obtain the dynamical tropopause from them.

1.1.1.3 Chemical tropopause.

In the same way the thermal tropopause appeared as a distinctive feature in early soundings, separating a region in which temperature decreases with height from a region in which it increases, the tropopause was also obvious in the first tracer profiles displaying the abundance of trace gases in the atmosphere as a function of height. As shown in Fig. 1.6, ozone concentration increases in the stratosphere, and the change is greater right above the tropopause. Water vapour, on the other hand, decreases in the stratosphere, especially right

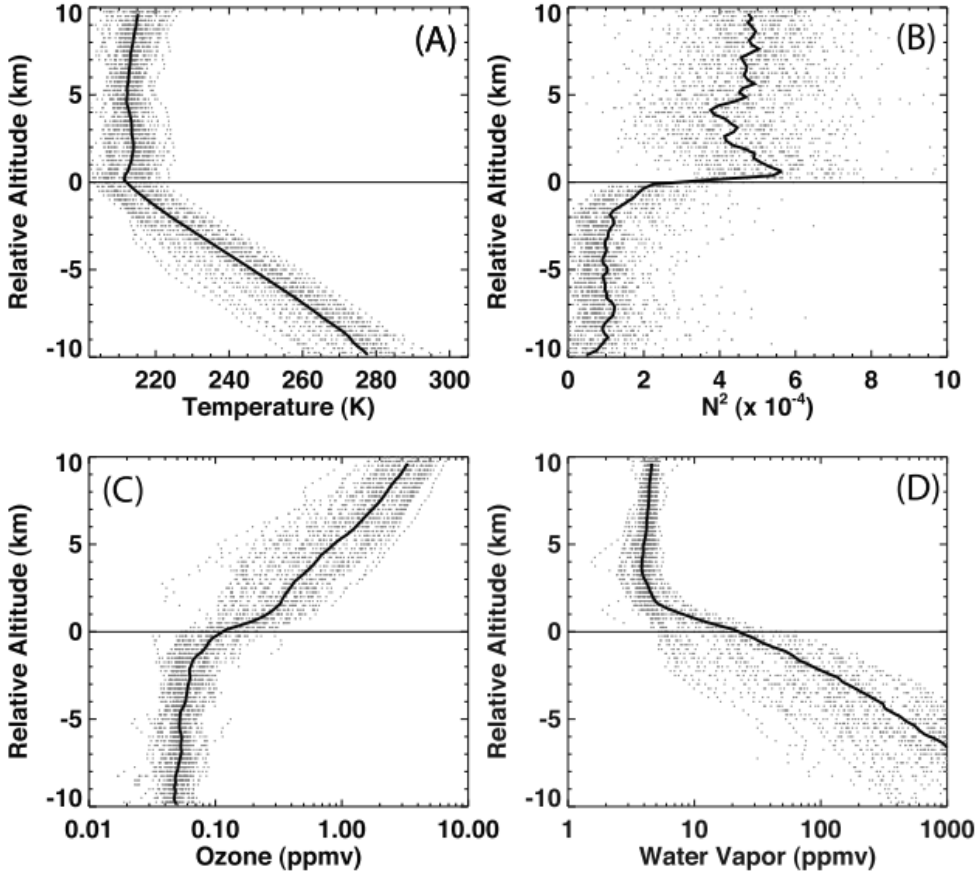

Fig. 1.6 45 vertical profiles from individual sounding over Boulder, Colorado (United States) during all months for (a) temperature, (b) Squared-Brunt-Väisäla frequency, (c) ozone and (d) water vapor concentrations. Profile altitudes are referenced to the thermal tropopause. Grey dots indicate individual measurements and the bold black line corresponds to their mean value (reproduced from Gettelman *et al.*, 2011).

above the tropopause. Motivated by these characteristics, Bethan *et al.* (1996) proposed a definition of the tropopause from the ozone profiles based on threshold values for the mixing ratio and its vertical gradient. This tropopause is usually located 800m below the thermal tropopause.

Another way of determining the approximate level of the tropopause is from the so-called tracer-tracer correlations (Zahn and Brenninkmeijer ,2003): if measurements of two tracers, one with high values in the stratosphere -such as ozone- and the other with high values in the troposphere -such as water vapour- are known at different altitudes, then it is possible, from the differences between the values measured and their typical values in the reservoir areas, to establish the levels in which (irreversible) exchange occurs, this is known as the "chemical tropopause" (see Fig. 1.7). Additionally, this method serves as a measure of the Stratosphere-Tropospheric Exchange (STE) of mass across the tropopause.

Both the ozone tropopause and the chemical tropopause are calculated from individual profiles or local measurements of tracer abundances, so it is difficult to establish a global view of the tropopause based on them. With the introduction of high-resolution satellite measurements of radiances this is becoming possible.

1.1.2 Meridional structure of the tropopause.

As explained above, the time-mean tropopause is quite symmetric in longitude, with weak zonal asymmetries appearing near the extratropical jets, especially in winter (Hoinka, 1998), but it varies greatly along the meridians. Hence, there has been much interest in explaining the tropopause zonal-mean structure. The classical view is that the tropopause is broken in three parts corresponding to the tropical, midlatitude and Polar Regions, as seen in individual cross-sections (Hess, 1948). The mean values, however, do not show these discontinuities, smoothed in the average, but regions with large meridional gradients (Hoinka, 1998). As can be seen in Fig. 1.8, the subtropical gradient is apparent in the mean meridional profile of the tropopause, separating the tropical tropopause and the extratropical tropopause, much lower than the former. The meridional structure is similar with the thermal and the dynamical definitions of the tropopause, although the 1.6PVU threshold tends to overestimate the tropopause pressure, at least in reanalysed data (Hoerling *et al.*, 1991; Hoinka, 1998). In the tropics, the tropopause pressure is more or less constant, while in the extratropical region the tropopause pressure increases toward the poles. Although both hemispheres appear quite symmetric in the meridional profile shown in Fig. 1.8, higher resolution measurements show that the mean

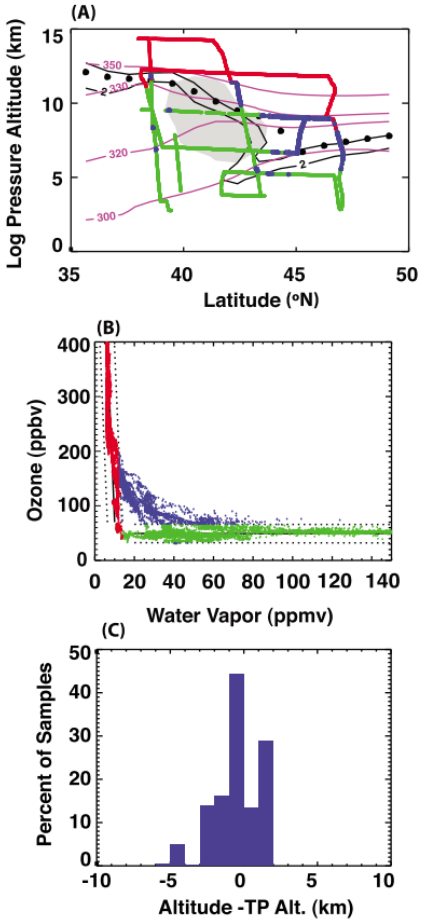

Fig. 1.7 Example of the tracer-tracer correlation method from data taken from a flight in December, 2005. In (a), trajectory of the flight (green line denotes the tropospheric air, as inferred from the tracer abundance measured, red is used for the stratospheric air and blue for the mixed air). Solid lines are isentropes, the black dotted line is the thermal tropopause and the shaded area represents zonal wind over 50 m s^{-1}. b) A tracer- tracer diagram with measurements of tracer abundance in the flight. Colours are the same as in a); c) Histogram of heights for the air with mixed tracer values relative to the thermal tropopause (adapted from Gettelman *et al.*, 2011)

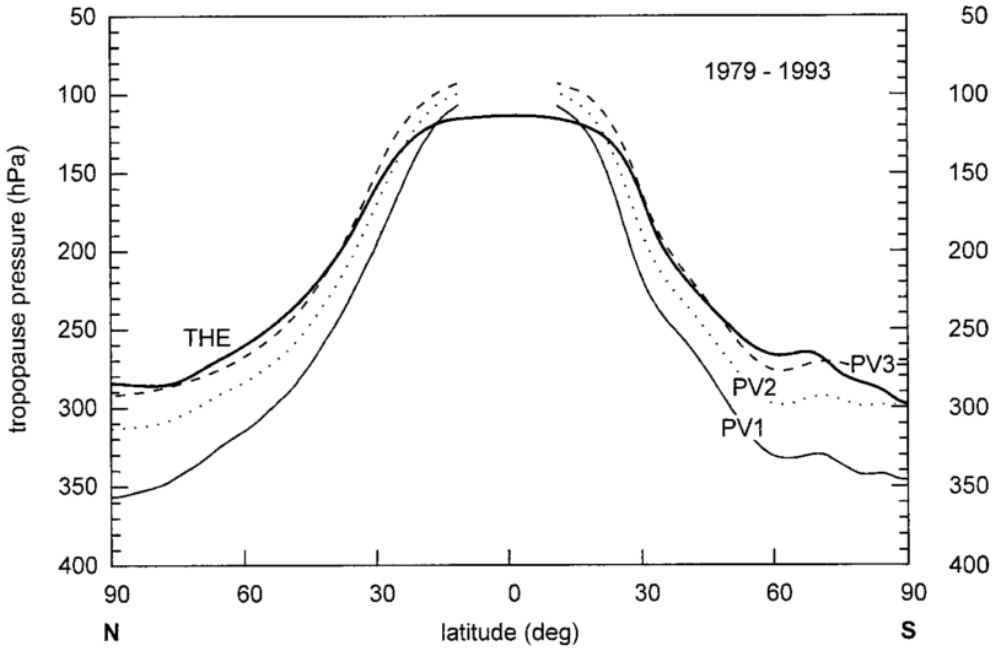

Fig. 1.8 Annual mean meridional profile of the zonally averaged tropopauses (1979-1993, 12 UTC): thermal tropopause (bold solid line), dynamical tropopause with 1.6PVU (thin solid line), 2.5 PVU (dotted line) and 3.5 PVU (dashed line) (reproduced from Hoinka, 1998).

tropopause pressure is lower in the NH than in the SH (Fig. 1.9); this is also in agreement with radiosonde data (Seidel and Randel, 2006).

Histograms of the tropopause pressure for selected latitudes (Fig. 1.10) show that the tropopause distribution is bell-shaped at the centre of the classical regions commented above -Tropics, midlatitudes and poles-, while bimodal distributions appear in the latitudes located near the edge of these regions, with peaks centred on the characteristic levels for the neighbouring regions. Hence, in these areas the tropopauses of the two regions coexist, and the method identifies one or another depending on the position of the discontinuity. This is particularly apparent in the subtropical areas, as the distance from the tropical to the midlatitude tropopause is greater. High-resolution tropopause distributions depict a similar picture, with typical values

Fig. 1.9 Annual- and zonal-mean tropopause (thick line), temperature (contours) and meridional temperature gradient (shaded) derived from Constellation Observing System for Meteorology, Ionosphere and Climate (COSMIC) Formosa Satellite Mission 3 mission (reproduced from Son *et al.*, 2011).

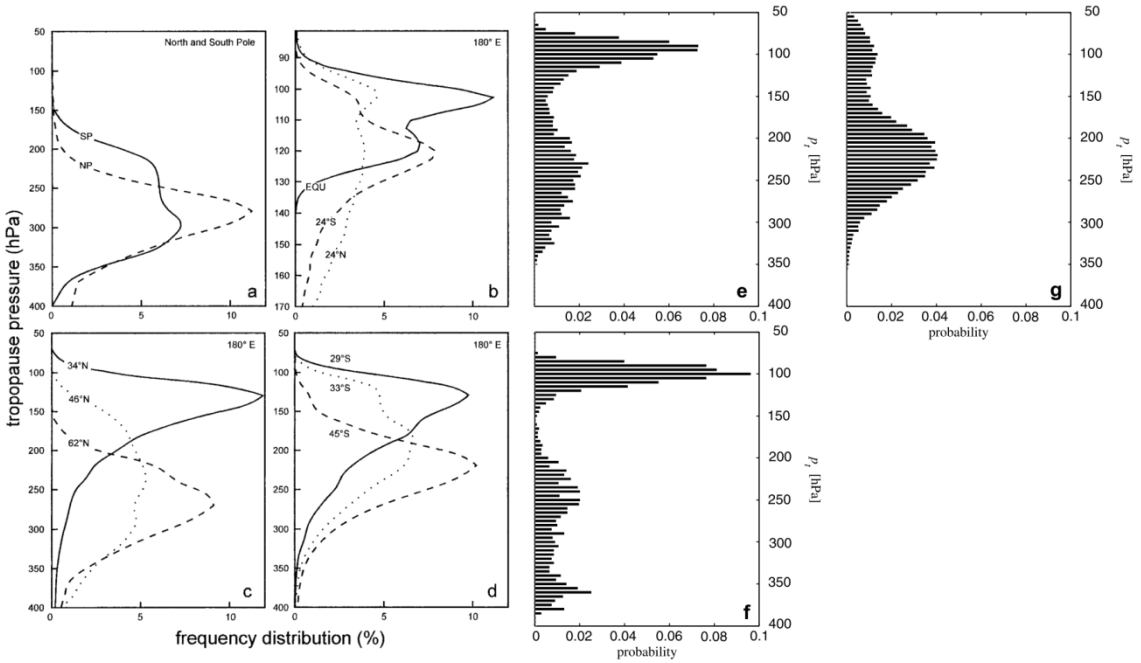

Fig. 1.10 Frequency distributions of the tropopause in (a) North and South Poles and (b,c,d) for selected latitudes along the 180ºE meridian in the ERA40 reanalysis; and (e) in the subtropical Asia (25º-35ºN, 60º-120ºE) for DJF, (f) in the Tibetan Plateau (34º-44ºN, 72º-100ºE) in JJA and (g) in Antarctica (70º-90ºS) during JJA derived from COSMIC GPS occultation measurements (adapted from Hoinka, 1998, and Son *et al.*, 2011).

around 100hPa for the tropical tropopause, around 250hPa for the midlatitude tropopause and between 250 and 300hPa for the Polar Regions. The southern pole tropopause is somewhat higher in the high-resolution measurements (Fig. 1.10). While it is true that this is a winter distribution, when the polar tropopause is higher as described below, note that a secondary peak appears in the histogram –sometimes erroneously identified as the tropopause- as the polar lower stratosphere is very nearly isothermal during the polar night (Highwood and Hoskins, 2000). In the boundaries between regions the occurrence of multiple tropopauses increases (Fig. 1.11), especially in the proximities of the subtropical jet stream in both hemispheres and of the polar jet stream in the Southern Hemisphere (Seidel and Randel, 2006; Añel *et al.*, 2007). This has been related to both intrusions of tropospheric tropical air into the midlatitude stratosphere above the subtropical jet (see, for example, Gettelman *et al.*, 2011) and to

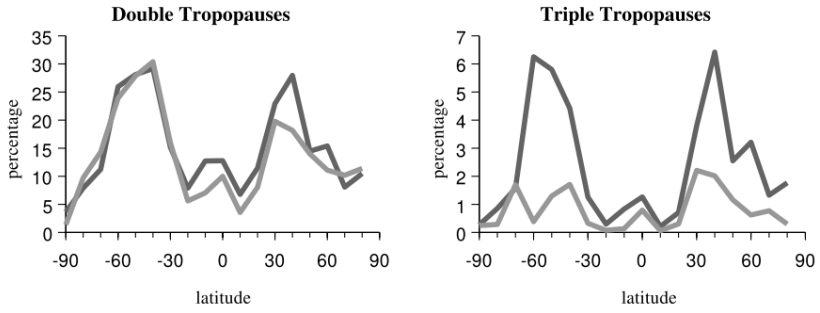

Fig. 1.11 Latitudinal distribution of the percentage of (left) double tropopauses and (right) triple tropopauses occurrence from radiosonde data (extracted from Añel *et al.*, 2007).

tropopause foldings associated with stratospheric intrusions along the polar front in higher latitudes, as discussed in section 1.1.1.2.

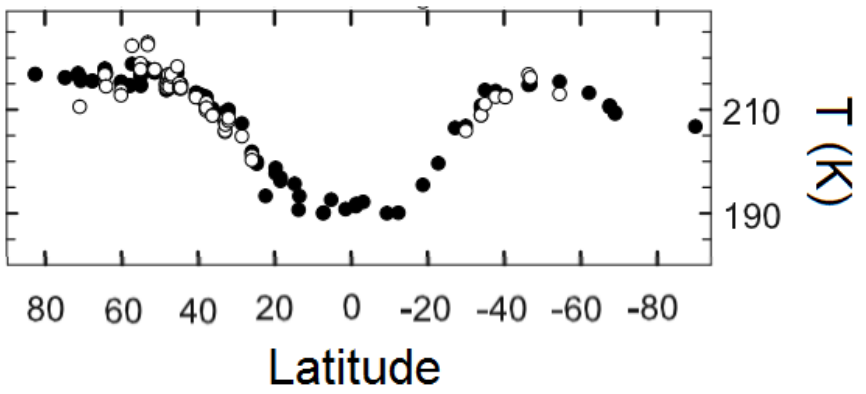

Fig. 1.12 Climatological average temperature of the tropopause as a function of latitude derived from radiosonde data (reproduced from Seidel and Randel, 2006).

Tropopause temperature varies meridionally in a similar manner as tropopause pressure (Fig. 1.12); hence, the tropopause is colder in the Tropics than in the extratropics, where its temperature is more or less constant with latitude. In the SH, tropopause temperature decreases slightly toward the pole as does tropopause pressure.

1.1.3 Tropopause Inversion Layer.

Using tropopause-based coordinates (see section 3.2 of this thesis for details) and high-resolution radiosonde data, Birner (2002) discovered the existence of a thin layer just above the tropopause level where the stratification locally reaches very large values exceeding the stratospheric stratification (see Fig. 1.13). This layer, named the Tropopause Inversion Layer (TIL), has a vertical extension of about 2km (Birner, 2002); hence the sharp increase in temperature is not seen in coarse datasets as the reanalysed data (Birner, 2006). Associated with this sharp increase in temperature, there is a wind minimum due to thermal wind balance (Birner, 2006)-note that, as the tropopause height is lower in the poles, a gradient of

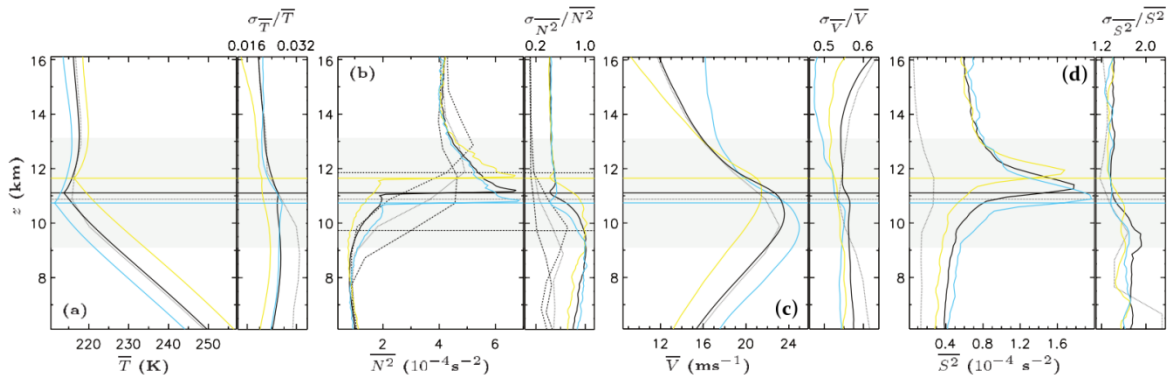

Fig. 1.13 Mean profiles and corresponding standard deviations of (a) temperature, (b), buoyancy frequency squared, (c) absolute wind speed and (d) vertical wind shear squared (reproduced from Birner, 2002).

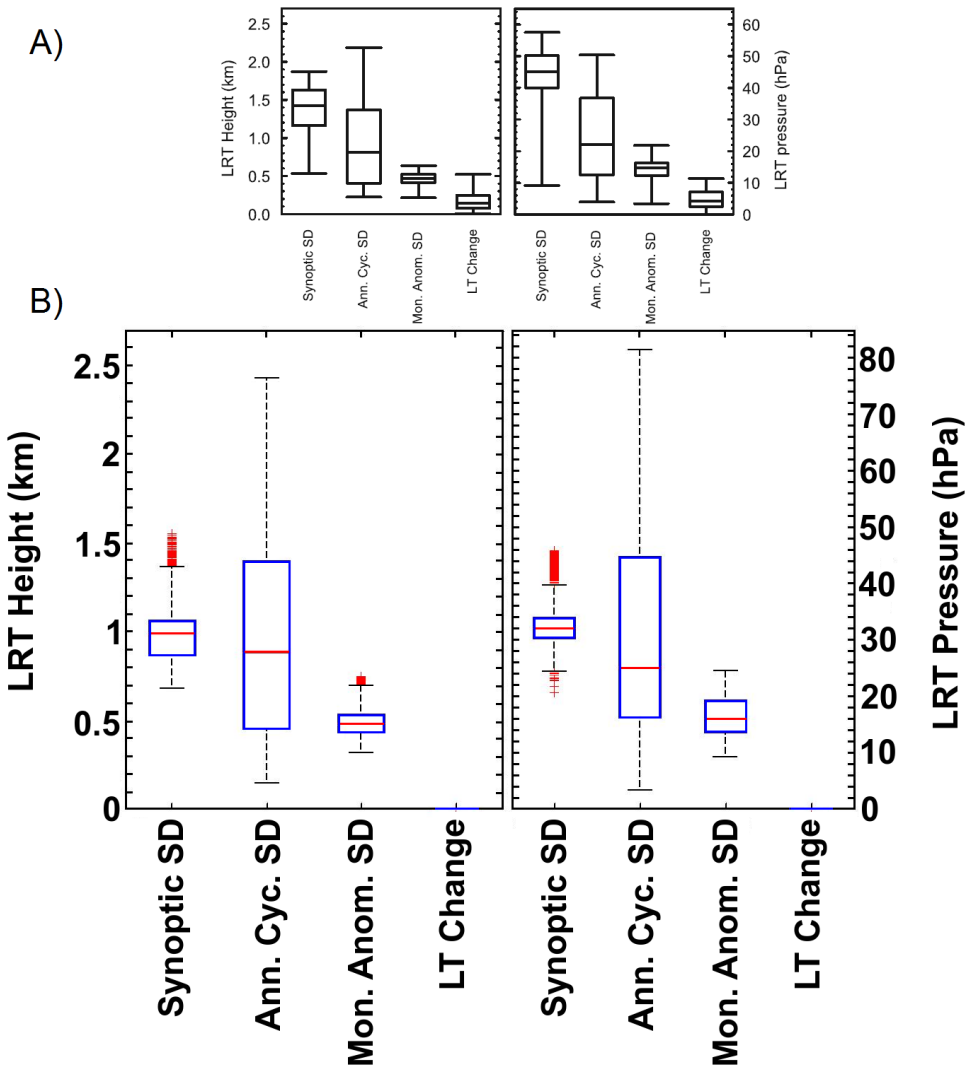

Fig. 1.14 Box plots showing the distribution of the standard deviations of the tropopause pressure (left) and height (right) in several temporal scales: synoptic (left box), annual cycle (left center box), month-to-month (right center box) and linear long-term trend (right box) for (A) the radiosonde and (B) the NCEP/NCAR Reanalysis-1 datasets (A is reproduced from Seidel and Randel, 2006).

temperature in the tropopause level is also a meridional gradient of temperature. As occurred with the discovery of the tropopause itself, the TIL was later proved to be a ubiquitous feature of the atmosphere (Birner, 2006). The TIL is apparent in satellite data (Grise *et al.*, 2010) and can also be simulated by models of varying complexity (Son and Polvani, 2007; Birner, 2010; Hegglin *et al.*, 2010).

The TIL is most intense over the Polar Regions in summer and above the tropical tropopause, although its vertical extension is larger in summer (Birner, 2006; Grise *et al.*, 2010).

There is still no complete satisfactory explanation of the mechanisms creating the TIL and modulating its characteristics. Some studies associate the TIL with cyclonic and anticyclonic circulations, which sharpen the stratification right above the tropopause (Wirth and Szabo, 2007), while others emphasize the radiative effect of tracer gases above the tropopause for enhancing the stratification in that region (Randel *et al.*, 2007) and still others point to the role of heating by the residual circulation in the lower stratosphere (Birner, 2010).

1.1.4 Variability of the tropopause pressure.

Analysis of the standard deviation of tropopause pressure in several scales of variability (Fig. 1.14) shows that the largest variations occur for the synoptic scales (Seidel and Randel, 2006), although in the reanalyses this variability may be underestimated due to their coarser resolution. Variations associated with the seasonal cycle are also of great importance, while month-to-month variations are half the magnitude of the synoptic variability.

The observed synoptic variability is mainly concentrated in the midlatitudes, as the synoptic variability in the Tropics is very small (Seidel and Randel, 2006). As shown in Fig. 1.15, the largest variations are found in the subtropics in winter, associated with multiple tropopause events (Son *et al.*, 2011), over the Tibetan plateau in summer, and along the oceanic stormtracks in winter, associated with the cyclonic activity in this region (Seidel and Randel, 2006; see section 6.2.2 of this thesis).

As in the case of the synoptic variability, the seasonal variability is higher in midlatitudes (Seidel and

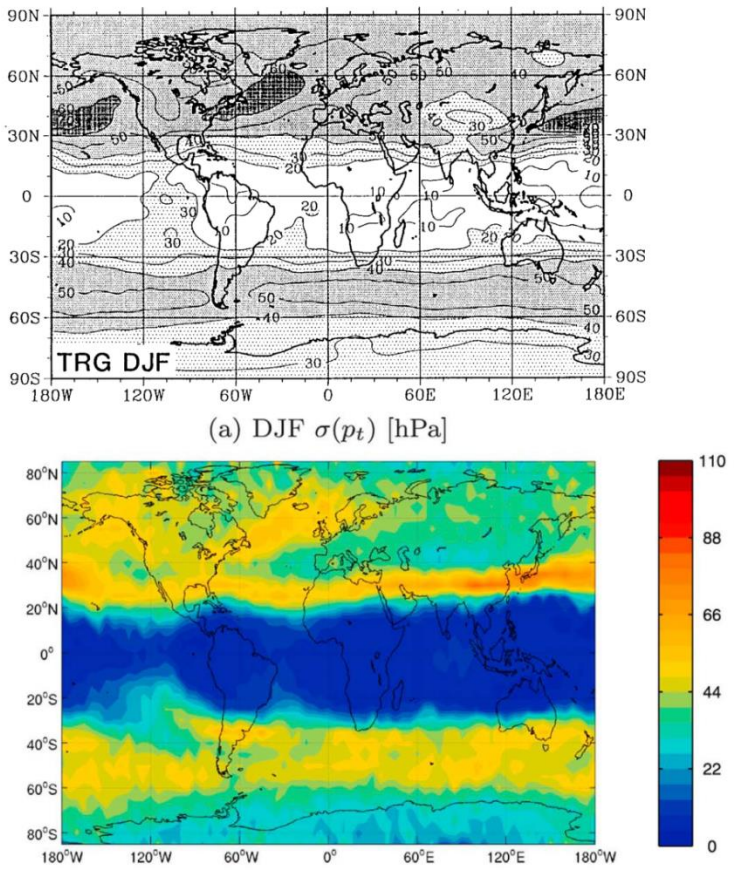

Fig. 1.15 Standard deviation of the tropopause pressure in DJF in (top) the ERA40 reanalysis and (bottom) derived from COSMIC observations (top reproduced from Hoinka, 1998; bottom reproduced from Son *et al.*, 2011).

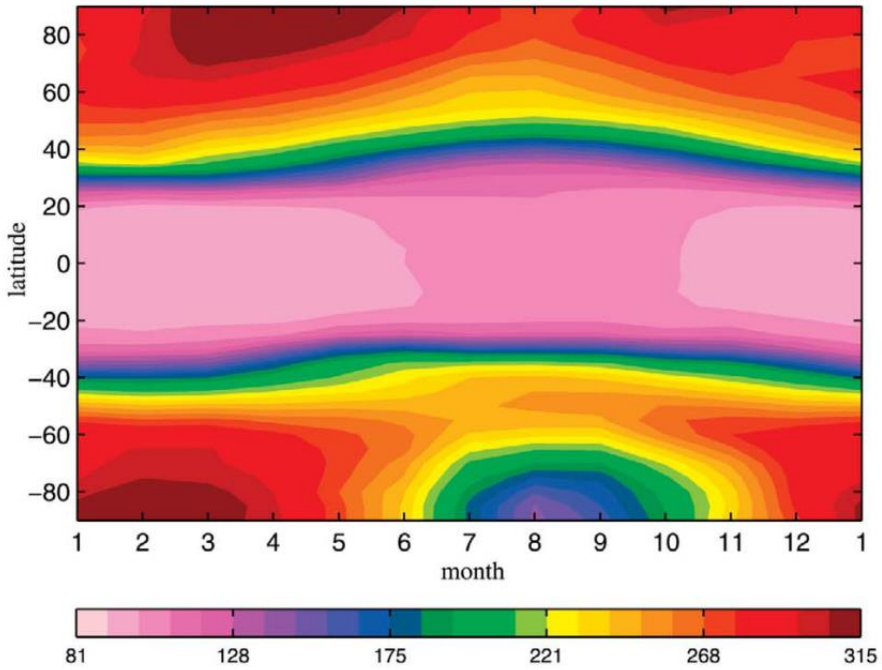

Fig. 1.16 Seasonal cycle of the zonal-mean tropopause (hPa), as derived from COSMIC observations (reproduced from Son *et al.*, 2011).

Randel, 2006), and it is also quite zonally symmetric. The seasonal cycle of the zonal-mean tropopause pressure is shown in Fig. 1.16. It can be seen that the tropical tropopause seasonal cycle is very weak, although tropopause is a bit higher in boreal winter than in boreal summer. Convection seems to play at best only a secondary role in the zonal-mean tropical-tropopause seasonal cycle (Seidel *et al.*, 2001), which seems to be more related to the upward branch of the Brewer-Dobson circulation (Randel *et al.*, 2002). In the NH the extratropical tropopause is higher in summer and lower in winter, while in the SH the tropopause follows the same annual evolution in the midlatitudes (40°-60°S) but the opposite evolution at higher latitudes. Note, however, that the maximum tropopause pressure in the NH occurs in spring for latitudes north of 60°N, with a secondary maximum in autumn.

The seasonal evolution of the tropopause was already related with the difference in temperatures between the lower stratosphere and upper stratosphere since the early times of the aerological science (Hoinka, 1997). For example, the rising of the tropopause during winter in the southern polar areas can be attributed to the greater amplitude of seasonal temperature variations in the polar lower stratosphere compared to the weaker upper-troposphere seasonal cycle (Möller, 1938; Hoinka, 1998; Zängl and Hoinka, 2001). As such, the seasonal evolution has a high degree of zonal symmetry (Zängl and Hoinka, 2001).

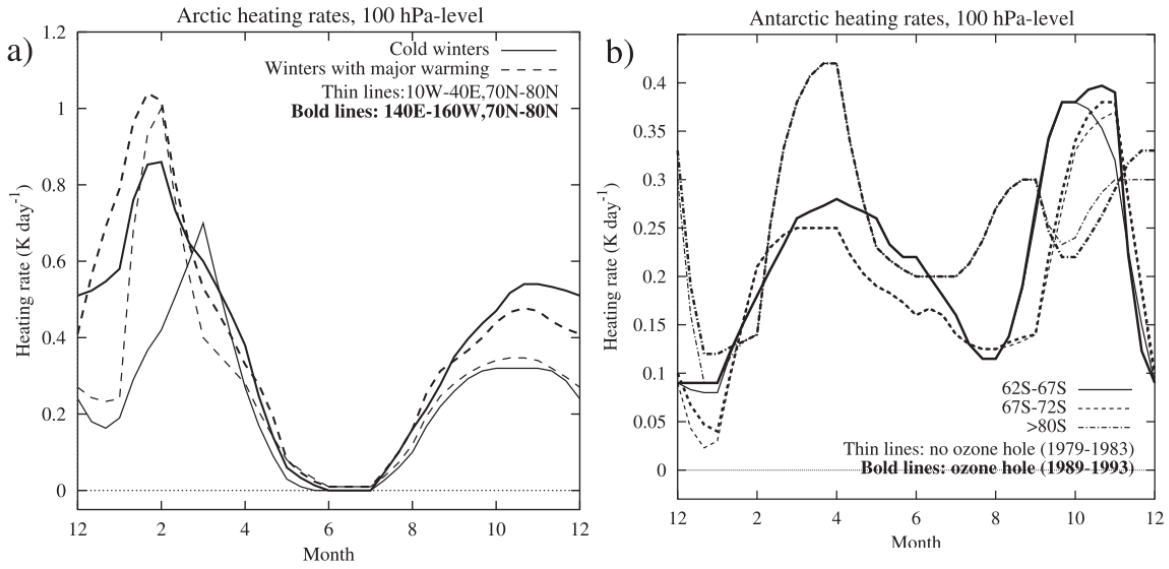

Fig. 1.17 Dynamical heating rates (K d $^{-1}$) at 100hPa for (a) high-latitude regions separated into cold winters and winters with major stratospheric warming and (b) for selected Antarctic regions, separated in simulation with and without ozone hole. The dynamical heating was obtained from a radiative-convective model (reproduced from Zängl, 2002).

In the midlatitudes, the seasonal cycle of lower-stratospheric temperatures is opposite to that of upper-tropospheric temperatures, hence the maximum temperature difference -and tropopause height- is reached in summer, and the minimum in winter (Hoinka, 1998); latent heat release may also play a role in the summer rising of the NH midlatitude tropopause (Wong and Wang, 2000).

The peculiar double-wave pattern of the northern Polar Regions is associated with an early increase in lower-stratosphere temperatures in spring, thus reducing the temperature difference with the upper-troposphere in this season (Zängl and Hoinka, 2001). The seasonal evolution of the Arctic tropopause is less zonally symmetric than in the Antarctic, with the double-wave pattern being characteristic of subpolar areas of northern Europe, western Siberia and very high latitudes (Zängl and Hoinka, 2001). Using a radiative-convective model to simulate the observed seasonal temperatures, Zängl (2002) found that the spring maximum tropopause pressure was associated with a maximum in dynamical heating (Fig. 1.17a) and that this heating was stronger in areas with a double-wave seasonal cycle. He related this heating to warming events in the polar vortex associated with the residual circulation forced by Rossby waves, which is in agreement with the correlation found by Highwood and Hoskins (2000) between the polar tropopause the Arctic Oscillation Index,

and with the observed tropopause pressure during the 2009 Sudden Stratospheric Warming Event (Son *et al.*, 2011).

Antarctic dynamical heating is smaller (Fig. 1.17b), consistent with the weaker residual circulation there in the absence of orographic forcing (Holton *et al.*, 1995), except in the austral summer (DJF), when the dynamical heating in the Arctic is close to zero. The origin of this dynamical heating is not clear (Zängl, 2002), but Rosenlof (1996) suggests that gravity waves and/or waves with zonal wavenumber greater or equal to 8 may induce the required circulation. Additionally, a double-wave pattern is observed in the Antarctic dynamical heating. Zängl (2002) speculated it might be caused by the downward motion within the vortex area associated to the ageostrophic circulation necessary to maintain geostrophic balance in a vortex with differential heating, as is the case for the southern polar vortex in spring and autumn.

1.2 Theories on the average height of the tropopause.

We have explained in previous sections the characteristics and variability of the tropopause. However, the very existence of the tropopause has not been addressed yet.

The first explanation can be found in so-called radiative-convective models (Houghton, 1977). Fig. 1.18a shows the temperature profile of an atmosphere that is transparent to solar radiation but absorbs thermal radiation emitted from the ground. As can be seen, temperature drops quickly in the lower levels, leading to static instability near the ground. At higher levels, a nearly isothermal profile is established. The classical picture states that the instability near the ground favours the growth of dynamical perturbations that tend to stabilize the profile (Fig. 1.18b); this leads to a uniform lapse rate over the adjusted region and an abrupt change in lapse rate at the boundary with the radiative-equilibrium region, which is identified as the tropopause. The new tropospheric lapse rate has to be neutral or stable -in a mean sense- to the dynamical perturbations that create it, or new perturbations would grow to adjust it.

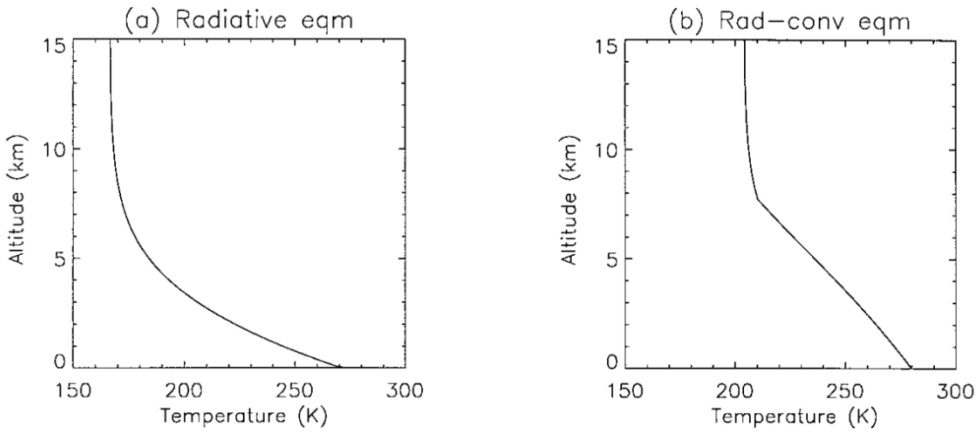

Fig. 1.18 (a) Radiative equilibrium temperature profile; (b) radiative–convective equilibrium temperature profile (reproduced from Thuburn and Craig, 1997).

While this simple model explains the existence of a tropopause, in truth the problem has only been rephrased: the dynamical mechanisms that adjusted the tropospheric profile to the observed values still need to be determined. The most obvious dynamical mechanism is some form of dry or, more generally, moist convection. In the Tropics, the observed mean lapse rate is close to moist adiabatic (see, e.g., Fueglistaler *et al.*, 2009), so the radiative-convective model may have physical relevance -note, however, that in the layer just below the tropopause level the observed lapse is much more stable than moist adiabatic, and that, as noted above, the seasonal cycle seems to be more correlated with the wave-forced residual circulation. However, the observed lapse rate in the extratropics is far more stable than the dry or moist adiabatic, with values near 6K km^{-1} (e.g., 6.5K km^{-1} for the U.S. Standard Atmosphere) or less. Hence, it is clear that other processes different from moist convection have to account for the adjusted profile.

Eddies generated by baroclinic instability dominate the energy transport in the extratropics, hence it seems natural to assume that they also act to maintain a neutral or stable lapse rate to baroclinic instability. Baroclinic adjustment is a classical problem in atmospheric dynamics, but the conditions for the instability are not as clear as in the moist convection case. Assuming the quasi-geostrophic and Boussinesq approximations to be valid, then suffcient conditions for baroclinic instability are that the meridional gradient of the zonal-mean potential vorticity

$$\overline{q}_y = \beta - \overline{u}_{yy} + f\left(\frac{\overline{\theta}_y}{\overline{\theta}_z}\right)_z$$

is greater or equal to 0 and that the meridional gradient of potential temperature at the surface is greater or equal than 0 (Charney and Stern, 1962). Subscripts denote derivatives along the directions indicated, β is the meridional derivative of f, the Coriolis parameter and the overbars stand for the zonal averages. Hence, neglecting the relative vorticity term:

$$\bar{q}_y \approx \beta + f\left(\frac{\bar{\theta}_y}{\bar{\theta}_z}\right)_z \geq 0 \Rightarrow h \leq -\frac{\beta}{f}\left(\frac{\bar{\theta}_y}{\bar{\theta}_z}\right) \qquad (1)$$

where the vertical derivative was approximated by a finite difference along the depth of effective potential vorticity mixing by the eddies (Held, 1982). It is expected, based on the conceptual model introduced above, that this scale height should be the same as the tropopause height. As $f/\beta \sim a$, the radius of Earth, this implies that an isentrope leaving the surface at the Tropics should reach the tropopause level at the Poles for the atmosphere to be neutral to baroclinic instability according to this model. Thus, the effect of eddies is to transport heat upwards and/or northwards and to flatten the isentropic slope until the meridional potential vorticity gradient is eliminated over a layer with depth h. As shown in Fig. 1.4 (section 1.1.1.2), the observed mean isentropic slope in the troposphere roughly coincides with what is expected from baroclinic adjustment and, as noted in section 1.1.1.2, the tropopause is associated with a sharp increase in potential vorticity from the low tropospheric values to high stratospheric values (though the dynamical tropopause is defined using Ertel's potential vorticity, which is not exactly the same as the potential vorticity

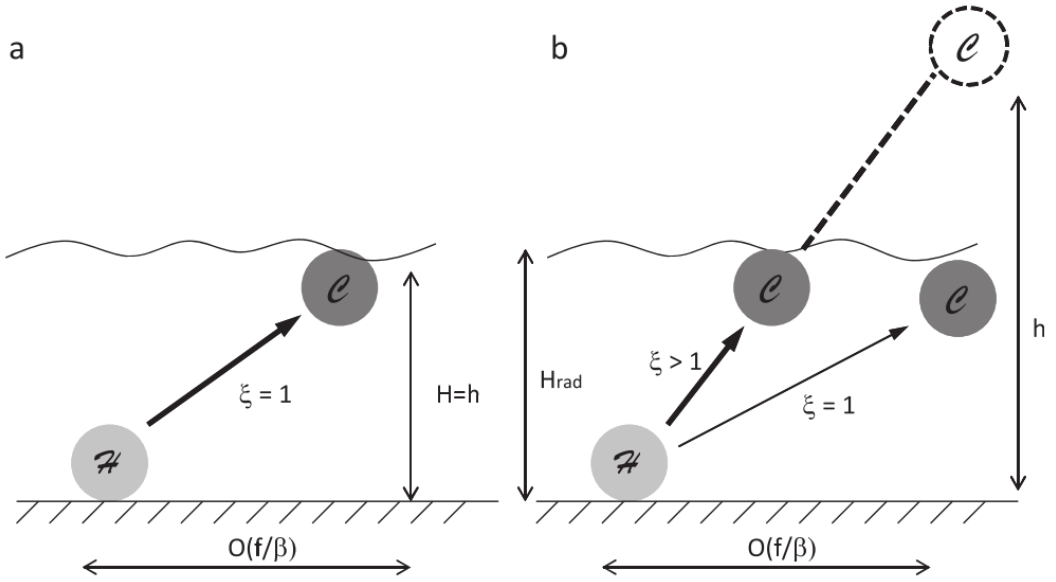

Fig. 1.19 (a) The characteristic isentropic slope when the scale of the eddies and the scale of radiative equilibrium is the same; (b) the isentropic slope (thick line) when the vertical scale of the diabatic heating limits the tropopause height (H_{rad} < h). In that case, the flow is supercritical unless the isentropic slope flattens to the thin line (reproduced from Zurita-Gotor and Vallis, 2011).

considered here). This relationship poses a constraint on tropopause height, which is known as the *dynamical constraint* after Held (1982).

The problem is not closed, as the temperature profile adjusted by the baroclinic eddies should coincide with the radiative equilibrium temperature at the tropopause level. This poses a second constraint on tropopause height, called the *radiative constraint* by Held (1982). This is equivalent to saying that the dynamical heating produced by the eddies in the tropospheric column to adjust the profile must match the radiative cooling at the tropopause. As pointed out by Zurita-Gotor and Vallis (2011), as a statement of the energy conservation this relation must always be satisfied. The radiative constraint introduces a problem in the system: the radiatively determined tropopause height and the vertical extent of dynamical heating by the eddies must exactly coincide. For example, Fig. 1.19 shows a situation in which both coincide (a) and a situation in which the radiative constraint prevents the eddies from mixing potential vorticity as high up as demanded by baroclinic adjustment. It is unclear whether baroclinic adjustment has some role in determining the tropopause level or other mechanisms are in charge of the tropospheric adjustment.

Using a General Circulation Model, Thuburn and Craig (1997) tested the validity of baroclinic adjustment in a series of experiments. In simulations using Earth-like parameters the mean state was found to be consistent with baroclinic adjustment (as is also the case in the observed atmosphere). However, when the parameters were varied from that setting, the mean state did not change as predicted by baroclinic adjustment. In contrast, the results were consistent with the radiative constraint in all cases. Thus, Zurita-Gotor and Vallis (2011) have argued that a tight radiative constraint may constrain the sensitivity of tropopause height to dynamical forcing, consistent with the good agreement found by Thuburn and Craig (1997). On the other hand, simulations varying tracer abundances and the intensity of the stratospheric circulation show that these factors, which are not included in the radiative constraint, may greatly impact tropopause height (Thuburn and Craig, 2000).

Consistent with the PV mixing idea, Haynes *et al.* (2001) obtained a tropopause as a discontinuity created by eddy PV mixing in an idealized model. On the other hand, Egger (1995) found in a baroclinic channel model that while baroclinic eddies modify the height

and meridional structure of the tropopause through horizontal and vertical eddy heat fluxes, rising the tropopause on the northern part of the channel, the final state does not agree with baroclinic adjustment in the form of (1). Using reanalysis data, Dell'Aquilla *et al.* (2006) studied the impact of intense synoptic wave activity on the tropopause -hence the driving of intraseasonal tropopause variability by baroclinic eddies-, finding results consistent with Egger (1995): the tropopause rises to the north of the enhanced eddy activity. However, Son *et al.* (2007) have more recently found in their analysis of intraseasonal tropopause variability in the midlatitudes that the main process driving tropopause ascent is not the tropospheric heat flux but the heating above the tropopause by the upward propagating planetary waves (see Fig. 1.20).

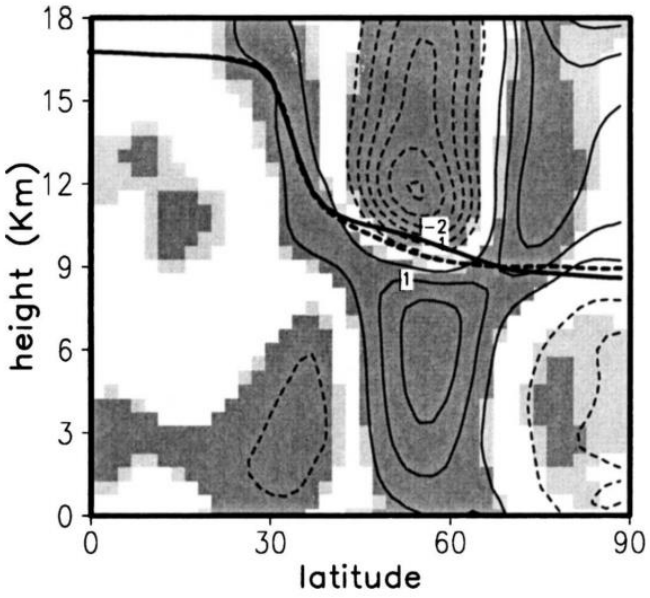

Fig. 1.20 Heating (contours), as measured by as the increment increase in of the anomalous potential temperature, during the developing phase growth of a positive tropopause anomaly, associated with the shown rising of the tropopause height (indicated by the thick solid thick line). Dashed thick solid line stands for the composite tropopause. The thick dashed line is the climatological tropopause (reproduced from Son *et al.*, 2007).

Juckes (2000) proposed yet another mechanism for adjusting the tropospheric profile. As commented above, the observed tropospheric lapse rate is more stable than the moist adiabatic. Using equivalent potential temperature, this means the vertical gradient of this magnitude is strictly positive. Juckes argued that moist convection on the warm sectors of extratropical cyclones might set the tropopause temperature, so that the difference in equivalent potential temperature between the surface and the tropopause is exactly oK over these regions. This would set the minimum stratification along a latitude circle but, because the surface temperature is colder in other parts of the wave, the surface-to-tropopause equivalent potential temperature difference there and in the zonal mean would still be positive. Juckes' model predicts that the observed mean stratification should be the minimum (oK km^{-1} in terms of the equivalent potential temperature) plus half its variance (corresponding to a Gaussian distribution), and that the latter should be proportional to the

meridional temperature gradient, as these gradients are meridionally advected to create surface temperature anomalies. Thus, Juckes' model gives a similar closure to baroclinic adjustment, except that the closure uses equivalent potential temperature instead of temperature. This is a key difference, as several studies have found that moist processes may have a role in the extratropical tropospheric adjustment (see Wu and Pauluis, 2014 for a review). For example, Pauluis *et al.* (2010) demonstrates that the moist residual circulation is stronger than its dry counterpart, and Wu and Pauluis (2014) find a connection between the potential temperature at the tropopause and the statistical distribution of equivalent potential temperatures at the surface.

Still, there is no unanimity as to what processes determine the tropopause height, and the roles played by the baroclinic waves, stratospheric processes and moisture.

1.3 Brewer-Dobson circulation

As commented above, the meridional structure of the tropopause has been linked to the heating by the BD circulation. This circulation, first discovered by Brewer (1949), consists of air rising at tropical latitudes and penetrating into the stratosphere, moving poleward quasi-horizontally, and sinking in the midlatitudes and Polar Regions. The BD circulation may be regarded as the stratospheric branch of a global thermally-direct cell, in which air moves poleward at upper levels and returns to the equator near the surface (a sketch is shown in Fig. 1.21). This circulation is only apparent when a Lagrangian perspective is used (i.e., following the particle trajectories, for example using tracers as ozone or water vapour –as Brewer did). Still, an approximation to the Lagrangian circulation can be computed in the Eulerian framework by means of a special transformation –known as the Transformed Eulerian-mean (see Section 3.6 for details). The resulting circulation is called the residual circulation and will be used extensively in this thesis

The importance of the BD circulation for the tropopause is due to the heating effects associated with the vertical movement of the air masses in a stratified atmosphere: upward (downward) movement is associated with adiabatic cooling (warming) along the vertical branches of the BD circulation –we refer to this heating as the *dynamical* heating (as opposed to the *diabatic* heating, which is primarily radiative in the stratosphere). As noted above,

changes in the temperature field above and/or below the tropopause level are associated with changes in its pressure. Hence, the tropical tropopause will be higher (as the lower stratosphere is colder) and the extratropical tropopause will be lower (as the lower stratosphere is warmer) than they would be if the stratosphere were in radiative equilibrium; this is consistent with the meridional tropopause structure described in the previous section (Haqq-Misra, 2002). While the tropopause slope has been traditionally linked to the stratospheric Brewer-Dobson circulation, Zurita-Gotor and Vallis (2013) found that separation between the tropical and extratropical tropopauses also occurs in an idealized model in the absence of a *deep* stratospheric circulation. In their model, the tropopause break is forced by the shallow branch of the stratospheric residual circulation, which is forced by tropospheric synoptic waves as described below.

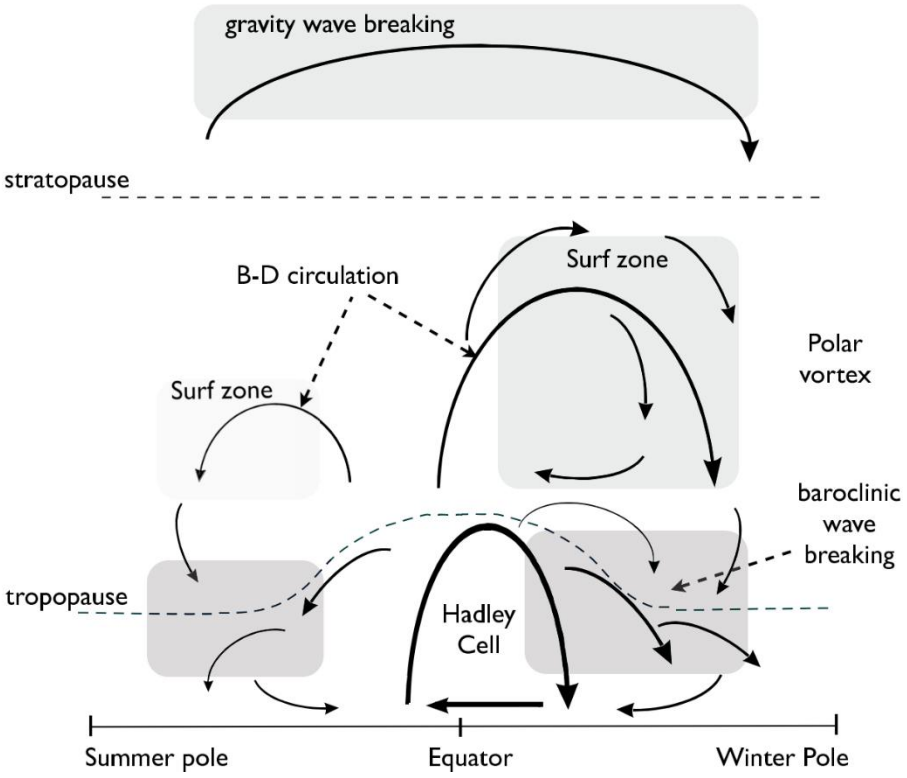

Fig. 1.21 A schema of the residual mean meridional circulation of the atmosphere. The solid arrows indicate the residual circulation and the shaded areas the main regions of wave breaking associated with the circulation (reproduced from Vallis, 2005).

From a dynamical point of view, this circulation is forced in response to Rossby wave breaking in the stratosphere (the so-called 'Rossby wave pump'). The Coriolis force associated with the poleward flow produces an eastward torque that balances the westward acceleration by the breaking waves. Note that the tropical and polar vertical motions, necessary by continuity, are non-local responses to the wave breaking (which mainly occurs in the midlatitudes in the area known as the *surf zone*, extending from the edge of the stratospheric polar vortex to the subtropics, corresponding to the shaded areas in the sketch of Fig. 1.21). Plumb (1999) notes that the BD circulation consists of two different branches: a

shallow branch right above the tropopause forced by the breaking of synoptic tropospheric waves near the subtropical jet, and a deep branch associated with the propagation of planetary Rossby waves into the stratosphere. Since the upward propagation of Rossby waves is only possible in winter in the stratosphere, when zonal winds are westerly (see section 3.6), the Brewer-Dobson circulation is stronger in the winter hemisphere, depressing the midlatitude tropopause during this season. Further details on the residual circulation-tropopause connection will be given where relevant in this thesis.

For further details on the BD and residual circulations, see for example Andrews *et al.*, (1987) or Vallis (2005)

1.4 Motivation and objectives.

From the above, it can be deduced that there are still significant gaps in our understanding of the processes determining the tropopause level and driving its variability. Based on the lapse rate definition, a warming in the upper troposphere and/or a cooling in the lower stratosphere will raise the tropopause, and vice versa (Shepherd, 2002). This seems to be the case for synoptic and monthly variability of the tropopause, both of which are characterized by large, opposite-sign correlations at levels above and below the tropopause (Seidel and Randel 2006); a similar potential temperature dipole was also found by Son *et al.* (2007) for the intraseasonal variability of the zonal-mean tropopause (see Fig. 1.20). This pattern could be produced by dynamically balanced circulations characteristic of cyclones and anticyclones in the case of synoptic variability (Seidel and Randel, 2006; Zängl and Wirth, 2002) and by the accumulated effects of the synoptic variability in the case of monthly variability (Seidel and Randel, 2006). Yet despite all of these studies, a systematic analysis of the variability of the zonal-mean tropopause is still lacking. To the author's knowledge, there is not any previous work discussing the leading modes of intraseasonal extratropical tropopause variability and their dynamics, although principal component analysis has been previously applied to tropopause height variability on interannual time scales (Wong and Wang, 2003). While local variations in tropopause height are expected to be dominated by tropopause deformations on synoptic scales (Hoskins *et al.*, 1985), the driving of the zonal-mean tropopause variability is not as obvious and different mechanisms may contribute to

that variability. Two different scenarios can be conceived. If baroclinic equilibration played the dominant role for tropopause variability, it might be expected this variability to be driven by changes in eddy heat fluxes and by tropospheric baroclinic dynamics. Alternatively, tropopause variability might be associated with changes in the barotropic flow and with adjustment to balance accompanying the surface pressure changes associated with the annular mode variability (Thompson and Wallace, 2000). In that scenario, stratospheric dynamics might also be important (Son *et al.*, 2007) and eddy momentum fluxes may play a more important role than eddy heat fluxes in the troposphere.

The discontinuity between the tropospheric and the stratospheric characteristics motivates a number of possible definitions for the tropopause (Ivanova, 2013), as the level at which certain variables reach specific values. These thresholds are chosen empirically and do not reflect any fundamental property of the tropopause, which is determined by the complex interaction of dynamical, diabatic and chemical processes over the upper troposphere – lower stratosphere (UTLS) region (Gettelman *et al.*, 2011). As a result, standard definitions of the tropopause may not be appropriate in climates very different from present-day climate (e.g., in glacial climates) or may not work equally well in all regions. (For example, over the tropics tropopause definitions based on potential vorticity do not work well and the cold-point tropopause is often used in place of the traditional thermal definition). This prompts the question of whether traditional tropopause definitions are optimal or alternative definitions might be superior for separating the troposphere and the stratosphere, at least in some regions/climates. For example, the thermal definition of the tropopause is motivated by the observation that the tropospheric and stratospheric stratifications follow distinct distributions because they are determined by different physical processes (Held, 1982). The standard 2 K km^{-1} criterion provides a reasonable separation between both distributions and has been used operationally to define the tropopause with much success. However, this threshold is unlikely to work well in climates with very different distributions of tropospheric and/or stratospheric stratifications, or in models where the parameter space is located further from the observed values (Birner, 2010).

The main objectives of this thesis are:

▪ Assess if the thermal definition is the best criterion for locating the tropopause, that is, for separating the tropospheric and stratospheric air masses.

▪ Explore objective definitions of the tropopause that are based on its phenomenology rather than on empirical thresholds appropriate for present-day climate and that can therefore be applied to very different climates.

▪ Analyse the causes of the seasonal cycle of the zonal-mean tropopause in reanalysis data and assess the relevance of the mechanisms using an idealized model.

▪ Find the leading modes of intraseasonal variability of the zonal-mean tropopause and analyse their underlying dynamics to ascertain the relevance of baroclinic adjustment for this variability.

▪ Investigate using the idealized model the mechanisms involved in the internal variability of tropopause height.

1.5 Thesis outline.

This thesis is structured as follows:

▪ Chapter 2 introduces all the datasets used in this thesis: radiosonde data obtained from a global archive (IGRA) and the reanalyses NCEP/NCAR Reanalysis-1 and ERA-Interim. It is also described the idealized model used in this thesis and its setup.

▪ Chapter 3 is dedicated to explaining the different methodologies used in this thesis, from the determination of the tropopause height and the use of Tropopause-based coordinates to the analysis of time series -including time filtering, Principal Component Analysis and periodogram techniques. It is also discussed the use and significance of key dynamical concepts like the Eliassen-Palm fluxes or the residual circulation.

▪ Chapter 4 analyses optimal thresholds for defining the tropopause, with insights on the thermal characteristics above and below the tropopause level. Additionally, two new objective definitions for the tropopause level are proposed.

▪ Chapter 5 describes the analysis of the seasonal variability of the zonal-mean tropopause in both reanalyses and the idealized model. The results demonstrate the important role of the residual circulation associated with orographic forcing for the tropopause seasonal evolution, especially over the polar region.

▪ Chapter 6 describes and explains the leading modes of intraseasonal variability of the zonal-mean tropopause in the reanalysis. The results highlight the important role played by both eddy flux anomalies near the tropopause and anomalies in the polar vortex. Additionally, the leading modes of zonal-mean tropopause variability in a set of simulations with the idealized model are presented.

▪ Chapter 7 summarizes the main conclusions of this thesis on the separation between the tropospheric and stratospheric air masses and the variability of the tropopause in seasonal and intraseasonal scales.

The references used in this thesis are listed at the end of this document, where we also list the publications and contributions to scientific meetings resulting from this thesis.

2. Data sources: radiosondes, reanalyses and model.

Several sources of data are employed in this thesis to assess the robustness of the results. When studying the tropopause, the vertical resolution of the data plays a key role because the tropopause is defined using the vertical gradient of temperature. Radiosonde data have the best vertical resolution but, as a drawback, they have very poor coverage: they are irregularly spaced over the world, which makes them less useful for studying large-scale spatial patterns such as modes of variability, and the time series are incomplete. For this reason, data from reanalysis are also employed in this thesis. Specifically, we use NCEP/NCAR Reanalysis 1 and ERA-Interim to produce global fields of tropopause height on a regular grid and to analyse large-scale patterns of tropopause variability.

The main disadvantage of reanalysis data is their lower vertical resolution compared to the radiosonde data, which may affect the determination of tropopause height. Nonetheless, several studies (Randel *et al.*, 2000; Kiladis *et al.*, 2001; Ribera *et al.*, 2008) have shown that the biases in tropopause height are constant in time, so that tropopause variability is similar

in the radiosondes and in the reanalyses, and that tropopauses calculated using radiosonde and reanalysis data are quite similar except in the subtropics (Reichler *et al.*, 2003). The reanalysis data have been widely used in the study of the mean tropopause (Hoinka, 1998), its variability (Zängl and Wirth, 2001; Son *et al.*, 2007; Dell'Aquila *et al.*, 2007) and its long-term trends (Santer *et al.*, 2003), validating them as a good representation of the atmospheric system even though they are not actually an observational dataset like the radiosondes. Other possible sources of data with high vertical resolution, such as GPS radio occultation observations, show a similar tropopause structure to the reanalyses (Liu *et al.*, 2014).

Finally, an idealized model is used to study the dynamics of tropopause variability. For the purpose of this study, we regard the model output as an additional 'data source', even though this is obviously not observed data and the idealized model is much simpler than the real atmosphere.

2.1 IGRA dataset.

Radiosonde data were obtained from the Integrated Global Radiosonde Archive (IGRA) from the National Oceanic and Atmospheric Administration (NOAA); this consists of a worldwide net of radiosonde stations with several years of information, mostly extending from the 1960s to the present. The data come from a wide variety of sources (see Table 2.1) and constitute the largest radiosonde dataset freely available (Durre *et al.*, 2006). All data are subjected to quality tests before being included in IGRA in order to eliminate duplicate soundings (many of the stations have periods of record coming from different sources that overlap for some time), detect data transmission errors, identify changes in the name or location of the station, etc. Other quality checks include: elimination of soundings with data outside the known periods of record and missing or impossible launching hour, as well as data that clearly exceed all known world extremes; elimination of duplicate data with the same pressure or geopotential height; correction or elimination of surface data due to inconsistencies in the surface elevation; internal checks on the physical coherence of the data (for example, checking that the hypsometric equation is satisfied or that geopotential height increases monotonically with pressure) and climatological checks (eliminating outliers to the statistical distribution of the data).

	Data source	Period of record	Area of coverage	Number of stations	Percent of IGRA soundings
Core	NCDC historical GTS	1963-70	Global	820	7.94
	NCEP/NCAR GTS	1970-72	Global	848	3.01
	NCEP GTS	1973-99	Global	1517	64.06
	NCDC real-time GTS	2000-present	Global	1093	7.13
Other large scale	Russian GTS	1998-2001	Global	923	1.59
	U. S. Air Force	1946-73	Global	292	4.49
	Australian GTS	1990-93	Southern Hemi-sphere	170	0.15
Country specific	United States	1946-2001	United States +U.S. Military	150	9.81
	Australian	1938-89	Australia and its territories	17	1.63
	Argentine	1958-91	Argentina	8	0.18
	South Korean	1984-92	South Korea	4	0.01

Table 2.1: Data sources for IGRA. Acronyms correspond to: the National Climatic Data Center (NCDC); Global Telecommunication System (GTS); the National Center for Environmental Prediction (NCEP) and the National Center for Atmospheric Research (NCAR). For each source, IGRA contains the periods of record, number of stations, and percentage of soundings listed (adapted from Durre et al, 2006).

The number of stations per year included in the dataset after all these checks is shown in Fig. 2.1. Note that not all the stations included are still operative, so the number of stations is less than the total available in the IGRA dataset. Fig. 2.2a shows the location of each of the stations included in IGRA. It can be seen that most of the stations lie over the continental areas of the Northern Hemisphere, especially in the subtropical areas and midlatitudes. As shown in the histogram of Fig. 2.2b, nearly half of the stations (719 out of 1539) are located between 30°N and 65°N. This is representative of the sparse nature of radiosonde data, both in space and time, which makes the climatological analysis very difficult.

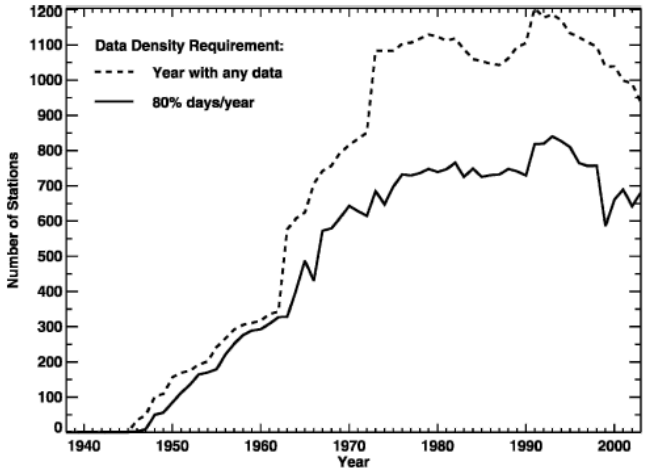

Fig. 2.1: Number of stations in IGRA for each year where data are available on at least one day of the year (dashed line) and at least 80% of the days in the year (solid line) (extracted from Durre et al, 2006).

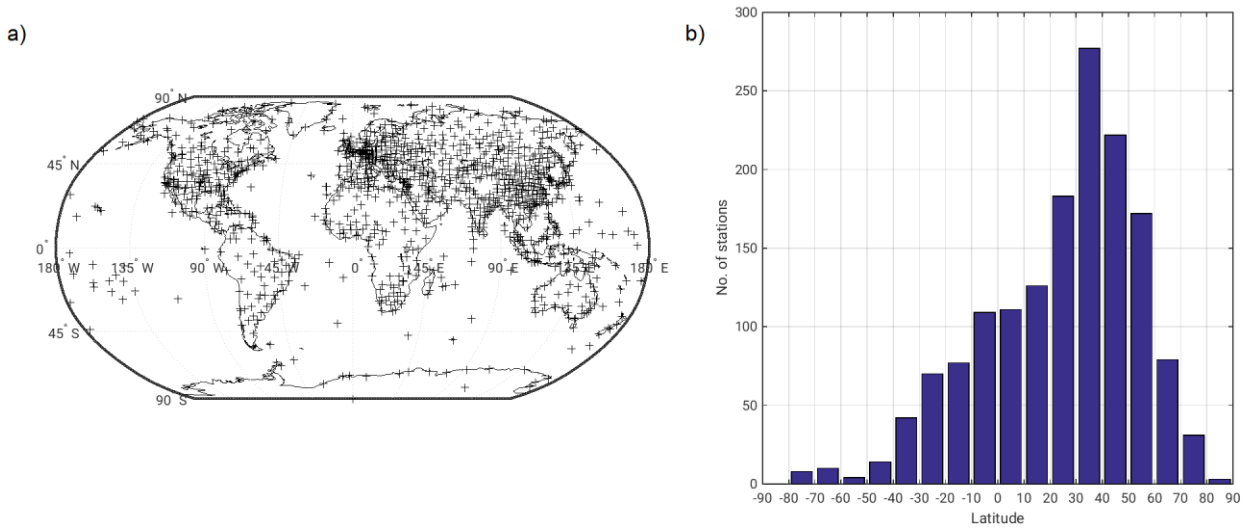

Fig. 2.2: a) Locations of the IGRA stations. b) Number of IGRA stations in each 10o-latitudinal band.

IGRA dataset has already been used for the analysis of multiple tropopauses (Añel *et al.*, 2007) and tropopause variability (Seidel and Randel, 2006), although both studies deal with subsets of the complete dataset selected for their temporal and spatial homogeneity. IGRA includes reports of the tropopause level calculated in each sounding using the WMO definition. These reports, however, are not homogeneous spatially or temporally, and are frequently missing (Añel *et al.*, 2007). Defant and Taba (1958) showed that the tropopause in these reports tends to appear in levels ending with '50' or '0' and Endlich (1954) and Hoinka (1997) showed that there was a tendency to assign the tropopause level to the mandatory levels, presumably due to the process followed in the analysis of the sounding (Hoinka, 1997), see Fig. 2.3. These reports were thus not used in this thesis; instead, we calculated the tropopause from the temperature profiles as described in the next chapter.

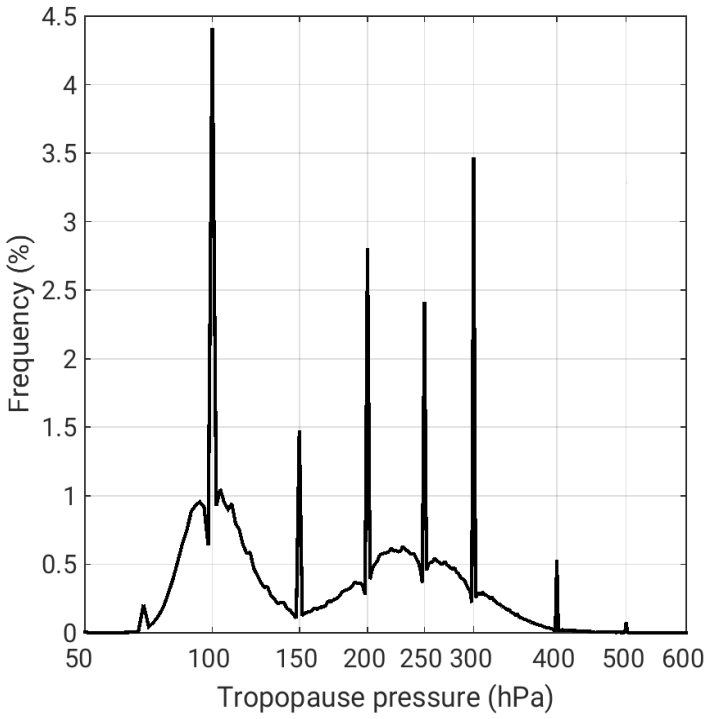

Fig 2.2: Histogram of the reported tropopause pressures (hPa) in the PATXI dataset (a subset of IGRA; for more details, see Añel et al, 2007).

The tropopause determined from the temperature profiles is not, however, free of errors. On the one hand, temporal inhomogeneities may arise due to biases introduced by changes in instru

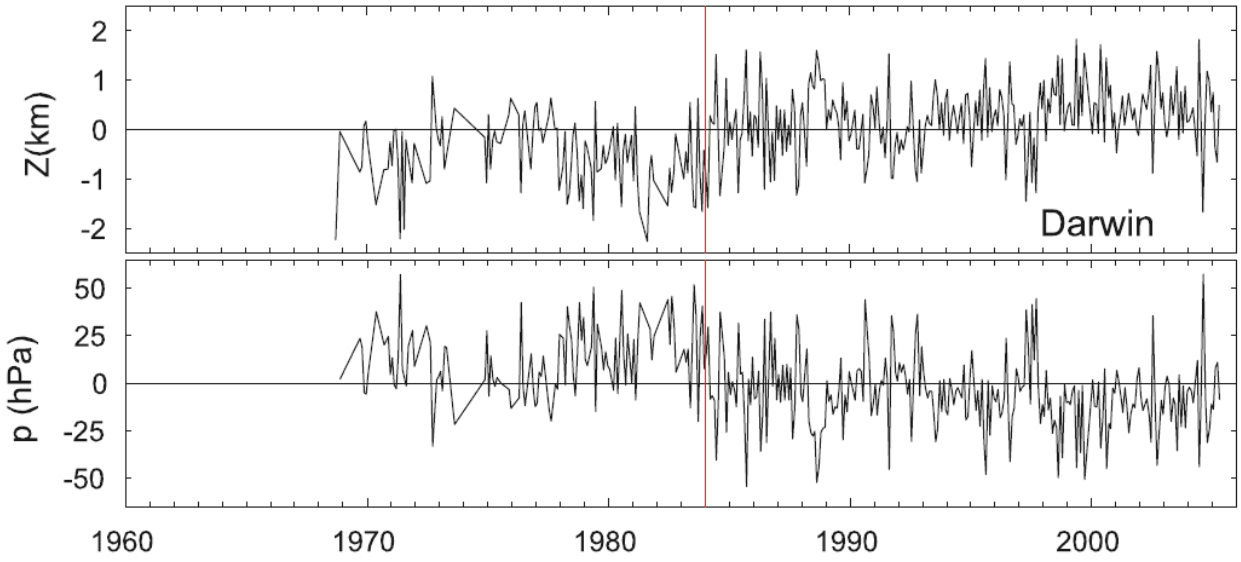

Fig. 2.3: Time series of monthly anomalies (mean annual cycle removed) of tropopause height (top) and pressure (bottom) at 0000 UTC at Darwin, Australia (adapted from Seidel and Randel, 2006). A discontinuity is apparent around 1984.

mentation, as shown in Fig. 2.4, which is problematic when using these data for long-term studies. In this thesis, however, radiosonde data are not used in the variability analysis, so this is not an issue. On the other hand, problems may appear due to the fact that not all the soundings reach the tropopause level and that, occasionally, some intermediate pressure levels are missing. As can be seen in Fig. 2.5, the percentage of soundings reaching 100hPa is around 70%, although this pressure level may not always be high enough to detect the tropical tropopause. The vertical resolution, as indicated by the number of levels measured by the soundings, has increased over time (but note that the increase in the number of soundings reaching the 10hPa level is much lower, so that much of the growth in the number of meas-

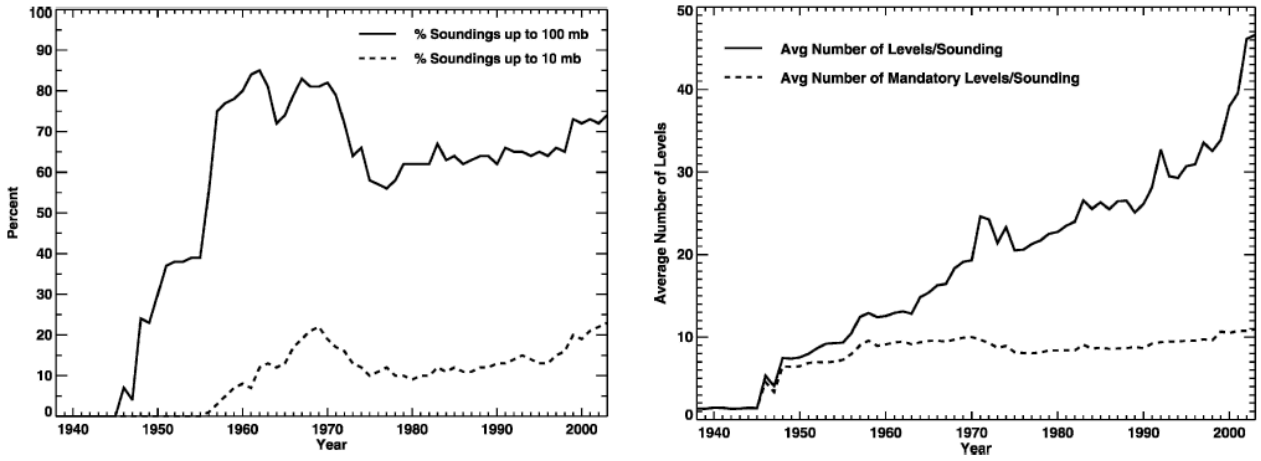

Fig 2.5: : (Left) Percentage of soundings reaching up to at least 100 (solid line) and 10 hPa (dash line) and (right) average number of mandatory (dash line) and total (solid line) levels per sounding for each year of data in IGRA (adapted from Durre et al, 2006).

ured levels can be attributed to increased vertical resolution rather than to increased elevation of the soundings). Limited vertical resolutions may constitute a source of error in tropopause determination in some soundings, as shown by Seidel and Randel (2006). The lack of intermediate levels is particularly disturbing, as it may introduce jumps in the lapse rate, affecting tropopause determination. As shown in Fig. 2.6, the absence of data over a deep region, particularly near the tropopause, introduces spurious discontinuities in the temperature profile that lead to an erroneous identification of the tropopause level.

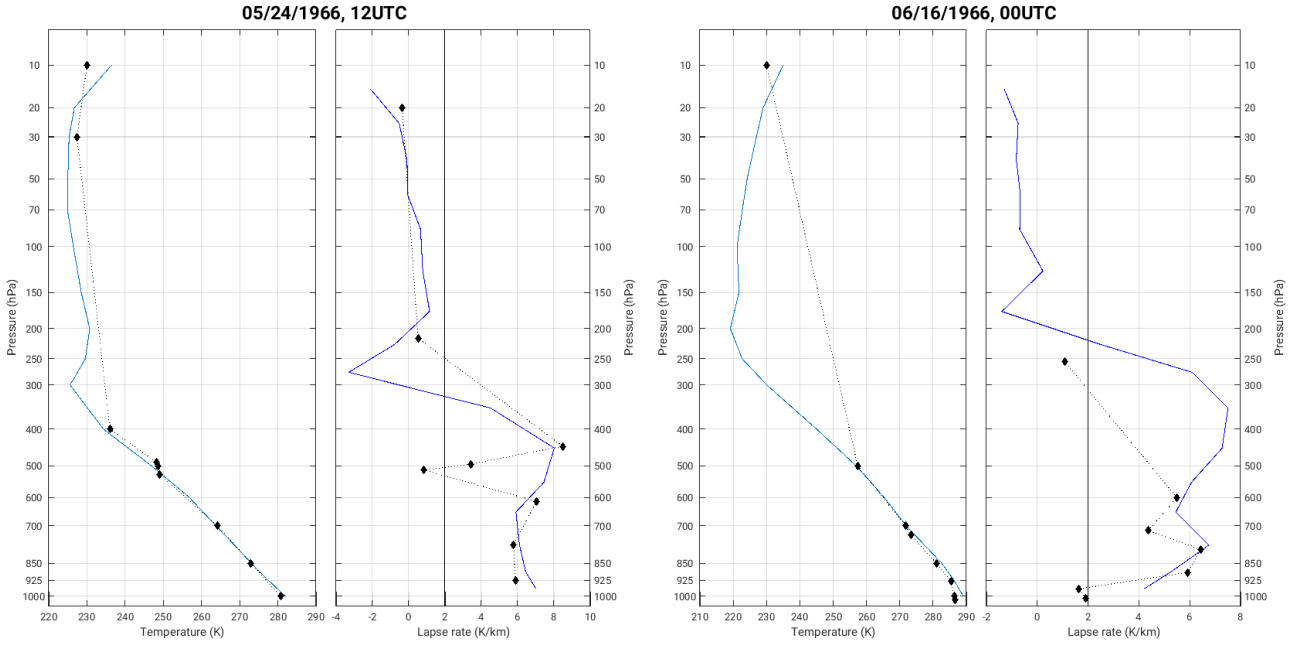

Fig. 2.4: (Left) Percentage of soundings reaching up to at least 100 (solid line) and 10 hPa (dash line) and (right) average number of mandatory (dash line) and total (solid line) levels per sounding for each year of data in IGRA (adapted from Durre et al, 2006).

There is another possible source of errors in the IGRA dataset, although it does not always affect tropopause location: in some soundings, there are repeated temperature measurements at two or more different pressure levels. As an example, Fig. 2.7 left shows a sounding in which the temperature reported at three pressure levels (278, 300 and 360hPa) is exactly the same, implying a zero lapse rate. While the three levels are relatively close and nearly isothermal behaviour is not unreasonable in the region, it is quite improbable that the thermometer on board the radiosonde recorded exactly the same temperature at three different levels. Another example is the nearly isothermal layer observed in the lower troposphere (810 and 785hPa), a region where the lapse rate is more or less constant with values between 5 and 10K km^{-1} (this layer, nonetheless, may be actually real, as such layers have been related with gravity waves). These errors do not have a big impact on tropopause height because the rec-

orded profile is not too far from the actual profile. Profile in Fig. 2.7 right, however, shows that this kind of error may also affect the determination of the tropopause level: four consecutive levels share temperature (360, 400, 500 and 505hPa) thus making the lapse rate goes to 0 in the upper half of the troposphere. The thermal tropopause objectively determined for this profile (see next chapter for details of this calculation) is located around 550hPa, while inspection of the sounding suggests that the actual tropopause is situated around 326hPa. These repeated values may reflect an attempt to complete missing information not registered by the instrument. In the two cases shown, the repeated measurement involves a mandatory level, which suggests that the temperature at these levels was assigned *a posteriori* using the measurement from a neighbour pressure level. In most instances, levels with repeated measurements are closer than in the examples shown in Fig. 2.7, separated by no more than a few hectopascals. Hence, a possible explanation is that the significant levels -levels reported, other than the mandatory levels, because of unusual characteristics in temperature, wind, etc.- , which are defined from the original data (Hoinka, 1997), have their temperature assigned as that of the nearest measured level. Given that repeated temperature measurements may introduce noise and errors in the analyses, all consecutive levels with the same temperature were removed from the dataset.

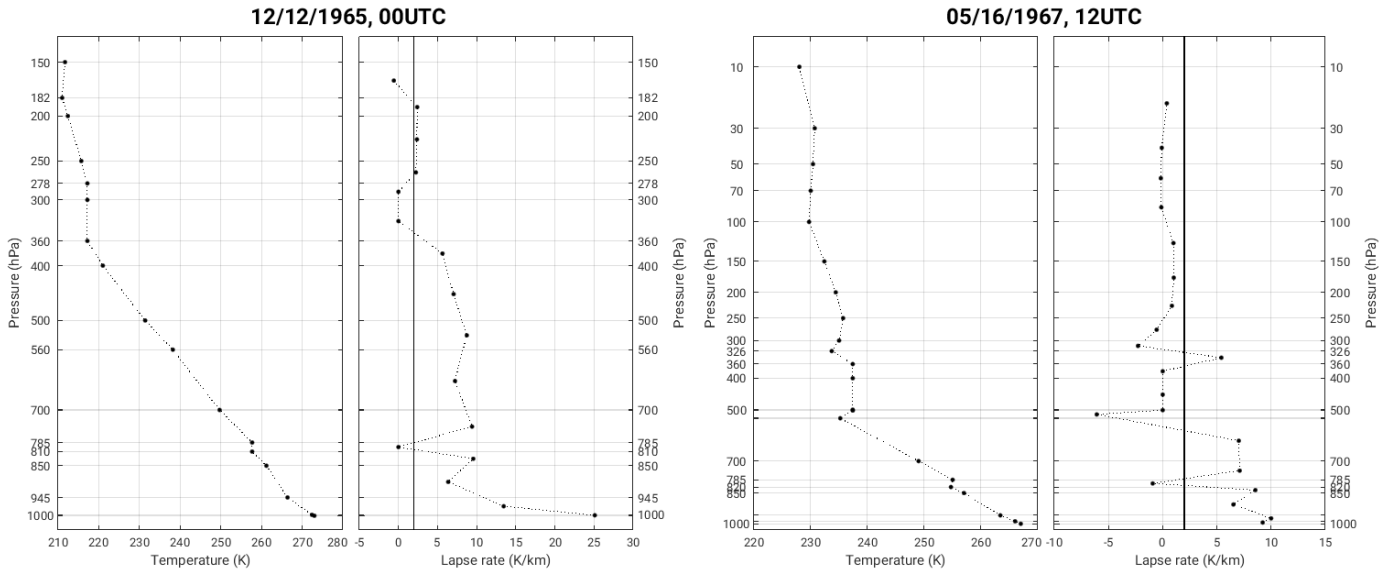

Fig. 2.5: As in Fig. XX, but for Jan Mayen Island, Norway (70.93ºN, 8.67ºW) on 12/12/1965 at 00UTC (left) and on 05/16/1967 at 12UTC

The IGRA dataset is freely available at the NCDC-NOAA website, *https://www.ncdc.noaa.gov/*. A complete description can be found in Durre *et al.*, 2006.

In this thesis, data from all the stations were used in their original format, that is, in

cluding all the levels, both mandatory and significant, as long as they include temperature and pressure data (some levels only include information about the wind), with the only exception of the repeated temperature measurements mentioned above. There is no attempt to correct for other errors in the data or to homogenize the profiles, which have a wide variety of vertical and temporal resolutions. Since the IGRA dataset is only used for analyses of the tropopause mean state, and given the huge amount of data included, we expect the statistical distributions to be reliable, as shown by previous studies.

2.2 NCEP/NCAR Reanalysis 1.

This reanalysis dataset is provided by the National Center for Environmental Prediction (NCEP) in collaboration with the National Center for Atmospheric Research (NCAR). Data from several sources (land surface and ship data, radiosondes, aircrafts, satellites, etc.) are reanalysed by using an atmospheric model such as those utilized in operational weather forecasting. The original data are first pre-processed in order to exclude wrong values or measurements and then ingested by the spectral model using a three-dimensional variational scheme; the result of this data assimilation process is the so-called reanalysed data. These outputs are validated using statistical tests.

The model used for the data assimilation process is a global spectral model with T62 horizontal resolution (roughly 2.5^{o} x 2.5^{o} in Cartesian coordinates) and 28 sigma levels in the vertical. The levels are distributed as shown in Table 2.2. As can be seen, data are only available at the 17 mandatory pressure levels (right column). The top level (3 hPa) data are not provided as they may be affected by the top boundary conditions of the model (Kalnay *et al.*, 1996).

Model level	Midlevel pressure (hPa)	Mandatory pressure level (hPa)
28	2.73	3
27	10.06	10
26	18.34	20
25	28.75	30
24	41.79	--
23	58.05	50
22	78.15	70
21	102.78	100
20	132.61	--
19	168.23	150
18	210.06	200
17	258.23	250
16	312.48	300
15	372.05	400
14	435.68	--
13	501.68	500
12	568.09	--
11	632.90	--
10	694.26	700
9	750.76	--
8	801.42	--
7	845.79	850
6	883.84	--
5	915.92	925
4	942.55	--
3	964.37	--
2	982.08	--
1	995.00	1000

Table 2.2. Pressure levels of the spectral model used in the NCEP/NCAR Reanalysis 1 (adapted from Kalnay et al, 1996).

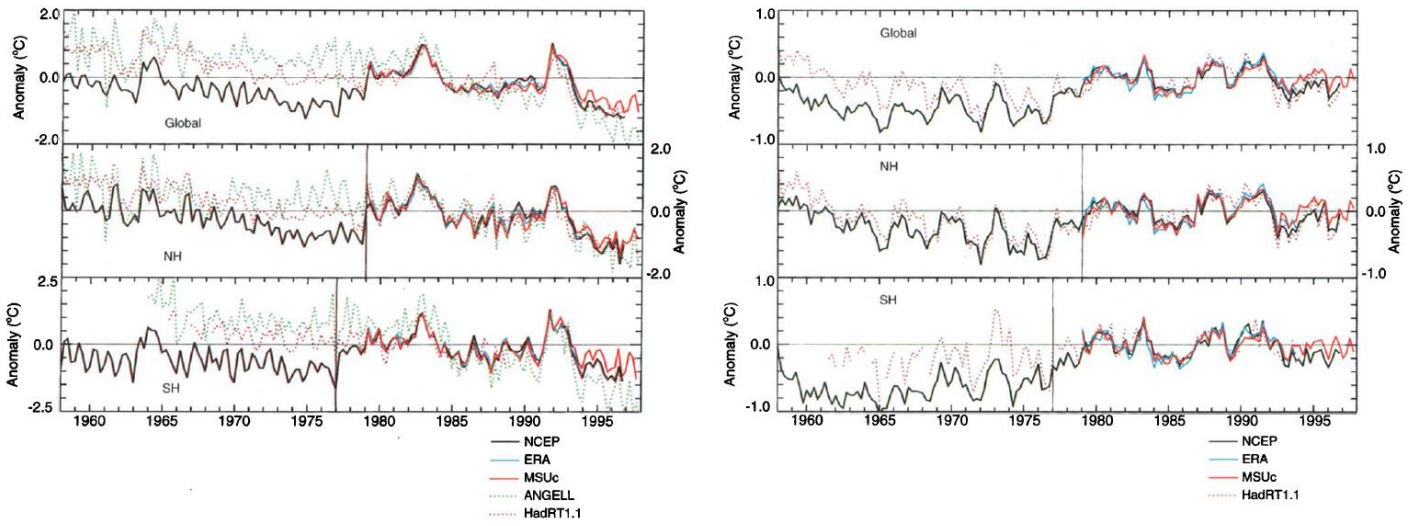

Fig. 2.6: Time series of global- and hemispheric temperature anomalies in the lower stratosphere (left) and in the midtroposphere (right). Temperatures are estimated from radiosondes (Angell, HadRTI.1), the satellite-based Microwave Sounding Unit (MSU version c, or MSUc) and reanalyses of the European Centre for Medium-Range Weather Forecasts (ERA-15) and NCEP/NCAR. Anomalies are in the form of seasonal averages with respect to the 1979-1993 climatological seasonal means (adapted from Santer et al, 1999)

The reanalysis process is performed four times a day at 0Z, 6Z, 12Z and 18Z (where "Z" denotes "Zulu time", equivalent to the Coordinated Universal Time, UTC), beginning in 1948 and till present. Since atmospheric models have much improved since 1948 and this may introduce inhomogeneities in the data time series (Tiedtke, 1988), the same spectral model and assimilation method are used throughout the project, based on the state of the art at the beginning of the project. Notwithstanding this, discontinuities still appear in the reanalysed time series, mainly as a result of the inception of new sources of data, such as the satellite infrared and microwave data between 1975 and 1978 (Santer *et al.*, 1999; Sturaro, 2003). As shown in Fig. 2.8, there was a cold bias in lower-stratosphere temperatures in the NCEP/NCAR reanalysis in comparison to radiosondes that was corrected with the assimilation of satellite data, in 1977 in the Southern Hemisphere and in 1979 in the Northern Hemisphere. There was also a cold bias in the mid-troposphere temperatures in the Southern Hemisphere in the pre-satellite era. These discontinuities make NCEP/NCAR reanalysis dataset not suitable for long-term climatic studies, at least those covering the period 1948 – 75 (Pawson and Fiorino, 1999; Santer *et al.*, 1999).

Apart from the discontinuities arising from the new available data, there are some well-known biases in the NCEP/NCAR reanalysis. The most important ones are those affecting the temperature field. The greatest discrepancies with the radiosonde data are found in the lower

stratosphere, especially near the 100hPa level. As can be seen in Fig. 2.9, there is a warm bias in the tropical belt at this level of about 2.5–3K, likely due to the method used to ingest satellite data in the assimilation scheme (Pawson and Fiorino, 1998). Note that this level is very close to the tropical tropopause, so that the bias also affects the tropical tropopause, which is about 3 to 5K too warm and about 2 to 6hPa too low (Pawson and Fiorino, 1998; Randel *et al.*, 2000). Randel *et al.* (2000) note that, because this bias is constant in time, it does not affect the variability of the tropical tropopause at seasonal and interannual scales. Since the temperature biases in the extratropical area seem to be even smaller, it is reasonable to expect that the extratropical tropopause, the focus of this thesis, is well represented in NCEP/NCAR reanalysis.

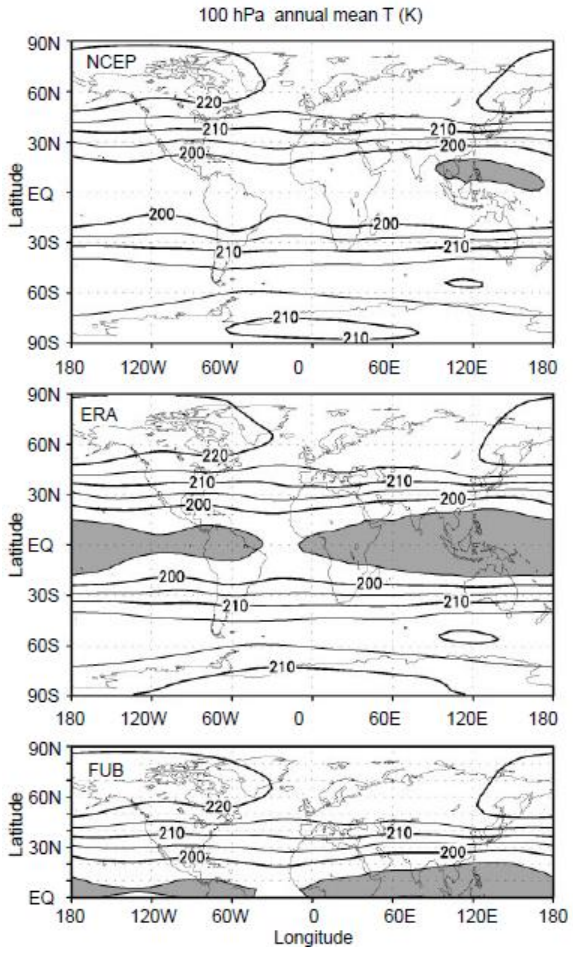

Fig. 2.7: The annual mean 100hPa temperature from the global NCEP/NCAR (top) and ERA-15 (center) reanalyses and the northern hemispheric subjective analyses derived from radiosonde data at the Freie Universität Berlin data (bottom). The means are for the period January 1979-December 1993. The contour interval is 5K and regions with T<195K are shaded (extracted from Pawson and Fiorino, 1998).

The NCEP/NCAR Reanalysis 1 dataset are freely available at the NOAA/OAR/ESRL PSD website *http://www.esrl.noaa.gov/psd/*. The complete description of the dataset can be found in Kalnay *et al.*, 1996.

We use in this thesis the daily data provided by the reanalysis, computed as the mean of the four analyses performed each day. The reanalysis dataset includes tropopause pressure and temperature data, derived using the temperature field on the model sigma levels; this is a class-A variable, which means that it is "strongly influenced by the observed data" and weakly affected by the model (Kalnay *et al.*, 1996). The variables of this type are regarded as the most reliable among those provided by the NCEP/NCAR reanalysis. The tropopause level is computed using the standard thermal definition:

"The tropopause is identified by the lowest level above 450mb where the temperature lapse

rate –dT/dz becomes less than 2K/km. The tropopause is not allowed higher than 85mb. Interpolations of variables to tropopause are done linearly in log of pressure."

Other daily variables used in this thesis from the NCEP/NCAR Reanalysis 1 include the geopotential height of the pressure levels, temperature and zonal and meridional components of the wind at the pressure levels, all of them being class-A variables, and pressure vertical velocity at the pressure levels (only available between 1000 and 100hPa), a class-B variable (which means that, although the variable is related to observational data, its value is strongly affected by the model used in the analysis). Only data from 1979 to 2011 were considered, aiming to avoid the discontinuities described above due to the assimilation of satellite data.

2.3 ERA-interim reanalysis.

This reanalysis is a project by the European Centre for Medium-Range Weather Forecasts (ECMWF). It represents an improvement from the previous ECMWF reanalysis, ERA-40, as it was specifically designed to solve some of the problems detected in that reanalysis. Areas of improvement include a better representation of the hydrological cycle (correcting the precipitation), the stratospheric circulation (which was too strong due to a problem with the assimilation of the radiances measured by satellites) and enhanced temporal consistency of the data (targeting discontinuities caused by the introduction of new observational data, biased data, etc.).Finally, the new reanalysis also makes use of technical advances in the data assimilation scheme and in the model (Dee *et al.*, 2011).

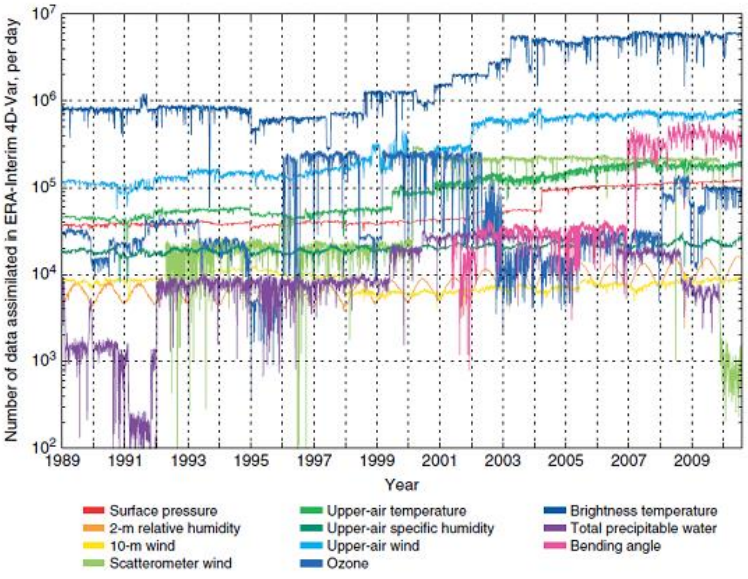

Fig. 2.8: Daily counts, on a logarithmic scale, of observations assimilated in the atmospheric analysis component of ERA-Interim.

Different from its NCEP/NCAR counterpart, ERA-interim reanalysis uses a 4D varia-

tional technique for the assimilation of observational data, which means that the observational data are combined with the forecast made by the model in a previous step for the same time and location as the observed data. This scheme has proven, for example, to increase the ability of the models to properly represent the large-scale tropospheric circulation (Thépaut *et al.*, 2006; Whitaker *et al.*, 2009). 4D variational schemes are now standard in most operational weather forecast centres across the world due to their many advantages compared to 3D variational assimilation.

Model level	Midlevel pressure (hPa)	Mandatory pressure level (hPa)	Model level	Midlevel pressure (hPa)	Mandatory pressure level (hPa)
1	0.10	--	31	228.84	225
2	0.29	--	32	257.36	250
3	0.51	--	33	287.64	300
4	0.80	--	34	319.63	--
5	1.15	1	35	353.23	350
6	1.58	--	36	388.27	400
7	2.08	2	37	424.57	--
8	2.67	3	38	461.90	450
9	3.36	--	39	500.00	500
10	4.19	--	40	538.59	550
11	5.20	5	41	577.38	--
12	6.44	7	42	616.04	600
13	7.98	--	43	654.27	650
14	9.89	10	44	691.75	700
15	12.26	--	45	728.16	750
16	15.19	--	46	763.20	775
17	18.81	20	47	796.59	800
18	23.31	--	48	828.05	825
19	28.88	30	49	857.34	850
20	35.78	--	50	884.27	875
21	44.33	--	51	908.65	900
22	54.62	50	52	930.37	925
23	66.62	70	53	949.35	950
24	80.40	--	54	965.57	--
25	95.98	100	55	979.06	975
26	113.42	125	56	989.95	--
27	432.76	--	57	998.39	1000
28	154.00	150	58	1004.64	--
29	177.12	175	59	1009.06	--
30	202.09	200	60	1012.05	--

Tabla 3: As in Table 2.2, but for the ERA-interim reanalysis (adapted from Berrisford et al, 2009).

The model is spectral, with a horizontal resolution T255 (about 0.7° x 0.7° in Cartesian coordinates) and 60 vertical levels in hybrid sigma-pressure coordinates (Table 2.3). The analyses are performed in 12-h cycles, although estimates of the variables are available at 00, 06, 12 and 18UTC of each day. The fields are provided both on model levels and on 37 fixed pressure levels (also included in Table 2.3). This is the vertical resolution used in this thesis. As can be seen in the table, use of full model levels does not significantly increase the vertical resolution near the tropopause but it does significantly increase the computational costs of computing derived variables.

As in NCEP/NCAR reanalysis, a large list of observational data is ingested in the model (see Fig. 2.10): radiosonde, aircrafts, wind profilers, buoys, land stations, etc. Satellite data, however, plays a predominant role due to the great amount of information that it provides: clear sky radiance measurements, atmospheric motion vectors, scatterometer wind data, ozone measurements, total precipitable vapour estimates, etc. Several statistical tests were applied to the observational data before their ingestion in the data assimilation to remove possible biases and temporal discontinuities based on the experience gained from the previous ECMWF reanalysis, ERA-40; special care was put on the radiances measured by satellites, which were one of the main sources or error in NCEP/NCAR reanalysis (Pawson and Fiorino, 1998). In general, local comparisons with observational datasets show good agreement and only small biases in temperature, which seem to be bigger over the sea than over land areas (Mooney *et al.*, 2010; Szczypta *et al.*, 2011; Bao and Zhang, 2013). Studies of stratosphere-troposphere exchange in ERA-Interim reanalysis suggest that this process is well represented, even across the extratropical tropopause, as is the seasonal cycle of ozone over the tropopause even though ERA-Interim does not include chemistry (Škerlak *et al.*, 2014). The assimilation of observations derived from the Global Positioning System radio occultation (GPSRO) technique from 2006 onwards reduced the reanalysis biases, especially at levels near the tropopause (Poli *et al.*, 2010; Dee *et al.*, 2011). The ERA-interim dataset has already been used for the study of tropopause properties with good results (Wilcox *et al.*, 2012a; Wilcox *et al.*, 2012b).

Parts of the ERA-Interim dataset are freely available at the ECMWF website *http://www.ecmwf.int/*. A complete description of the data can be found in Dee *et al.*, 2011 and Berrisford *et al.*, 2009.

In this thesis, daily data from ERA-Interim, interpolated to a regular 2.5° x2.5° grid, are used. The resolution of the grid was chosen to be the same as in NCEP/NCAR Reanalysis 1 to prevent sensitivity of the results on the horizontal resolution of the model. ERA-Interim only provides the results of the four analyses per day, so the daily means were computed as the average of these four outputs. Temperature, geopotential height of the pressure levels and zonal and meridional components of the wind were used for the period 1979 to 2011. ERA-interim reanalysis does not provide tropopause data, which had to be computed from the available data; the method is described in the next chapter of this thesis.

2.4 The idealized model.

While the analysis of observational or reanalysed data may provide us with a picture of the atmospheric behaviour and allow us to analyse the statistical relations between the variables, a satisfactory scientific explanation of the phenomena requires a careful study of the underlying dynamics. General Circulation Models (GCM) aid us develop this dynamical understanding by solving the equations of motion with some specified conditions. Idealized models, which use a set of simplified physics, are very useful in this context as they are devoid of the complexity associated with physical parameterizations.

In this thesis, an idealized atmospheric model, based on the formulation of Held and Suarez (1994), is used. The basic idea is to "replace the detailed radiative, turbulence and moist convective parameterizations with very simple forcing and dissipation" (Held and Suarez, 1994). The model integrates the global primitive equations when the heating is determined by temperature relaxation to a specific atmospheric state, the so-called radiative equilibrium state, and the only dissipation included is simple linear friction over the atmospheric boundary layer. As this "dynamical core" reaches statistical equilibrium, the governing dynamics are more easily interpreted than in comprehensive GCMs, in which the complex physical parameterizations may obscure the interpretation of the results.

Specifically, the forcing (Newtonian heating) and dissipation (Rayleigh damping) in the model are defined by the following expressions:

$$\frac{\partial T}{\partial t} = \ldots - \mathrm{k}_T \left(T - T_{eq} \right) = \ldots - \frac{T - T_{eq}}{\tau_T}$$
$$\frac{\partial v}{\partial t} = \ldots - k_v v$$

The exact forms of T_{eq} and k_T and k_v define the model setup, so several formulations are possible using the same model. The simplest model setup is the formulation of Held and Suarez (1994) (hereafter, HS94 setup), in which the equilibrium temperature is zonally symmetric, decreasing away from the Equator and with height, until it becomes isothermal at 200K (Fig. 2.11, left). The relaxation time scale is 40 days everywhere in the free atmosphere (σ<0.7) and latitude-dependent over the "boundary layer", decreasing to 4 days near the equatorial surface (Fig. 2.11, right). Friction is non-zero only over the boundary layer (σ>0.7), where its strength increases as we approach the surface. The parameters of the formulations are defined as follows:

$$T_{eq} = \max \left\{ T_T, \left[T_0 - \delta T \left(\phi, P \right) \right] \left(\frac{P}{P_0} \right)^{\kappa} \right\}$$
$$k_T = \frac{1}{\tau_a} + \left(\frac{1}{\tau_s} - \frac{1}{\tau_a} \right) \max \left(0, \frac{\sigma - 0.7}{0.3} \right) \cos^4 \phi$$
$$k_v = k_f \max \left(0, \frac{\sigma - 0.7}{0.3} \right)$$

where ϕ is the latitude, P is the pressure, P_0 = 1000hPa, κ =2/7 and σ is the sigma coordinate. The frictional damping rate is k_f = 1 day^{-1}, while the heating formulation is defined by the relaxation time scales in the free atmosphere and at the equatorial surface (τ_a = 40 and τ_s = 4 days, respectively), the stratospheric temperature T_T = 200 K. and T_0 = 315 K. δT defines the latitudinal and vertical structure of the radiative equilibrium profile and has the form:

$$\delta T = \delta_y \sin^2 \phi + \delta_z \log \left(\frac{P}{P_0} \right) \cos^2 \phi =$$
$$= 60 \sin^2 \phi + 10 \log \left(\frac{P}{P_0} \right) \cos^2 \phi$$

As can be seen, this is a very basic setup that does not include seasonality, orography,

etc. Additionally, because the model was designed with a tropospheric focus, the forcing structure is very simple in the stratosphere (just relaxation to an isothermal layer) and the model does not produce a stratospheric jet or polar vortex. Thus, the HS94 model cannot be expected to simulate stratosphere–troposphere interactions realistically and more sophisticated setups are required to study tropopause variability.

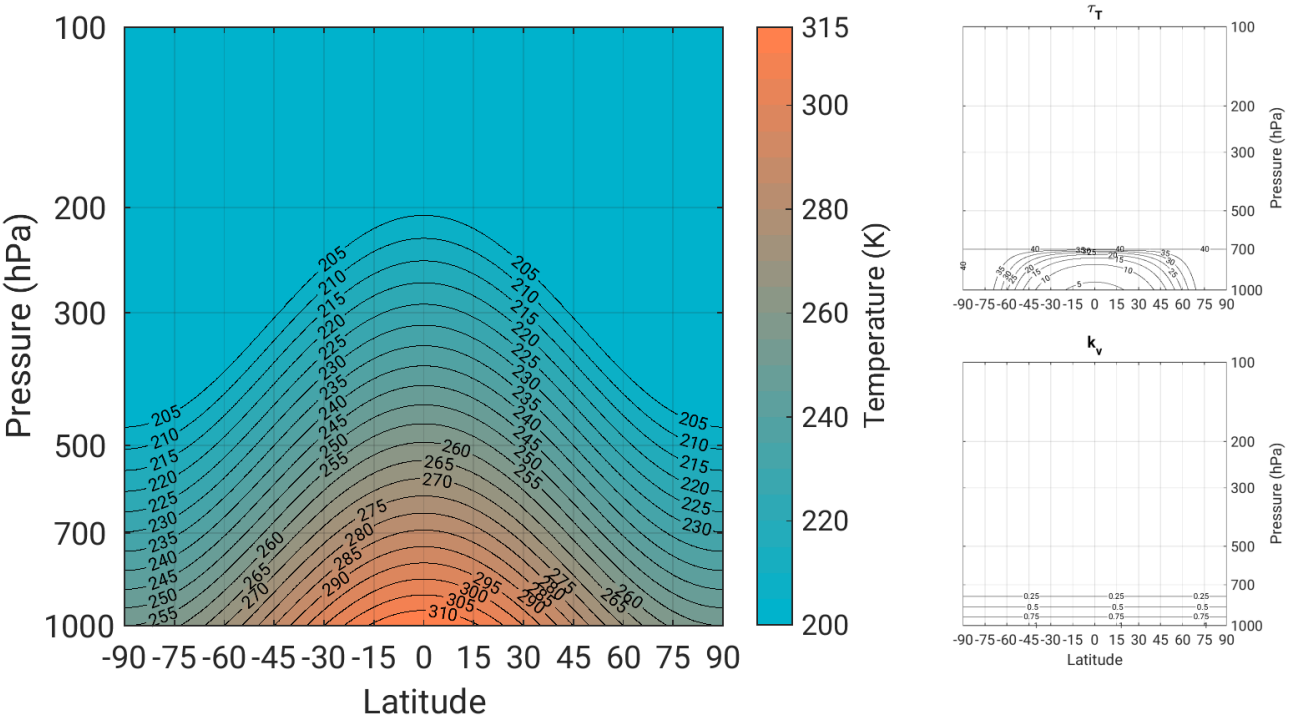

Fig. 2.9: Equilibrium temperature (left) and time scale of the Newtonian relaxation (top right) and the coefficient of the Rayleigh.

Several authors have proposed model setups with a more realistic stratospheric structure, seasonal evolution of the equilibrium temperature and orography (Polvani and Kushner, 2002; Kushner and Polvani, 2004; Gerbert and Polvani, 2009; Jucker *et al.*, 2013). In this thesis, the formulation by Jucker, Fueglistaler and Vallis (hereafter, JFV setup), described in Jucker *et al.* (2014), will be used with some slight modifications. This formulation is based on an analytical approximation to a state representing a linearization of radiative equilibrium about the mean state of the atmosphere, calculated as follows. First, a radiative transfer model is used to compute radiative heating in a mean state defined by the climatological values of several variables, including temperature and water vapour (from ERA-Interim), ozone and other tracer gases mixing ratios, and solar insolation. Then, the mean state is perturbed with a small 0.1K temperature perturbation (with a 10-km height scale), and the radiative heating for this new state is computed. Modelling the heating with a Newtonian approximation, the relaxation

time scale can then be estimated as the ratio between the temperature perturbation and the perturbed heating rates. Once the relaxation time scale is known, it is easy to compute the equilibrium temperature. This process is repeated monthly for each grid point in latitude and pressure, yielding a spatially and temporally dependent $T_{eq}(\phi, P, t)$ and $\tau_T(\phi, P, t)$. Because this formulation cannot account for the heating associated with latent heat release in the troposphere, a modification of the HS94 setup is used instead of this linearization below 100hPa. The main modification to the HS94 setup is the inclusion of seasonality in the tropospheric equilibrium temperature, with a stronger seasonal cycle in the Northern than in the Southern Hemisphere. The transition from the tropospheric to the stratospheric setup is relatively smooth with a reasonable choice of the temperature perturbation height scale (10km), which gives a radiative equilibrium temperature at 100hPa very close to the HS94 value T_T = 200K. See Jucker *et al.* (2013) for additional details.

To facilitate reproducibility of this setup by other researchers, Jucker *et al.* (2014) provide analytical polynomial fits to the equilibrium temperature and relaxation time scale obtained with the process described above. Key features of the equilibrium temperature field can be controlled using a number of parameters whose default values are based on the best approximation to the radiatively determined setup described in the previous paragraph (see Table 2.4). Because we have found it necessary to modify some aspects of the JFV setup (for reasons discussed below), we describe in some detail how the radiative equilibrium temperature is constructed in that setup. First, the equinoctial temperature profile at the Equator is adjusted using two different polynomials (Fig. 2.12a), one below and one above the 1hPa level (note that the former is designed to give a 200K temperature at 100hPa so as to meet the HS94 profile). Away from the Equator, this structure is modulated using a coefficient that depends on latitude and pressure (Fig. 2.12b), which produces the equinoctial equilibrium temperature shown in Fig. 2.12c. To account for seasonal variations, a term representing a solstitial temperature correction (Fig. 2.12d, e) is added to the equinoctial temperature field just described. The amplitude of this correction is scaled with a sinusoidal function of time (Fig. 2.12f) to produce a seasonal cycle. The solstitial correction is defined by two parameters, A^0 and A^1 that control the strength of the polar vortex (in terms of its temperature). As is apparent in the figure, the default values of these parameters are different in both hemispheres: the Southern polar vortex is colder in winter than its Northern counterpart (in summer, however, the solstitial amplitudes are symmetric) (Fig. 2.12g, h). Finally, the HS94 equilibrium temper-

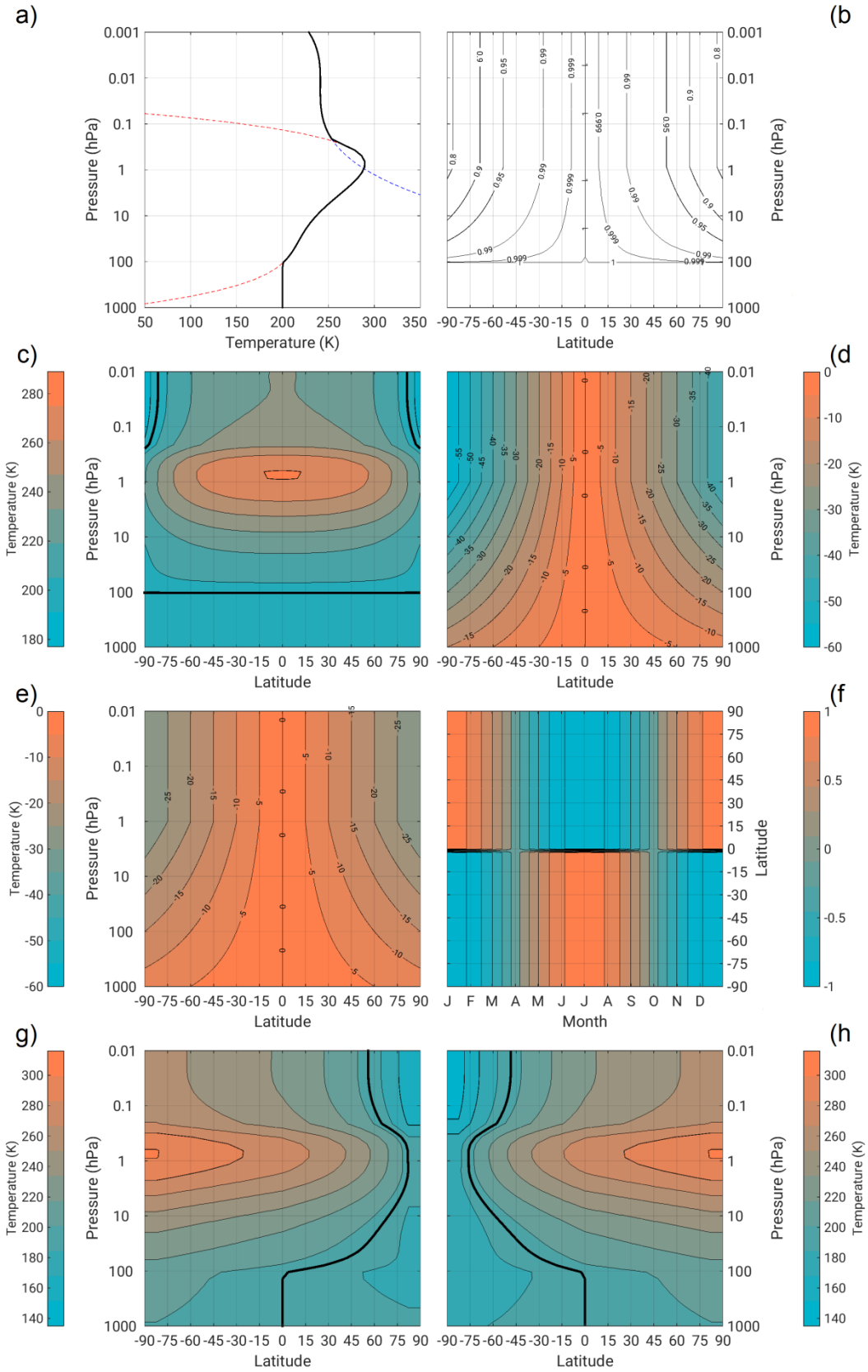

Fig. 2.12: Characteristics of the JFV setup. a) Adjusted equatorial temperature profile, TeEQ (solid black lines) and the polynomials that generate it, P1 and P2 (dashed red and blue lines). b) Coefficient modulating the temperature profile shown in a) as a function of latitude and pressure, P4. c) Equinoctial (Apr, 1st and Oct, 1st) equilibrium temperature, obtained as TeEQ · P4 (for reference, the 200K isotherm is shown with thick black line). d) Winter- solstice correction in both hemispheres, AW. e) Summer-solstice correction in both hemispheres, AS. In NH winter (summer) solstice, AW (AS) is added to the equinoctial temperature from 0o to 90oN, while AS (AW) is added from 0o to 90oS. f) Coefficient modulating the seasonal evolution of the equilibrium temperature, D. g) NH winter solstice (Dec, 31st) equilibrium temperature in the stratosphere. H) NH summer solstice (Jul, 1st) equilibrium temperature in the stratosphere. Note that the equilibrium temperature is computed as TeEQ · P4 + AW · D when D ≥ 0 and as TeEQ · P4 + [AS – TeEQ · (1 – P4)] · D when D < 0.

ature is used below the level p_T (a linear interpolation between both profiles is performed when this level is different from 100hPa).

Parameter	Meaning	Default	Parameter	Meaning	Default
P_0	Surface pressure	1000hPa	P_0	Surface pressure	1000hPa
P_t	Lower stratosphere reference pressure	100hPa	P_t	Lower stratosphere reference pressure	100hPa
P_1	Upper stratosphere reference pressure	1hPa	τ_T	Relaxation over the Tropics at $P = P_t$	40 days
T_T	Minimum temperature below P_t	200K	τ_m	Shortest relaxation time over the Tropics	5 days
A^0_{NH}	Amplitude at $P = P_t$, 90ºN (winter)	-15K	$\Delta\phi$	Meridional width over the Tropics	30º
A^0_{SH}	Amplitude at $P = P_t$, 90ºS (winter)	-25K	τ_p^S	Relaxation time over South Pole	20 days
A^1_{NH}	Amplitude at $P=P_1$, 90ºN (winter)	-45K	τ_p^N	Relaxation time over North Pole	20 days
A^1_{SH}	Amplitude at $P=P_1$, 90ºS (winter)	-60K	--	--	--
A_S	Amplitude at $P = P_t$, Summer Pole	-15K	--	--	--

Table 2.4 Input parameters defining the analytical profile for the relaxation temperature (left) and time (right) (adapted from Juker et al, 2014)

One problem with the JFV setup when studying the tropopause is that subpolar non-equinoctial temperature profiles have a jump in the UTLS region because the upper troposphere in the HS94 setup is warmer (200K) than the lower stratosphere temperature in JFV (200 – A^0K). In actual simulations, the dynamical heating smooths this discontinuity to some extent, but the thermal tropopause definition still tends to identify the tropopause with this level. Thus, the HS94 setup was modified to remove this discontinuity by making the upper troposphere temperature in that profile agree with that of JFV's lower stratosphere. The modified full equilibrium temperatures for the winter solstice (December 31st in the model) and the summer solstice (July 1st) are shown in Fig. 2.13.

As for the relaxation time, the HS94 formulation is used below 100hPa. Above 100hPa,

the relaxation time decreases gradually with height, reaching its minimum value at the top of the atmosphere (Fig. 2.14)

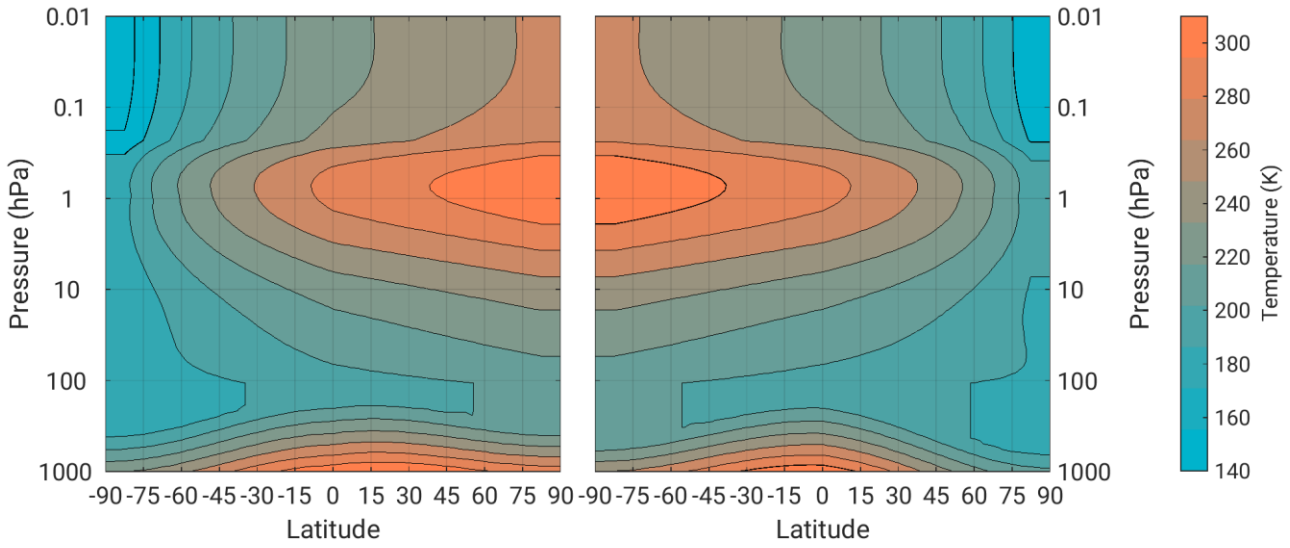

Fig. 2.13: Solstitial equilibrium profiles in the modified JFV-setup. (Left) Northern Hemisphere summer solstice (July, 1st) and (right) Northern Hemisphere winter hemisphere (December, 31st).

The frictional Rayleigh damping at the surface is kept as in HS94, but a sponge layer is added to the top of the atmosphere to prevent spurious reflection (Polvani and Kushner, 2002). The sponge damping is applied above 0.5hPa and has a maximum damping rate of 0.5 $days^{-1}$ at ohPa.

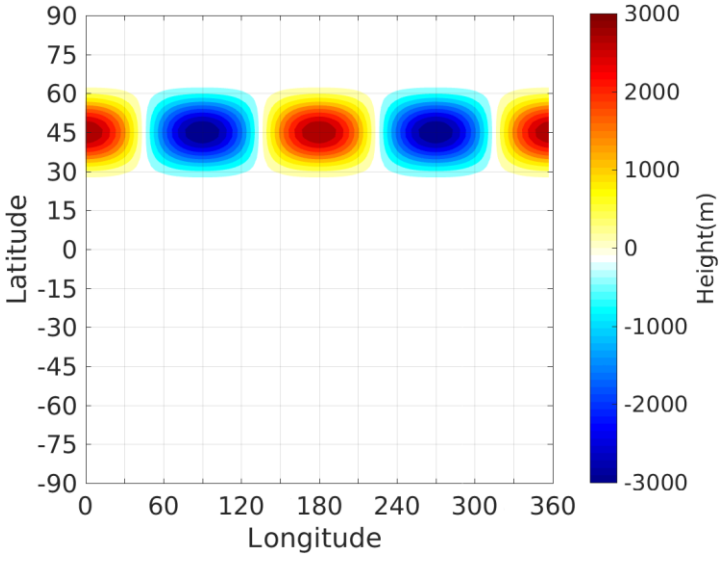

Fig. 2.14: Topography used in the simulation with orography, as defined in Gerber and Polvani (2009).

Full details of the JFV setup can be found in Jucker *et al.*, 2014. The code is freely available at *https://github.com/mjucker/JFV-strat*.

Orography was included as a sinusoidal function of both latitude and longitude as in Gerber and Polvani (2009), centered at 45°N and extending from 25°N and 65°N (see Figure 2.14). The maximum height of the topogra-

phy is set to 3000m.

The idealized model solves the dry, hydrostatic primitive equations by using the spectral-transform method with a triangular truncation in spectral space. This involves the decomposition of the atmospheric variables of interest in spherical harmonics so as to formulate the equations of motion in the spectral domain, truncating the expansion at some zonal wavenumber. The spectral-transform method transforms these variables to physical space for an efficient computation of the nonlinear terms. This requires the use of a Gaussian grid in physical space, equally spaced in longitude but not in latitude. In this thesis, the resolution of the Gaussian grid is chosen to have 64 latitudinal grid points, which corresponds in the triangular truncation to 128 longitude grid points. This resolution is usually used in combination with a triangular truncation in the 42^{th} mode, known as T42, and corresponds to approximately 2.8^{o} x 2.8^{o} in the regular grid. Vertical levels are located following the scheme by Simmons and Burrigde (1981). 40 vertical levels are used so as to have a good representation of the stratosphere; their values in pressure coordinates are given in Table 2.5 The rest of the computational details are standard in numerical modelling, including use of a semi-implicit leapfrog scheme for the time steps followed by a Robert-Asselin time filter, hyperdiffusion for the non-resolved scales, etc.

The code is freely available at the Flexible Modelling System (FMS) website of the Geophysical Fluid Dynamics Laboratory (GFDL) at *https://www.gfdl.noaa.gov/fms/* .

Model level	Midlevel pre-assure (hPa)	Model level	Midlevel preasure (hPa)
1	0,007	21	54,3
2	0,032	22	66,3
3	0,074	23	80,3
4	0,15	24	96,6
5	0,278	25	115
6	0,483	26	137
7	0,795	27	162
8	1,25	28	190
9	1,89	29	222
10	2,78	30	258
11	3,97	31	298
12	5,53	32	344
13	7,55	33	394
14	10,1	34	451
15	13,4	35	514

16	17,4	36	584
17	22,3	37	661
18	28,3	38	747
19	35,5	39	841
20	44,2	40	945

Table 2.5. Pressure levels used in the idealized model.

3. Methodology.

Given the wide variety of data sources used in this thesis and the scales of the variability of interest, it is necessary to process the data so that the underlying dynamics can be extracted from the noise and the mechanisms that drive the tropopause variability explained. This chapter describes the computation of the dynamical variables of interest, the methodology used for the determination of the tropopause, and the statistical techniques used to analyse the relevant time series. We also describe some techniques specific to the study of the tropopause, such as the tropopause – based vertical coordinate.

3.1 Tropopause height determination.

There are several possible definitions for the tropopause based on different aspects of the transition between the tropospheric and the stratospheric characteristics. Each definition is associated with a different method to determine the tropopause level, with its own advantages and disadvantages. In this thesis, the so-called thermal definition is used. This criterion is based on the different nature of the stratification in the troposphere and in the stratosphere, and was formally established by the World Meteorological Organization (WMO, 1957). It is the simplest method that can be used to define the tropopause, as it only requires a vertical temperature profile.

The methodology used for the determination of the tropopause level follows the formulation of Reichler *et al.* (2003). This formulation was specifically designed for gridded data regularly spaced at relatively coarse vertical resolution, so its use is optimal for reanalysed data. The method has been widely used in previous works, both in reanalysis and in models. In this thesis, Reichler's technique is also applied to radiosonde data as in Añel *et al.* (2007).

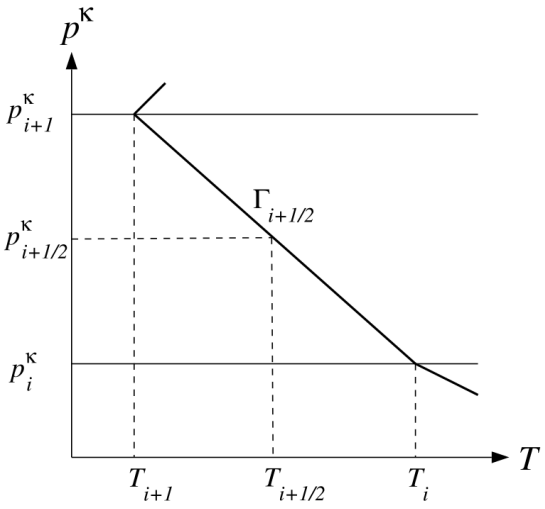

Fig. 3.1: Temperature as a function of Pκ, assuming a linear dependency of T with Pκ in each layer (extracted from Reichler *et al*, 2003).

The method is based on the traditional thermal definition. It requires finding the level at which the lapse rate decreases below 2K km^{-1} for the first time, provided that the mean vertical gradient over a layer 2km deep above this level does not exceed this value. The originality of Reichler's method relies on the use of P^κ (where κ is the ratio between the gas constant and the specific heat capacity at constant pressure for dry air) as the vertical coordinate instead of more commonly used pressure, P or geometrical height, z. This is equivalent to assuming that temperature varies linearly with P^κ (Fig. 3.1) in each layer rather than with pressure. Thus, the lapse rate Γ is:

$$\Gamma(P) = -\frac{\partial T}{\partial z} = -\frac{\partial T}{\partial P^\kappa}\frac{\partial P^\kappa}{\partial P}\frac{\partial P}{\partial z}$$

where P is pressure, T is temperature, z is height and $\kappa = R/c_P = 2/7$, as noted above. Using the hydrostatic relation, the lapse rate can then be expressed as:

$$\Gamma(P) = \frac{\partial T}{\partial P^\kappa}\frac{P^\kappa}{T}\frac{\kappa g}{R} \qquad (3.1)$$

where g is the acceleration of gravity. If T_i is the temperature at the pressure level P_i and assuming T varies linearly with P^κ between the levels P_i^κ and $P_{i+1}{}^\kappa$ then the average tem-

perature of the layer is the temperature at the half-level $P_{i+1/2}{}^{\kappa}$. Approximating derivatives by finite differences in eq. (3.1), the lapse rate at the half-levels can be calculated as:

$$\Gamma_{i+1/2} = \frac{\left(T_{i+1} - T_i\right)}{\left(P_{i+1}^{\kappa} - P_i^{\kappa}\right)} \frac{\left(P_i^{\kappa} + P_{i+1}^{\kappa}\right)}{\left(T_i + T_{i+1}\right)} \left(\frac{\kappa g}{R}\right)$$

Once the lapse rate is computed at all half-levels, we need to find the level at which Γ is smaller than the critical lapse rate Γ_T = 2K km^{-1} for the first time. After that, the average lapse rate over the 2km-deep layer above this level is calculated as half the difference between the interpolated temperature at the top of that layer and the temperature at the chosen level. We can calculate the pressure at the top of the 2km layer using the hypsometric equation:

$$P_{2\mathrm{km}}^{\kappa} = P_{j-1/2}^{\kappa} e^{-\frac{g\,\Delta z}{\kappa T_{j-1/2}}}$$

where $P_{j-1/2}{}^{\kappa}$ and $T_{j-1/2}$ are the pressure and temperature of the half-level where the critical lapse rate condition is satisfied, and Δz = 2km. If the average lapse rate thus calculated is also smaller than the critical lapse, then the tropopause is located between the half-levels $P_{j-1/2}^{\kappa}$ and $P_{j+1/2}^{\kappa}$ and its pressure can be computed by linear interpolation:

$$P_T^{\kappa} = P_{j-1/2}^{\kappa} + \frac{P_{j+1/2}^{\kappa} - P_{j-1/2}^{\kappa}}{\Gamma_{j+1/2} - \Gamma_{j-1/2}} \left(\Gamma_T - \Gamma_{j-1/2}\right)$$

If the mean lapse rate above the half-level $P_{j-1/2}^{\kappa}$ is greater than the critical lapse rate, the next half-level with lapse rate smaller than Γ_T is chosen instead, and the process is repeated.

In some cases there are inversions or discontinuities in the temperature profiles at low levels and at higher levels in the stratosphere (this is especially true in the case of radiosonde data). Aiming to avoid unrealistic tropopause pressures as a result of erroneous identification of these inversions, the search for the critical lapse rate is restricted to levels above 550hPa and below 75hPa (these restrictions are standard).

When using gridded data, it is possible to define the tropopause pressure at any point where the method is unable to find a level satisfying the WMO conditions using the mean of its surroundings (Reichler *et al.*, 2003). Since the tropopause height has a sharp gradient in the subtropics as it transitions from its tropical to its extratropical values, in this thesis we only use the adjacent grid points along the same latitude circle to fill missing values. Nevertheless, some missing values remain as adjacent grid points frequently display similar temperature profiles. On the other hand, it is not possible to use this procedure to fill missing values with radiosonde data.

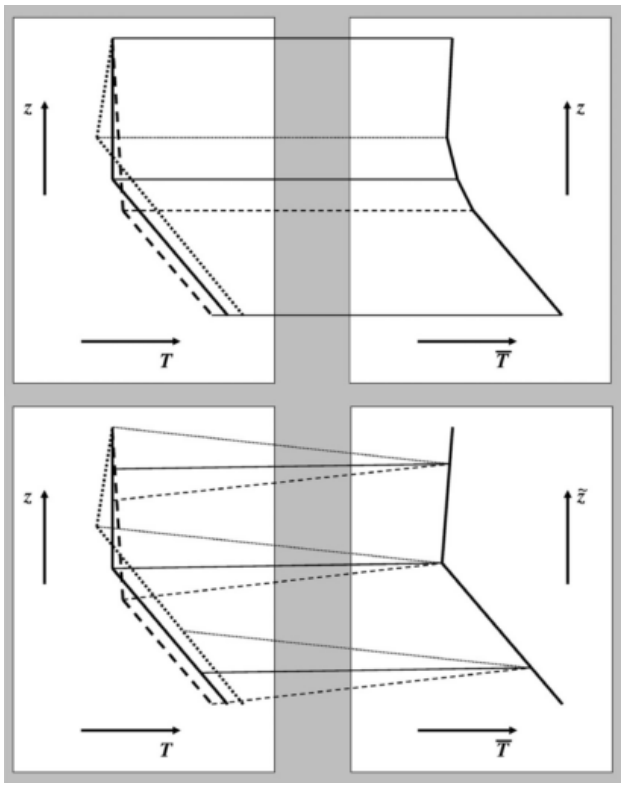

Fig. 3.2: Schematic illustration of the two methods of averaging. SLB average (conventional) (top) and TB average (bottom) temperature profiles that results from averaging (right) three hypothetical temperature profiles (left). See text for definition of z (reproduced from Birner, 2006).

Once the tropopause pressure for each day and grid point is found, the height of the tropopause is calculated by interpolation to height coordinates. We use cubic-spline interpolation to find $Z = Z(P)$ in terms of the geopotential height at the standard pressure levels provided by the reanalysis $Z_T = Z(P = P_T)$.

3.2 Tropopause-based coordinates.

As described in the introduction of this thesis, temperature has a fine-scale structure near the tropopause. Since tropopause height changes with time, this structure is smoothed out when averaging unless a special transformation of the vertical coordinate is used to shift the origin to the tropopause level. This is illustrated in Fig. 3.2. When averaging thermal profiles using standard Sea-Level-Based (SLB) coordinates, the climatological tropopause is less sharp than in the original profiles. In contrast, when temperature values are averaged at fixed distances from the tropopause in each profile, a sharper climatological tropopause is obtained (Birner, 2002). The new vertical coordinate is called the Tropopause-Based (TB) coordinate and is defined as:

$$\hat{z}(t,\lambda,\phi) = z - z_T(t,\lambda,\phi)$$

where z_T is the height of the tropopause. Note that the coordinate transformation is temporally and spatially dependent, as is the tropopause. It is also possible to shift the origin back to the surface by adding to this coordinate the climatological height of the tropopause, hence recovering an approximate SLB coordinate:

$$\tilde{z} = \hat{z} + \langle z_T \rangle = z - z_T + \langle z_T \rangle$$

Using this definition, any variable $x = x(z,t)$ can be transformed to TB coordinates as $x = x(\tilde{z},t)$ at each grid point and time step. However, note that because the transformation is not constant the resulting vertical levels will be different in each case. We thus interpolate the variables to a grid of uniformly spaced vertical levels around the tropopause using cubic-spline interpolation.

As both reanalysis and radiosonde data are defined on pressure levels rather than at constant height, and aiming to avoid unnecessary interpolations, the TB coordinates are defined in this thesis using pressure coordinates instead of geometric height. Specifically, variables are cubic-spline interpolated to a series of equidistant P^{κ} levels centred on the tropopause. The number of equidistant levels is chosen to be consistent with the resolution of the native data in the SLB coordinates. Depending on latitude, this corresponds to 10 to 13 levels for ERA-Interim reanalysis and around 5 to 10 for NCEP/NCAR reanalysis. Due to the great variability in the number of vertical levels in the radiosondes, the number of levels in this case is chosen to match the average vertical resolution near the tropopause, roughly 15hPa

3.3 Time-series analysis.

3.3.1 Anomalies.

The analysis of the temporal variability of a meteorological field is aided by several techniques intended to separate the different scales of variability in the time series. First, we

need to isolate this variability from the mean state, obtaining the so-called *anomaly*. If x is the time series of a certain meteorological variable, then its anomaly is defined as:

$$x'(t) = x(t) - \bar{x}$$

Depending on the scale of variability of interest, different anomalies can be computed by using different definitions of the mean state. In this thesis, the focus is on the seasonal and intraseasonal scales so the *mean state* is defined to include all variations with periods longer than the seasonal cycle. The natural choice of mean state for the seasonal variability is the annual average, so that interannual variations are eliminated. As for the intraseasonal scale, it is important to eliminate the seasonal variability, which has a strong influence on tropopause height (as shown in the introduction to this thesis).

We compute the mean seasonal cycle using the long-term daily climatology. Following Lorenz and Hartmann (2001), the mean seasonal cycle is defined as the annual average and the first four Fourier harmonics of the daily climatology. These harmonics correspond to the lowest frequencies of variability of the daily long-term average, presumably associated with the annual cycle. The process involves the computation of both the direct and inverse Fourier transforms.

The focus of this thesis is the variability during the winter season, when the eddy activity increases and the stratosphere is dynamically active (Thompson and Wallace, 2000). Specifically, we focus on the extended winter, from November to March in the Northern Hemisphere (NH) and from May to September for the Southern Hemisphere (SH). We define intraseasonal variability as the variability during these periods (to 151 days per year for the NH and 153 for the SH).

3.3.2 Time filtering

Even when the seasonal cycle is removed, longer frequency variability (i.e., interannual or decadal variations) may still be present in the data. Aiming to eliminate the variability at time scales longer than the intrannual scale, we apply time filtering to the anomalies prior to the statistical analysis. We use a Lanczos filter due to its good compromise between the at-

tenuation at the cut-off frequency and the distortion introduced by the finite Fourier series in comparison with other filters (see, for example, Duchon, 1979).

In general, filters are defined by a series of coefficients multiplying the lagged observations, as indicated below:

$$y(t) = \sum_{k=-M}^{M} \sigma_k \, x(t-k) \qquad (3.2)$$

where x is the original time series, y is the filtered time series and the σ_ks are the weights of the filter. Running means are an example of a filter with equal weights. Filters are most naturally designed in frequency space in terms of a cut-off frequency up or down to which the variations of that scale are attenuated –high- and low-pass filters, respectively. It can be seen in eq. (3.2) that the filtered time series is the discrete convolution in the time domain of the original time series and the weights of the filter; thus, in the frequency domain (i.e., taking the discrete Fourier transform), the filter can be expressed as:

$$Y(\omega) = H(\omega) \cdot X(\omega)$$

ω being the frequency. H is usually called the transfer function of the filter. An ideal filter would set to 0 all frequencies under/over the cut-off frequency and leave the rest un-

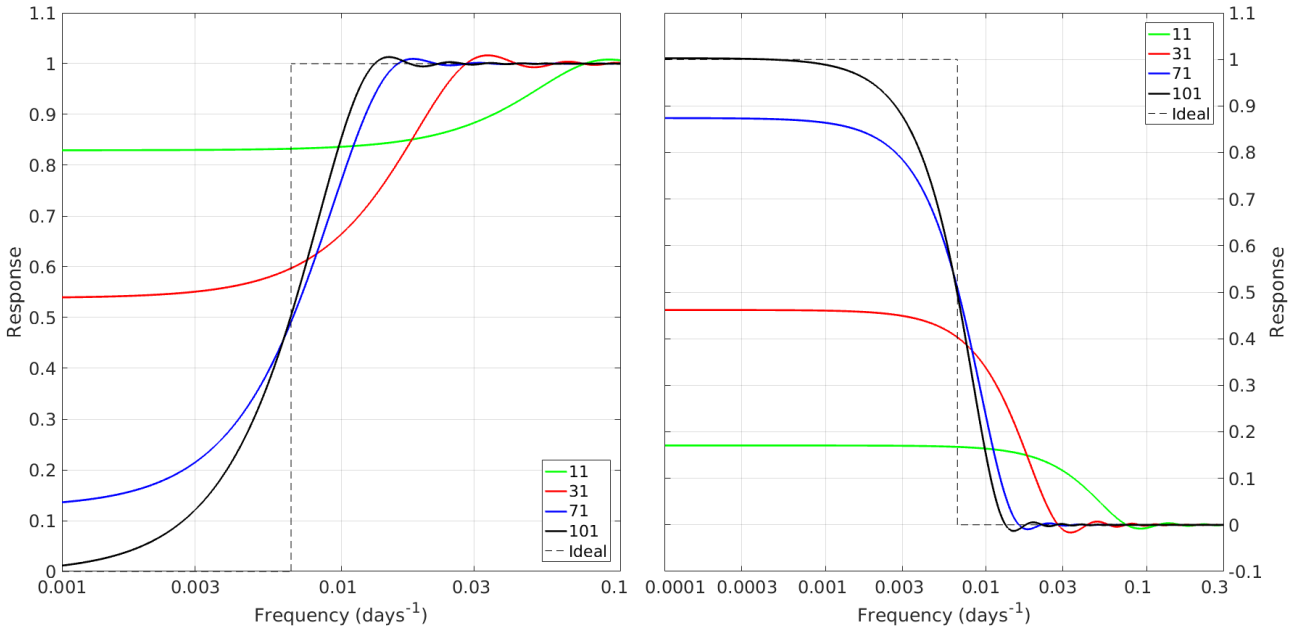

Fig. 3.3: Transfer function of the Lanczos filter with cutoff frequency of 1/151days ¹ in a high- □ (left) and lowpass (right) configurations using 11 (green solid line), 31 (red solid line), 71 (blue solid line) and 101 (black solid line) coefficients. See text for details. Also shown is the ideal filter with the step function as transfer function (black dashed line).

changed (see Fig. 3.3). However, with finite sampling the Fourier expansion of a periodic piecewise function inevitably introduces some distortion at the function edges –the so-called Gibbs phenomenon. Thus, several filters have been designed aiming to reduce the Gibbs phenomenon without compromising the attenuation of the undesired frequencies. Lanczos filter makes use of the observation by Lanczos that the amplitude of the Gibbs phenomenon is proportional to the frequency of the first neglected component in the Fourier expansion. Thus, averaging the Fourier transform of the rectangular function over an interval with length the frequency of the last retained term will attenuate the distortions, at the cost of broadening the transition at the cut-off frequency. In practice, this requires multiplying the Fourier transform of the rectangle window by some sigma coefficients, as indicated by the following transfer function for the high-pass Lanczos filter:

$$H(\omega) = 1 - \frac{\omega_c}{\omega_N}\left[1 + 2\sum_{k=1}^{M}\sigma(M,k)\sin\left(\frac{\frac{\pi k\omega_c}{\omega_N}}{\frac{\pi k\omega_c}{\omega_N}}\right)\cos\left(\frac{\pi k\omega_c}{\omega_N}\right)\right]$$

where

$$\sigma(M,k) = \frac{\sin\frac{\pi k}{M}}{\frac{\pi k}{M}}$$

are the Lanczos' sigma-factors that attenuate the Gibbs phenomenon. In these expressions, ω_c is the cut-off frequency; ω_N is the Nyquist frequency (the inverse of half the sampling time) and M is number or coefficients kept in the truncation. Fig. 3.3 shows the transfer function of the Lanczos filter for the cut-off frequency ω_c = 1/151 days^{-1} used in this thesis as a function of the number of coefficients retained for both the low- and the high-pass filters. It can be seen that as the number of coefficients retained increases the transition at the cut-off frequency steepens. While the Gibbs phenomenon increases in general with the number of coefficients, the smoothing effect of the Lanczos filter keeps the distortions under control and approximately constant. A good compromise is obtained when 101 coefficients are retained, and this is the configuration used in this thesis.

3.4 Principal Component Analysis

One of the biggest difficulties when analysing the temporal variations of a meteorological field is the large number of degrees of freedom involved. For example, the zonal mean extratropical tropopause in the NCEP/NCAR reanalysis consists of 24 time series, one per latitude. However, it is reasonable to expect that not all the 24 series vary independently; at least those located nearby may share some of the variations –as expected, for example, for nearby sounding stations. If there is some correlation between the time series at different latitudes, the number of degrees of freedom of the system can be expected to be less than the dimension of the system. Finding them is the objective of Principal Component Analysis (PCA).

The goal of PCA is finding those spatial patterns in a meteorological field that capture the most variance in the time series, exploiting the covariance structure of the data mentioned in the previous paragraph. The hope is that a limited number of such patterns may account for most of the variability, so that any field state can be expressed as a linear combination of these patterns. The method requires imposing a null correlation between the patterns, equivalent to orthogonality in time space. The patterns thus obtained are called the Empirical Orthogonal Functions (EOF) of the system or modes of variability, in analogy with the normal modes of a dynamical system, and provide a basis in which to represent the variability of the field. Thus, each state of the field can be projected along the direction of the EOFs to obtain the corresponding *coordinate*; the time series of these coordinates are called the Principal Components (PC) of the system, or simply the expansion coefficients.

Mathematically, the method consists in finding a vector **e** that has the highest resemblance (as measured by the squared inner product) with the set of N vectors **x** of observations that define the state of the field. These can be grouped as the columns of a matrix of observations **X**, so that

$$\frac{\left(\mathbf{e}\cdot\mathbf{X}\right)^2}{N} = \frac{\left(\mathbf{e}^T\cdot\mathbf{X}\right)^2}{N} = \frac{\mathbf{e}^T\cdot\mathbf{X}\cdot\mathbf{X}^T\cdot\mathbf{e}}{N} = \mathbf{e}^T\cdot\mathbf{C}\cdot\mathbf{e} \qquad (3.3)$$

needs to be maximized. The product is normalized by N so that the result does not depend on the number of observations, and $\mathbf{e}$ is defined to be a unit vector

$$\mathbf{e}^T \cdot \mathbf{e} = 1 \tag{3.4}$$

If anomalies $\mathbf{x}'$ are used instead of direct observations, then $\mathbf{C}$ is the covariance matrix

$$\mathbf{C} = \frac{1}{N} \mathbf{X}' \cdot \mathbf{X}'^T$$

The problem of maximizing eq. (3.3) under condition (3.4) is a variational problem involving the use of Lagrange multipliers. If λ is the maximum value of (3.3), then the problem requires solving $\mathbf{e}^T \cdot \mathbf{C} \cdot \mathbf{e} = \lambda$ .Using (3.4), this can be written as $\mathbf{C} \cdot \mathbf{e} = \lambda \mathbf{e}$ so that the system only has a solution when

$$\left| \mathbf{C} - \lambda \mathbf{I} \right| = 0 \tag{3.5}$$

This is the well-known problem of the diagonalization of matrix $\mathbf{C}$, and the solution of eq. (3.5) leads to the eigenvalues λ_i and the associated basis of eigenvectors $\mathbf{e}_i$ in which $\mathbf{C}$ is diagonal. Since the covariance matrix $\mathbf{C}$ is real and symmetric, its eigenvalues will be positive. Thus, the EOFs are the eigenvectors of the covariance matrix of the data and the variance explained by each of them is proportional to its associated eigenvalue as:

$$v_i = \frac{\lambda_i}{\sum_{j=1}^{M} \lambda_i}$$

where M is the length of the state vectors $\mathbf{x}$. The idea is that the first few eigenvalues may account for a large fraction of the variance of the field, so that the number of vectors necessary to describe the system is reduced from its dimension M. This basis allows to express any possible state of the system in terms of its coordinates with respect to the EOFs $\mathbf{x}(t) = \sum_i \alpha_i(t) \mathbf{EOF}_i$. The time series of these coordinates α_i are the PCs for the i-th EOF and can be calculated by projecting $\mathbf{X}'$ onto the EOF:

$$\mathbf{PC}_i(t) = \mathbf{X}'^T \cdot \mathbf{EOF}_i \qquad (3.6)$$

Some care must be taken when performing PCA on a regular grid on the sphere. As shown by North *et al.* (1982a), due to geometric effects the variance of such a field increases toward the pole because the variable samples along the latitude circle are more correlated. If the spatial autocorrelation of the field decreases with a length scale L, then many of the grid points at the poles lie within this length scale and are thus not independent (this happens to a greater or lesser extent for all the meteorological fields), so that modes with large polar amplitude will appear to capture more variance. North *et al.* (1982a) noted that by multiplying the variable of interest by the cosine of the latitude its variance remains more or less constant with latitude. Since PCA makes use of the covariance matrix, the matrix of anomalies $\mathbf{X}'$ has to be multiplied by the square root of the cosine of the latitude if realistic EOFs are to be obtained.

Since EOFs are computed using a finite number of observations, they are subject to statistical errors due to limited sampling of the population that represents the field. Consider a field displaying random variability in time (white noise). The real covariance matrix should have equal eigenvalues in this case, as no single spatial pattern explains more variance than the others. However, when PCA is performed on a sample of this population, the eigenvalues (i.e., the sampling variances for each of the patterns) will be statistically distributed about their mean value (the actual population variance), with some patterns explaining more variance than others (see Fig. 3.4) due to sampling. Thus, PCA will produce preferred modes of variability in this case even though the states of the original variable are randomly distributed. The effect is aggravated in real meteorological fields, which tend to have some autocorrelation in time and are better character-

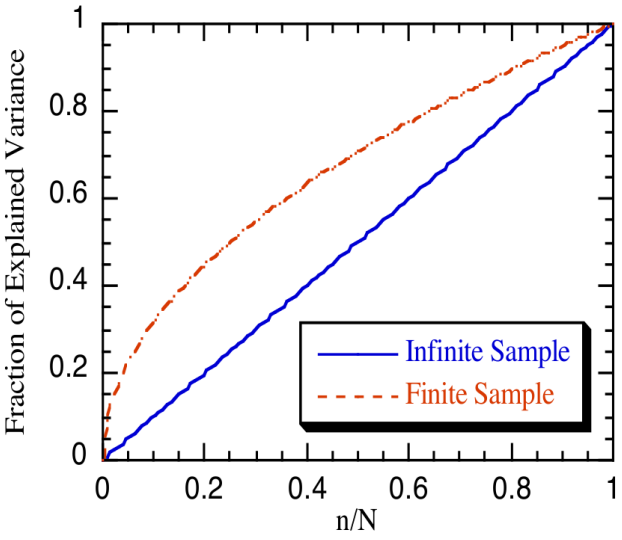

Fig. 4.4: Explained variance as a function of the number of principal components retained, n, out of the total possible, N, for a data set with no real structure, as explained in the text. Because of sampling errors, some EOFs will always appear to explain more of the variance than others do (extracted from Hartmann, 2014)

ized as red noise. North *et al.* (1982b) studied the statistical significance of EOFs in the presence of sampling errors, finding that two eigenvectors are statistically different when their corresponding eigenvalues are separated by more than:

$$\Delta\lambda_i \geq \lambda_i \sqrt{\frac{2}{N_{eff}}} \tag{3.7}$$

where λ_i is the eigenvalue of the ith EOF and N_{eff} is the effective number of degrees of freedom, taking into account the temporal autocorrelation of the field. Following Bretherton *et al.* (1999), this can be estimated as:

$$N_{eff} = \frac{N}{\sum_{\tau=-(N-1)}^{(N-1)} \left(1 - \frac{|\tau|}{N}\right) \rho_\tau^2} \tag{3.8}$$

where ρ_τ^2 is the square of the autocorrelation of the time series at lag τ.

Even when all the factors mentioned above are taken into account, there is no guarantee that PCA will produce physically meaningful patterns, as this is just a mathematical construction in which the various restrictions imposed (independence of the EOFs, null correlation of the PCs, etc.) may constrain the results. It is thus important to make sure that the EOFs are both robust and governed by physically meaningful dynamics. The former can be assessed by performing PCA on subsets of the variable (both temporal and spatial), and the latter by analysing the coupled variability with relevant dynamical fields. We will make heavy use of PCA in this thesis.

3.5 Composite and regression maps.

The modes of variability obtained using PCA can be represented in various ways. The simplest choice is to show the EOFs, for they are the spatial patterns associated with each mode. This plotting, however, does not provide information on the actual magnitude of the variability associated with the mode, as all EOFs have amplitude 1 by construction. Projecting the field on the standardized mode along the time dimension gives a more meaningful representation, as the magnitude of the variability now has the same units as the variable. From eq.

(3.6) in the previous section it can be deduced that $\mathbf{EOF}^T = \mathbf{PC}^T \cdot \mathbf{X}'^T$, as **X'** is an orthogonal matrix. Normalizing by the standard deviation of the **PC** and by the number of observations *N,* the **EOF** will have the same units as the original variable and represents the anomaly **X'** associated with one standard deviation of the **PC**. This type of plot is called a *regression map*, as one may envision the expansion as a least square fitting to **X'** (Hartmann, 2014). One can intuitively understand this by interpreting the product $\mathbf{PC}^T \cdot \mathbf{X}'^T / N$ as a weighted average of **X'**, with days when the field is close to the EOF having weights of 1, days with no resemblance having 0 weight and days with anomalies of the opposite polarity having weight -1.

A second type of representation of the modes of variability and related variations in other meteorological fields is used in this thesis. Instead of the weighted average described in the previous paragraph, one can compute the mean considering only those days in which the PC exceeds some threshold value, which will produce a spatial pattern very close to the EOF. This is called a *composite map*. The greater the critical value used when selecting the days to composite, the lesser the number of samples taken in the average and the smaller the statistical signification. Hence, there is a compromise between statistical signification and similarity with the EOF when choosing the critical value. A good compromise can be obtained using for the critical value one standard deviation of the PC, and this is what is done in this thesis. When the samples entering the composite are selected a fixed number of days before or after the day exceeding the critical value a *lagged composite map* is obtained, representing the average situation on the days preceding or following the peak of the mode.

We assess the statistical significance of the patterns shown in the composites or lagged composites performing a two-tailed Student's *t*-test for the difference of means between the full and the composite time series, using a significance level of 1%.

Pearson's correlation is also used to study the relation between the PCs and some other variables, as well as in lagged correlations aimed at exploring causality. The statistical significance is assessed using a *t*-test for the correlation, taking into account the effective number of degrees of freedom (Bretherton *et al.*, 1999, see equation 3.8).

3.6 Eddy and Eliassen-Palm fluxes.

The region of interest in this thesis is the extratropical area, with a particular focus on the midlatitudes. In this section, we review some aspects of extratropical dynamics and their representation, which will be useful for analysing tropopause variability.

As is apparent in Fig. 3.5, the horizontal pressure field is more or less zonally symmetric in the tropical latitudes, but important deviations are found along latitude circles in the extratropical areas, particularly in the midlatitudes. This difference is due to the important constraint on the circulation exerted by the Coriolis force in the extratropics. Hence, when analysing extratropical fields it is natural to separate the variables into a term representing their zonally symmetric part and the deviations from it. Any variable A can be expressed as the sum $A = \bar{A} + A'$, where $\bar{A}$ is the zonal average:

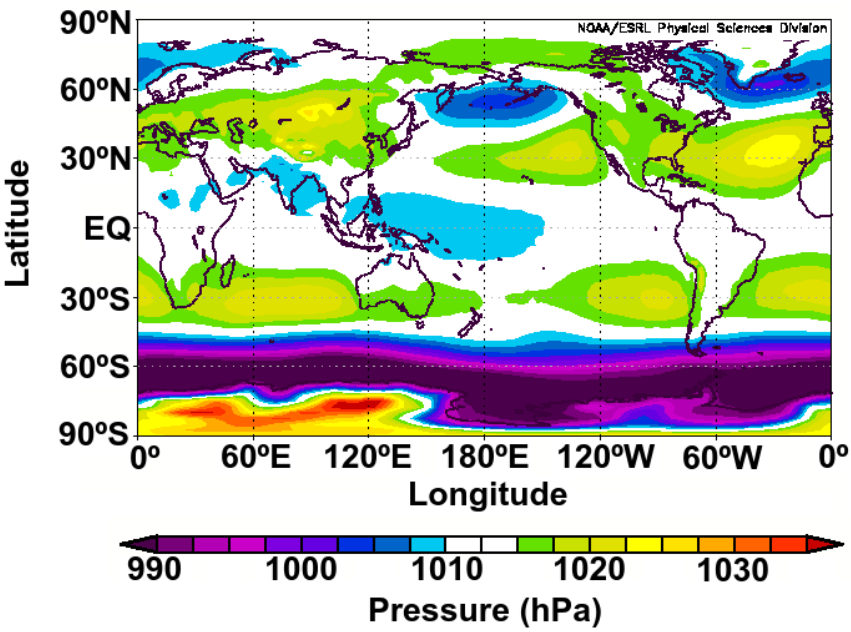

Fig. 3.5: Average of the zonal component U of the wind at 500hPa during 1986 in the ERA-Interim reanalysis.

$$\bar{A} = \frac{1}{2\pi}\int_0^{2\pi} A\, d\lambda$$

λ is longitude, and $A' = A - \bar{A}$ is called the *eddy* part of A. As noted above, the eddy part is usually more important in the extratropics, but note that some zonal asymmetries are also present in the tropics (Walker circulation, Madden-Julian Oscillation, etc.).

These differences also play a role on the mechanisms of energy transport in each region. Energy is mainly distributed by the zonally symmetric part of the circulation in the Tropics, associated with the large mass transports by the Hadley cell, while the eddy circulation accounts for much of the poleward transport of energy in the extratropics, where the zonally averaged circulation is weaker. For illustration, the vertically- and zonally-averaged

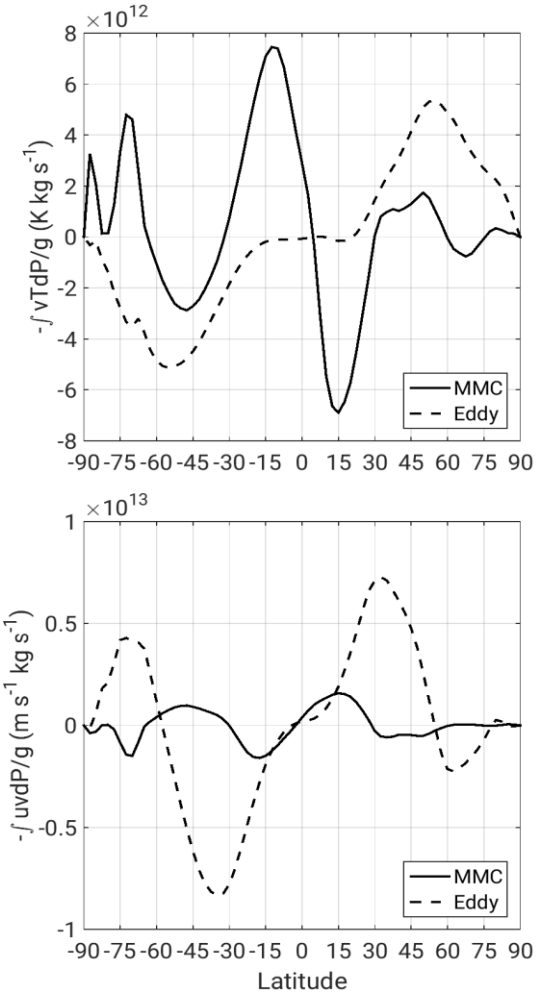

Fig. 3.6: Meridional zonally averaged and vertically integrated heat transport (top) and zonal momentum transport (bottom) by the Mean Meridional Circulation (solid line) and by the eddies (dashed line).

meridional heat transport by both components of the circulation is shown in Fig. 3.6. Eddy transport becomes dominant poleward of about 30° in each hemisphere. It can also be seen in Fig. 3.6 that the momentum transport displays a similar behaviour.

The zonally symmetric part of the circulation is forced by the differential heating, namely radiative heating, between the low latitudes and the poles, while the eddy part is the dynamical response to it, trying to eliminate the meridional temperature gradients under the constraints exerted by the Coriolis force. This zonally symmetric part can be interpreted as the *basic* or *mean* state of the circulation, perturbed by the perturbations that develop within it. The hope is that when linearizing the system of equations describing the atmosphere the interaction between the basic state and the eddies can be properly described.

Consider the zonal momentum and thermodynamic equations on the beta plane (for reasons of simplicity):

$$\begin{aligned} &\frac{Du}{Dt} - fv + \frac{\partial \Phi}{\partial x} + \mathsf{F} = 0 \\ &\frac{D\theta}{Dt} = \mathsf{Q} \end{aligned} \qquad (3.9)$$

where $\Phi = -P/\rho$, ρ is density; F and Q are friction and diabatic heating, respectively and D/Dt represents the Lagrangian temporal derivative (the rest of the notation is standard). Splitting the variables into their zonal-mean and eddy components, and zonally averaging the resulting expressions, (3.9) becomes:

$$\begin{aligned}
&\frac{\partial \bar{u}}{\partial t}+\bar{v}\left(\frac{\partial \bar{u}}{\partial y}-f\right)+\bar{\omega}\frac{\partial \bar{u}}{\partial P}=-\frac{\partial}{\partial y}\overline{u'v'}-\frac{\partial}{\partial P}\overline{u'\omega'}+\bar{\mathsf{F}}\\
&\frac{\partial \theta}{\partial t}+\bar{\omega}\frac{\partial \bar{\theta}}{\partial P}=-\frac{\partial}{\partial y}\overline{v'\theta'}-\frac{\partial}{\partial P}\overline{\omega'\theta'}+\bar{\mathsf{Q}}
\end{aligned} \tag{3.10}$$

These are the so-called Eulerian-mean equations for zonal momentum and potential temperature. Given the time and length scales of the eddies of interest in this thesis, the quasi-geostrophic approximation can be used to simplify the equations by neglecting all the vertical eddy flux terms and all ageostrophic velocities except when multiplied by f or the reference stratification $\partial\bar{\theta}/\partial P$. Then (3.10) transforms into:

$$\begin{aligned}
&\frac{\partial \bar{u}}{\partial t}=f\,\bar{v}-\frac{\partial}{\partial y}\overline{u'v'}+\bar{\mathsf{F}}\\
&\frac{\partial \theta}{\partial t}=-\bar{\omega}\frac{\partial \bar{\theta}}{\partial P}-\frac{\partial}{\partial y}\overline{v'\theta'}+\bar{\mathsf{Q}}
\end{aligned} \tag{3.11}$$

The thermodynamic equation in this form is not quite satisfactory because the first two terms on the right hand side tend to cancel each other in the extratropics (Vallis, 2005), namely, the convergence (divergence) of eddy heat fluxes tends to be balanced by adiabatic rising (sinking) that cools (warms) the air masses. Something similar occurs for the momentum equation, with eddy momentum convergence (divergence) being balanced by the Coriolis force acting on an indirect (direct) meridional circulation (the Ferrel cell, as eddy momentum convergence dominates in the midlatitudes). Because of these compensations the net eddy forcing of the mean flow is not apparent in these equations. Likewise, the role of diabatic heating in driving the overturning circulation is not obvious –this term appears as a residual while being the ultimate driver. A more transparent description can be obtained by applying the following change of variables to the Eulerian-mean equations (3.11):

$$\begin{aligned}
&\bar{v}^{*}=\bar{v}-\frac{\partial\left(\overline{v'\theta'}/\bar{\theta}_{P}\right)}{\partial P}\\
&\bar{\omega}^{*}=\bar{\omega}+\frac{\partial\left(\overline{v'\theta'}/\bar{\theta}_{P}\right)}{\partial P}
\end{aligned} \tag{3.12}$$

where subscript P indicates pressure derivative. These expressions define a non-divergent two-dimensional velocity field in the latitude-height plane known as the *residual circulation.* With these definitions, eq. (3.11) transforms into:

$$\begin{aligned} &\frac{\partial \bar{u}}{\partial t} - f\,\bar{v}^* - \bar{\mathsf{F}} = \nabla\cdot\mathbf{F} \\ &\frac{\partial \bar{\theta}}{\partial t} + \bar{\omega}^* \frac{\partial \bar{\theta}}{\partial P} - \bar{\mathsf{Q}} = 0 \end{aligned} \tag{3.13}$$

Note that the eddy fluxes do not appear directly in the thermodynamic equation, so that in steady state diabatic heating (cooling) induces adiabatic rising (sinking). As an additional result, the zonal momentum equation adopts a simpler form as all eddy terms are now grouped on the right hand side of the equation in the form of the divergence of a vector. This vector is known as the *Eliassen-Palm flux* (Edmon *et al.*, 1980) and has components:

$$F_{(y)} = -\overline{u'v'}; \quad F_{(P)} = f\,\frac{\overline{v'\theta'}}{\bar{\theta}_P}$$

(subscripts in parentheses denote a vectorial component). Whence the horizontal component of this flux is opposite to the meridional eddy momentum flux and the vertical component is proportional to the meridional eddy heat flux, normalized by the stratification of the mean state. This combination of the eddy fluxes produce a net zonal forcing on the mean flow.

There is another important property of the Eliassen-Palm flux that will be used in this thesis. Consider the potential vorticity, defined as:

$$q = \frac{\partial v}{\partial x} - \frac{\partial u}{\partial y} + f\left(\frac{\theta}{\theta_P}\right)_P$$

where we use the quasi-geostrophic approximation (i.e., the velocities in the equation are the geostrophic velocities and $\theta'_P \ll \bar{\theta}_P$). Separating between the zonal-mean and eddy components, the quasi-geostrophic eddy (pseudo)potential vorticity is

$$q' = \frac{\partial v'}{\partial x} - \frac{\partial u'}{\partial y} + f\left(\frac{\theta'}{\bar{\theta}_P}\right)_P$$

Multiplying by v', zonally averaging and noting that $\partial u'/\partial x = -\partial v'/\partial y$ for geostrophic flow, the meridional eddy flux of potential vorticity is:

$$\overline{v'q'} = -\frac{\partial}{\partial y}\overline{u'v'} + \frac{\partial}{\partial P}\left(\frac{\overline{v'\theta'}}{\bar{\theta}_P}\right) = \frac{\partial F_{(y)}}{\partial y} + \frac{\partial F_{(P)}}{\partial P} = \nabla \cdot \mathbf{F}$$

Hence, the divergence of the Eliassen-Palm flux is equal to the meridional flux of quasi-geostrophic potential vorticity by the eddies. Since perturbations in the potential vorticity field near the tropopause are related with variations in its height (Hoskins *et al.*, 1985), this is an important relation for understanding tropopause height variability.

Finally, if the tendency equation of eddy quasi-geostrophic potential vorticity

$$\frac{\partial q'}{\partial t} + \bar{u}\frac{\partial q'}{\partial x} + v'\frac{\partial \bar{q}}{\partial y} = \mathsf{D}$$

(neglecting second order eddy terms; D is the dissipative term) is multiplied by q', zonally averaged and divided by $\partial\bar{q}/\partial y$ (which we assume here independent of time for simplicity), then the following conservation equation is obtained:

$$\frac{\partial\left(\overline{q'^2}/2\bar{q}_y\right)}{\partial t} + \overline{v'q'} = \mathsf{D}\frac{q'}{\bar{q}_y} \Rightarrow \frac{\partial A}{\partial t} + \nabla \cdot \mathbf{F} = \mathsf{D}$$

A is a measure of local wave activity, proportional to eddy potential vorticity amplitude (normalized by the meridional gradient of the potential vorticity of the mean state). This relation states that, in the absence of dissipative processes (diabatic heating or frictional effects) the divergence of the Eliassen-Palm flux is non-zero where growth or decay of the eddies occurs. By virtue of (3.13), in general eddy growth occurs at the expense of the mean-flow momentum while eddy decay is associated with a transfer of momentum from the eddies to

the mean flow. It is important to note that, according to (3.13), the interaction of the eddies with the mean flow occurs only where $\nabla\cdot\mathbf{F}$ is nonzero. Finally, it can be shown that the direction of the Eliassen-Palm indicates the direction in which the eddies propagate.

Some graphical conventions are necessary to properly represent the Eliassen-Palm flux and its divergence, as noted by Edmon *et al.* (1980). In spherical coordinates:

$$F_{(\phi)} = -a\cos\phi\,\overline{u'v'}; \qquad F_{(P)} = a\cos\phi\, f\,\frac{\overline{v'\theta'}}{\bar{\theta}_P}$$

$$\nabla\cdot\mathbf{F} = \frac{1}{a\cos\phi}\frac{\partial F_{(\phi)}\cos\phi}{\partial\phi} + \frac{\partial F_{(P)}}{\partial P}$$

where a is the radius of Earth and ϕ is latitude. Additionally, in order for the vector components to represent the total eddy fluxes across the latitude circles we weight them by mass. In the latitude-pressure plane, this corresponds to:

$$\hat{F}_{(\phi)} = -\frac{2\pi a^2}{g}\cos\phi\,\overline{u'v'}; \qquad \hat{F}_{(P)} = \frac{2\pi a^3}{g}\cos^2\phi\, f\,\frac{\overline{v'\theta'}}{\bar{\theta}_P}$$

$$\nabla\cdot\mathbf{F} = \frac{\partial\hat{F}_{(\phi)}}{\partial\phi} + \frac{\partial\hat{F}_{(P)}}{\partial P}$$

We also scale the components of the vectors for graphical convenience. This is particularly useful when extending the Eliassen-Palm diagram into the stratosphere, where the Eliassen-Palm fluxes are much smaller than in the troposphere.

Not mention has yet been made of the size of the eddies, as the eddy term so-defined does include eddies of all spatial scales. The scale of the eddies nevertheless is determinant in their propagation and dissipation and, hence, in their interaction with the basic flow. For instance, stationary Rossby waves -a kind of eddy- can only propagate when the mean flow is westward and slower than a certain value which depends inversely on their wave number (Charney-Drazin criterion), meaning that only the longest waves are allowed to propagate upwards into the stratosphere -as the smaller waves need slower mean flows to propagate than those observed in the stratosphere. Eddies are thus separated into two major groups ac-

cording to their size, as measured by their zonal wavenumber: eddies with zonal wavenumber greater or equal than 4 -termed as *synoptic* eddies following Son *et al.* (2007), although eddies with scales longer than the synoptic scale are included- and eddies with zonal wavenumber lesser or equal than 3, termed as planetary eddies. The filtering in the zonal wavenumber is done by setting to 0 all the components of the zonal Fourier transform of the field greater or lesser than the critical wavenumber.

4. Objective definitions for the tropopause.

Before analyzing the variability of the tropopause, this chapter focuses on the nature of the thermal tropopause and its characteristics. Beyond the scientific interest of the topic, the insight gained will aid out understanding of the mechanisms driving tropopause variability in subsequent chapters.

Based on the analysis of the structure of the thermal tropopause, several *objective* definitions for the tropopause are provided in the second part of this chapter. These definitions are objective in the sense that they are based on the characteristics of the atmosphere and not on any particular thresholds deduced from observations. Of course these definitions, in spite of their conceptual advantage, come with their own problems as shown below.

4.1 Optimal thermal tropopause.

4.1.1 Definitions of the thermal tropopause.

As noted in the introduction to this thesis, the thermal definition of the tropopause is motivated by the observation that the tropospheric and stratospheric stratifications follow distinct distributions because they are determined by different physical processes (Held, 1982). The standard 2 K km^{-1} criterion provides a reasonable separation between both distri-

butions and has been used operationally to define the tropopause with much success. However, this threshold is unlikely to work well in climates with very different distributions of tropospheric and/or stratospheric stratifications. This prompts the question of whether traditional tropopause definitions are optimal or alternative definitions might be superior for separating the troposphere and the stratosphere, at least in some regions/climates. In particular, given that the thermal tropopause arises from a discontinuity in the stratification, an optimal lapse rate threshold for a given climate would be such as to produce the highest stratification contrast (i.e., the highest curvature in the thermal profile) at the tropopause level.

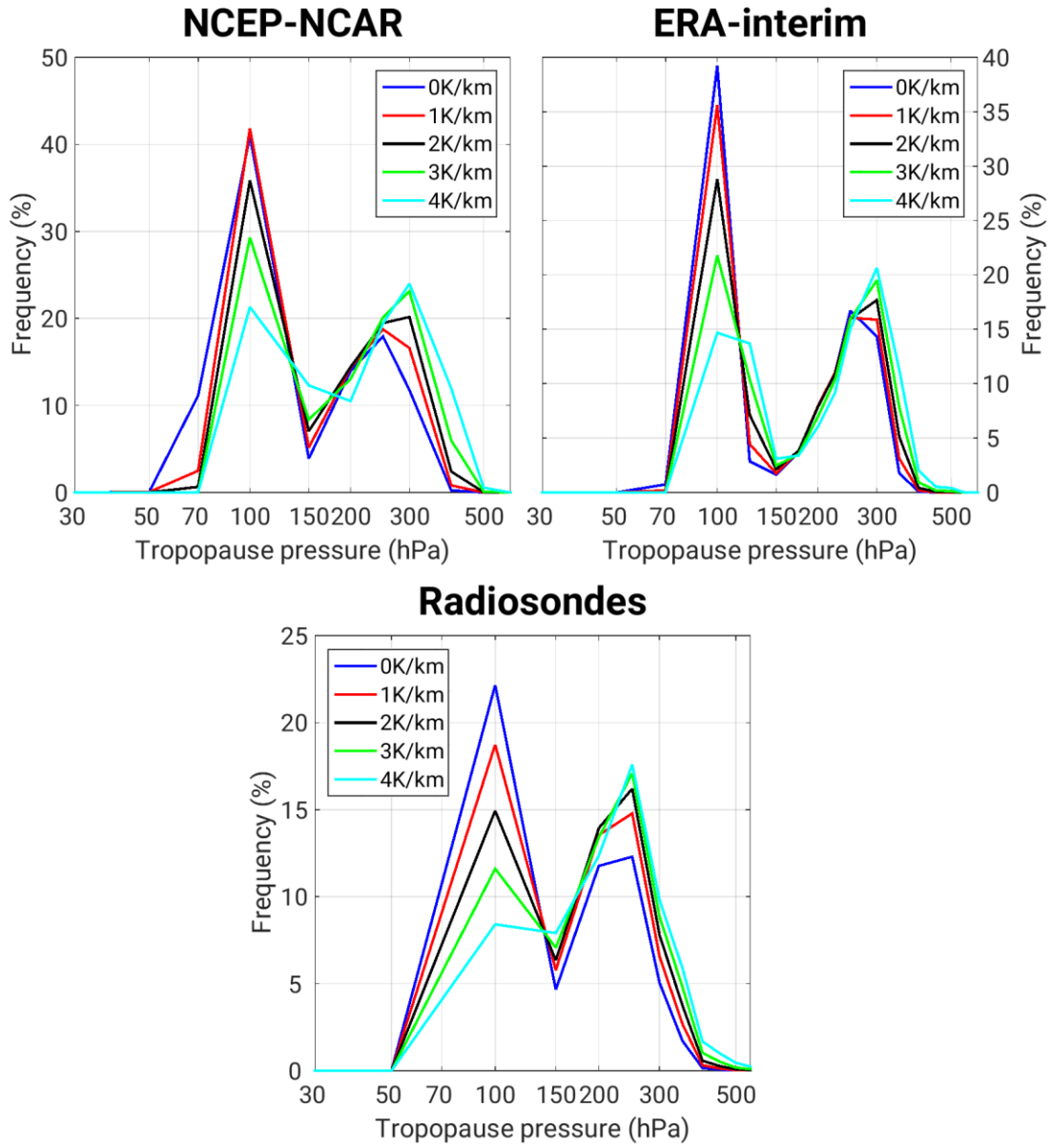

Fig. 4.1: Histogram of the tropopause pressure (hPa) in the NCEP-NCAR reanalysis (top left), ERA-interim (top right) and the IGRA radiosondes (bottom), when the tropopause is determined using different values for the critical lapse rate. The resolution is given by the spacing of the pressure levels for the reanalyses, and by the mean vertical resolution in the case of the radiosondes. Each station of the IGRA dataset and each grid point in the reanalysis are regarded as independent observations. Colours denote the critical lapse rate used for the tropopause.

Searching for an optimal threshold, several critical lapse rates are used for the determination of the tropopause in addition to the usual 2K km^{-1}, ranging from 0 to 4 K km^{-1} in 0.25 K km^{-1} intervals. With each of these choices, we determine the tropopause height using the formulation of Reichler *et al.* (2003) as described in Section 3.1. Fig. 4.1 shows the frequency distributions of the tropopause pressure obtained with each critical lapse rate in all datasets; it can be seen that tropopauses tend to be distributed around two maxima: around 100hPa, corresponding to the tropical values, and around 250-300hPa, corresponding to the extratropical areas (Hoinka, 1998). The tropopause pressure distributions are displaced to higher pressure values -lower altitudes- when the critical lapse rate is increased. When the frequency distributions are computed at higher resolution -by using tighter bins (Fig. 4.2)-, a multimodal distribution appears with minima halfway of the reanalysis pressure levels. These are the points used for the determination of the tropopause in the method, which tends to produce

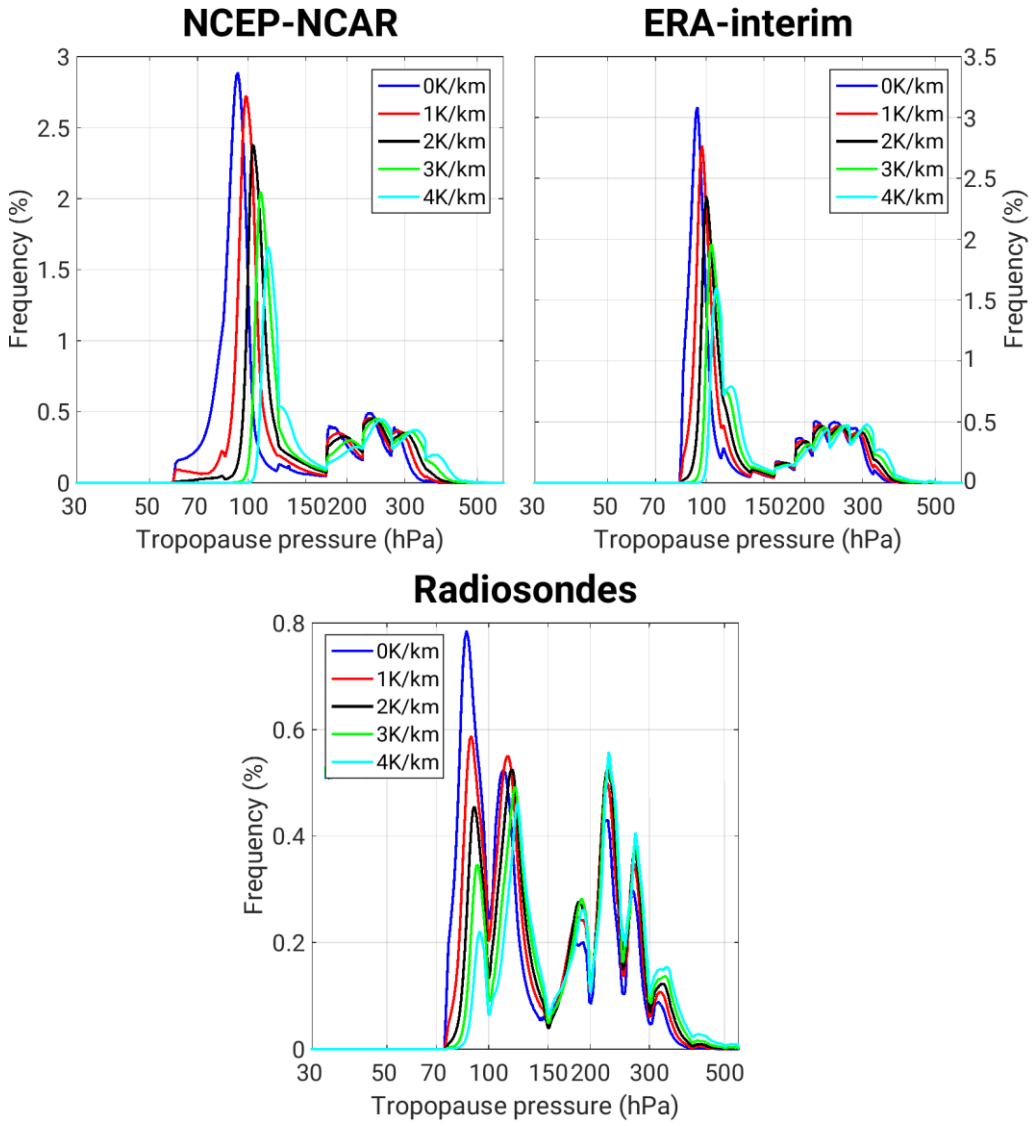

Fig. 4.2: Same as Fig. 4.1 but with a higher resolution than the resolution of reanalysis and the radiosondes.

independent bell-shaped distributions between those levels, so that this multimodal distribution is an artefact of the method used for the tropopause determination. For the radiosondes, in contrast, minima of the distribution are found at the standard pressure levels.

Because the mean tropopause varies more with latitude than with longitude (Hoinka, 1998), in all of the following analyses the distributions are computed grouping together the thermal profiles within the same latitudinal band.

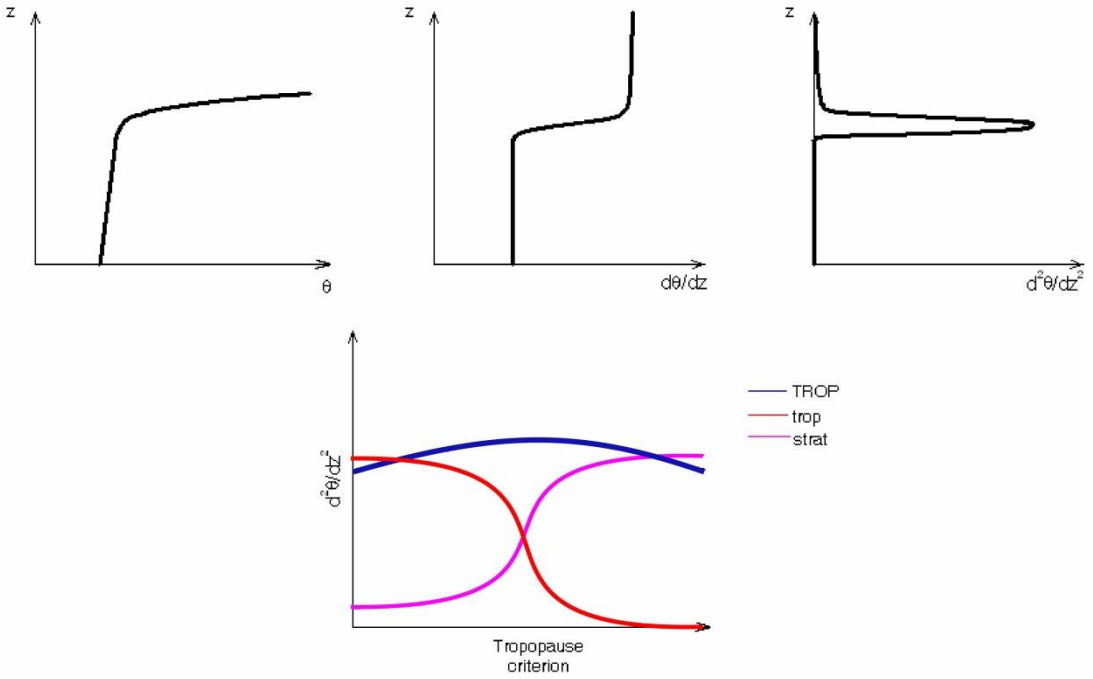

Fig. 4.3: Schematics of the ideal thermal tropopause: (top left) potential temperature profile, (top middle) its first derivative, (top right) its curvature -second derivative- and (bottom) the corresponding distribution of the curvature (blue) at the tropopause level, (red) below the tropopause and (pink) above the tropopause as a function of the critical lapse rate.

4.1.2. Critical lapse rate of maximum curvature.

As commented above, the optimal lapse rate threshold for the tropopause should provide the most contrast between the tropospheric and stratospheric air masses. A possible criterion for determining the level at which this occurs is the maximization of the curvature of the potential temperature profile , which would be associated with a sharp lapse rate change across the tropopause and high troposphere-stratosphere contrast, as shown in Fig. 4.3. Birner (2010) used a similar idea to provide a *global* definition of the climatological tropopause, applicable both in tropics and extratropics. Hence, if the curvature of the potential temperature is computed for each of the tropopauses defined in the previous section, then the optimal critical lapse rate will be that one maximizing the tropopause curvature (Fig. 4.3,

bottom). The use of potential temperature instead of the usual temperature is motivated by its conservation in quasi-adiabatic process; potential temperature acts as a tracer, allowing us to discriminate between the tropospheric and stratospheric air masses.

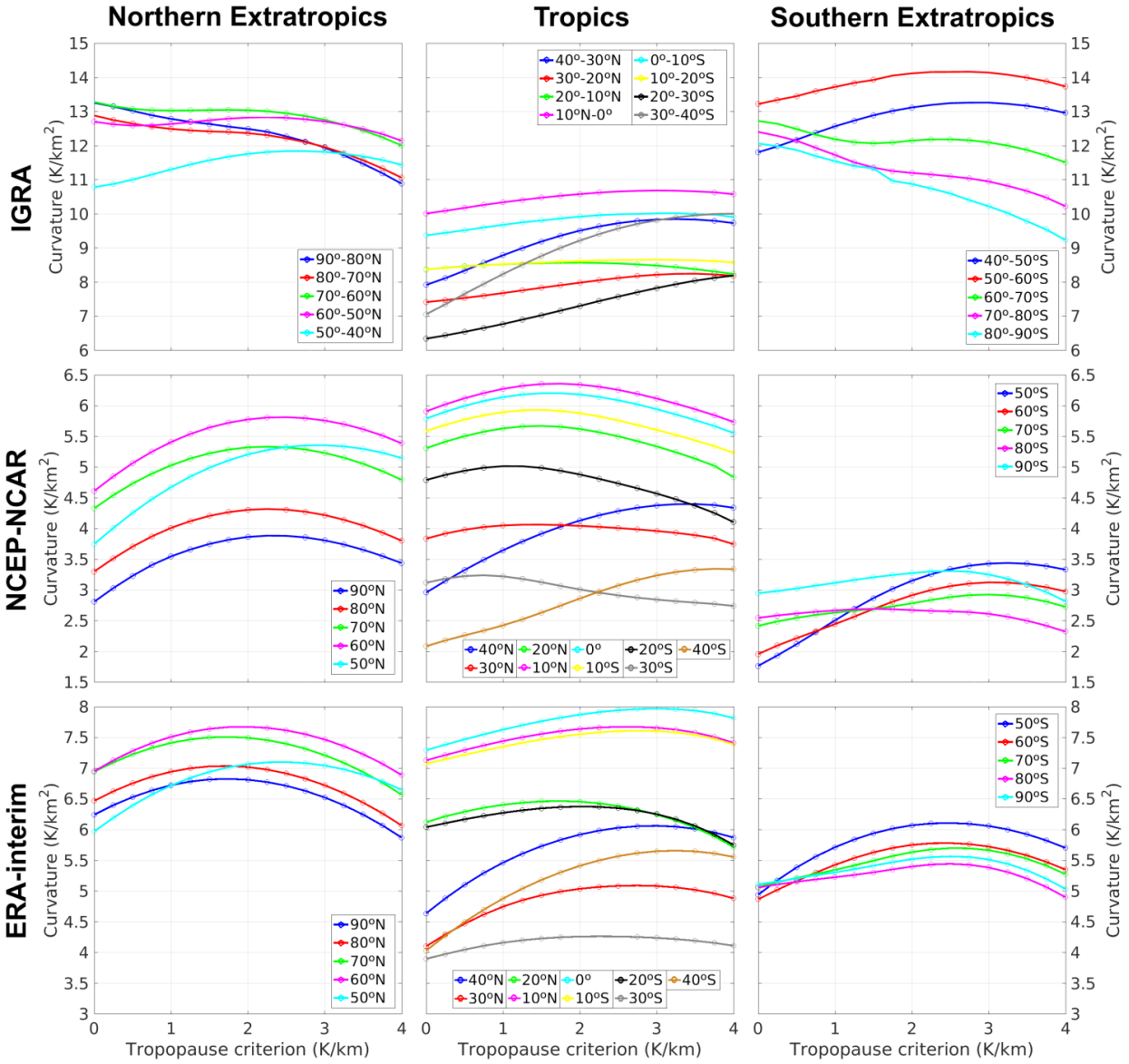

Fig. 4.4: Mean curvature at the tropopause level as a function of the lapse rate threshold used in each latitudinal band of the Northern Extratropics (left column), the Tropics (middle column) and the Southern Extratropics (right column) for radiosonde dataset (top row), NCEP-NCAR reanalysis (middle row) and ERA-interim reanalysis (bottom row). Circles indicate means significantly (95%) different from the maximum curvature according to a t test for the difference of means.

Fig. 4.4 shows the mean value of the distribution of potential temperature curvature at the tropopause level as a function of the critical lapse rate used to define the tropopause (similar figures are obtained for other percentiles of the distribution). As our analysis focusses on the region surrounding the tropopause, and aiming to eliminate the blurring when averaging in the standard sea-level-based coordinates (see Section 3.2), all curvatures are interpolated to tropopause-based coordinates (note that each tropopause has its own coordinates). The

results are presented in three groups: Northern and Southern Extratropics and the Tropics. Note that we do not distinguish between the different seasons and use whole-year data to construct this figure.

In the Northern Extratropics a critical lapse rate of 2 – 2.5K km^{-1} maximizes the curvature of the potential temperature profile; thus, a tropopause defined using these values provides the best separation between the tropospheric and stratospheric air masses. This supports the use of the WMO definition, though the optimal critical lapse rate does depend on latitude, being lower at high latitudes (around 1.5K km^{-1} for polar areas) and higher at low latitudes (around 3K km^{-1}). The optimal values agree well in the IGRA and ERA-interim datasets, though the maximum is less marked with the radiosondes (especially with low lapse rates), probably due to the tropopause inversion layer (TIL, see section 4.1.3). The results with

NCEP-NCAR reanalysis are slightly different but 2K km^{-1} still seems to provide the optimal threshold for defining the northern extratropical tropopause. Note that the WMO definition was originally established based on observed soundings in this area.

As for the tropical region, again radiosondes and ERA-interim display good qualitative agreement, pointing to 3 – 3.5K km^{-1} as the optimal value for the tropopause critical lapse rate. This implies that the WMO tropopause will, in general, lie above the point of maximum curvature and provide less contrast between the stratospheric and the tropospheric air masses. The cold-point tropopause (defined using a 0K km^{-1} critical lapse rate) would be located even further away from the level of maximum curvature, although it is true that this definition is the most relevant for the dehydration of the tropospheric air masses entering the stratosphere. For NCEP-NCAR reanalysis the results are quite different, pointing to 1 – 1.5K km^{-1} as the optimal lapse rate for the tropical tropopause.

Finally, results for the extratropical Southern Hemisphere are similar to those for the Northern Hemisphere. For the radiosondes, the optimal lapse rate ranges from 3K km^{-1} at low latitudes to the WMO threshold 2K km^{-1} at mid- and subpolar latitudes. This latitude dependence is not as apparent in ERA-interim reanalysis, for which 2.5K km^{-1} seems to be optimal over most latitudes. Once again, the NCEP-NCAR results are slightly different from the two previous datasets: the curvature maxima are less pronounced and a bit shifted.

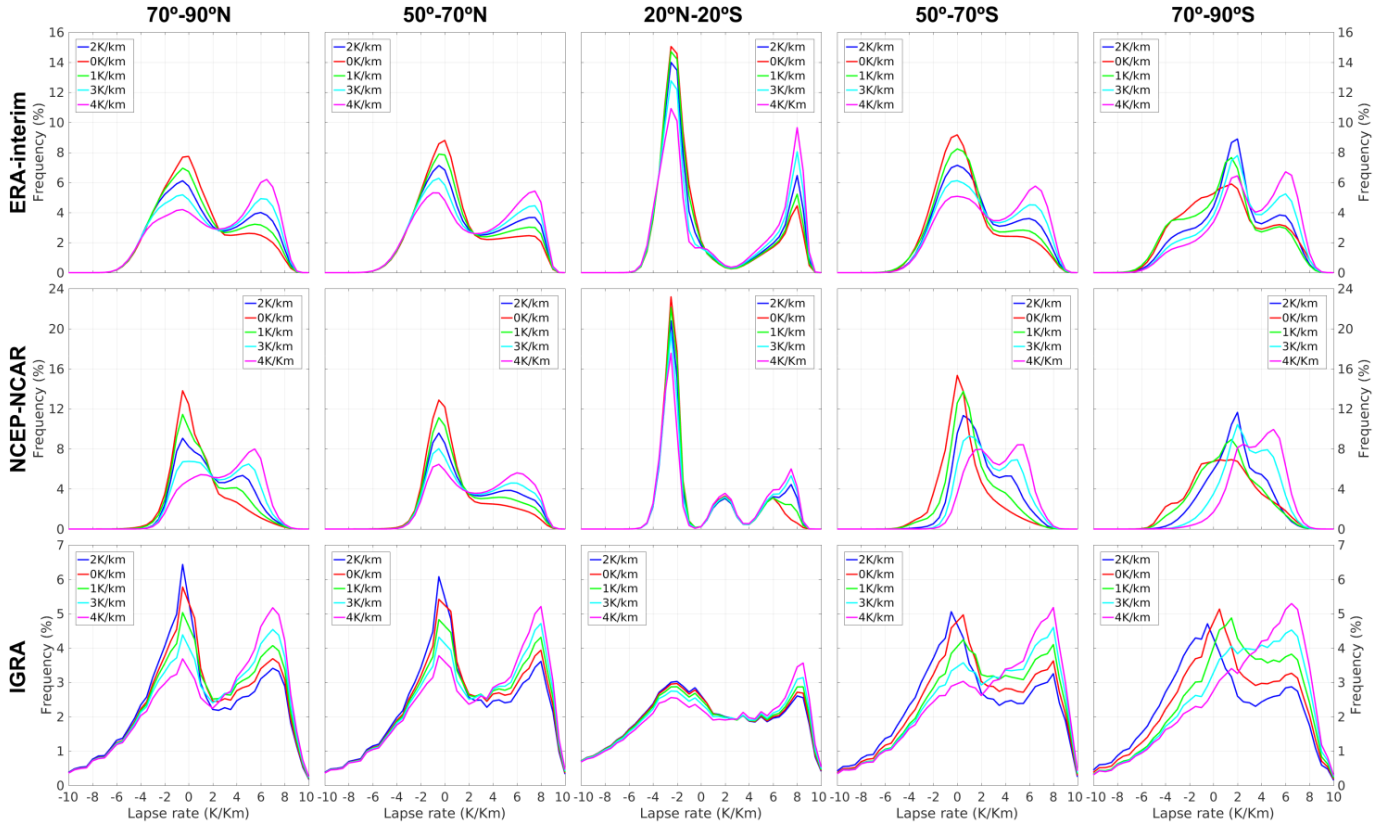

Fig. 4.5: Histograms of lapse rate at the levels located between 100hPa below the tropopause and 100hPa above the tropopause in the Northern Polar region (first column), Northern Extratropics (second column), Tropics (third column), Southern Extratropics (fourth column) and Southern Polar region (fifth column) in ERA-interim reanalysis (top row), NCEP-NCAR reanalysis (middle row) and radiosondes (bottom row). Each station (grid point) in the radiosondes (reanalyses) is considered as an independent data point. Colours are different depending on the critical lapse rate used to define the tropopause.

The differences in the NCEP-NCAR reanalysis seem to be due to its lower vertical resolution, especially at tropical latitudes. In these latitudes, the tropopause lies near the 100hPa level (see the frequency distributions in Fig. 4.2), where NCEP-NCAR reanalysis has a vertical resolution of about 50hPa (specifically, the pressure levels used are 70, 100 and 150hPa) while ERA-interim has about 25hPa resolution (70, 100, 125, 150hPa), coarser than the radiosondes. Thus, the results using NCEP-NCAR data may be less relevant than for the other two datasets. It can also be seen that the actual curvature values are very different for the three datasets, ranging from 1.5 to 6.5 K km^{-2} in NCEP-NCAR reanalysis, from 3.5 to 8 K km^{-2} in ERA-interim, and from 8 to 15 K km^{-2} with the radiosondes. These differences are also due to the different vertical resolution of the datasets. Since the TIL lies just above the tropopause level, there is a very sharp peak in curvature near that level, which is captured to different degrees in the three datasets.

4.1.3 Lapse rate distribution near the tropopause level.

We have shown that the WMO lapse rate threshold 2 K km^{-1} is close to optimal when maximizing the contrast between the tropospheric and stratospheric lapse rates. To understand this result, it is useful to examine the distribution of lapse rates over the Upper-Troposphere/Lower-Stratosphere (UTLS) region.

Fig. 4.5 shows the frequency distributions of the daily lapse rate (using again whole-year data) for all levels extending from 100hPa below the daily tropopause to 100hPa above, for different latitudinal bands in all datasets. To assess the sensitivity to the tropopause definition criterion, distributions of 0 K km^{-1}, 1K km^{-1}, 2K km^{-1}, 3 K km^{-1} and 4 K km^{-1} are plotted. In general, the lapse rate values near the tropopause tend to be distributed according to a bimodal distribution with maxima around 6 to 7 K km^{-1} –a typical lapse rate for the Upper Troposphere (UT)- and around 0 to -2 K km^{-1} -corresponding to the Lower Stratosphere (LS). The UT (LS) peak weakens as the critical lapse rate decreases (increases), but the minimum frequency between the two maxima lays around 2K km^{-1} in all cases. As a result, this is the lapse rate that best separates the two layers from a thermal perspective. It should be noted that 2 K km^{-1} is not in general exactly equidistant from the UT and LS peaks because the LS distribution has a long tail to low lapse rates. The transition from tropospheric to stratospheric lapse rates is more gradual below than above the tropopause, probably due to the TIL, which produces a discontinuity in the lapse rate just above the tropopause. The tail to negative lapse rates (associated with thermal inversions) is most obvious in IGRA and almost non-existent in NCEP, which has a very weak TIL due to its low vertical resolution (Birner, 2006).

Focusing on the different regions, it can be seen that the above conclusions hold especially well in the extratropical areas of the Northern Hemisphere, including the Polar Regions. In the Southern Hemisphere, the results depend on the dataset: while for the radiosondes the histograms are similar to those for the Northern Extratropics, the situation is less clear for the reanalysis. In the southern mid-latitudes a bimodal distribution can still be observed (especially for ERA-interim), but the histograms have a different character over the southern polar region. This area is problematic: it appears that the reanalyses -especially NCEP/NCAR- are not able to reproduce the thermal structure of the upper troposphere-lower

stratosphere layer in this region, which might be due to low resolution or to problems with the available data. As for the tropical area, the observed bimodal distribution has its maxima shifted relative to the extratropical histograms: around 8 K km^{-1} for the tropical UT and around -2 or -3 K km^{-1} for the LS. The 2 K km^{-1} threshold lies between these two peaks but we can see again that the distributions are not symmetric in IGRA. Because the lower-stratosphere lapse rate has a greater dispersion, the minimum frequency is more distant from that peak, at about 3 – 4 K km^{-1}, consistent with the results of the previous section. For NCEP-NCAR reanalysis, a third maximum appears around 0 – 2 K km^{-1}, which seems to be spurious (This maximum may be due to the fact that pressure levels are more separated at the height of the tropical tropopause in this reanalysis: since the tropical tropopause variability is small, the pressure levels that enter our analysis tend to be the same, which tends to produce discrete values and the observed trimodal distribution.)

4.2 Maximum-curvature tropopause

We have shown that the critical lapse rate 2K km^{-1}, used by the WMO to define the thermal tropopause, is usually nearly optimal for separating the upper troposphere from the lower stratosphere. However, we have also seen that there could be better values depending on the dataset used, especially outside the midlatitudes, so that using a fixed value for the critical lapse rate could lead to tropopauses located in either the troposphere or the stratosphere instead of on the layer separating them. Additionally, being purely empirical, this definition is intellectually unsatisfactory and it is unclear whether the same threshold can be applied to climates different from present-day climate. We discussed in previous sections the relation between the level of maximum curvature of the potential temperature profile, the level of maximum separation between the upper troposphere and the lower stratosphere and the WMO definition of the thermal tropopause. This relation can be used to formulate an alternative tropopause definition that does not require specifying any empirical threshold. We propose the following method to determine a curvature-based tropopause:

1. Calculate the second vertical derivative of the potential temperature profile (curvature).

2. Find the level of maximum curvature within the sampled data. Among the nearest

levels, find where the third derivative of potential temperature changes sign.

3. Lineally interpolate to find the zero of the third derivative. This is the tropopause level.

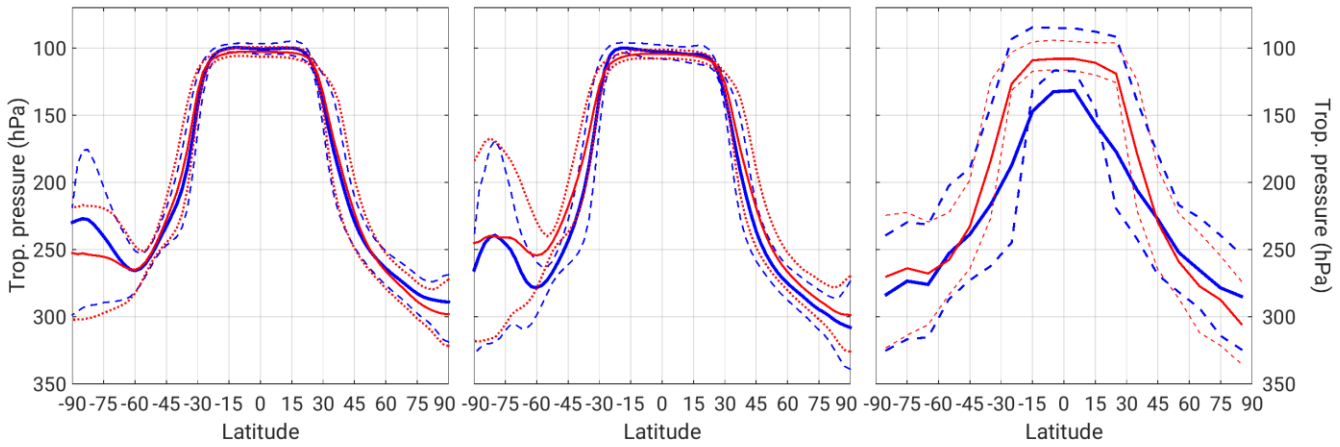

Fig. 4.6: Zonal- and temporal averaged tropopause pressure obtained by the maximum-curvature definition (solid blue line), and by the WMO's definition (solid red line) for the (left) ERA-Interim reanalysis, (middle) NCEP/NCAR Reanalysis-1 and (right) IGRA dataset. Also shown are the 1st and 3rd percentiles (dashed blue lines for the maximum-curvature definition, dotted red lines for the WMO's definition).

In this manner, a tropopause can be defined using only the vertical temperature profile as in the WMO definition. A similar idea has been used by Birner (2010) to define the climatological tropopause. Note that only levels above 550hPa are considered to prevent contamination from the lower-troposphere, consistent with the traditional thermal definition. In the reanalysis, it is not necessary to establish an upper limit to the pressure range where the tropopause is sought. However, because radiosonde data can be noisy in the lower stratosphere, it is convenient to limit the tropopause search to levels below 50hPa in this dataset. Without this constraint, the method gives tropopauses well above 50hPa in a 3% of the cases; the problem is especially bad in the

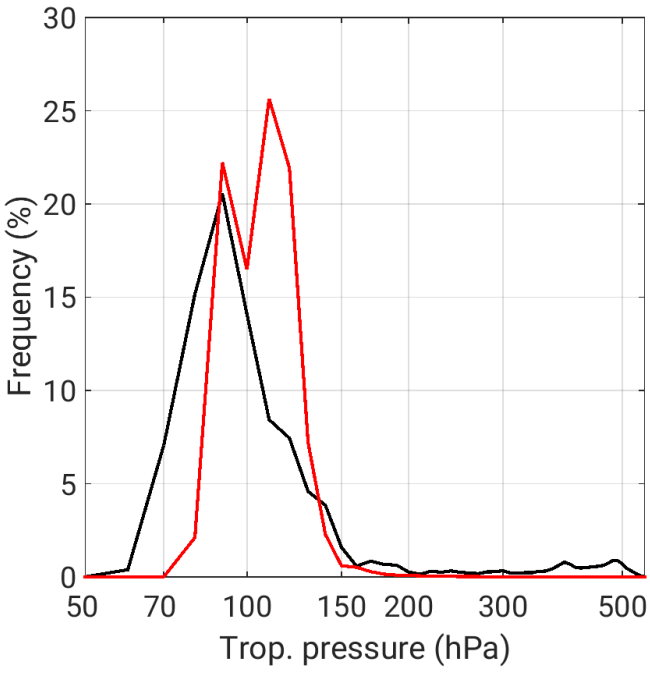

Fig. 4.7: Histograms of the tropopause pressure in the tropical latitudes (20ºN-20ºS) obtained with the maximum-curvature definition (black) and the WMO's definition (red).

subtropics and southern Polar Regions, where tropopauses above 50hPa can be found in 9% of the cases.

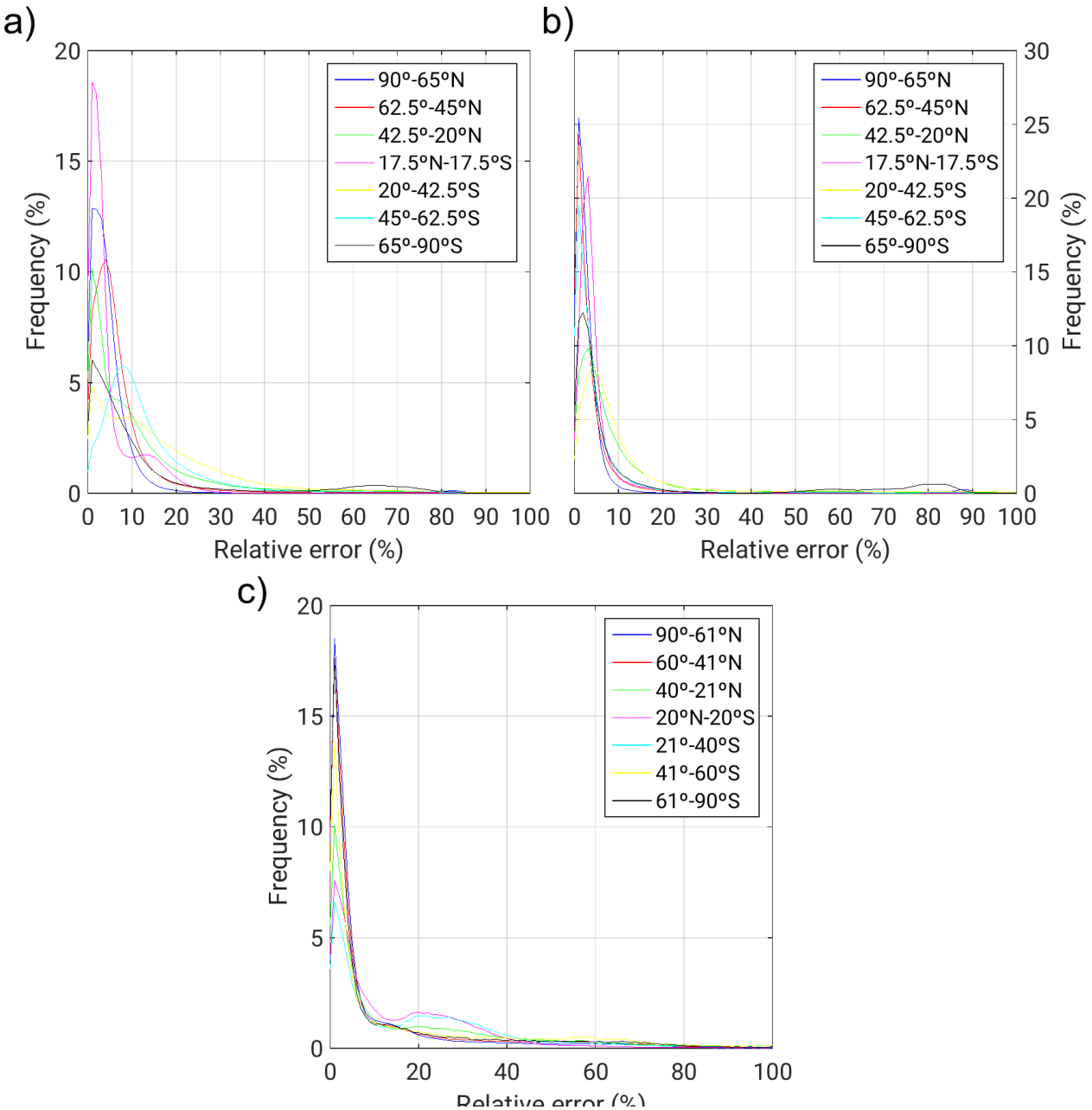

Fig. 4.8: Histograms of the relative differences between the maximum-curvature and the WMO's definition of the tropopause at several latitudes for (a) NCEP/NCAR Reanalysis-1, (b) ERA-Interim reanalysis, and (c) IGRA dataset.

We show in Fig. 4.6 the mean tropopause and the 1st and 3rd quartiles of the distribution with this definition for the reanalyses and the radiosonde datasets. It can be seen that this definition produces a mean tropopause similar to that of the traditional WMO definition, consistent with what was seen above. The agreement is especially good in the reanalysis and in the extratropical areas; in the IGRA dataset, the differences are larger, especially in the tropics and the subtropical areas. Nevertheless, the statistical distribution is very similar to

the WMO definition. In the frequency distributions shown in Fig. 4.7 it can be seen that the difference in the mean tropopause is due to some very low spurious tropopauses occasionally identified by the maximum-curvature method in the mid-troposphere, which bias the mean tropopause low. However, the median and other percentiles of the distribution are quite similar to the WMO tropopause. Looking at the distribution of the relative differences between both tropopauses (Fig. 4.8), we can see that in the reanalyses the differences are quite small: in less than 1% of the cases the differences are greater than 10% of the WMO tropopause pressure in the ERA-Interim reanalysis, or less than 20% in the case of the NCEP/NCAR Reanalysis-1. Most of the differences are below 10 to 30hPa in ERA-Interim and below 20 to 60hPa in the NCEP/NCAR Reanalysis-1, so they are less than the vertical resolution of each reanalysis at levels near the tropopause. By latitudes, it can be seen that differences are largest in the subtropics, where double tropopauses appear frequently (Añel *et al.*, 2007) –the maximum-curvature definition will choose the discontinuity that maximizes the curvature of potential temperature.

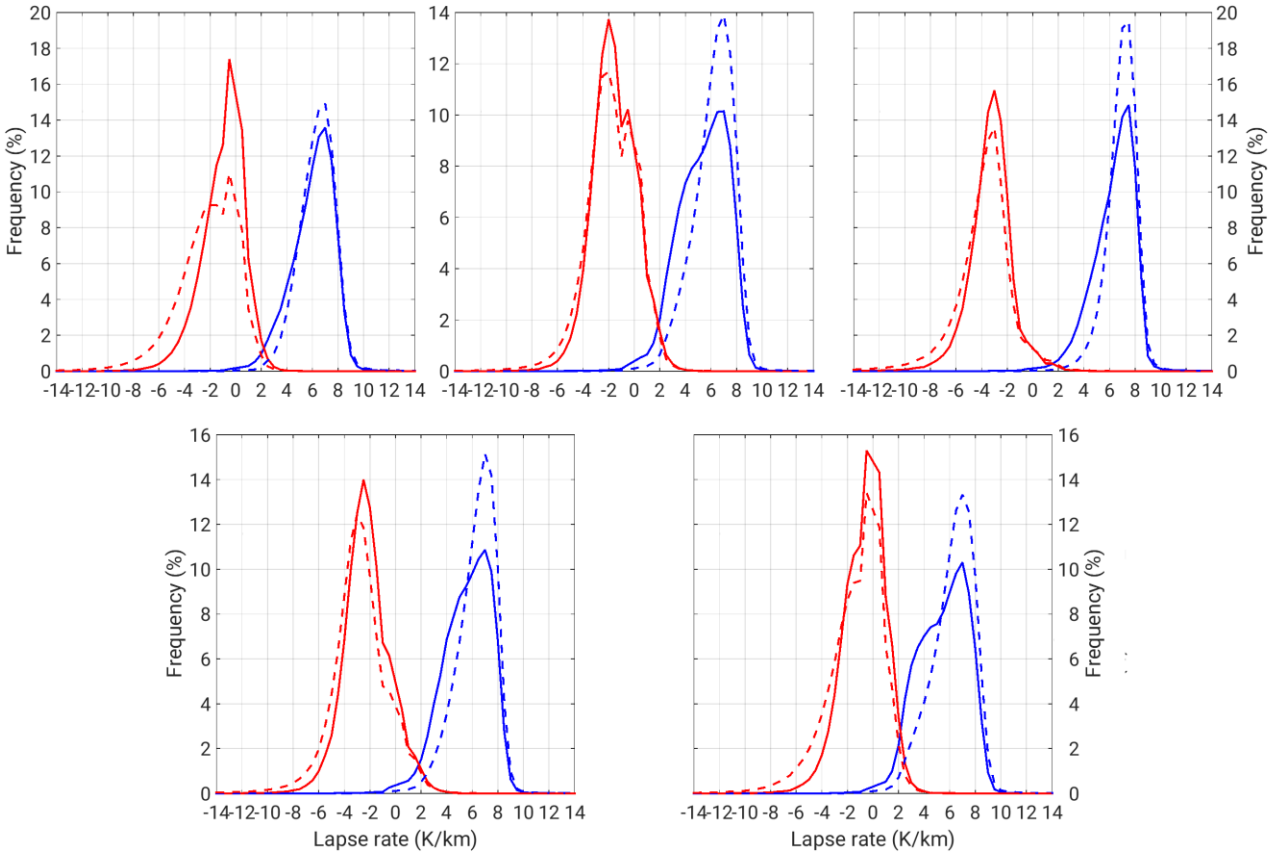

Fig. 4.9: Histograms of the lapse rate at levels in a layer of 150hPa below the WMO's tropopause (blue) and in a layer of 100hPa above the tropoause (red) for the cases when the relative separation between the maximum- curvature and the WMO's tropopause is greater than 40% (solid lines) and for all days (dashed lines) in the northern extratropics (90º-40ºN, upper left), the northern subtropics (35º-20ºN, upper middle), the tropics (15ºN-ºSºS, upper right), the southern extratropics (20º-35ºS, lower left) and the southern extratropics (40º- 90ºS, lower right).

In the case of the radiosondes the differences are still small, but bigger than with reanalysis. One reason for this is that the vertical profiles are much noisier, which makes it problematic the use of higher-order derivatives required by the method. Many of the differences can be tracked to erroneous measurements in the dataset, for example when two near levels have very different temperatures, so that the derivative has a sharp increase that can be erroneously identified as the tropopause. Additionally, as shown in Fig. 4.9, many of the cases in which the tropopauses are very different occur when the stratification of the upper-troposphere and of the lower-stratosphere are little separated, so the maximum curvature at the tropopause level is less pronounced. In particular, the method fails at high latitudes when the lower-stratosphere is nearly isothermal, a situation that also hinders the identification of the tropopause with the WMO method (Highwood and Hoskins, 2000).

4.3 Maximum-stratification tropopause.

The maximum-curvature tropopause proposed in the previous section has clear limitations for its application to the radiosonde dataset: the noisy nature of these data makes it difficult to determine the tropopause level using high-order derivatives. Thus, we propose an alternative method based on the characteristics of the temperature profile that does not rely on any empirical thresholds by using the squared-Brünt-Vaisalla frequency, N, instead of curvature. As shown by Birner (2006), the troposphere-stratosphere transition is usually associated with a sharp increase in N just above the tropopause level: the TIL. We can take advantage of this feature to define the tropopause in terms of the maximum value of N. There is, however, a problem: as the value of N gradually increases in the stratosphere, in some cases the maximum in N is found at higher levels, far apart from the maximum at the tropopause level. Thus, instead of using the Brunt-Väisäla frequency directly we normalize it by potential temperature. Since potential temperature also increases with height, N/θ usually reaches its maximum at the TIL and can thus be used as a guide to find the tropopause level.

We also impose a second condition that the N/θ maximum must satisfy to be accepted as the tropopause. It must also maximize the relative difference between the N value below the tropopause and over a layer 2km deep above the maximum. This is a similar condition to the thickness criterion in the WMO's definition, and it is introduced with the same motivation of preventing association of the tropopause with common mid-tropospheric inversions.

The process of determining the tropopause by this method is then the following:

1. Find the peaks in the N/θ profile.

2. Compute the difference, for each peak, of the average Brünt-Vaisalla frequency below it and in a layer 2km deep above the maximum.

3. For the peak that maximizes the contrast in N interpolate to find the maximum in $\partial N/\partial P$, which corresponds to the tropopause level (the level of maximum change in the stratification).

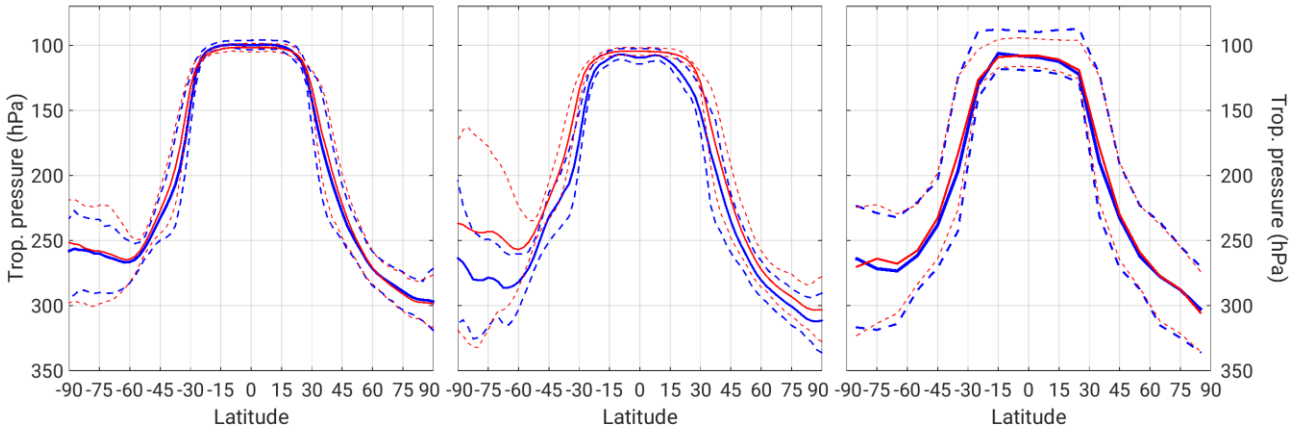

Fig. 4.10: As in Fig. 6, but for the maximum-stratification tropopause.

As in the case of the maximum-curvature definition, the mean tropopause defined by the maximum stratification is very close to the WMO definition (Fig. 4.10). Improvement is especially clear in the Tropics with the IGRA dataset, where the mean tropopauses are now nearly indistinguishable using both methods. In NCEP/NCAR Reanalysis-1, the maximum-stratification tropopause tends to lie below the WMO tropopause. This is easy to understand: as the lower resolution of this reanalysis produces a smoother transition from tropospheric to stratospheric stratification, the maximum is located slightly lower than with the traditional definition. The mean tropopause is again almost identical to the WMO definition in ERA-Interim reanalysis, presumably due to its higher vertical resolution, which allows the method to correctly identify the sharp increase in stratification at the tropopause level.

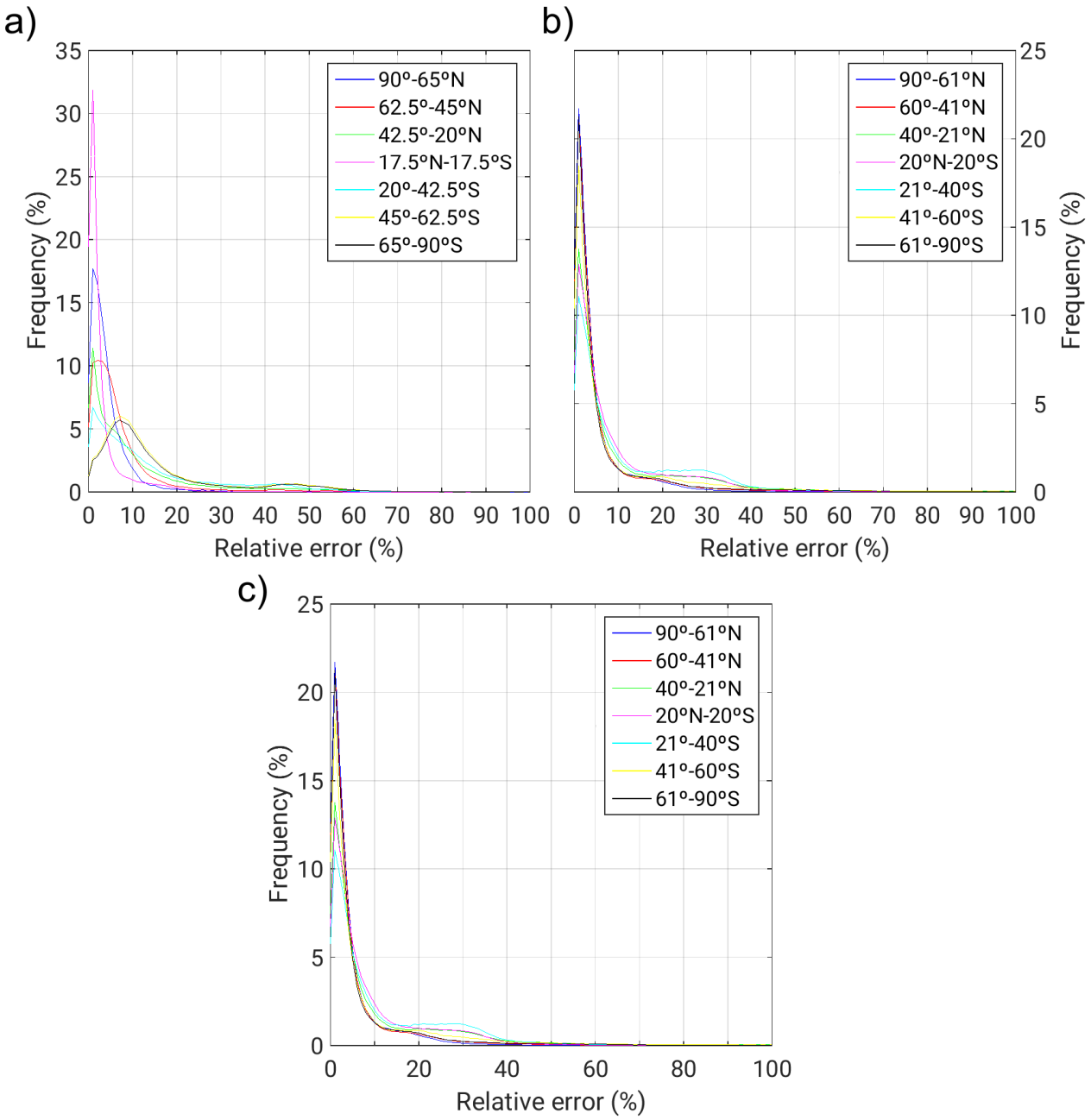

Fig. 4.11: As in Fig. 8, but for the maximum-stratification definition of the tropopause.

Looking at the frequency distribution of the daily relative differences (Fig. 4.11) it can be seen that this definition is closer in general to the WMO definition. Improvement occurs at all latitudes, although some differences persist in the subtropics and in the polar areas. It is shown in Fig. 4.10 that the cases in which this tropopause is very different from the WMO tropopause are typically associated with very low contrast between the lower-stratosphere and upper-troposphere stratifications. This method is able to identify correctly the tropopause even though the contrast in stratifications is smaller than with the maximum-curvature tropopause of the previous section, as shown by the closer distributions in Fig. 4.12.

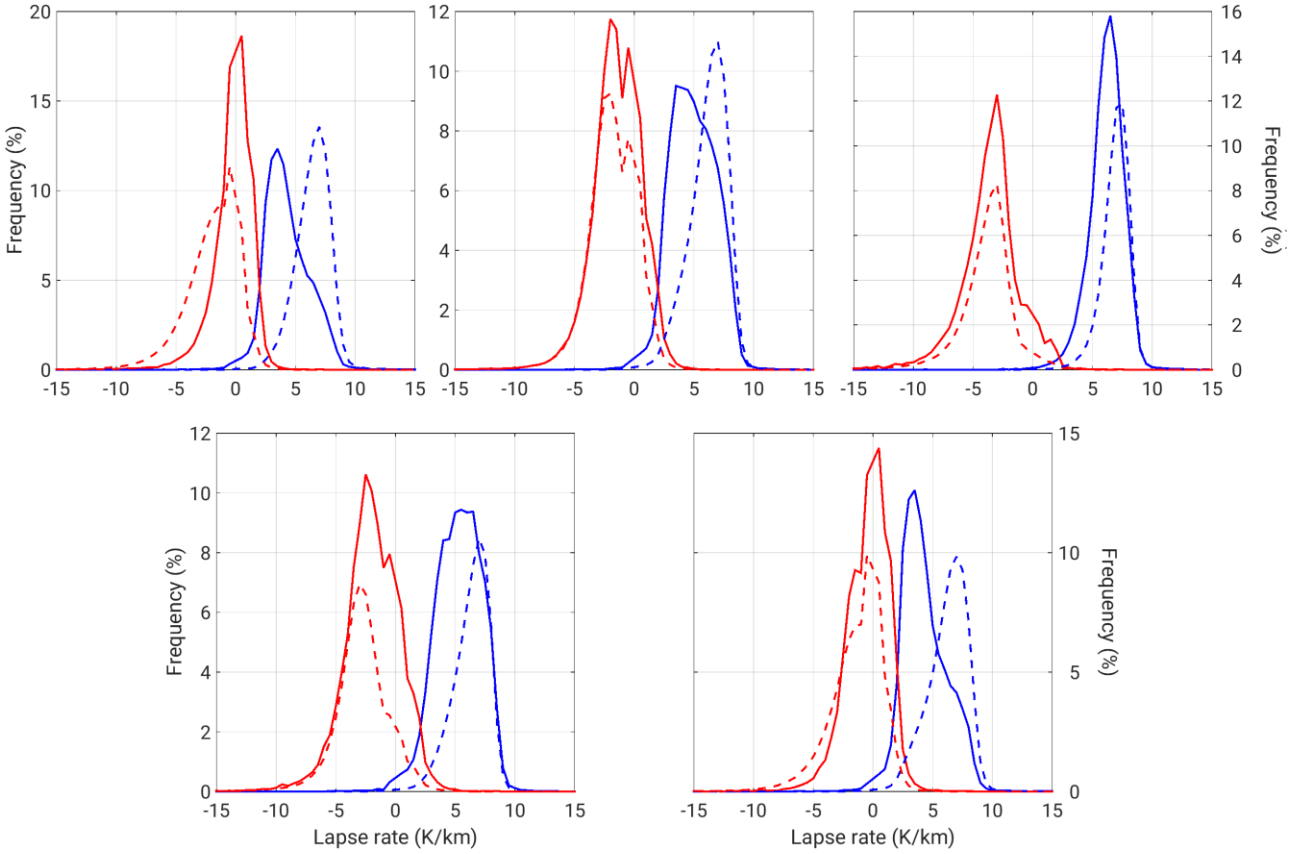

Fig. 4.12: As in Fig. 9, but for the maximum-stratification definition of the tropopause.

4.4 Discussion.

The lapse rate structure in the area surrounding the tropopause has been analysed in this chapter. The characteristics of this region, usually known as the Upper Troposphere and Lower Stratosphere (UTLS) region, are very important for the Stratosphere – Troposphere Exchange (Holton *et al.*, 1995), as can be seen in tracer gases abundances (Gettelman *et al.*, 2011). Focusing on the thermal characteristics of this area, it is concluded that the typical lapse rate of the Upper Troposphere (UT) is around 6 – 7K km^{-1} in the extratropics and around 8K km^{-1} for the tropical area, while in the Lower Stratosphere (LS) values of 0K km^{-1} and -2K km^{-1} are common in the extratropics and the tropics, respectively. In general, it can be seen that the ERA-interim and the IGRA datasets are better sources of information than NCEP-NCAR reanalysis for the UTLS study (especially in the Tropics), due to the coarser vertical resolution of the latter (Randell *et al.*, 2000).

Based on the distribution of lapse rates in the UTLS region we can understand why 2K

km^{-1}, which is close to the minimum-frequency lapse rate separating the UT and the LS distributions, provides the best separation between the troposphere and the stratosphere. This lapse rate is not exactly the mean value between the typical UT and LS lapse rates because the LS lapse-rate distribution has a slightly longer tail towards lower values. Although this picture fits well in the Northern Extratropics, in the Tropics the situation seems to be slightly different: the UT lapse rate is close to dry adiabatic (Fueglistaler, 2009) while the LS lapse rate is less than isothermal, thus leading to a bigger separation between both distributions. This makes it more difficult to establish the optimum critical lapse rate, as there is not a clear minimum between the distributions but a smooth transition between them. Looking at the curvature, it appears that lapse rates around 3K km^{-1} seem to maximize the contrast, but there is no unanimity in all datasets. The cause for this uncertainty may be the characteristics of the tropical tropopause: in general, the transition from the tropospheric to the stratospheric lapse rates is more gradual in the tropics than in the extratropics. As a result, it is more difficult to find a unique value separating the troposphere and the stratosphere in these latitudes. Indeed, the tropical tropopause is usually regarded as a transition layer, the Tropical Tropopause Layer TTL (Fueglistaler, 2009), which shares characteristics with both the troposphere and the stratosphere. On the other hand, in the Southern Hemisphere the optimum critical lapse rate seems to be displaced to slightly higher values (around 3K km^{-1}), apparently due to its weaker TIL (Grise *et al.*, 2010), which moves the LS distribution to higher lapse rates.

Based on the analysis of the UTLS thermal characteristics, two new objective definitions of the tropopause are proposed either as the level of maximum curvature of the potential temperature profile or the level of maximum Brünt-Vaisalla frequency normalized by potential temperature. The first definition is similar to the method used in Birner (2010), except that he uses the climatological temperature profile instead of the potential temperature profile. Although the mean tropopause and its latitudinal structure are similar with the new methods and with the traditional definition, as in Birner (2010), there are some differences between the three definitions.

Using the maximum curvature method, the differences with the WMO definition are smaller in the extratropical regions in the reanalyses (in general lesser than the vertical resolution at those levels) and higher in the subtropical areas and in the radiosondes. This

may be due to the existence of a strong TIL in mid- and polar latitudes, which constrains the maximum curvature level to be near the 2K km^{-1} level, while the relatively weaker subtropical TIL allows a bigger separation between the two. Nevertheless, the maximum-curvature tropopause tends to lie below the 2K km^{-1} tropopause in the extratropics and above it in the tropics. The larger differences with the radiosondes compared to the reanalyses may be due to the higher vertical resolution of the former, which makes them noisier. Thus, we expect the maximum-curvature definition to work well in datasets with low to medium vertical resolution. Still, the maximum-curvature definition is useful in the radiosonde dataset as long as there is enough contrast between the tropospheric and the stratospheric lapse rates.

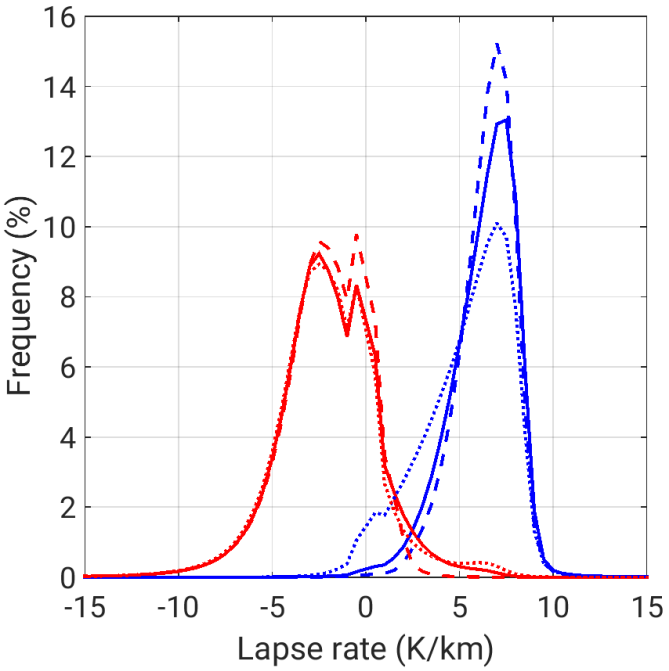

Fig.4.13: Histograms of the lapse rates in a layer of 150hPa below the tropopause level (blue) and in a layer of 100hPa above it (red) with reference on the maximum stratification definition (solid lines), on the WMO's definition (dashed lines) and on the maximum-curvature definition (dotted lines).

The maximum-stratification tropopause works better in high-resolution datasets than in low-resolution datasets. Moreover, this method is able to identify the tropopause with less contrast than the maximum-curvature method. Additionally, as shown in Fig. 4.13, this method produces a slightly better separation between the tropospheric and the stratospheric lapse rates: the average difference between them is of 8.5K km^{-1} with the maximum-stratification tropopause, of 8.9K km^{-1} with the WMO tropopause and 7.8K km^{-1} with the maximum-curvature tropopause. The maximum-stratification definition is thus slightly worse than the WMO definition for separating the stratosphere and the troposphere from a thermal point of view in the IGRA dataset, mainly due to the noise present in this data.

The main advantage of the objective definitions proposed in this chapter is that they can be applied to any climate or region, as they are only based on the characteristics of the UTLS thermal structure and not on any observed lapse rate distribution. Their main disadvantages

are the need to compute high-order derivatives, which may introduce some noise, and the fact that they cannot identify multiple tropopauses as the WMO definition.

5. Seasonal variability of the extratropical tropopause.

Once the analysis of the mean state and characterization of the tropopause is finished the focus turns now to the study of its variability. This chapter addresses the seasonal variability, which can be considered as forced variability, while the next chapter is dedicated to the intraseasonal -thus internal- variability of the extratropical tropopause height.

The dominant seasonal variations in tropopause height have great zonal symmetry (see for example Hoinka, 1998), as expected due to the nature of the radiative forcing. Hence, our study of the variability focusses on the zonally averaged tropopause height.

The first part of the chapter will focus on the seasonal variability of tropopause height in the reanalyses, while the second part analyses the dynamics modulating this variability using simulations with the idealized model.

5.1 Seasonal cycle in the reanalyses.

5.1.1 Observed characteristics of the seasonal cycle.

As commented in the introduction to this thesis, previous studies have shown that the annual cycles of high-latitude tropopause height in the northern and southern extratropics

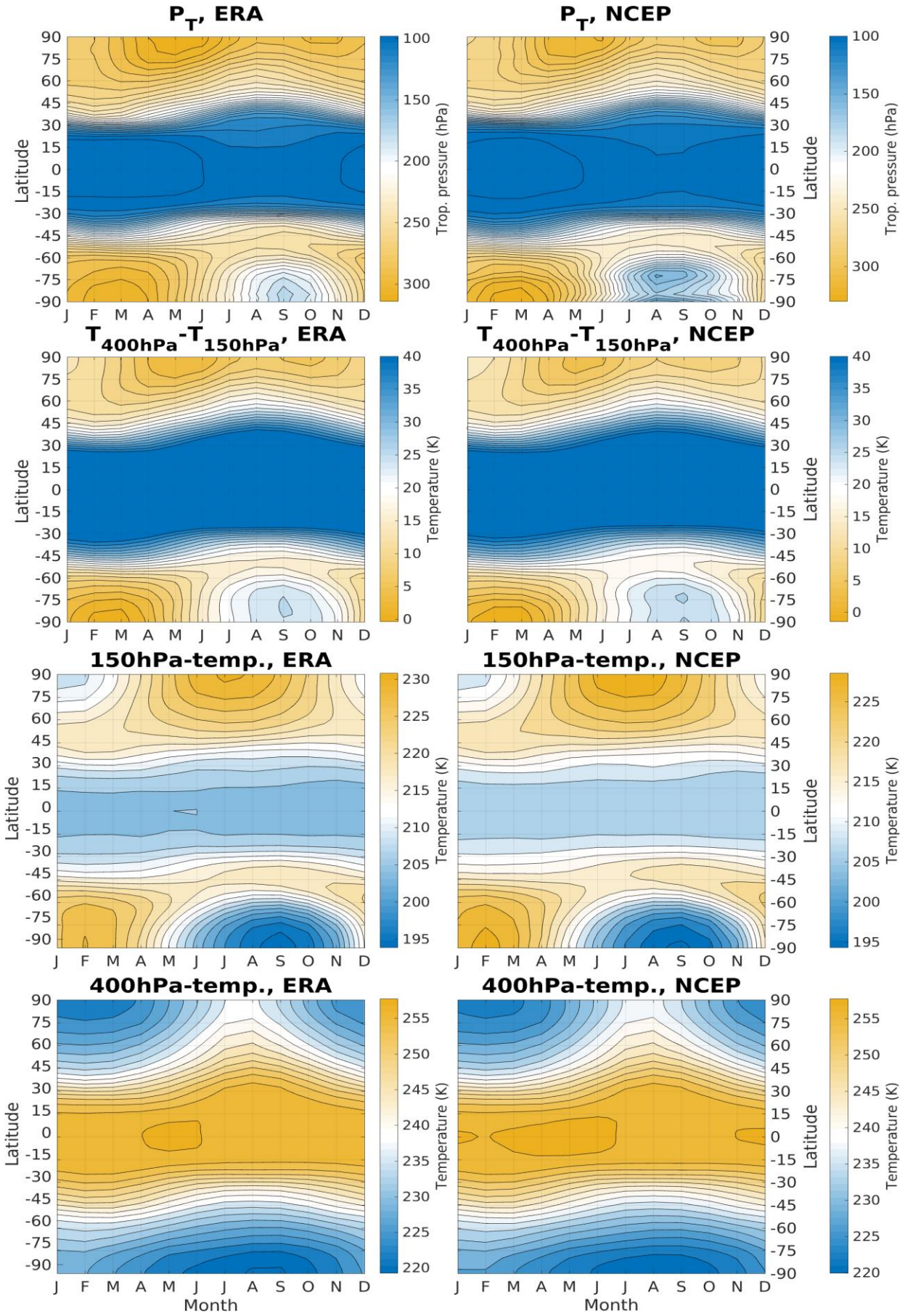

Fig. 5.1: Seasonal cycle of (top row) tropopause pressure (hPa), (upper middle row) difference in the temperature at 150- and 400hPa (K), (lower middle row) temperature at 150hPa and (bottom row) temperature at 400hPa, for the ERA-Interim reanalysis (left column) and the NCEP/NCAR Reanalysis-1 (right column). Data are average on running windows of 20 days.

are not symmetric, but somehow *in phase*. Both tropopauses are low during the boreal winter months and high during the boreal summer months, although the Northern Hemisphere (NH) tropopause is warmer in summer than in winter, contrary to its Southern Hemisphere (SH) counterpart.

The seasonal cycle of tropopause pressure for both reanalyses is shown in Fig. 5.1. In the SH, the traditional picture of a high tropopause during austral winter and a low tropopause during austral summer is clear, so the seasonal cycle can be viewed as a single wave with minimum height in March and maximum height in September. In the NH, the seasonal evolution is a bit more complex as there are two relative maxima and minima: the tropopause is low in late spring and autumn and high in winter and summer. This suggests that the boreal seasonal cycle of tropopause height is better characterized as a double wave than as a single wave. The periodogram (Fig. 5.2) confirms that northward of 60°N there is a statistically significant peak at the semi-annual frequency dominating the annual peak characteristic of other latitudes. The semi-annual signal of tropopause height over the northern polar cap was already noted by Zängl and Hoinka (2001) and is also apparent in recent high-resolution measurements using radio occultation tecniques (Liu and Taoling, 2014). This asymmetry has been explained as a result of the dynamical warming caused by the residual circulation in the NH lower stratosphere (Zängl, 2002).

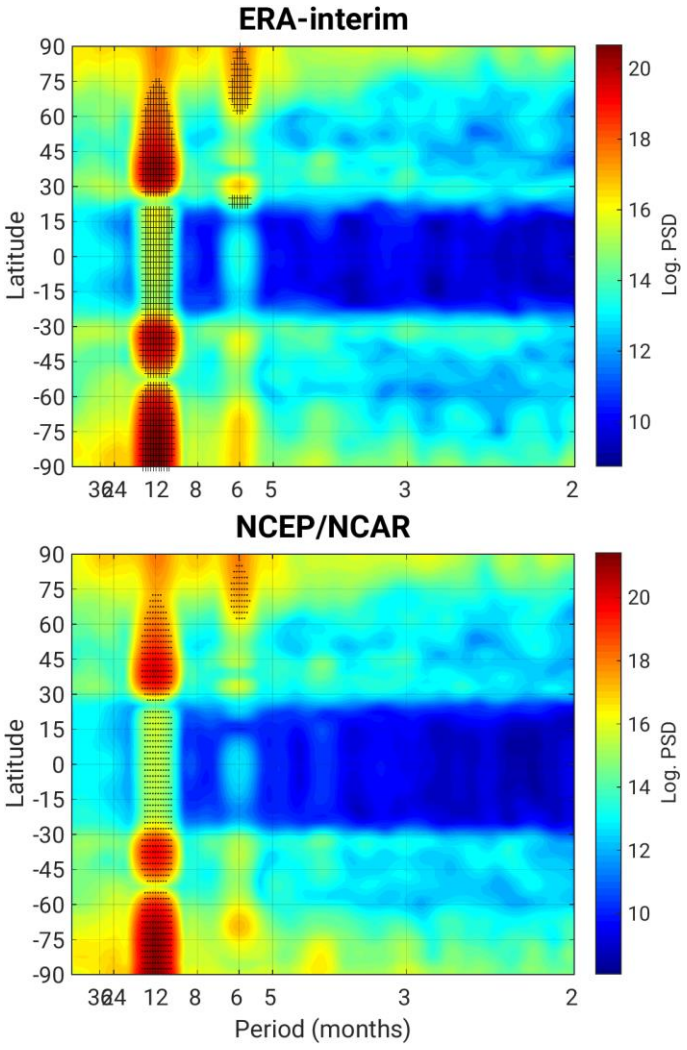

Fig. 5.2: Periodograms of tropopause pressure for (top) ERAInterim and (bottom) NCEP/NCAR Reanalysis-1 datasets. Crosses stand for the latitude and frequencies at which the Power Spectral Density (PSD) is statistically different from the PSD of a red noise. Note that PSD is displayed using a logarithmic scale.

As a first approximation for understanding the annual evolution of the tropopause we examine the temperature

difference between levels above and below the tropopause, for it is known that there is a significant correlation between the tropopause level and temperatures in the upper troposphere and lower stratosphere (Seidel and Randel, 2006). It can be seen in Fig. 5.1 that the temperature difference between 400 and 150hPa has a seasonal evolution nearly identical to that of the tropopause, at least in the extratropics -the results are independent of the particular levels chosen as long as they are not far from the tropopause. As long as the stratification in levels near the tropopause does not vary too much throughout the year -and, as shown in Chapter 4, the stratification tends to remain constant above and below the tropopause -, a greater temperature difference between levels above and below the tropopause is associated with a higher tropopause, and vice versa (see Fig. 5.3). This was used by Möller (1938) to explain the anomalous behaviour of polar tropopauses, which are higher in winter than in summer due to the stronger seasonal cycle of temperature in the lower stratosphere than in the upper-troposphere (Hoinka, 1998). Fig. 5.1 shows that while this is true for the SH, the situation is not as clear in the NH.

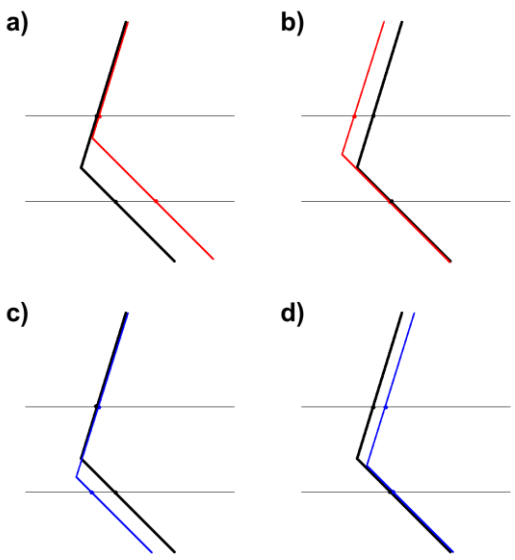

Fig. 5.3: Schematics of the relation between the tropopause and the difference of temperatures above and below it. Difference may grow by (a) a warming of the troposphere or (b) a cooling of the stratosphere, and may decrease by (c) a cooling of the troposphere or (d) a warming of the stratosphere. In cases a) and b) the difference grows and the tropopause rises, while in cases c) and d) the difference decreases and the tropopause sinks.

Fig. 5.4 shows the seasonal evolution of tropopause pressure and upper troposphere/ lower stratosphere temperatures averaged over the polar cap (poleward of 60°) –note that the SH annual cycles are shifted 6 months to facilitate direct comparison with the NH. The double-wave of the NH and the single-wave of the SH tropopause pressure are apparent. The seasonal cycle of polar temperatures shows that the northern upper-troposphere during boreal summer is warmer than the southern upper-troposphere during austral summer, which leads to higher temperature differences and thus a higher tropopause height in the NH during summer (Fig. 5.4). On the other hand, the lower-stratosphere is warmer in winter in the NH than in the SH, consistent with the much smaller tropopause rise in the NH than in the SH during their respective winters. Finally, the lower-stratosphere spring warming begins earlier

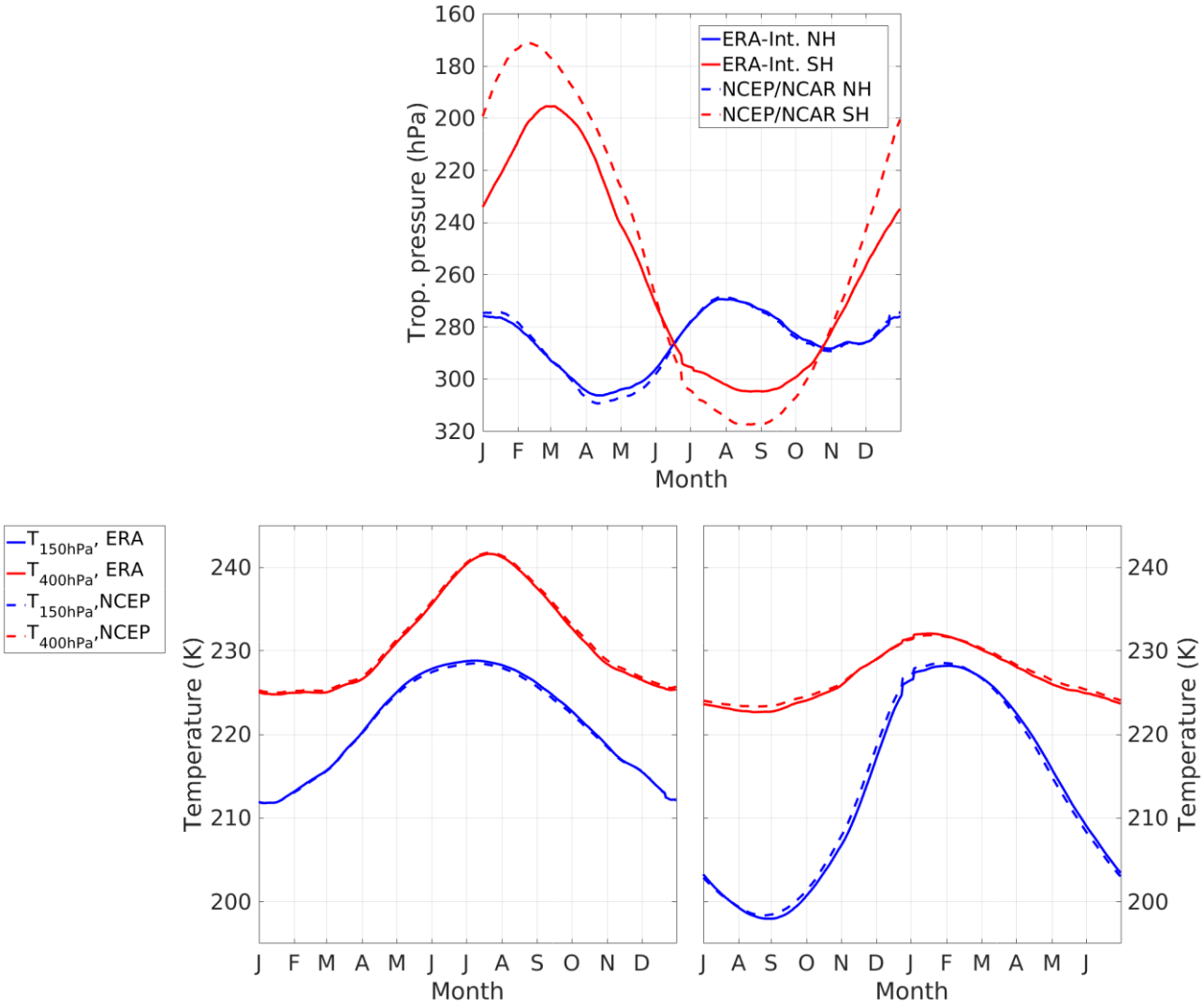

Fig. 5.4: Seasonal evolution of (a) tropopause pressure in the NH (blue) and SH (red) polar caps and of (b) temperature at 150hPa (blue) and 400hPa (red) for the (left) NH and (right) SH polar caps. Solid lines are for ERA-Interim reanalysis and dashed lines for the NCEP/NCAR Reanalysis-1. Note that SH data have been shifted 6 months for easier comparison with the NH seasonal cycle.

in the NH and the warm summer temperatures also persist for a longer period of time in this hemisphere; as a result, the lower-stratosphere starts to warm while the upper-troposphere is still cold, leading to reduced upper troposphere-lower stratosphere temperature differences in spring and tropopause sinking. A similar situation is observed during autumn, when the polar vortex cools more slowly than the upper-troposphere. Overall, these results suggest that while the seasonal cycle in the SH can be approximately understood as purely radiatively forced, understanding the NH seasonal cycle requires consideration of both radiative and dynamical forcings. Note that the highest temperature in the lower stratosphere and the lowest temperature in the upper-troposphere are similar in both hemispheres, so that differences in the seasonal cycle are associated with differences in the winter lower-stratosphere and in the summer upper-troposphere. A final note on the SH: it can be seen that the highest tropopause is found during austral spring, as the lower-stratosphere is coolest during September.

This is likely associated with the generation of Polar Stratospheric Clouds and ozone loss in the ultra-cold vortex before the warming starts.

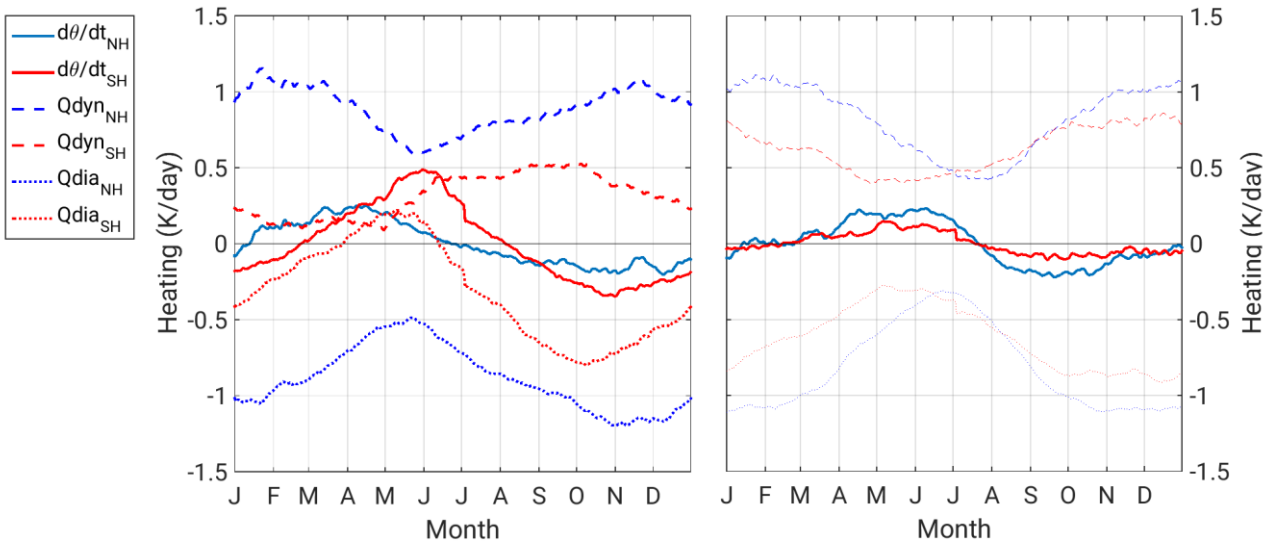

Fig. 5.5: Seasonal evolution of (solid) net heating, (dashed) dynamical heating and (dotted) diabatic heating in the (blue) NH and (red) SH polar caps. Data were average on running windows of 20 days.

5.1.2 Forcings of the seasonal cycle.

Looking at the individual terms in the thermodynamic equation (see Chapter 3, the diabatic term is a computed as a residual), we can confirm that the warming in the lower-stratosphere starts very early in the NH as the dynamical heating is not completely balanced by diabatic cooling (Fig. 5.5); this warming is mainly due to the convergence of the meridional eddy heat flux over the polar cap (Fig. 5.6). Note that the diabatic term has a cooling effect in the NH throughout the whole year, even during the summer months, due to enhanced infra-red radiative cooling (Wong and Wang, 2000). During the second half of the year, the diabatic cooling is stronger than the dynamical warming and the temperature in the lower-stratosphere decreases. In contrast, the seasonal cycle of the net heating in the SH low stratosphere closely follows the diabatic heating seasonal cycle, with the dynamical heating increasing the warming in summer and limiting the cooling in winter. Focusing now on the upper-troposphere, the net heating has weak seasonal variability as the dynamical and diabatic heating roughly balance each other for all seasons. However, note that there are quantitative differences between the hemispheres, as the NH seasonal cycle in net heating nearly doubles that in the SH (also compare the red lines in the bottom panels in Fig. 5.4). The weaker SH seasonality is consistent with the larger thermal inertia of the southern hemisphere surface. On the other hand, it is striking that the diabatic cooling is very similar in both hemispheres during the summer, even though the NH is significantly warmer during this season (Fig. 5.4).

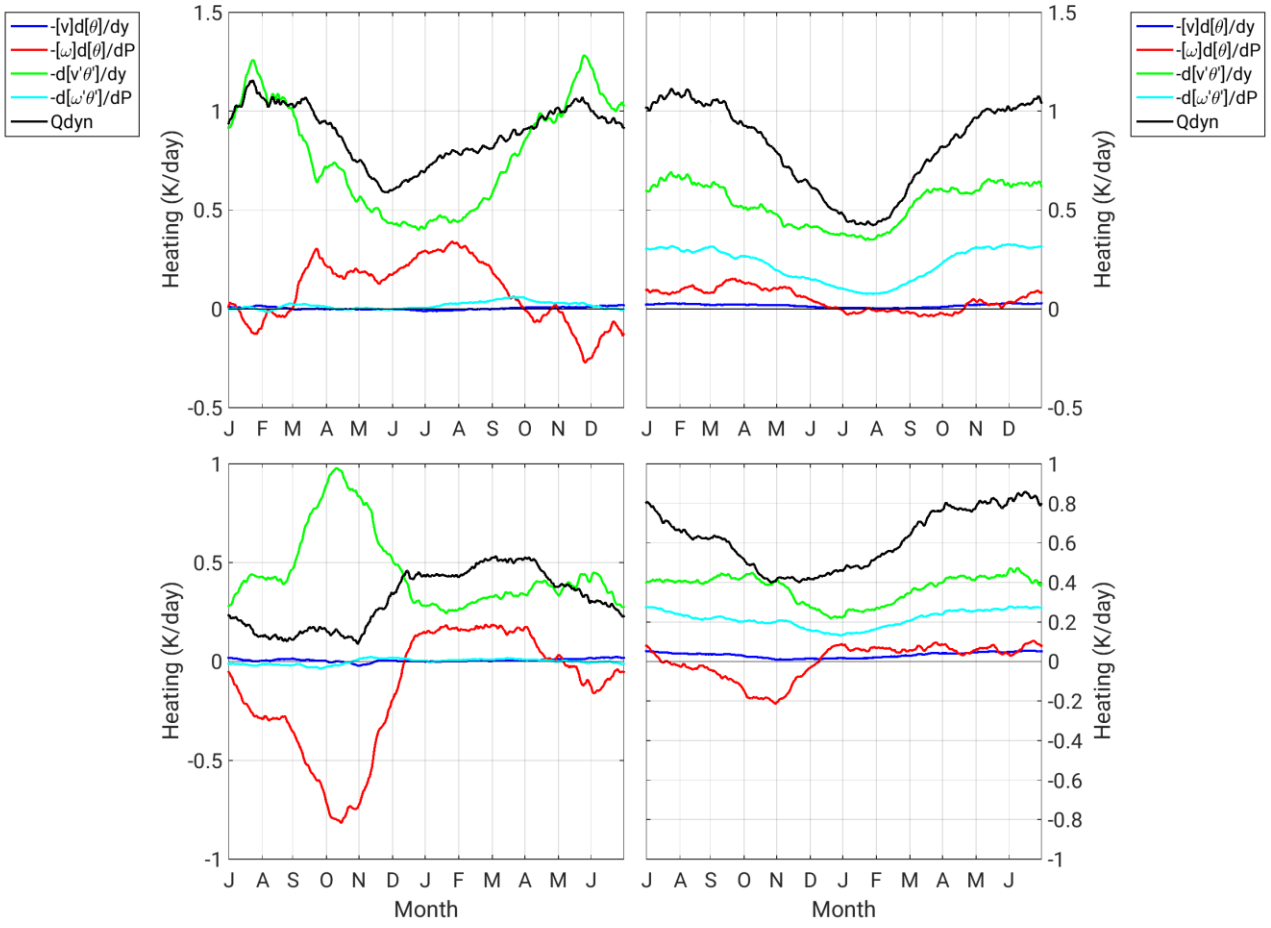

Fig. 5.6: Seasonal evolution of (dark blue) meridional heat advection, (red) vertical heat advection, (green) meridional eddy heat flux convergence, (light blue) vertical eddy heat flux convergence and (black) the total dynamical heating at (left column) 150hPa and (right column) 400hPa in the (top row) NH and (bottom row) SH polar caps. Data wer averaged on 20days-running windows.

This suggests that latent heat release may play some role in warming the upper troposphere and raising tropopause height during summer, consistent with previous studies (Juckes, 2000; Wu and Pauluis, 2014).

Decomposing the dynamical heating into its different contributions (Fig. 5.6), it can be seen that the term responsible for most of the lower-stratosphere warming is the convergence of meridional eddy heat flux. In the NH, this term reaches its maximum during the winter months, while in the SH the maximum is found well into the spring. Note, however, that the convergence of meridional eddy heat flux in the SH is largely balanced by adiabatic cooling by the mean meridional circulation. The net dynamical heating does not increase until late spring/early summer, when this circulation changes sign. The adiabatic cooling by the mean meridional circulation also opposes the eddy heating during the winter months in the NH, but to a much lesser extent; additionally, it changes sign much earlier in

the year than in the SH, adding up to the eddy heat flux heating during spring and summer. As for the upper-troposphere, it can be seen that eddy terms clearly dominate, especially in the NH. The magnitude of the vertical eddy heat flux convergence is similar in both hemispheres, but meridional eddy heat flux convergence is larger in the NH.

In summary, these diagnostics suggest that differences in the seasonal cycle of tropopause height between both hemispheres may be explained by the enhanced eddy activity in the winter NH lower stratosphere due the upward propagating planetary waves, which prevent the polar vortex from becoming too cold, and by the weaker seasonal cycle in the SH upper troposphere. Latent heating may also be important for raising the NH tropopause during summer.

	Sim. 1	**Sim. 2**	**Sim. 3**	**Sim. 4**
ε_N	0	0	40	40
ε_S	0	0	10	10
$A1^{NH}$	45	45	45	45
Orography	No	Yes	No	Yes

Table 5.1: Parameters of the idealized model for each of the simulations: ε_N, amplitude of the tropospheric seasonal cycle in the NH (K); ε_S, amplitude of the tropospheric seasonal cycle in the SH (K); $A_{1\,NH}$, amplitude of the seasonal cycle at 1hPa (K); orography (see Chapter 2 for details).

5.2 Seasonal cycle in the idealized model.

5.2.1 Description of the simulations.

A series of simulations was performed with the idealized model aiming to test the ideas presented in the previous section. As shown by Jucker *et al.* (2013), this model can produce a realistic seasonal cycle in stratospheric temperature. It has a colder polar vortex in the Southern than in the Northern Hemisphere during their respective winters, and idealized topography is included in the Northern Hemisphere only. See section 2.4 for more details on the model setup.

Since the principal drivers of seasonal tropopause variability at high latitudes are the polar vortex and eddy activity, simulations were performed in the idealized model varying these two components. Some simulations have a seasonally varying polar vortex but no seasonal cycle in the tropospheric forcing, so that the generation of eddies by baroclinic in-

stablity is reduced relative to simulations with a tropospheric seasonal cycle, which have stronger meridional temperature gradient in winter (Jucker *et al.*, 2013). Table 5.1 summarizes the parameter configuration of each of the simulations. The simulations are run during 3650 days (10 model years), and the first year is discarded as spin-up.

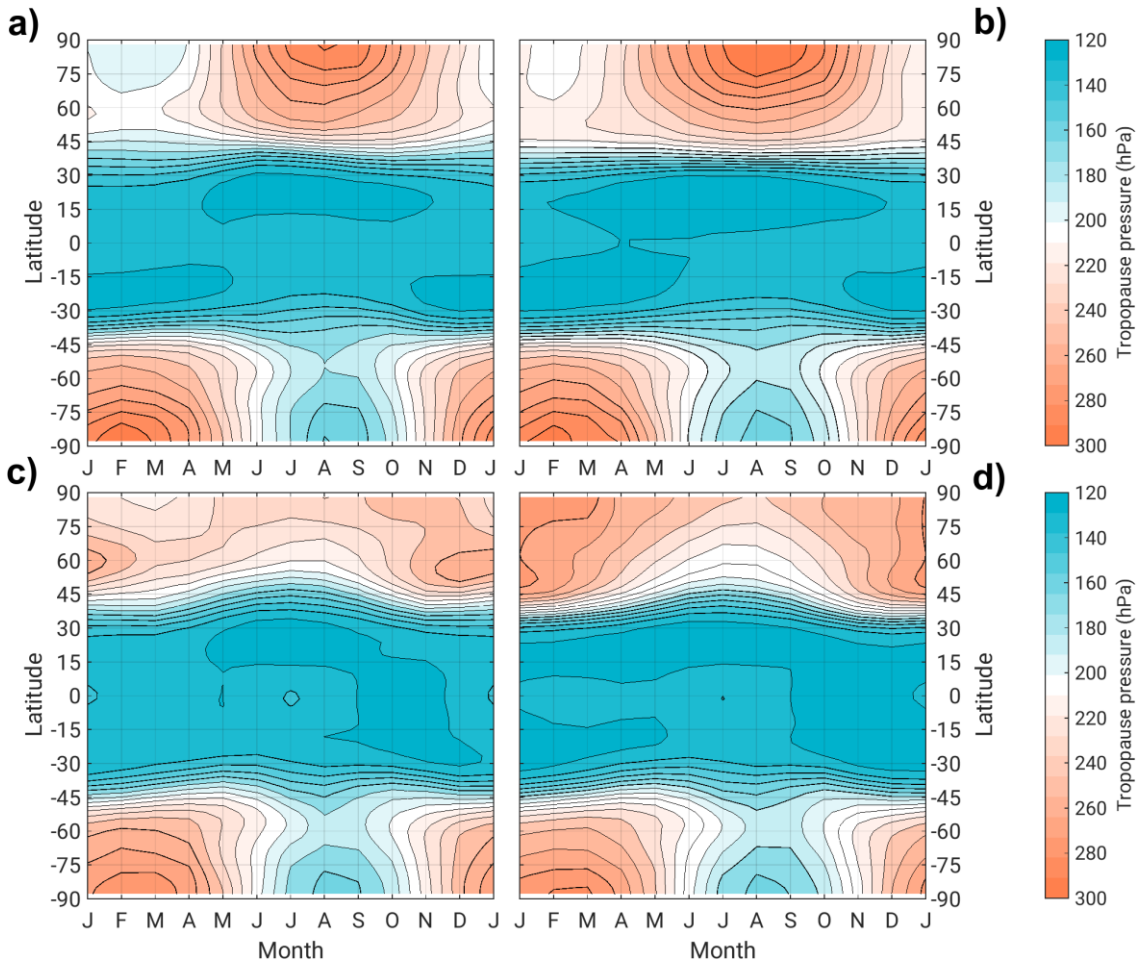

Fig. 5.7: Seasonal cycle of tropopause pressure in each of the simulations of Table 1. a) Simulation 1 (flat, no tropospheric seasonal cycle); b) Simulation 2 (mountains, no tropospheric seasonal cycle); c) Simulation 3 (flat, with tropospheric seasonal cycle); d) Simulation 4(mountains, with tropospheric seasonal cycle)

5.2.2 Tropospheric seasonal cycle and orographic influences.

5.2.2.1 Characteristics of the seasonal cycles.

a. Global tropopause seasonal cycle.

As shown in Fig. 5.7, if the troposphere has no seasonal cycle (Sim. 1), the annual cycle of tropopause height is hemispherically symmetric in both hemispheres: the tropopause rises in winter and sinks in summer. It can be seen that the extratropical tropopause is in general slightly lower when there is orography (Sim. 2) than when the surface is flat (Sim. 1), although the seasonal cycle is still symmetric. When seasonal variations in the tropospheric forcing are included (Sims. 3), the tropopause height annual cycle ceases to be symmetric and the north-

ern tropopause evolution becomes more complex. In the midlatitudes (40°N-60°N) the tropopause sinks in winter and rises in summer, while over the polar cap the seasonal cycle is very weak in this simulation: the tropopause rises slightly in spring and sinks during summer and autumn. The inclusion of orography (Sim. 4) finally produces a qualitatively similar seasonal cycle to the reanalyses, with the tropopause descending in winter and ascending in summer in the midlatitudes, while over the polar cap the tropopause height is minimum during spring and autumn (though the latter minimum is much weaker than in the reanalyses). In the model, the double-wave in the seasonal cycle seems to be constrained to higher latitudes than in the reanalyses -northward of 75°N. The inclusion of the tropospheric seasonal cycle (Sims. 3 and 4) also affects the southern tropopause, which is lower than in simulations 1 and 2, even if its annual evolution is qualitatively similar. Orography in the NH also affects the global tropopause, which is lower everywhere in simulations 2 and 4 than in the flat simulations 1 and 3, respectively.

b. Seasonal cycle in the Northern Hemisphere.

Looking at the temperatures in the lower-stratosphere and upper-troposphere over the polar latitudes (Fig. 5.8, top), it is clear that the tropopause evolution is determined by the lower-stratosphere temperature in the first two simulations (blue and red lines in Fig. 5.8), as the tropospheric temperature is more or less constant throughout the year. The only minor difference between simulations 1 and 2 is that the spring warming in the lower-stratosphere is somewhat steeper and the polar vortex reaches a slightly higher temperature in simulation 2. Larger changes are observed when the tropospheric seasonal cycle is included (green and black lines in Fig. 5.8). With seasonally varying upper troposphere temperatures, the temperature difference across the tropopause varies much less throughout the year in simulations 3 and 4 than in simulations 1 and 2, which explains the smaller amplitude of the tropopause seasonal cycle in the former. There are also changes in summer stratospheric temperatures, as simulations with tropospheric seasonal cycle (3 and 4) have a cooler summer stratosphere than simulations without it (1 and 2), which contributes to increasing the temperature difference across the tropopause during this season. This helps explaining the rising of the summer tropopause in simulations 3 and 4, not seen in the previous simulations. As for the winter season, the cooler UT in simulations 3 and 4 leads to a lower temperature difference and thus to a lower tropopause than in simulations 1 and 2. Focusing now on the transition seasons, a relative tropopause maximum is observed in April in simulation 3 as the

UT is even warmer than the UT in this month; beyond that date, the LS temperature stabilizes while the UT keeps warming, leading to a reduced summer tropopause height. Finally, the inclusion of mountains in Sim. 4 produces a drastic change in the LS winter temperature, which becomes much warmer than in the other simulations (black line). The warming starts in mid-December and continues through spring, preventing the lower-stratosphere from becoming too cold, as seen in the reanalyses. Hence, the tropopause sinks in winter in Sim. 4, reaching its minimum height in March.

In the midlatitudes (Fig. 5.8, bottom), with no tropospheric seasonal cycle (blue and red lines, corresponding to Sims. 1 and 2) the temperature difference across the tropopause is controlled by the seasonal cycle in LS temperatures. Thus, the tropopause evolution is opposite to that of the LS temperature, rising in winter and sinking in summer (as in the polar region). However, when the tropospheric seasonal cycle is included (green and black

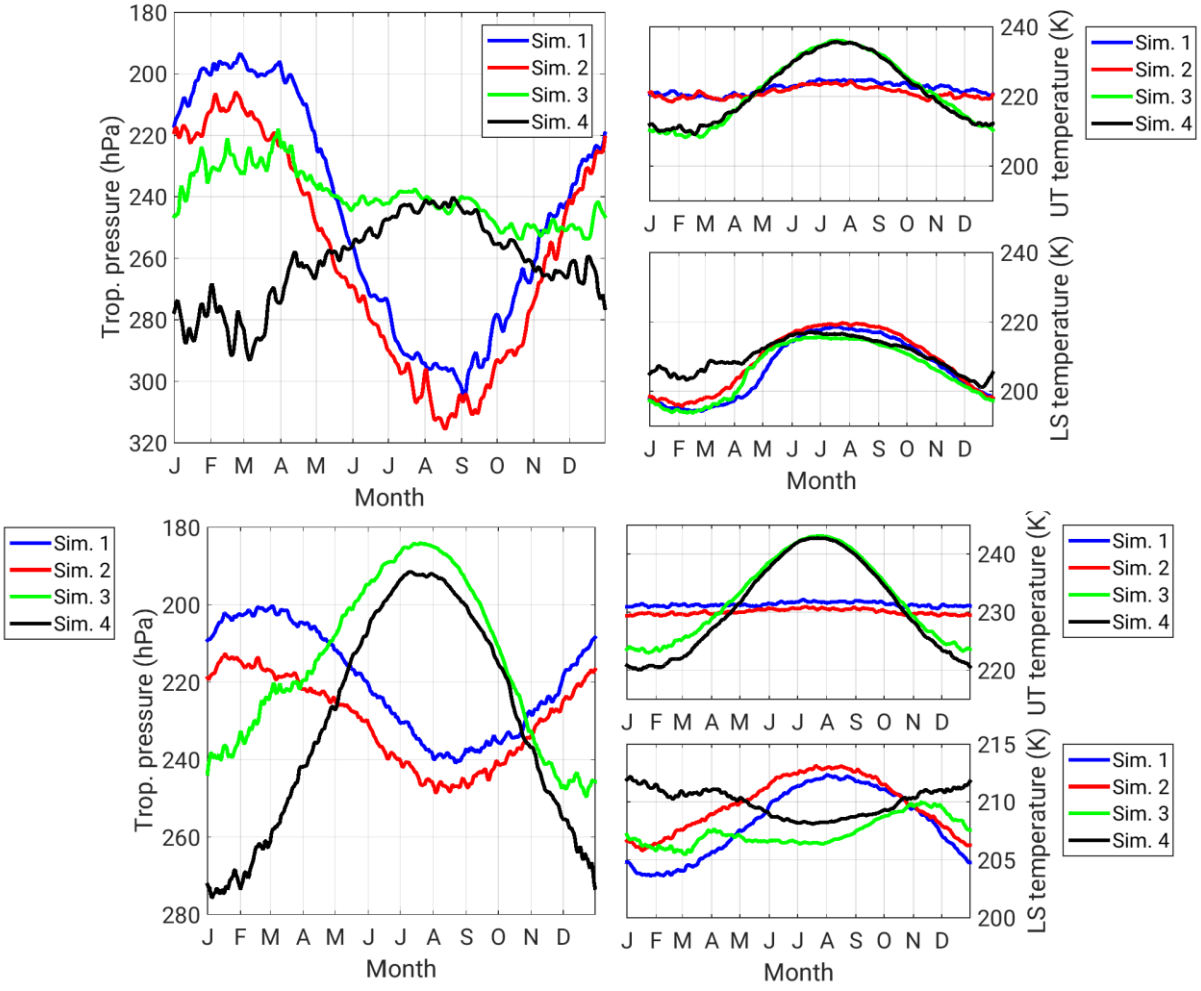

Fig. 5.8: Mean seasonal cycle of (left) tropopause pressure and (right) temperatures at 100hPa (LS, top right of each panel) and 400hPa (UT, bottom right of each panel) averaged over (top panel) 75ºN-90ºN and (bottom panel) 40ºN-60ºN in the first set of simulations. Blue is for sim. 1, red is for sim.2, green is for sim. 3 and black is for sim. 4.

lines, corresponding to Sims. 3 and 4), temperatures in the LS remain approximately constant during the year, especially in Sim. 4, so it is the UT temperature that dominates the seasonal cycle of the tropopause. Note that simulations including orography (red and black lines in Fig. 5.8, corresponding to Sims. 2 and 4) have in general colder tropospheric and warmer stratospheric temperatures than their flat counterparts (blue and green lines, corresponding to Sims. 1 and 3). As a result, the temperature difference is smaller and the tropopause is lower in the simulations with orography than in the flat simulations.

c. Seasonal cycle in the Southern Hemisphere.

In the SH (Fig. 5.9, top), the tropopause level does not follow so closely the temperature difference between 100 and 400hPa as in the NH, especially in the polar cap during southern summer, when the tropopause stays low till April even though the stratospheric temperatures already start cooling in February. The lag between the seasonal cycles in tropopause height and stratospheric temperature is due to our use of 100hPa as the reference strat-

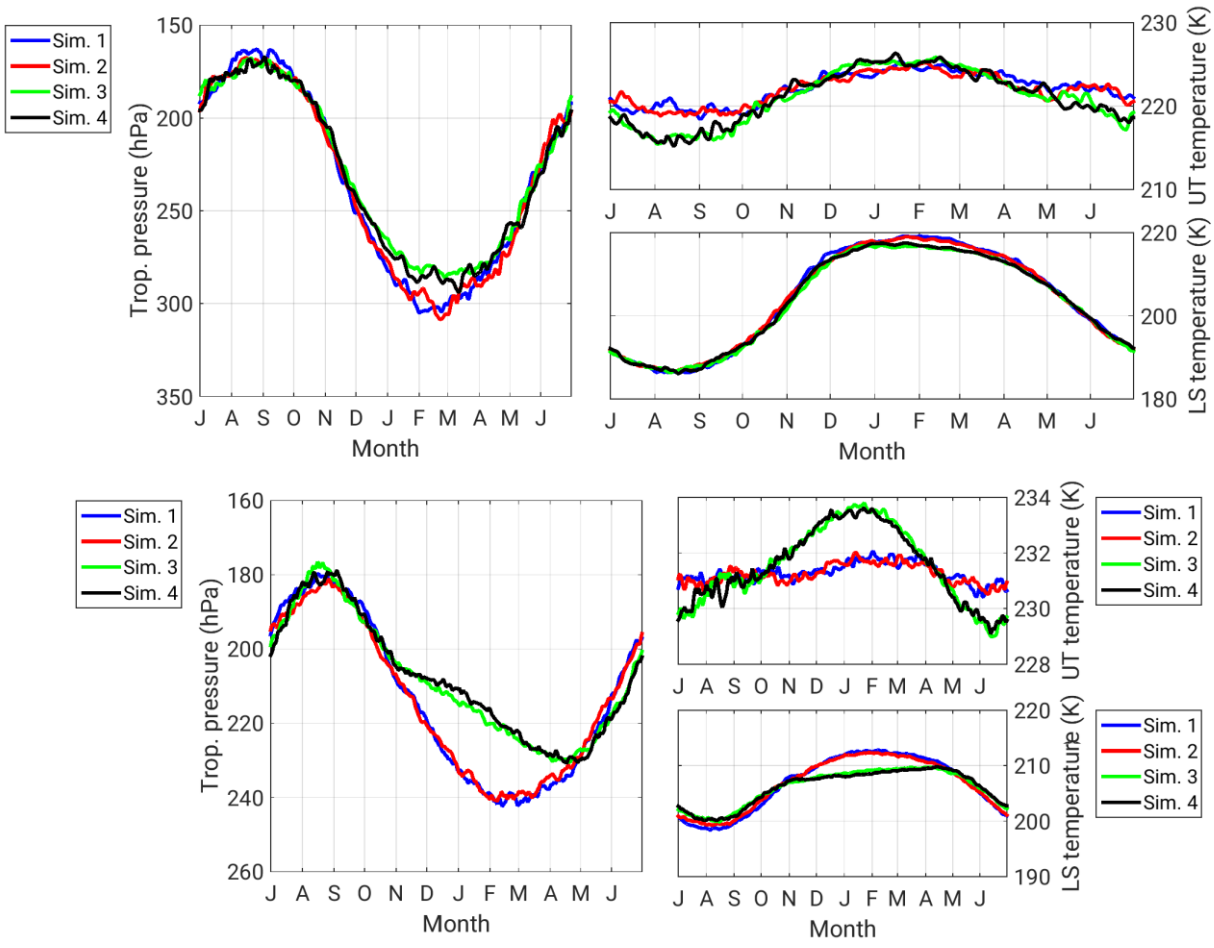

Fig. 5.9: As in Fig. 5.8, but for the Southern midlatitudes (40ºS-60ºS) and polar cap (75ºS-90ºS).

ospheric level, which is very far from the tropopause (150hPa above) during southern summer (the seasonal cycle in lower stratosphere temperature lags by a month that at 100hPa). Although this lag is also present in the northern polar cap, its magnitude is smaller and it does not affect as much the summer tropopause.

In the Polar Regions, the tropopause is very high during the winter months and lower during the summer and autumn months, especially in the first simulations (1 and 2) due to the nearly constant UT temperature and the large amplitude of the LS seasonal cycle. Little differences are apparent between the simulations; the inclusion of the tropospheric seasonal cycle (Sims. 3 and 4) produces a colder UT during the austral winter –leading to a lower tropopause during this season- and a slightly warmer LS in the southern summer –leading to a higher tropopause in summer.

In the southern midlatitudes, the seasonal cycle of the tropopause follows a similar evolution as in the Polar Regions (the winter tropopause is higher than the summer tropopause), although its amplitude is smaller in this case, as is the amplitude of the LS temperature variation. Inclusion of the tropospheric seasonal cycle (Sims. 3 and 4) impacts not only the UT temperatures but also the LS temperatures (green and black solid lines in Fig. 5.9), which are colder during southern summer (November to May) and slightly warmer during southern winter. Together with the upper-troposphere seasonal cycle, this leads to a reduced (increased) UT-LS temperature difference in winter (summer), attenuating the tropopause seasonal cycle. It also delays the timing of the maximum and minimum tropopause pressures, shifting the seasonal cycle as in polar areas. Fig. 5.7 shows that this "polar-like" seasonal cycle, with higher tropopause in winter than in summer, is found in the model throughout the midlatitudes, which differs from the observed seasonal cycle in the reanalysis (Fig. 5.1). In observations, the seasonal cycle is in phase with the polar seasonal cycle poleward of 50°S but is reversed equatorward of this latitude, with lower tropopause in winter than in summer. Hoinka (1998) attributed this behaviour to the LS seasonal cycle, which has been linked to the meridional displacement of the descending branch of the shallow Brewer-Dobson circulation. As the tropical cell moves southward during the austral spring, it brings enhanced adiabatic warming to southern latitudes associated with the descending motion; when it moves northward during the austral autumn it takes with it this adiabatic warming, and the lower stratosphere cools. It is apparent in Fig. 5.7 that the tropical cell in the model (as deduced

from the meridional extension of the tropical tropopause) displaces southwards during the austral winter instead of northward –the displacement is larger in simulations 1 and 2, and smaller in simulations 3 and 4. This is responsible for the semi-annual peak observed in the periodograms (Fig. Analysis of the residual circulation (see next section) suggests that the residual circulation responds to the strong winter polar vortex with a southward displacement, which anomalously extends the tropical cell to the south; hints of a double-wave seasonal pattern at 45°S are apparent in Fig. 5.7. Hence, the cause of the differences with the southern midlatitudes in the reanalysis seems to be that the influence of the southern polar vortex extends too far north in the model.

5.2.2.2 Dynamical analysis of the seasonal cycles.

Aiming to study the differences in the circulation in each simulation to understand the dynamical causes of the heating, the residual circulation is computed for each simulation and shown in Fig. 5.10 for the winter and summer months. As can be seen, in sim. 1 there is great symmetry in the troposphere, where there is a single cell extending from the equator to the poles. In the stratosphere, the circulation is stronger in the winter hemisphere, as observed in the reanalyses (see the introductory chapter), especially in the NH (in the SH the stratospheric circulation is somewhat weaker due to the stronger polar vortex). Weak reverse cells appear at tropopause levels in midlatitudes poleward of the jets (Zurita-Gotor and Vallis, 2013). As explained in Section 3.6, the warming caused by the eddies is given by the term $-\bar{\omega}^* \, \partial\bar{\theta}/\partial P$ (see eq. 3.13) and this is represented in colours in Fig. 5.10. Note that the maximum effect on the tropopause level will occur when there is a vertical differential heating –this is, heating of opposite sign above and below the tropopause. As such, in the tropical area the strong cooling effect of the ascending residual circulation in the LS raises the tropical tropopause while the adiabatic warming associated with the descent of the stratospheric circulation in higher latitudes depresses the extratropical tropopause. Isentropic transport by the eddies in midlatitudes is associated with lifting of the air masses, hence producing adiabatic cooling right below the tropopause, which tends to sharpen the meridional gradient of tropopause height in the subtropics. This behaviour is apparent in Sim. 3, though the dynamical processes are enhanced (weakened) in the winter (summer) hemisphere, especially in the NH. It is obvious that introducing the seasonal cycle increases the baroclinicity –more so in the NH winter, where the meridional gradient of the radiative-equilibrium surface temperature is greater than in the SH- and thus the residual circulation and its effects are stronger. This is specially

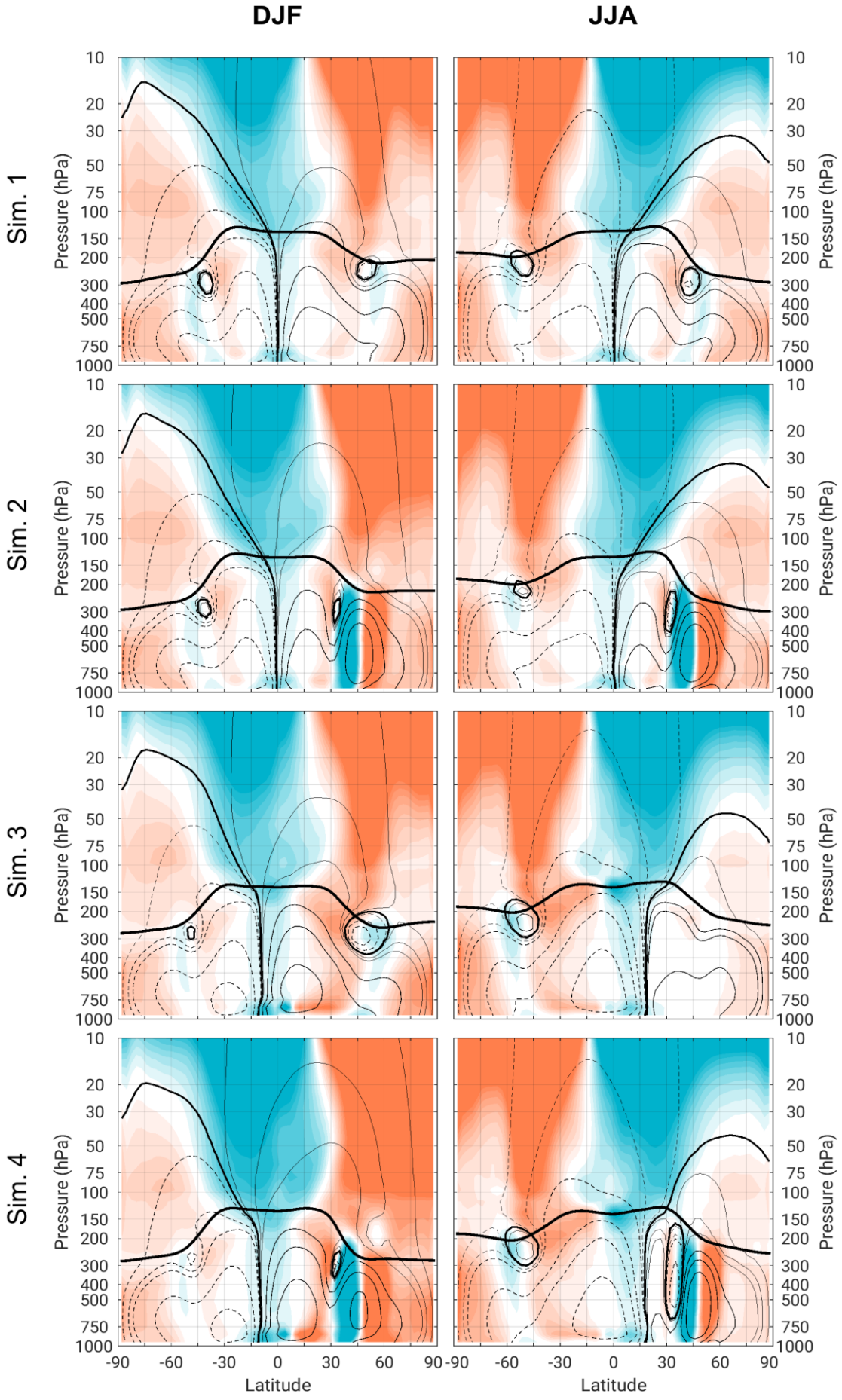

Fig. 5.10: Residual circulation (black contours), dynamical heating (colours) and tropopause level (bold black line) in JFM (left column) and JJA (right column) for simulation 1 (top row), simulation 2 (upper middle row), simulation 3 (lower middle row) and simulation 4 (bottom row).

apparent for the reverse cells in the winter hemisphere mentioned above, in connection with the steeper gradient between the tropical and the extratropical tropopause observed in this simulation.

Inclusion of orography in Sims. 2 and 4 has two main effects. On the one hand, it forces a direct cell right above the mountains throughout the year, preventing the tropical cell from extending too far north –especially during northern summer- and creating a sharper contrast between the tropical and the extratropical tropopause. On the other hand, it increases the magnitude of the residual circulation in the LS during the boreal winter, though it is striking that the deep circulation at high levels changes relatively little –less than expected- when mountains are included. This is consistent with the argument of Cohen *et al.*, 2013 that the stratospheric temperatures and winds exert a strong control on upward propagation, reducing the sensitivity of the deep Brewer-Dobston circulation to wave forcing. The stronger circulation in the LS in the presence of orography is associated with enhanced warming there, explaining the lower winter tropopause in the NH compared to Aims. 1 and 3 (this also happens during the boreal summer, albeit with reduced magnitude).

Regarding the seasonal cycle in the Polar Regions, the summer sinking of the tropopause in Sims. 1 and 2 is clearly related with the vertical contraction of the tropospheric cell, so that the descending branch of this circulation and the associated heating occur lower than in winter. Because there is no tropospheric seasonal cycle in these simulations, these changes must be driven from the stratosphere. It appears that the shallow Brewer-Dobson circulation strengthens in summer in these simulations, consistent with the warmer summer temperatures found in the stratosphere with no tropospheric seasonal cycle (c.f., Fig. 5.8). In the simulations with tropospheric seasonal cycle (3 and 4) the NH tropospheric cell expands in summer instead, leading to a higher tropopause in both the Polar Regions and midlatitudes than in the winter season.

5.3 Discussion.

Is has been shown in this chapter that the tropopause seasonal cycle is dominated by the annual component and hemispherically symmetric in the midlatitudes, while it is asymmetric over the Polar Regions. In midlatitudes, the tropopause rises in summer and

sinks in winter in both hemispheres, a behaviour attributed to greater dynamical warming in the lower-stratosphere in winter than in summer (Hoinka, 1998). Since the midlatitude upper-troposphere is cooler in winter than in summer, this implies that the temperature difference across the tropopause (which is related to tropopause height, as shown by Möller, 1938) is greater in summer than in winter, as is tropopause height. In the southern polar region the pattern is exactly the opposite: the lower-stratosphere cools during austral winter much more than the upper-troposphere, leading to a tropopause rise, while lower-stratosphere summer temperatures are close to upper-troposphere summer temperatures, which is associated with a low summer tropopause. In the northern Polar Regions, however, the tropopause seasonal cycle is dominated by the semi-annual component as already observed by Zängl (2001) at some locations: the tropopause sinks in spring and autumn and rises in summer and winter. The wintertime tropopause rise is similar –but weaker- to the SH, and finishes much earlier when the lower-stratosphere starts to warm, leading to a spring minimum in tropopause height.

Analysis of the terms in the thermodynamic equation shows that the dynamical heating by the convergence of meridional eddy heat fluxes over the polar cap at the end of the winter is responsible for this warming, which is absent in the winter SH. This agrees with the analysis of Zängl (2002), who showed that the dynamical heating by the residual circulation in the northern lower stratosphere is maximum during late winter, especially in February; this warming is associated with the breakdown of the vortex at the end of the winter (Zängl, 2002). This also agrees with the results of Appenzeller (1997), who found that the transport of stratospheric mass across the tropopause is maximum during boreal spring. The results in the SH are somewhat different from those in Zängl (2002); there are no hints of a double wave in the seasonal cycle of dynamical heating but a spring maximum in the horizontal convergence of eddy heat flux that it is almost completely balanced by the adiabatic cooling of the mean meridional circulation. Zängl (2002) associated the spring maximum in the dynamical heating with an ageostrophic meridional circulation associated to the differential heating of the vortex during the austral spring; hence, the maximum in the eddy heat flux convergence observed here may be a response to this circulation, so that the thermal wind balance is not violated. The cooling by the mean meridional circulation reverses by the summer solstice, producing the increase in dynamical warming during the summer observed by Zängl (2002).

In the boreal summer the dynamical warming in the NH polar cap is minimum but still important, contrary to Zängl (2002), partly due to the significant contribution by the mean meridional circulation. Diabatic cooling balances this dynamical heating during the second half of the year, leading to a cooling in the LS. However, because this cooling is weaker than in the upper-troposphere, the tropopause sinks during autumn. In the SH, there is maximum warming during the summer months due to diabatic heating in late spring (likely caused by radiative heating as the sunlight starts reaching the southern pole, although this term is computed as a residual) and to the increased dynamical warming during the summer, as commented above.

Results from simulations with an idealized model largely support the picture put forward above. When baroclinicity is weak (no tropospheric seasonal cycle), the tropopause is higher in winter, although locally depleted in regions with strong lower stratosphere warming by the descending branch of the residual circulation. This low tropopause is also forced by the midlatitude isentropic transport, which produces adiabatic cooling in the upper-troposphere associated with the reverse cell at tropopause levels. When the tropospheric seasonal cycle is included, baroclinicity increases and the tropospheric jet and eddy generation shift equatorward (due to the stronger cross-equatorial Hadley cell) in the winter hemisphere. The colder temperatures in the winter upper-troposphere lead to a lower tropopause than in the previous case –with a little help by the descending branch of the stratospheric circulation, slightly stronger now. The main impact of the orography in the troposphere is producing a secondary tropospheric cell on its southward flank, debilitating and displacing the tropospheric jet southward. As a result, the reverse cell in the upper troposphere nearly disappears and the region of ascent/tropospheric cooling shifts southward. These changes lead to a lower subtropical and midlatitude tropopause when orography is introduced, while the polar tropopause also sinks as the stratospheric circulation is now able to reach the polar region.

6. Intraseasonal variability of the extratropical tropopause.[1]

After discussing in previous chapters the structure of the mean tropopause and its seasonal cycle, this chapter focuses on higher frequency variability. We analyse the intraseasonal tropopause variability in reanalyses and in the idealized model, with a special emphasis on the dynamics. Relations are found between variability of tropopause height and that of the subtropical, extratropical and stratospheric jets due to their connection with eddy activity. It is also found that the extratropical-mean tropopause varies comparatively much less than the modes obtained, so that baroclinic adjustment seems to be of secondary importance for the internal variability of the tropopause. Our analysis focuses on Northern Hemisphere variability; the dynamics is similar in the Southern Hemispheres except for the smaller role played by planetary waves.

[1] Part of the results presented in this chapter is published in Barroso and Zurita-Gotor (2016) and in Barroso and Zurita-Gotor (in preparation).

One potential complication when studying the modes of variability of the extratropical tropopause is the confounding effect of extratropical incursions of tropical air with large tropopause height anomalies, together with the strong seasonal cycle in the meridional extension of the Hadley cell. Hence, we defined the extratropical northern region using a conservative latitude of 32.5°N, which seems to be the maximum northward extension of the tropical belt during the northern winter (Davis and Birner, 2013). This range of latitudes may include some variability associated to the subtropical jet.

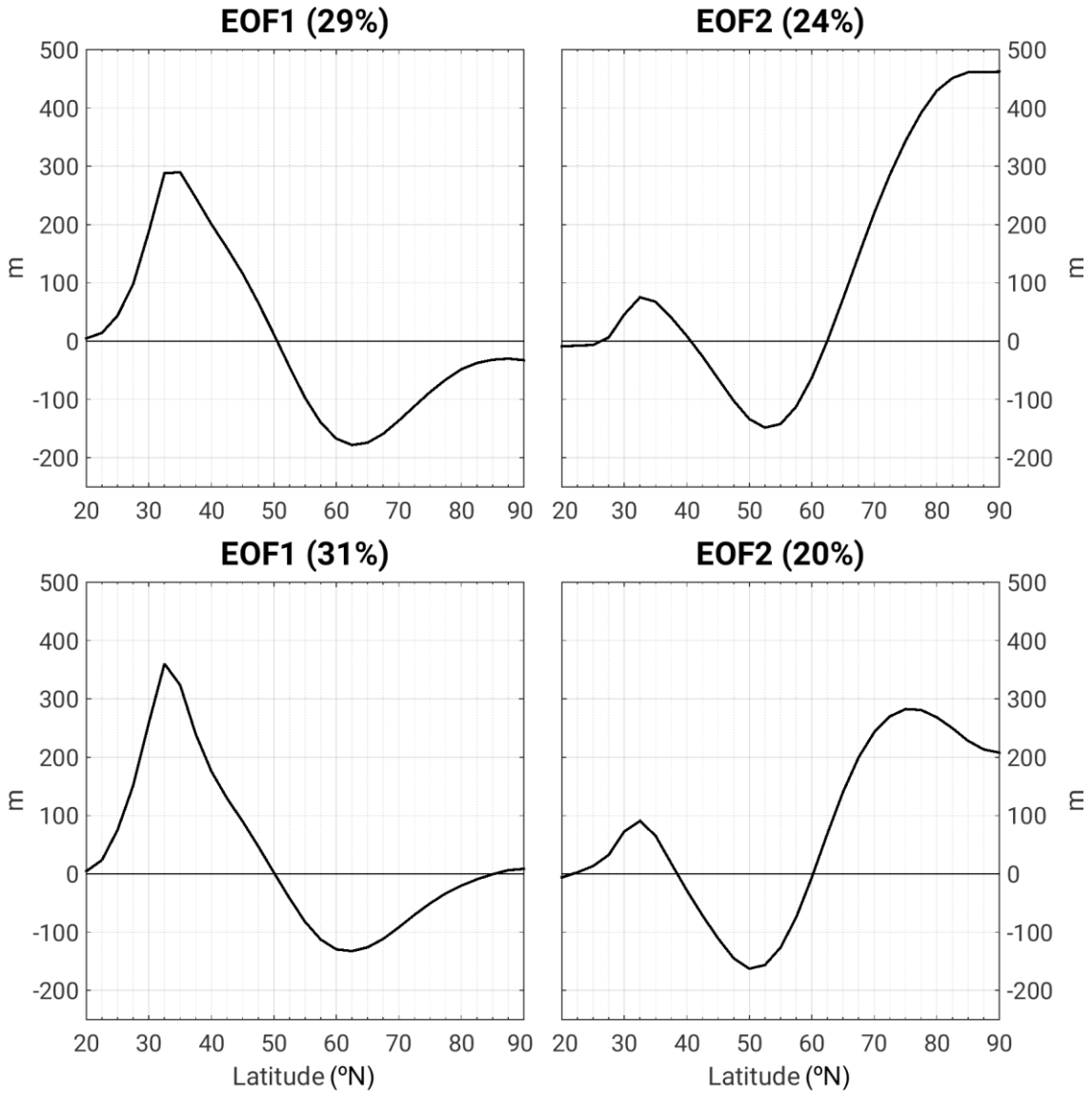

Fig. 6.1: Regression maps of anomalous zonal-mean tropopause height (m) on (left) PC1 and (right) PC2 for the (top) NCEP–NCAR Reanalysis-1 and (bottom) ERA-Interim datasets, during the extended NH winter.

6.1 Modes of variability of the extratropical tropopause.

As shown in Fig. 6.1, the first mode of variability of the northern extratropical zonal-mean tropopause in NCEP-NCAR reanalysis during the extended winter has a dipole struc-

ture with the node around 50°N and extrema at 35° and 65°N. The second mode corresponds to a tripole pattern with nodes at 45° and 65°N; the two modes are uncorrelated at all lags and well separated according to the North *et al.* (1982a) criterion when the effective number of degrees of freedom for the time series (eq. 3.13) is taken into account (Fig. 6.2). This structure is characteristic of many extratropical fields -for example, the zonal-mean zonal wind (Lorenz and Hartmann, 2001, 2003), the sea level pressure, and the geopotential height (Thompson and Wallace, 2000). This type of variability is generally described as an annular mode (Zonal Index in the case of the zonal wind, Arctic Oscillation in the case of the geopotential height), which physically represents a mass fluctuation between the poles and midlatitudes with a high degree of zonal symmetry (Thompson and Wallace, 2000), related to meridional displacements of the extratropical jet around its mean position (Lorenz and Hartmann, 2003; Wittman *et al.,* 2005) driven by interactions between the mean flow and the eddies. The relationship between the leading tropopause mode and the Zonal Index or the Arctic Oscillation will be discussed below. Also shown in Fig. 6.1 are the leading two modes calculated using ERA-Interim data. It can be seen that the patterns are quite similar to NCEP/NCAR reanalysis, though the polar centre of action in both EOFs is weaker in ERA-Interim than in NCEP/NCAR reanalysis. Additionally, the first mode explains more variance for ERA-Interim than for NCEP/NCAR reanalysis. The large correlations between the modes independently calculated for both reanalyses [0.88 for both principal components (PCs)] demonstrate that

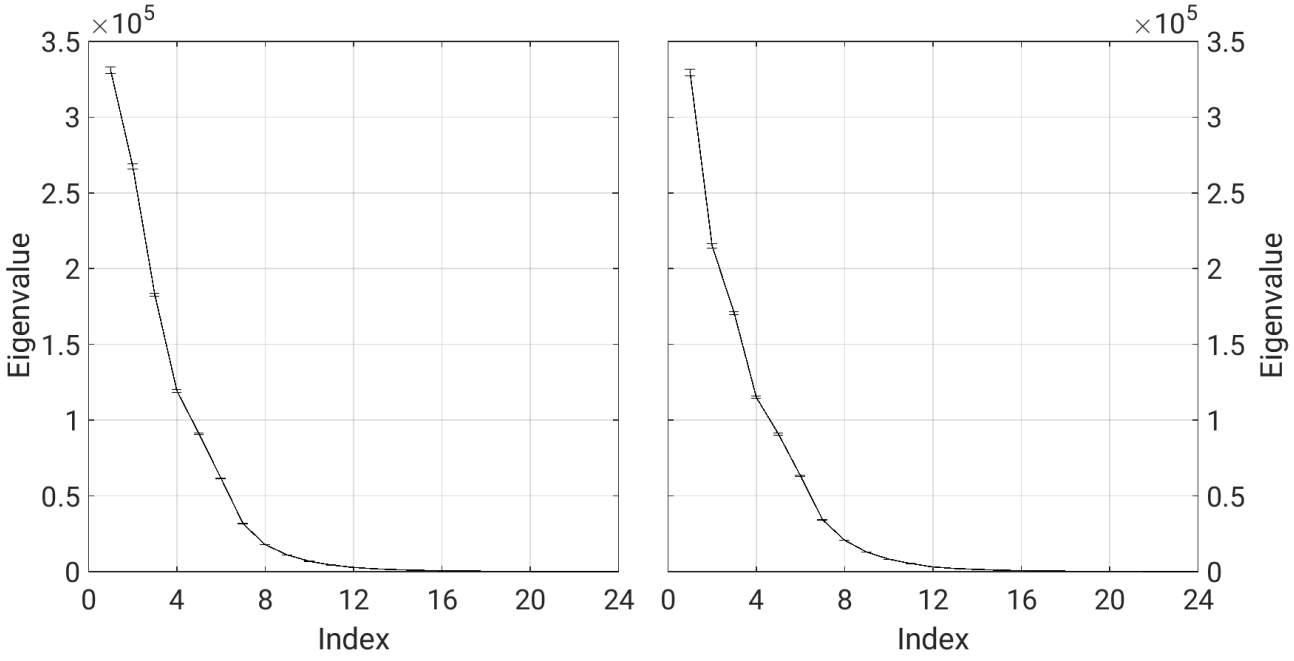

Fig. 6.2: Spectrum of the covariance matrix of anomalous zonal-mean extratropical tropopause height for the NCEP/NCAR dataset (left) and the ERA-Interim dataset (right). Error bars are calculated with North's rule of thumb (see Chapter 3).

these modes are robust in both datasets. The dynamical analysis in the next section uses NCEP/NCAR reanalysis data but results are similar with ERA-Interim (the corresponding figures are shown in the Appendix of this thesis).

Although the modes of variability are obtained from the zonally averaged tropopause height, we can look at the 2D structure by compositing the expansion coefficients, PC, with the complete field (Fig. 6.3). As expected there is great zonal symmetry, especially for EOF2 in the NCEP/NCAR reanalysis -the polar centre of action is displaced over Greenland in the ERA-Interim reanalysis-, though some minor asymmetries stand out for the first mode: a high tropopause over the oceanic storm tracks and a low tropopause over Iceland (which, together

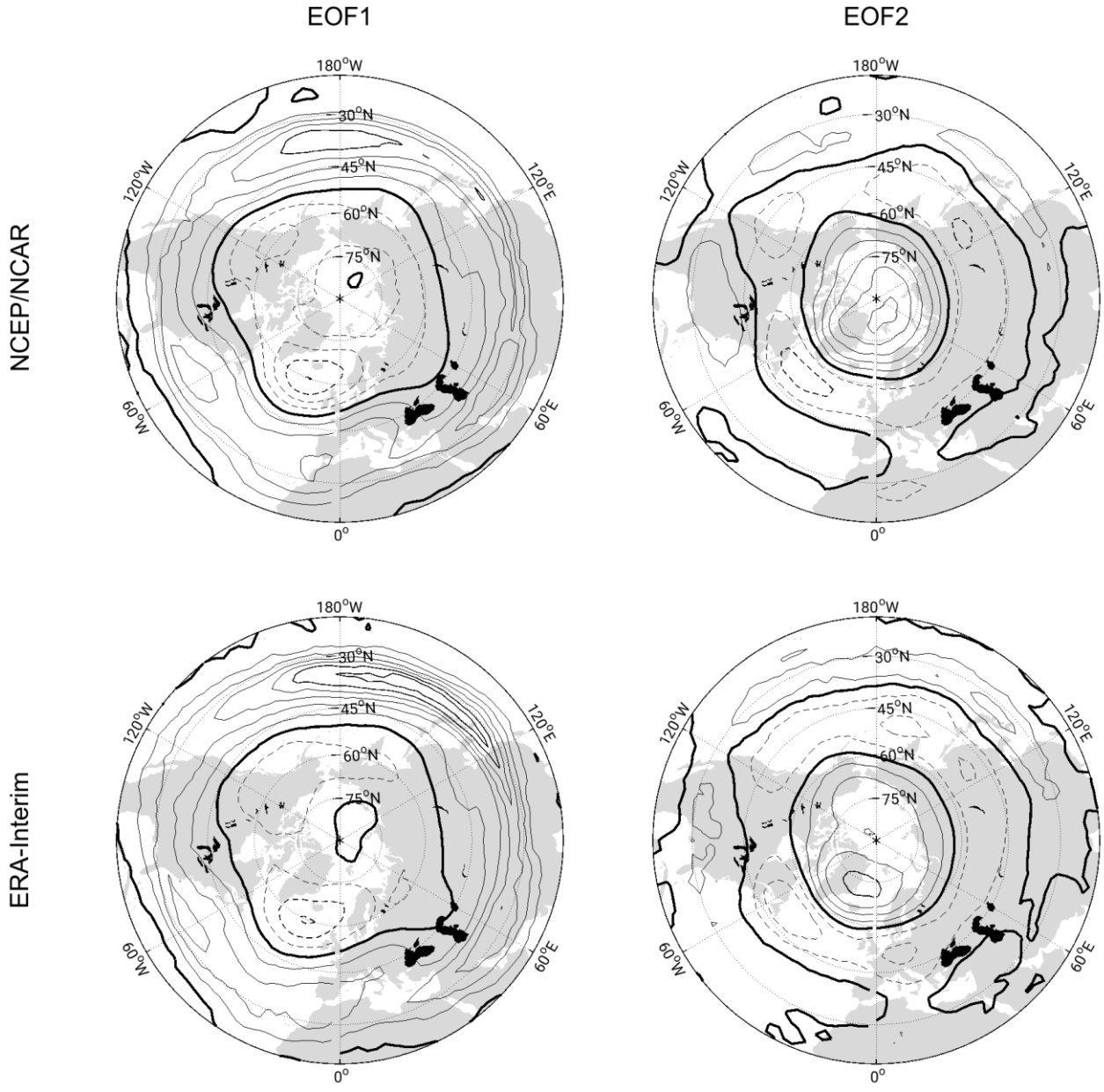

Fig. 6.3: Regression maps of anomalous tropopause height on PC1 (left column) and PC2 (right column) for the NCEP/NCAR (top row) and ERA-Interim (bottom row) reanalyses, during the extended NH winter. The contour interval is 100m, and is solid (dashed) for positive (negative) anomalies. Thick contour is for zero isoline.

with the anomaly to the west of Canada, produce the tropopause height minimum at 65°N). However, this annular pattern only represents the average of many non-symmetrical cases, while individual snapshots are dominated by wavy patterns as typically found in isentropic potential vorticity maps (Hoskins *et al.*, 1985).

	PC1	PC2
20°-90°N	28%	20%
20°-80°N	31%	20%
20°-70°N	36%	19%
20°-60°N	40%	18%
20°-50°N	46%	21%
20°-40°N	57%	21%
20°-30°N	71%	19%
30°-90°N	29%	22%
40°-90°N	33%	26%
50°-90°N	40%	27%
60°-90°N	49%	31%
70°-90°N	68%	25%
80°-90°N	91%	9%

Table 6.1: Variance explained by each of the first two modes of variability of the extratropical zonal-mean tropopause height for selected latitudinal ranges. Red (blue) indicates that the corresponding mode is highly correlated (and has a similar structure) with the "midlatitude" ("polar") mode shown in Fig. XX (top).

These modes of variability are highly insensitive to both the spatial and temporal ranges chosen for the analysis. In particular, the same modes are obtained when PCA is performed on the summer months or on the entire year although the explained variances vary (both modes explain more variance during the winter months than during the summer months or the whole year). From this, it can be concluded that the variability associated with these modes is representative of the intra-annual variability of the extratropical zonal-mean tropopause. As for the robustness of the patterns to the choice of latitudinal band, the first mode emerges as long as midlatitudes (30°–40°N) are included in the analysis and is insensitive to the northern boundary of the domain; this suggests that its structure (a dipole centred at 50°N) is characteristic of the variability of the tropopause and not an artefact of the region chosen for the study. When the midlatitudes are not included in the PCA, there is a permutation between the first two modes and the tripole becomes the leading mode of variability. This mode is robust as long as polar latitudes are included in the analysis, no matter where the southern edge lies. This suggests that the first mode is basically a phenomenon originating in midlatitudes, while the second mode may be more related to polar variability. The more the latitude range is restricted to one of the two areas (either mid- or high latitudes) the more dominant the corresponding mode is (see Table 6.1). Looking at the life cycle of the perturbations (Fig. 6.4) it can be seen that in general polar tropopause anomalies tend to be more persistent than midlatitude anomalies, especially in EOF2.

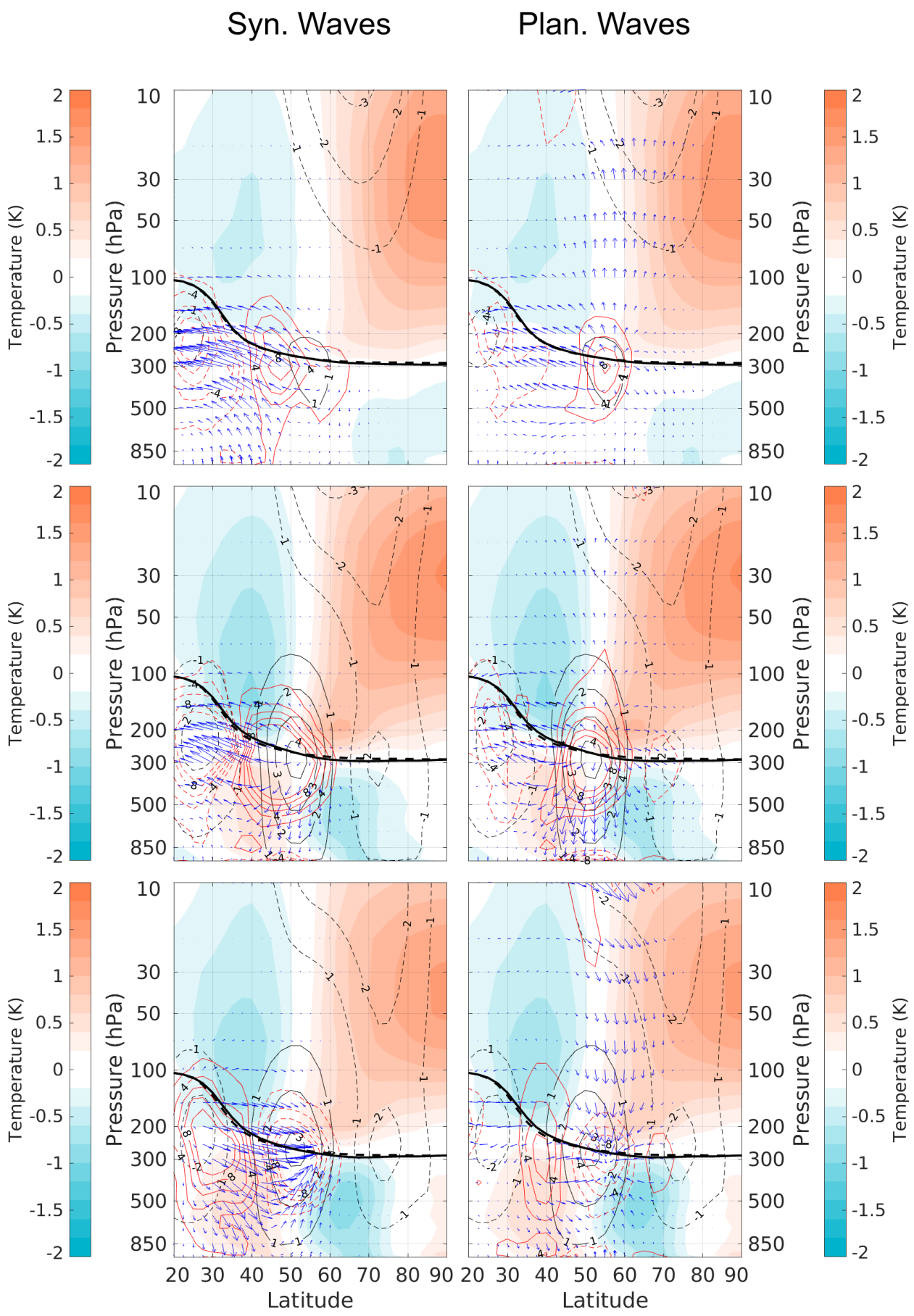

Fig. 6.4: Lagged composite of PC1 on anomalous EP flux (arrows), anomalous EP flux divergence (x1014 m2 s-2; red contours), anomalous zonal-mean zonal wind (m s-1; black contours), and anomalous zonal-mean temperature (K; colors) for (left) synoptic and (right) planetary waves at lags (top) -4, (middle) -1, and (bottom) +1 days. The climatological (extended winter) and composite tropopause heights are shown with thick dashed and solid lines, respectively. For clarity of representation, the vertical component of the EP vectors has been scaled as a function of pressure using a p factor.

6.2 Dynamical analysis of the intraseasonal variability.

6.2.1 Composite eddy forcing

Variations in midlatitude tropopause height are expected to be caused or at least associated with variations in the eddy activity (Dell'Aquila *et al.,* 2006; Son *et al.*, 2007), as suggested by the anomalies along the stormtracks in Fig. 6.3. As explained in Chapter 3, changes in eddy activity can be described by using the anomalous Eliassen–Palm (EP) fluxes and divergence (see Section 3.6 for details).

As can be seen in Fig. 6.5, the perturbation in tropopause height associated with PC1 is preceded a few days earlier by an upward burst of synoptic waves at low latitudes, which propagate southward at tropopause levels and break near the subtropical jet. This produces a pattern of anomalous divergence (convergence) of the EP flux in the midlatitudes (in the subtropics), which accelerates the zonal-mean zonal wind on the northern flank of the extratropical jet and decelerates the zonal wind in the subtropics, shifting the extratropical jet northward. The planetary waves produce a similar dipolar pattern of EP divergence at tropopause levels, except that enhanced vertical propagation into the stratosphere also reinforces the positive centre on the northern side of the extratropical jet in this case. The subsequent wave breaking in the stratosphere leads to a deceleration of the stratospheric jet (Andrews *et al.*, 1987) a few days later. The anomalies in the EP divergence evolve quite rapidly. For positive lags, increased synoptic wave breaking to the north of the extratropical jet damps the anomaly on the zonal-mean zonal wind, while the decay of planetary waves ceases the forcing on the stratospheric jet and also contributes to the return of the extratropical jet to its mean position (albeit to a lesser extent than synoptic waves).

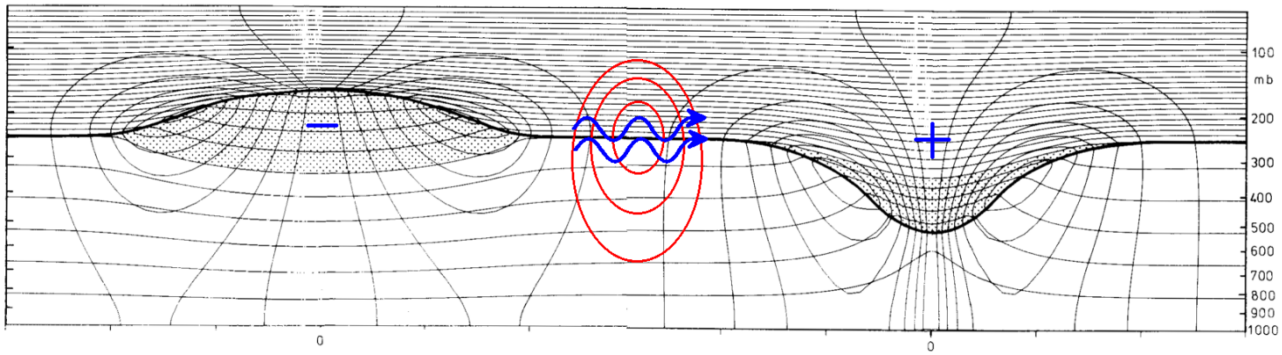

Fig. 6.5: Schematics of the dynamical forcings of the dipolar structure of EOF1. Anomalous wave breaking near the tropopause (black thick line) occurs where anomalous □□F≠0 (red contours) and is associated with a northward eddy flux of quasi-geostrophic potential vorticity (blue arrows), producing an anomalous dipole of potential vorticity centered around the anomalous wave breaking (adapted from Hoskins et al, 1985).

The anomalies in the EP flux divergence described above are consistent with the structure of the tropopause anomalies for this mode, which can be understood from the equivalence of $\nabla\cdot\mathbf{F}$ as a northward flux of quasigeostrophic potential vorticity by the eddies $\overline{v'q'}$ (see Section 3.6). Thus, the anomalous EP flux divergence to the north of the extratropical jet is associated with an anomalous northward flux of quasigeostrophic potential vorticity near the tropopause level, which will produce a positive (negative) anomaly of potential vorticity to the north (south) of the $\nabla\cdot\mathbf{F}$ anomaly -see Fig. 6.6. This is consistent with the rise of the tropopause (negative anomaly of potential vorticity) to the south of the positive $\nabla\cdot\mathbf{F}$ anomaly and its depletion (positive anomaly of potential vorticity) to the north. (Note that the maximum in the EP divergence is collocated with the node of the tropopause EOF.) The relation between potential vorticity anomalies and tropopause height is thus consistent with the classical model of a potential vorticity perturbation at upper levels (Hoskins *et al*., 1985; Zängl and Wirth, 2002) and with the results of the quasigeostrophic theory (Juckes, 1994). It is shown in Fig. 6.7 that the anomaly in the EP flux divergence is dominated by the eddy momentum flux convergence, especially at the tropopause level, for both synoptic and planetary waves.

The dipolar character of the EOF1 pattern is common to several meteorological fields in the Northern Hemisphere. In particular, the anomalous zonal-mean zonal wind field associated with the first EOF of the extratropical tropopause (black contours in Fig. 6.5) is very similar to the zonal index [see Fig. 3a in Lorenz and Hartmann (2003)] and indeed the correlation between both time series is highly significant (0.67). This is also consistent with our findings that eddy momentum fluxes are more important than eddy heat fluxes for the pattern of EP divergence associated with the variations in tropopause height. In contrast, the correlation of the leading tropopause PC with the Artic Oscillation (AO) index is much lower (0.26) even though zonal index and Arctic Oscillation are often regarded as the same variability. This may reflect the fact that the AO index includes several types of atmospheric variability [e.g., several patterns of zonal-mean zonal wind variability; see Feldstein and Lee (2014)], which could impact tropopause height in different ways.

The dynamical evolution of the second EOF exhibits some similar features to those described above for the leading EOF (Fig. 6.8). Anomalous vertical propagation of synoptic waves is initially found on the southern flank of the extratropical jet a few days ahead of the maximum tropopause anomaly. As time evolves, this develops into an anomalous EP

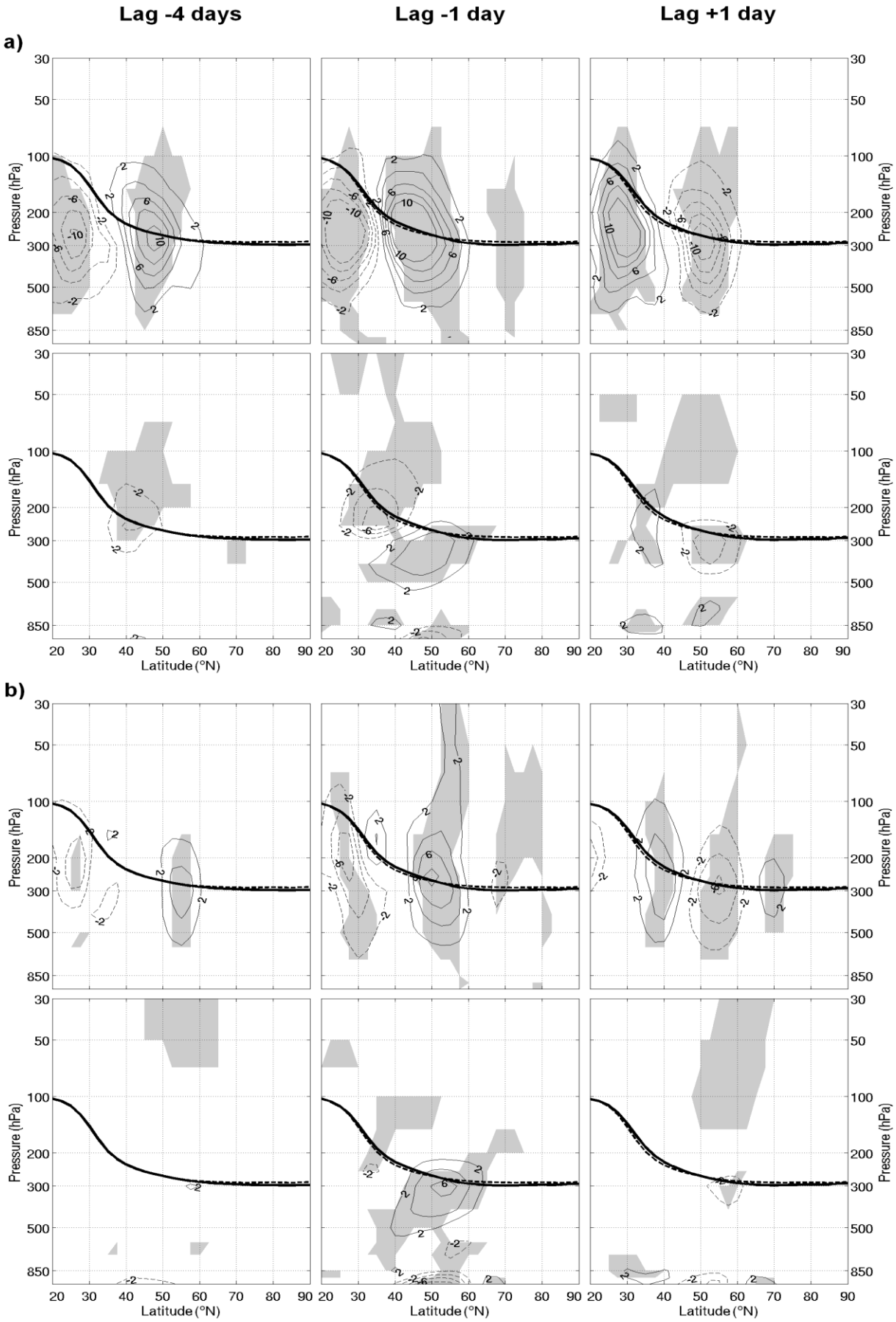

Fig. 6.6: Lagged composite of PC1 on the components of the EP flux divergence for(a) synoptic and (b) planetary waves. In each case, (top) meridional and (bottom) vertical divergence is shown at lags (left) -4, (center) -1, and (right) +1 days. Contours are labeled every 2x1014 m2 s-2 and shading represents areas where the component of the EP flux divergence is statistically different from its mean at 99%. The climatological (extended winter) and composite tropopause heights are shown with thick dashed and solid lines, respectively.

divergence pattern at upper levels characterized by EP flux divergence over the extratropical jet region and convergence on its flanks (but much stronger on the subtropical side). In this manner, the synoptic eddies produce an acceleration of the extratropical jet, mainly at the expense of the subtropical jet. As for the planetary eddies, the dominant feature is a centre of large EP convergence north of 55°N associated with enhanced vertical propagation in the troposphere and weakened propagation into the stratosphere (plausibly because of the anomalously strong stratospheric jet), which conspire to produce strong wave breaking at tropopause levels over that region. This is accompanied by weakened upward propagation of planetary waves on the south, which is associated with a positive EP divergence anomaly at upper levels over that region. The combined effect of the synoptic and planetary EP fluxes at upper levels is thus a tripolar EP flux divergence anomaly with a positive centre around 45°N and negative centres on the south (north) forced predominantly by the synoptic (planetary) eddies. This EP divergence pattern is consistent with the structure of the tropopause height perturbations in the manner discussed above for the first EOF. Also as before, anomalies in the EP flux divergence are mainly caused by the eddy momentum fluxes. Finally, for both the synoptic and planetary eddies the eddy forcing reverses and damps the zonal wind anomalies at positive lags.

6.2.2 Forcings of tropopause variability

The analysis of the EP fluxes and the zonal-mean zonal wind has identified some common factors involved in the development and decay of the perturbations in tropopause height: anomalies in synoptic and planetary wave breaking at tropopause levels and anomalies in the intensity of the stratospheric polar jet. All these factors are associated with potential vorticity changes at upper levels, caused by either the quasigeostrophic potential vorticity flux associated with wave breaking or the intensification/weakening of the cyclonic circulation at the polar vortex (Ambaum and Hoskins, 2002), and may thus be regarded as forcings of tropopause variability. To study the impact of each of these forcings on tropopause height, three indices are constructed by regressing the relevant field on the tropopause PC and projecting this map again onto the field, so that a time series is obtained. The anomalous EP flux divergence between 600 and 100hPa is used for both synoptic and planetary waves, while the zonal-mean zonal wind between 100 and 10hPa and 50°–80°N is used as a measure of polar vortex intensity. Note that we regard changes in the polar vortex and changes in the divergence of the planetary EP flux as two different forcings even though changes in the polar vor

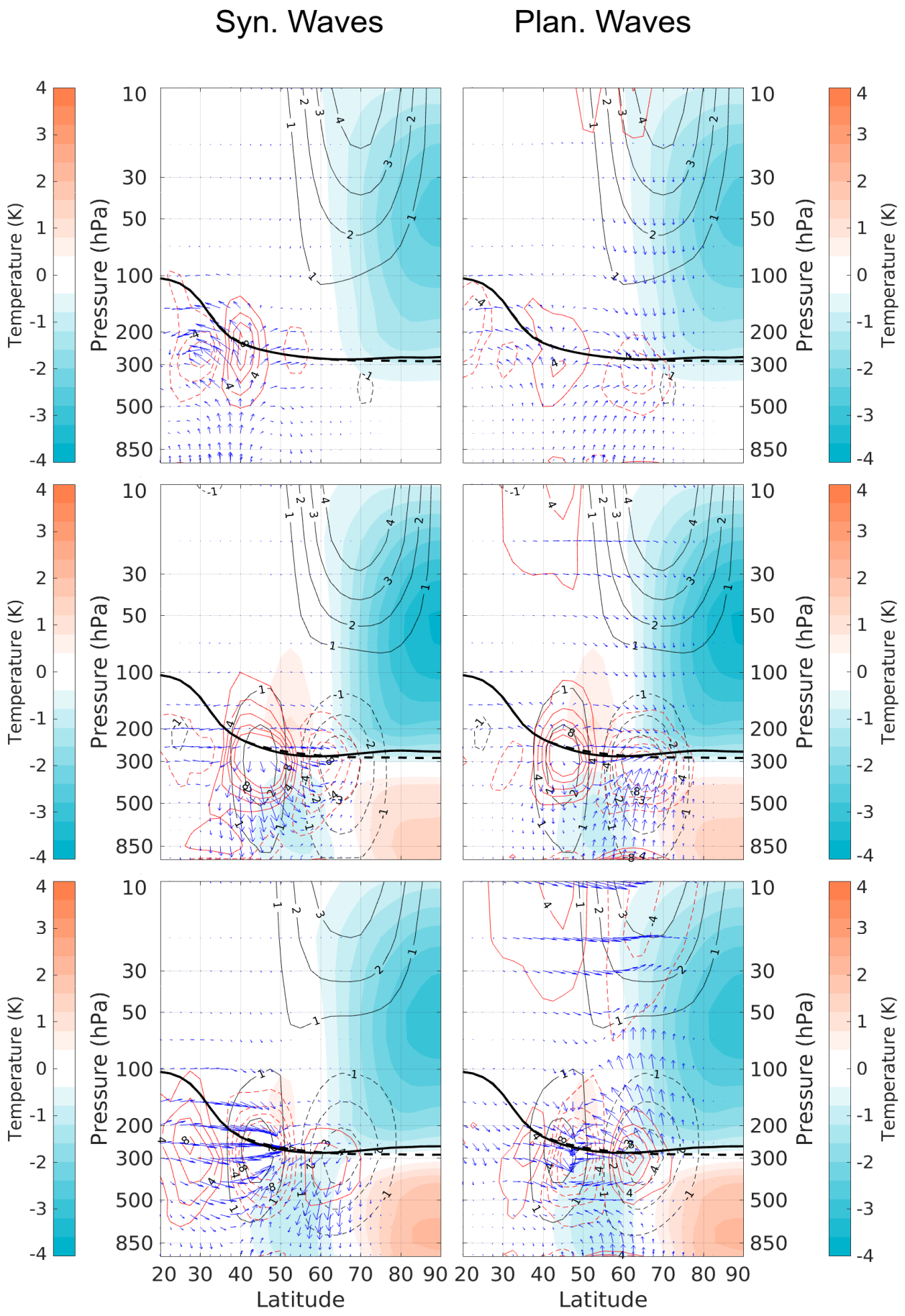

Fig. 6.7: As in Fig. 6.4, but for the second EOF, PC2.

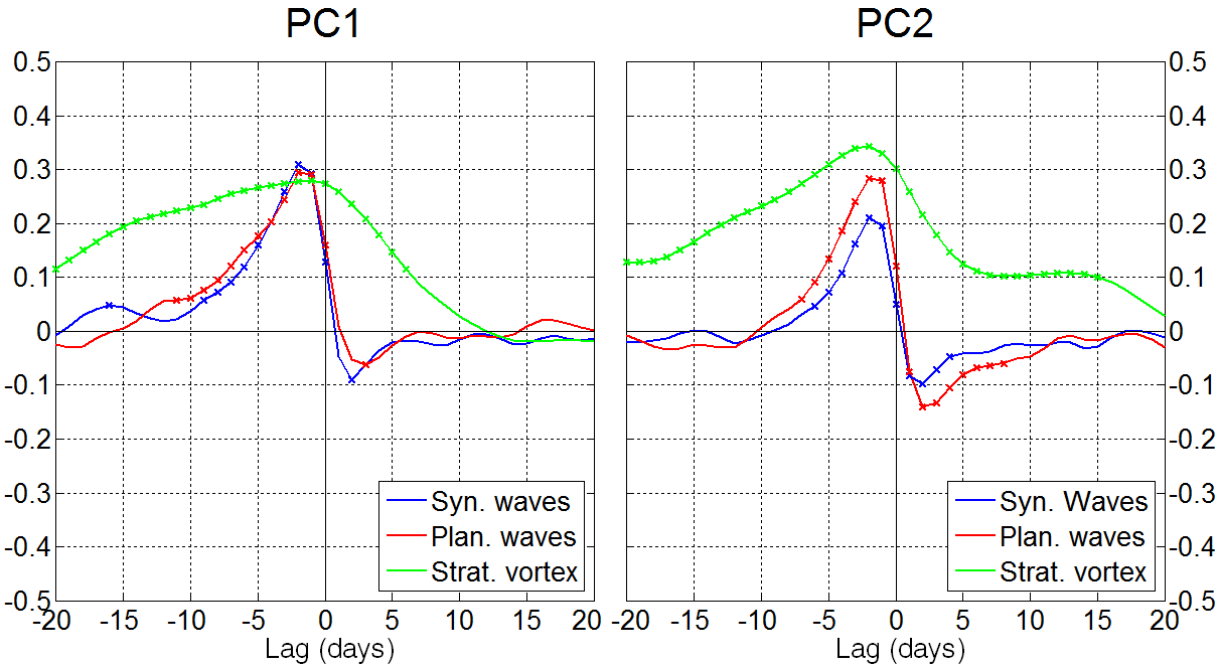

Fig. 6.8: Lagged correlations between the PCs and the indices described in the text representing tropopause forcings by the synoptic and planetary EP divergence and by the changes in the stratospheric polar vortex. Statistically significant correlations are emphasized using crosses.

tex affect planetary wave propagation, as described above. We do so because their correlation is low (not shown). Changes in stratospheric propagation only represent a small contribution to the full planetary EP flux divergence at tropopause levels, which is dominated by tropospheric dynamics.

It can be seen in Fig. 6.9 that both modes of tropopause variability are correlated in a similar way with the indices of EP flux divergence, with positive correlations for negative lags (especially from lag -7 to lag -1 days) and weak negative correlations for positive lags. As for the polar vortex index, this index is positively correlated with the PC on a longer time scale (over 20 and 40 days for the first and second modes, respectively; full range not shown), with the correlation peaking several days before lag 0. This suggests that the anomalous wave breaking that causes the variations in tropopause height develops in a pre-existing anomalous polar vortex while the perturbations (both in tropopause height and in the stratospheric jet) are damped by the waves for positive lags. Figure 6.10 shows the latitudinal structure of the tropopause anomalies associated with each of these indices, obtained using regression. We can see that while anomalies in the EP flux divergence are usually associated with tropopause anomalies in midlatitudes –with shorter time scales, see Fig. 6.4-, the polar vortex index mainly captures the rising or sinking of the polar and subpolar tropopause. The combination of both effects results in the observed EOF (the dashed line in Fig. 6.10 shows the sum of the

tropopause height changes associated to each of these forcings).

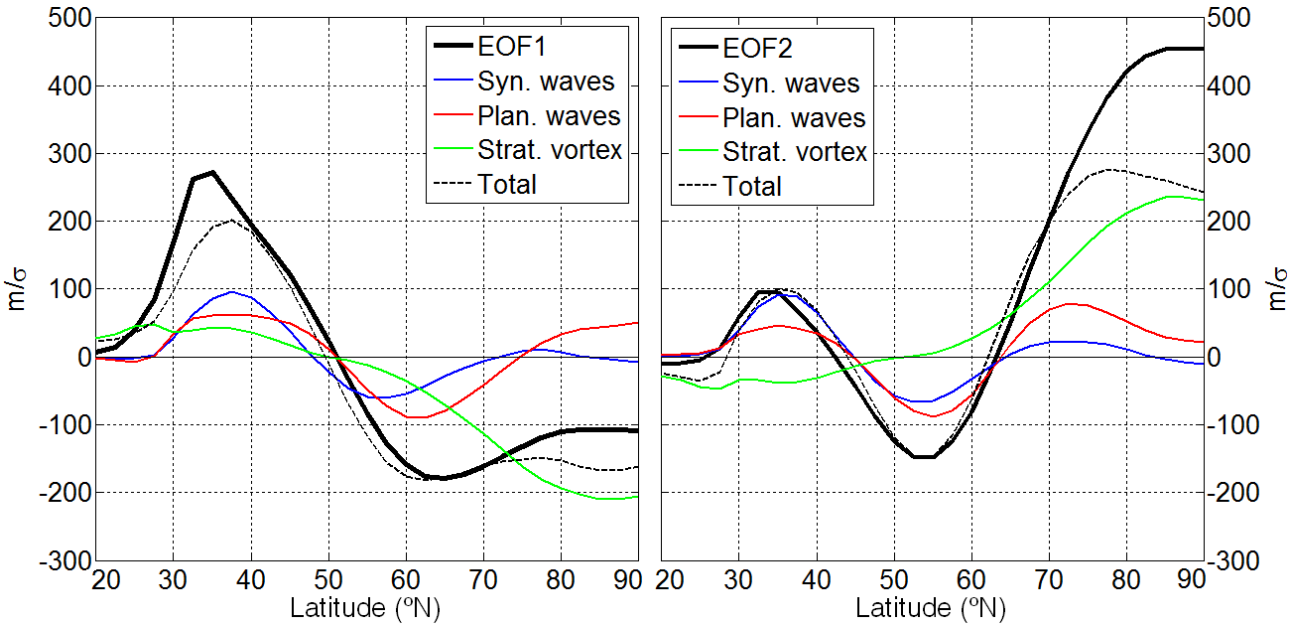

Fig. 6.9: Tropopause height changes associated with a standard deviation of each of the forcings in Fig. 6 (and their sum, dashed), compared with the full tropopause changes (per standard deviation of the PC).

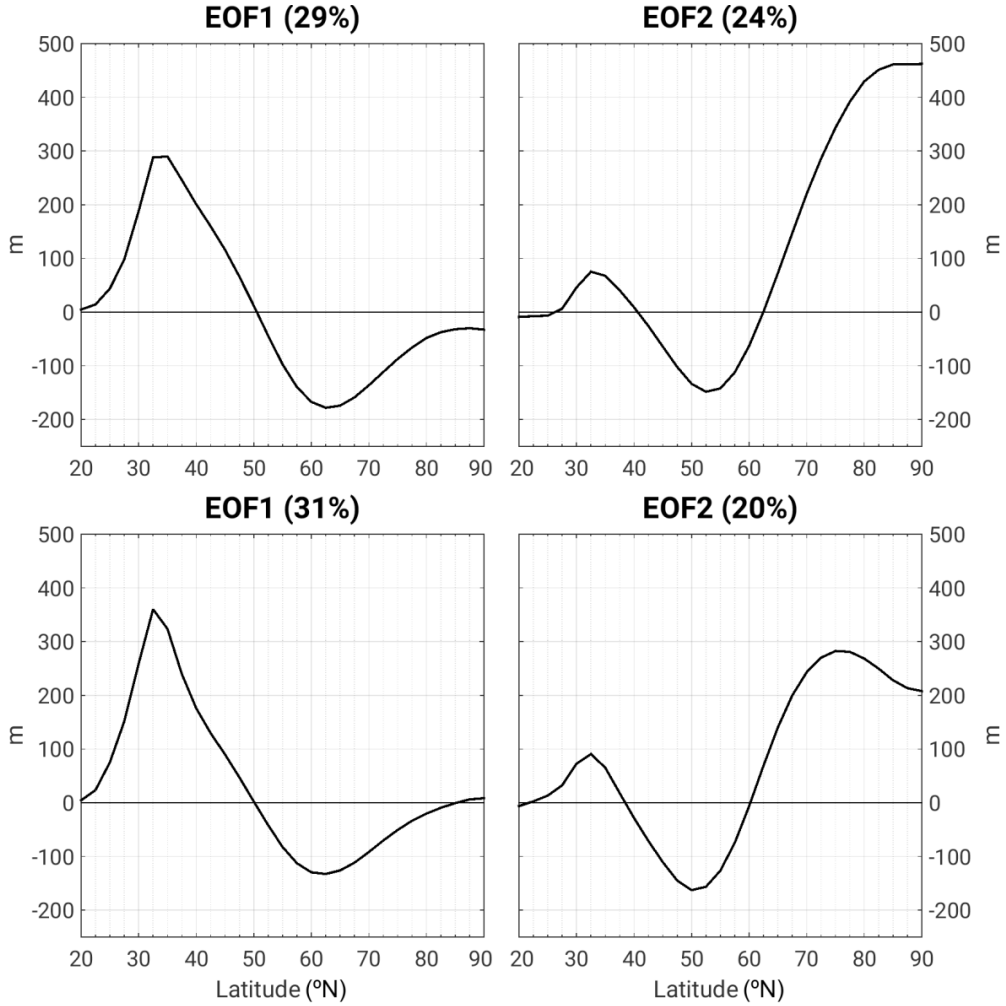

Fig. 6.10: First two EOFs of the extratropical zonal-mean tropopause height for (top) high- and (bottom) low-frequency intraseasonal variability. See text for details.

Given the different forcing time scales by the waves and the polar vortex, it is worth studying the modes of tropopause variability on short and long time scales. This was done filtering the data using a high-pass filter with cut-off 20^{-1} day^{-1} and a low-pass filter with cut-off 60^{-1} day^{-1}, respectively (the results are robust with other cut-off choices). It can be seen in Fig. 6.11 that the high-frequency variability of the tropopause is characterized by undulated patterns with maxima and minima of similar amplitude, while low-frequency variability consists mainly in a rising or sinking of the polar tropopause, with a secondary maximum at subtropical latitudes. This is what would be expected when the wave forcing dominates on short time scales, with the associated quasigeostrophic potential vorticity flux inducing a tropopause height dipole around the location of the anomalous wave breaking, and the polar vortex forcing dominates on long time scales, driving variations on the polar and subpolar tropopause on those time scales. The intraseasonal EOFs may be regarded as a combination of both forcings.

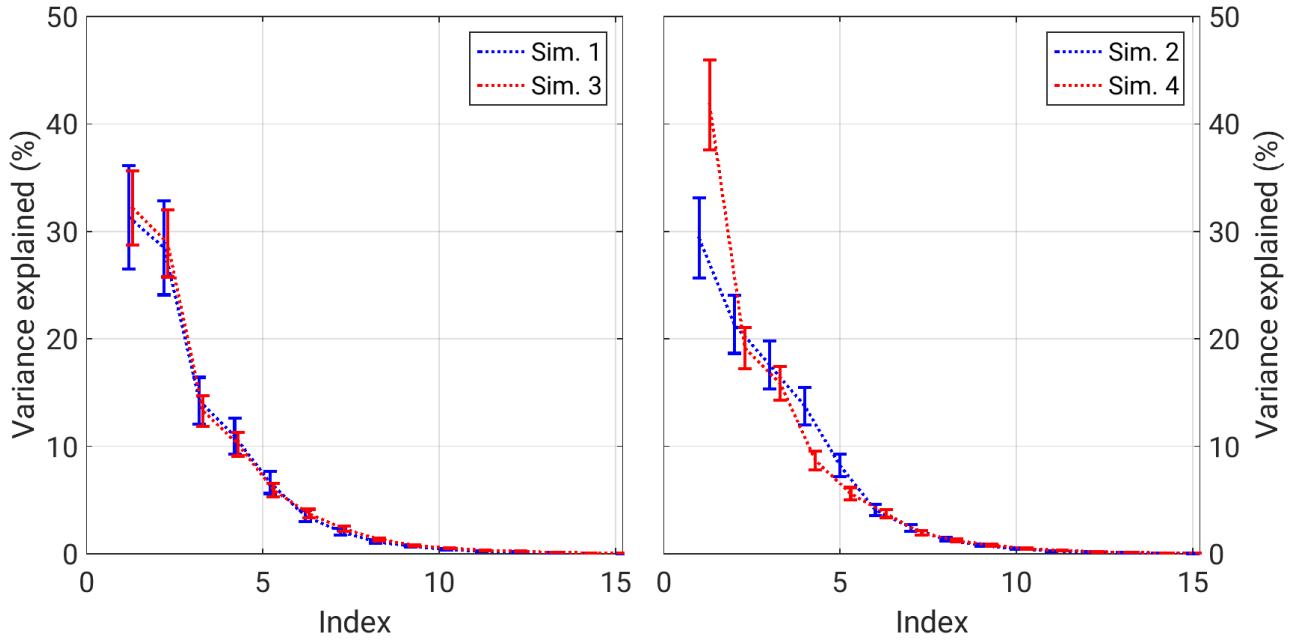

Fig. 6.11: Spectrum of eigenvalues of the covariance matrix in (left) flat simulations (1 and 3) and (right) simulations with orography (2 and 4). Blue lines shows results simulations with fixed equinoctial conditions in the troposphere (1 and 2) and red lines show results with a tropospheric seasonal cycle (and an increased meridional temperature gradient in winter, 3 and 4).

6.3 Modes of variability in the idealized model.

6.3.1 Description of the simulations.

Simulations with the idealized model can provide further understanding on the forcings of tropopause height variability. A set of simulations is performed aiming to test the influence of synoptic and planetary wave activity and the strength of the polar vortex. The

set of simulations is the same one used in the study of the tropopause seasonal cycle in Chapter 5 (see section 5.2.1); here, the focus is on the effect of increasing the meridional gradient (weak in simulations 1 and 3, strong in simulations 2 and 4) and of orography (flat surface in simulations 1 and 2, mountains in simulations 3 and 4). As a reminder, table 6.2 summarizes the setup of the simulations.

	Sim. 1	**Sim. 2**	**Sim. 3**	**Sim. 4**
ε_N	0	0	40	40
ε_S	0	0	10	10
$A1^{NH}$	45	45	45	45
Orography	No	Yes	No	Yes

Table 6.2: Parameters of each of the simulations used in the study of the intraseasonal variability (K). See chapter 2 for details.

The modes of variability are computed here for the complete year with the aim of increasing the statistical significance of the results. Results are unchanged when only the extended winter is used, although the amplitude of the variability is bigger, which means that the maximum intraseasonal variability also occurs during winter in the model.

6.3.2 Analysis of the modes of variability.

In this section, the influence of the magnitude of the meridional temperature gradient in the troposphere and the presence of mountains on the intraseasonal variability of the zonal-mean tropopause is studied. Fig. 6.12 shows the spectrum of eigenvalues of the covariance matrix in each simulation. As can be seen, the tails of the spectrum are greater when the meridional temperature gradient is weak (blue in the figure), while the variance tends to be more concentrated in the first PCs with strong baroclinicity. This is especially clear for the flat simulations (left in the figure), in which increasing the meridional temperature gradient produces a big separation between the first two PCs -now degenerate- and the rest. Orography, for its part, concentrates the variance in the first PC, as the others explain much less variance than in the flat simulations.

The spatial patterns associated with the first two modes of variability (Fig. 6.13) are very similar to those obtained in the reanalysis in the previous section, especially in simulation 1. EOFs of simulations 2 and 4 are somewhat different, although the first mode is remi

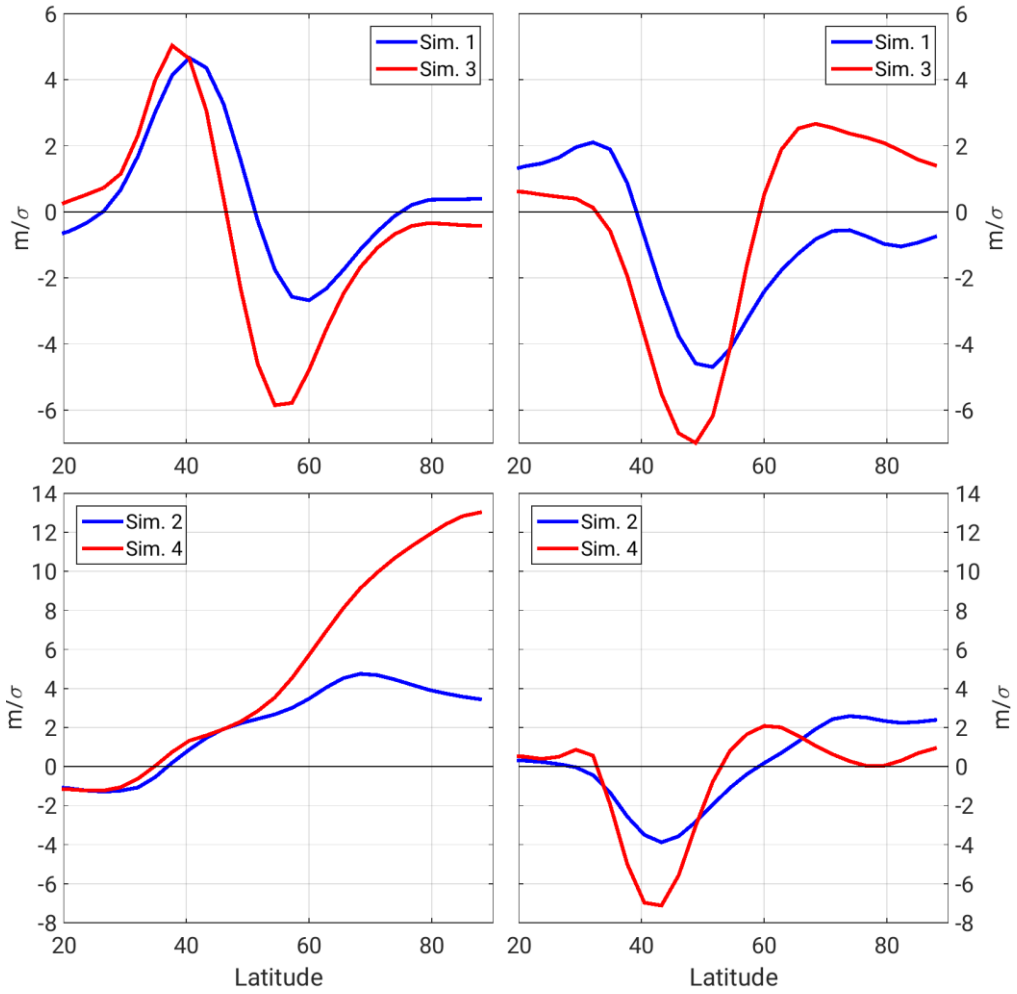

Fig. 6.12: First two EOFs of (a) flat simulations (1 and 3) and (b) simulations with orography (2 and 4). Colours are as in Fig. 11.

niscent of EOF2 in the reanalysis, with opposite anomalies in midlatitudes and in Polar Regions. An increase in the meridional surface temperature gradient (red in Fig. 6.13) seems to be associated with larger (smaller) amplitude of the anomalies in the midlatitudes (Polar Regions) in both the flat and orographic simulations, and with a southward displacement of the pattern in the simulations with orography.

Analysis of the Eliassen-Palm fluxes in lagged composites (Fig. 6.14) shows similar relations to the reanalysis for the synoptic fluxes in the flat simulations (1 and 3). Anomalous meridional propagation of synoptic waves produces a dipolar pattern of anomalous EP flux divergence at levels near the tropopause. The associated meridional eddy flux of potential vorticity induces dipolar anomalies in tropopause pressure, centred on the maximum zonal wind perturbation, associated with the anomalous eddy momentum flux by wave breaking. Besides the anomalous eddy activity, in the simulations with mountains there are anomalies in the stratospheric jet, although these are weak in simulation 2. In flat simulations there are

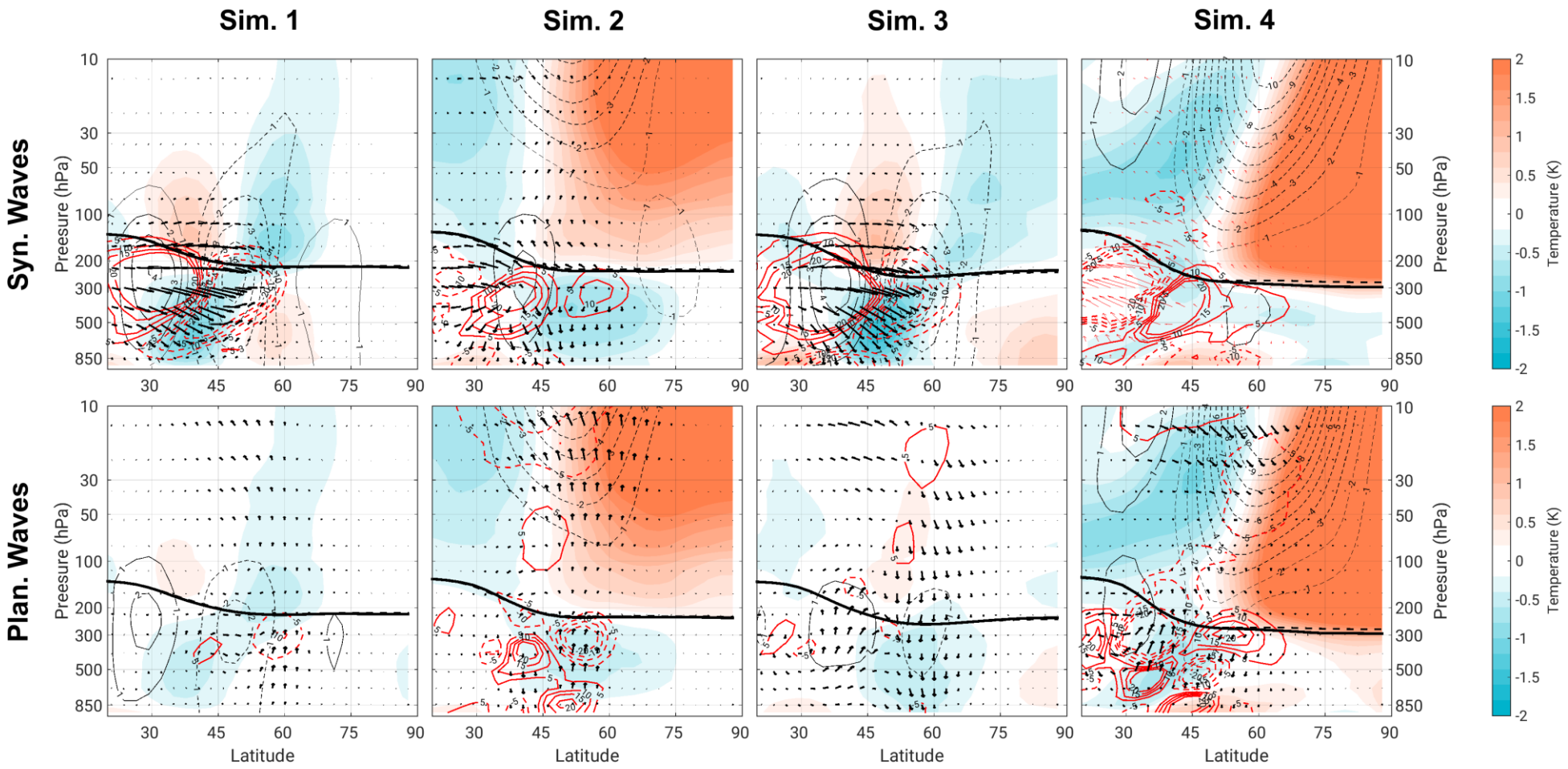

Fig. 6.13: Lagged composites of PC1 in (left) simulation 1, (left center) simulation 2, (right center) simulation 3 and (right) simulation 4 on anomalous temperature (K; coloured areas), zonal-mean zonal wind (m s-1; black contours), divergence of EP flux (x1014 m2 s-2; red contours) and EP flux (red arrows) for (top) synoptic and (bottom) planetary waves. Positive anomalies are indicated in solid contours and negative anomalies in dashed contours. The thick solid black line represents the composite zonal-mean tropopause pressure, while the thick dashed black line represents the climatological tropopause. Lag is -1day for synoptic waves and -3days for planetary waves.

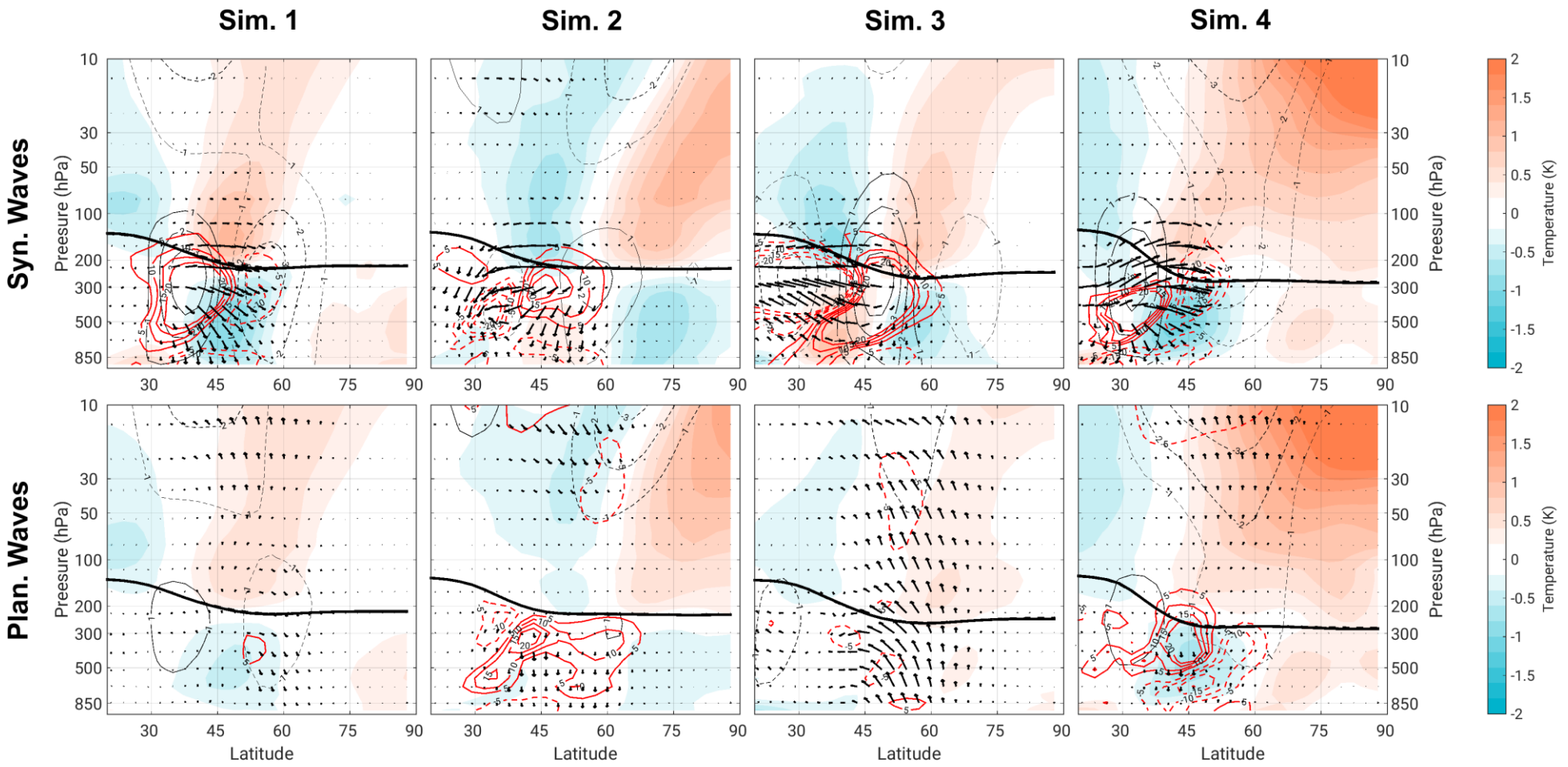

Fig. 6.14: As in Fig. 6.13, but for the second mode, PC2.

no anomalies in the planetary wave breaking or these are very weak; while they appear in simulation 2, they seem to be limited to changes in the planetary heat flux and their impact on tropopause is unclear.

For simulations 2 and 4, the second mode (Fig. 6.15) has similar characteristics to the first mode in flat simulations 1 and 2, as tropopause anomalies are associated with a dipole in the tropospheric jet caused by anomalous synoptic wave breaking on the northward flank of the subtropical jet. In contrast, EOF1 for these simulations has particular characteristics that make it different from all other modes of variability in the simulations and in the reanalyses. An intense anomaly in the stratospheric jet develops simultaneously to the tropopause anomaly, affecting almost the whole hemisphere. Tropopause variability for this mode appears to be associated with the propagation and breaking of planetary waves in the stratosphere and with the deceleration of the stratospheric jet, which is strongly reminiscent of sudden warmings of the polar vortex. Looking at the PC time series (Fig. 6.16), strong maxima are found at the end of the winter in 3 out of the 5 years included in the simulation. Following Jucker *et al.* (2014), we define Sudden Stratospheric Warmings (SSW) based on the reversal of the zonal wind at 60°N at the level of 10hPa. As seen in Fig. 6.17, all peaks in the PC series exceeding 2 standard deviations are SSWs according to this criterion. In many cases, the

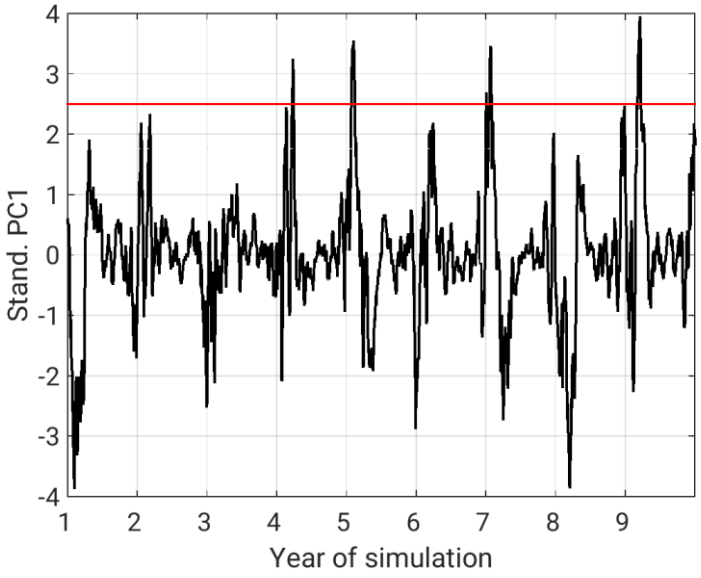

Fig. 6.15: Expansion coefficients (PC1) of the first mode of variability in simulation 4. Red line denotes the cases higher than 2.5 times the standard deviation of the series.

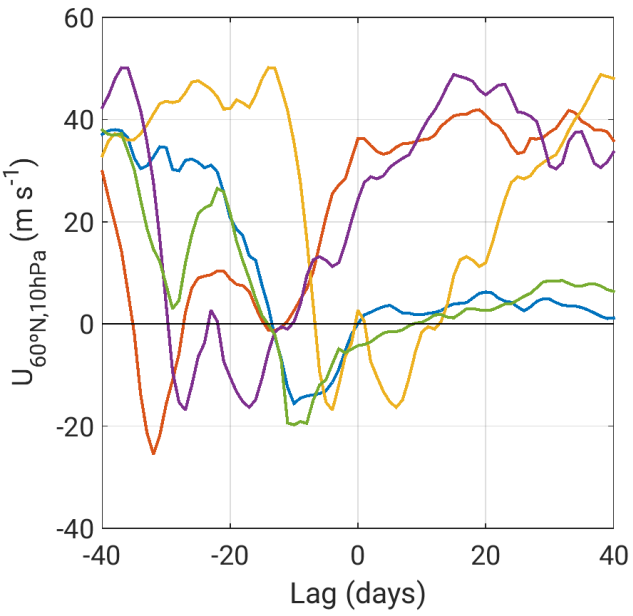

Fig. 6.16: Zonal-mean zonal wind at 60°N in the 10hPa level on days preceding (negative lags) and following the maximum PC1 (positive lags), for each of the cases with PC 2.5 standard deviation.

vortex recovers after a few days, except for the first event observed, in which the zonal wind remains eastward after the SSW. This case, which occurs later in the year than the others, is consistent with a stratospheric final warming and occurs following a long period of anomalously high tropopause (negative coefficient in the PC). All but 2 SSWs occur before the tropopause reaches its minimum height, generally by about 10 days. This suggests a downward propagation of the anomalies from higher levels to the tropopause, which is confirmed by Fig. 6.18. Anomalies take about 10 days to descend from 1hPa to the tropopause level. The tropopause is lower than normal for several days before lag 0, with the minimum occurring when a temperature anomaly of the opposite sign develops in the troposphere. It will be shown in Section 6.6 that this anomaly is stronger in observations (see Fig. 6.25).

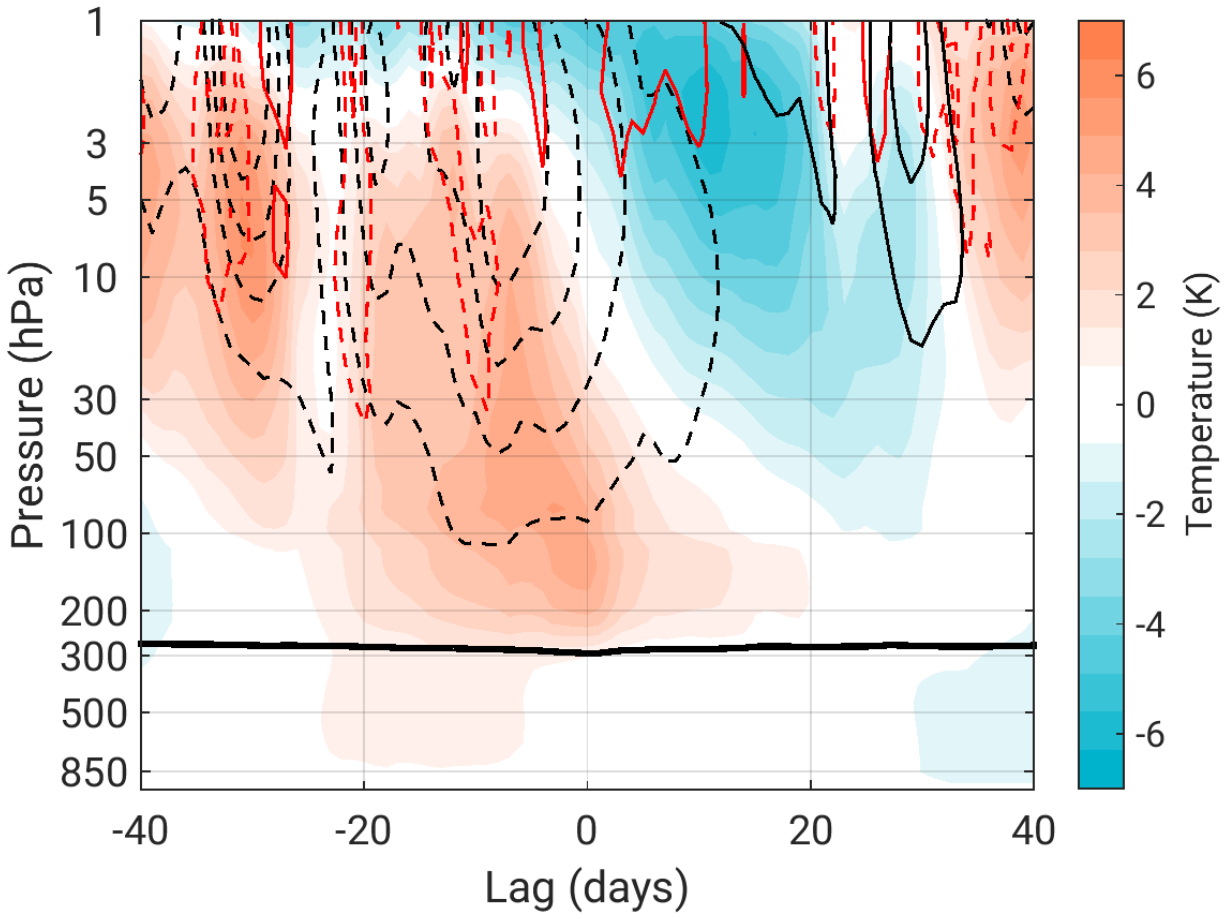

Fig. 6.17: Lagged composite of the zonal-mean zonal wind anomalies at 60ºN (colours) and temperature anomalies in the polar cap (60º-90ºN) for the PC1 of simulation 4. Black thick solid line stands for the composite zonal-mean tropopause pressure.

As was shown in Fig. 6.13, EOF1 for simulations 2 and 4 were very similar. However, the dynamical situation seems different between these two modes, although a similar, but weaker, pattern of temperature anomalies is still apparent near the pole. The time series for the first mode in simulation 2 (not shown) displays higher-frequency variability and, alt-

hough warmings of the vortex do occur, they do not seem as persistent as those in simulation 4, thus the anomalies are also weaker. This suggests that the enhanced baroclinicity and

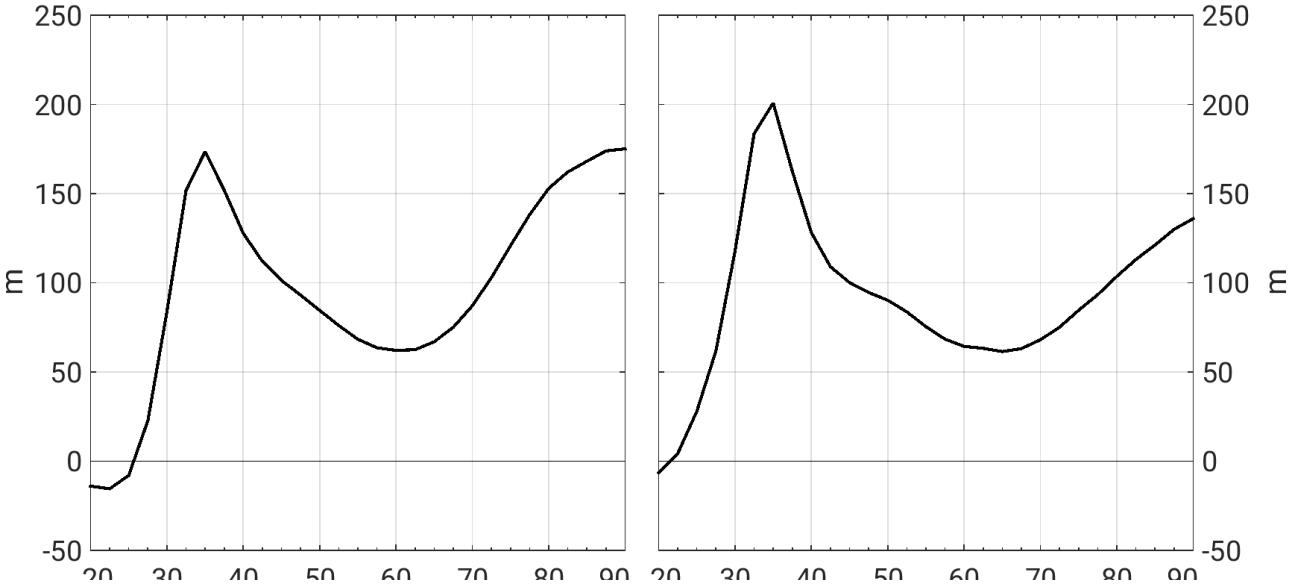

Fig. 6.18: Regression maps of anomalous zonal-mean tropopause height (m) on the extrattropical-mean index for (left) the NCEP/NCAR Reanalysis-1 and for (right) ERA-Interim datasets, during the extended NH winter.

associated wave generation plays a role for the SSW in simulation 4, at least for increasing the persistence of the anomalies in the polar vortex and/or their downward propagation.

6.4 Intraseasonal variability of the extratropical-mean tropopause.

As shown in the previous sections, the variability of the zonal-mean extratropical tropopause in the intra-annual scales is dominated by wavelike patterns with opposite-sign anomalies over different latitudinal bands—that is, with tropopause deformations rather than changes in the extratropical-mean tropopause height. Aiming to find a connection between baroclinic equilibration and tropopause height based on the ideas discussed in the introduction to this thesis, we define an index for the extratropical-mean tropopause height:

$$\left\langle \bar{Z}_T \right\rangle = \frac{\int_{32.5°N}^{90°N} \bar{Z}_T \cos\phi \, d\phi}{\int_{32.5°\mathrm{N}}^{90°N} \cos\phi \, d\phi}$$

where ϕ is latitude and $\bar{Z}_T$ is the anomalous zonal-mean tropopause height, time-filtered so as eliminate interannual variability. As can be seen in Fig. 6.19, the variability captured by this index is not a uniform elevation or rising of the extratropical tropopause, but presents two maxima in the subtropics and polar latitudes, with relatively little variability in the midlatitudes. The variations associated with one standard deviation of this index are

nevertheless of smaller amplitude than those associated with the EOFs (compare Figs. 6.19 and 6.1), and the standard deviation of this index is only a 20% of the leading EOF variance. Hence, changes in the extratropical-mean tropopause height explain a very small fraction of the full tropopause variability. Moreover, if a field of tropopause deformations is defined by subtracting the extratropical-mean tropopause to the full tropopause field, its modes of variability are nearly indistinguishable from those obtained previously (correlation between PCs higher than 0.98).

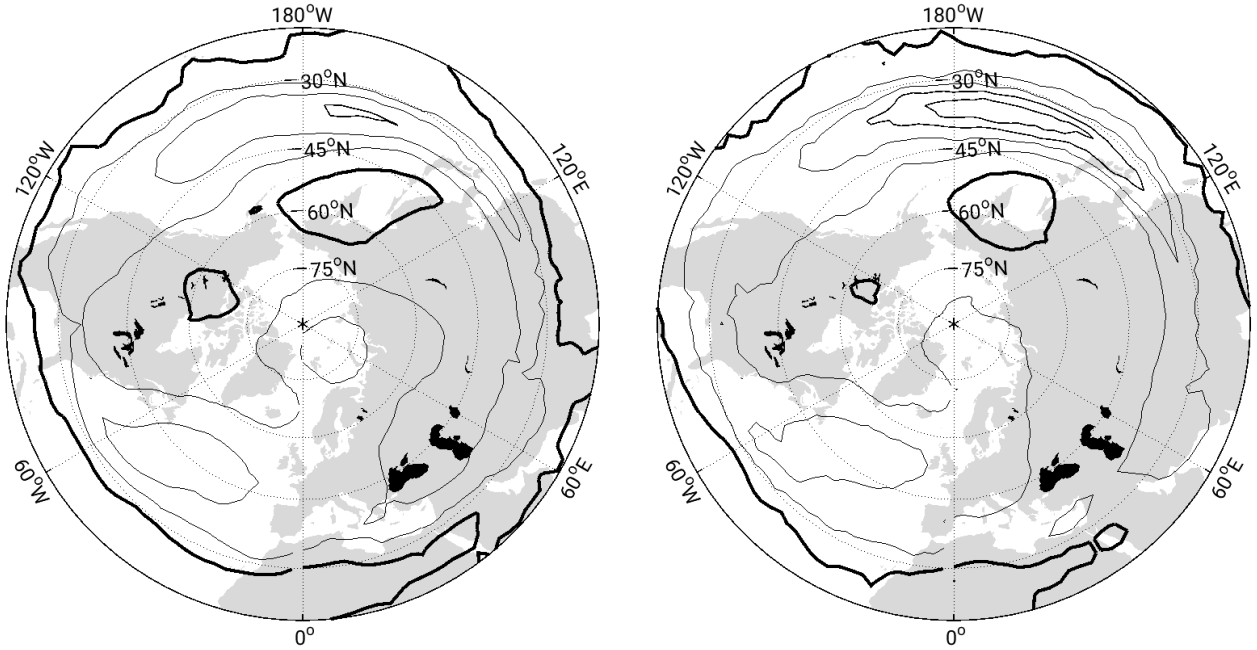

Fig. 6.19: Regression maps of anomalous tropopause height (m) on the extratropical-mean index for (left) NCEP/NCAR Reanalysis-1 and (right) ERA-Interim datasets, during the extended NH winter.

As found for the EOFs, projection of the extratropical-mean tropopause index on the complete field (Fig. 6.20) produces a pattern with great zonal symmetry, with centres of action to the south of the oceanic stormtracks, although zonal asymmetries are more pronounced in the polar and subpolar areas. Snapshots for individual cases show nonetheless wavy patterns, suggesting that the dynamics is very similar to that of the EOFs.

Eliassen-Palm-(EP)-flux lagged composites (Fig. 6.21) show indeed similar dynamical forcings to those identified in the previous sections for the leading modes of variability: anomalies in the propagation and breaking of waves and an anomalous stratospheric polar vortex, albeit with smaller anomalies in this case. In the presence of a slightly stronger polar vortex that slightly raises the polar tropopause, synoptic-wave anomalous vertical and

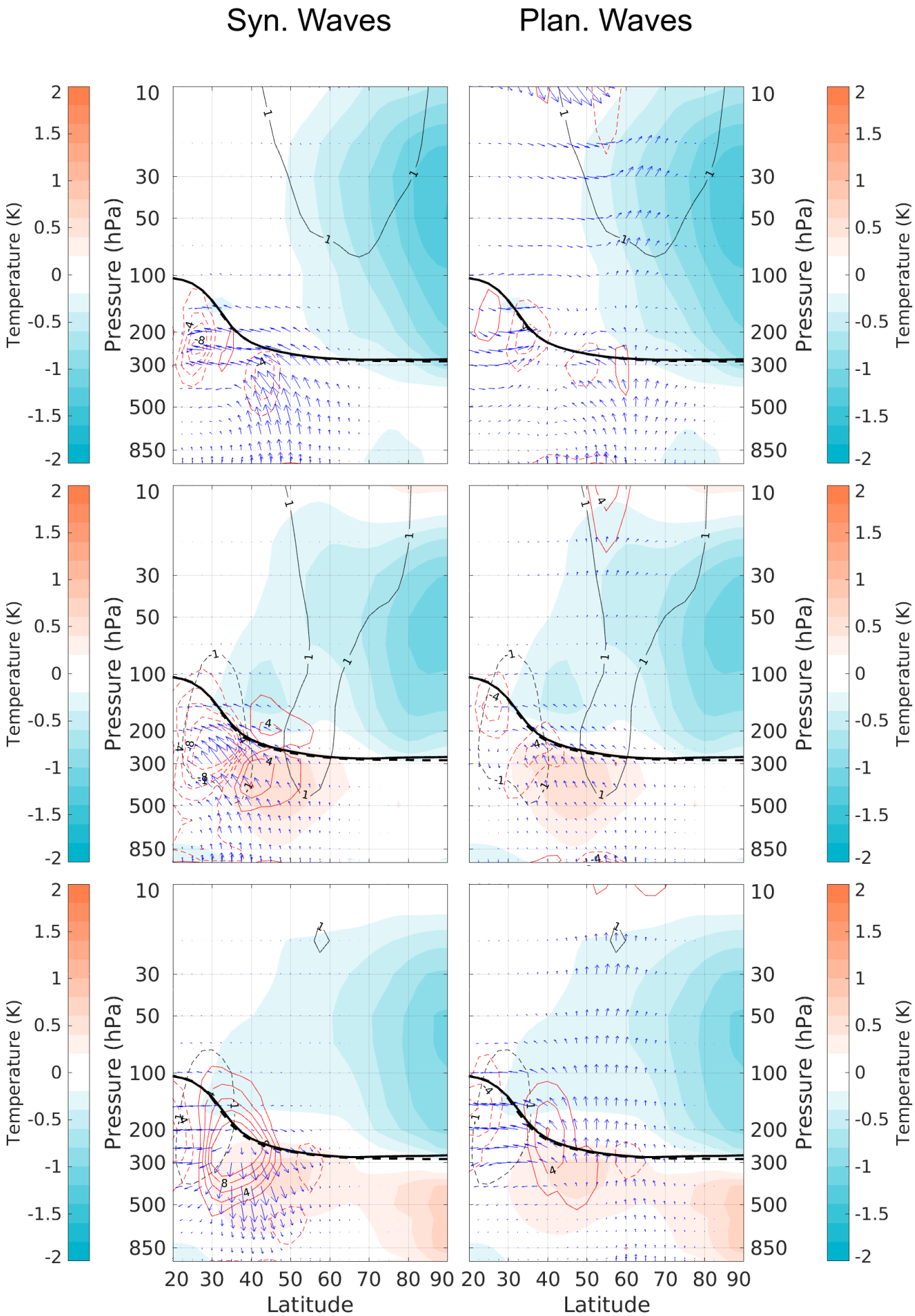

Fig. 6.20: As in Fig. 6.4, but for the extratropical-mean tropopause index.

southward propagation develops a few days before the maximum in the extratropical-mean index. This anomalous propagation is accompanied by anomalous wave breaking on the northward flank of the subtropical jet, so that a dipolar anomaly appears centred around 40°N, very similar to the situation for PC1 but without the concur of the planetary waves -note that the polar vortex is stronger than usual now, contrary to the what was found for PC1. For positive lags, the anomalies in synoptic-wave propagation and breaking reverse, damping the tropopause height anomalies in the subtropics, while the anomalies at polar latitudes are more persistent. Hence, the same conclusions on the role of meridional eddy potential vorticity fluxes at tropopause levels and modulations in polar vortex strength for tropopause height variability can be inferred from this index, with no hint of a baroclinic adjustment role. Instead, local changes in wave activity coupled with variations in the stratospheric polar vortex -whether caused by the eddies or not- appear to be responsible for variations in tropopause height over the extratropical region.

6.5 EOFs of the SH tropopause

To investigate the mechanisms responsible for the variability of the Southern Hemisphere zonal-mean tropopause, PC analysis was performed over the extratropical region from 32.5° to 90°S. As for the NH, the first two modes are well separated, but the first mode

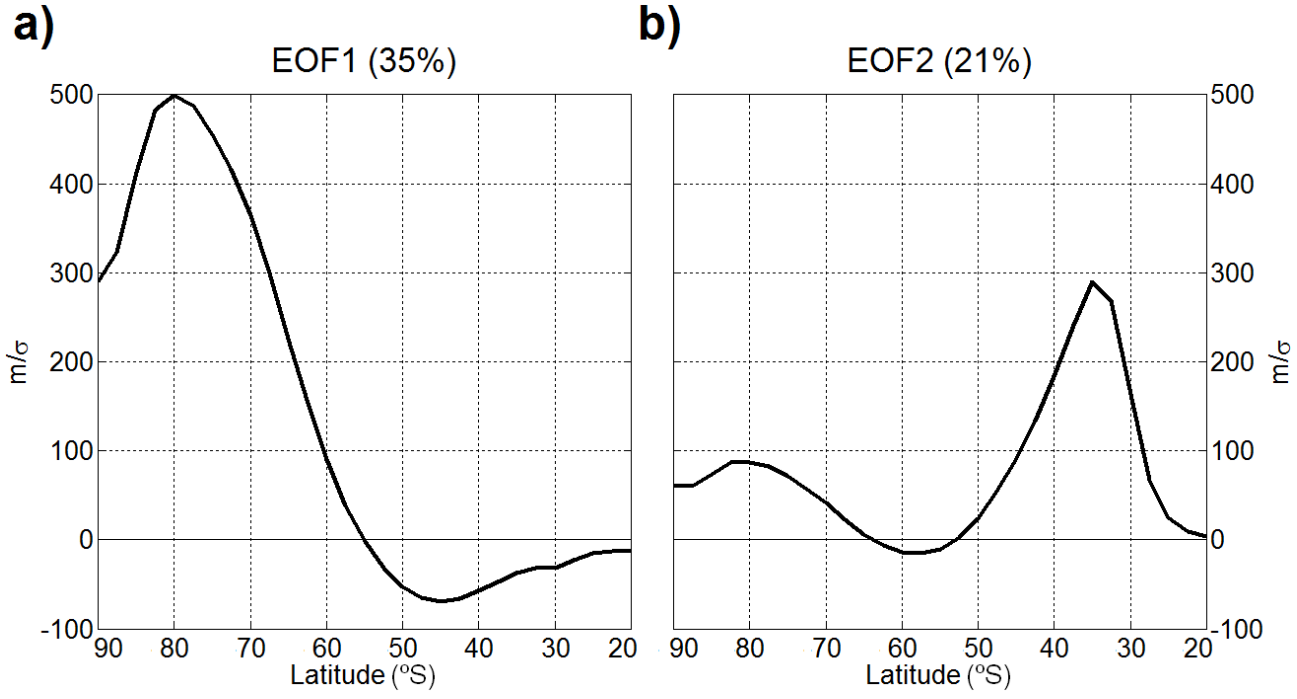

Fig. 6.21: Regression maps of anomalous zonal-mean tropopause height (m) on (a) PC1 and (b) PC2, for the SH.

now explains more variance than before (35%, compared to 21% for the second one). The first mode again has a dipole pattern (Fig. 6.22a), with a node at 55°S and extrema at 45° and 80°S; in this case, the southernmost maximum is farther south than that of the SH zonal index (Lorenz and Hartmann, 2001). The second mode (Fig. 6.22b) consists of two maxima, located at 35° and 80°S. The two modes have similar latitudinal structure except that tropopause anomalies in the mid- and high latitudes are negatively correlated for the first mode and positively correlated for the second mode. Lag-correlation analysis between the associated principal component time series suggests that the two modes of variability may not be independent, as there is a positive correlation when PC1 leads by 10–20 days (Fig. 6.23). The dynamical evolution of these modes is described in Fig. 6.24. As before, tropopause anomalies in the mid-latitudes can be linked to changes in the Eliassen–Palm divergence at tropopause levels resulting from changes in wave propagation (note that we no longer distinguish between synoptic and planetary waves, as the former dominate). For the first mode we observe a dipolar EP pattern in the midlatitude upper troposphere, with Eliassen–Palm divergence (convergence) on the equatorward (poleward) side of the jet. This pattern is initially driven by changes in meridional propagation at upper levels and subsequently reinforced by anomalous vertical propagation. The second mode is also associated with a dipolar EP-divergence pattern at upper levels (with the opposite polarity, as defined here), but the pattern is shifted equatorward and the wave driving is different from before. The tropopause anomaly is now initiated by enhanced baroclinic generation and Eliassen–Palm convergence in the subtropics. Finally, large tropopause anomalies are also observed over the polar region for both modes. Although the zonal wind anomalies are weak, significant changes in the vortex potential vorticity are found for these events (not shown), similar to the Northern Hemisphere.

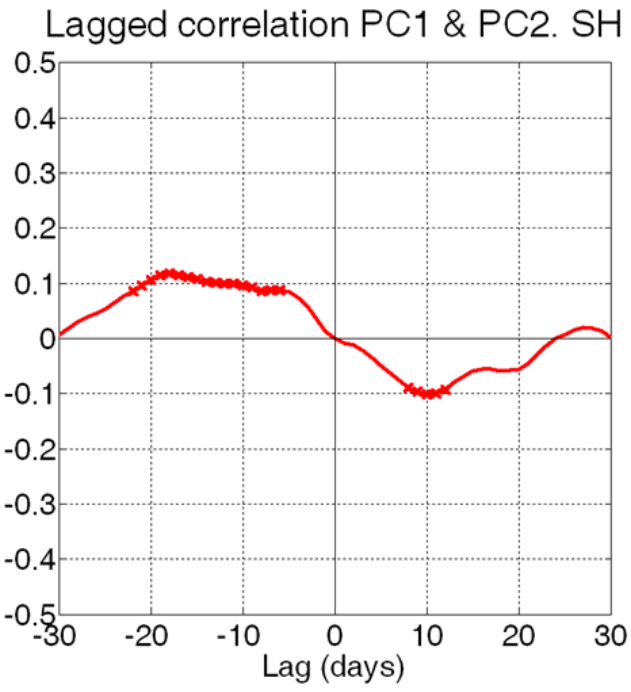

Fig. 6.22: Lagged correlation between PC1 and PC2 for the SH.PC1 leads (lags) PC2 for negative (positive) lags. Statistically significant correlations are emphasized using crosses.

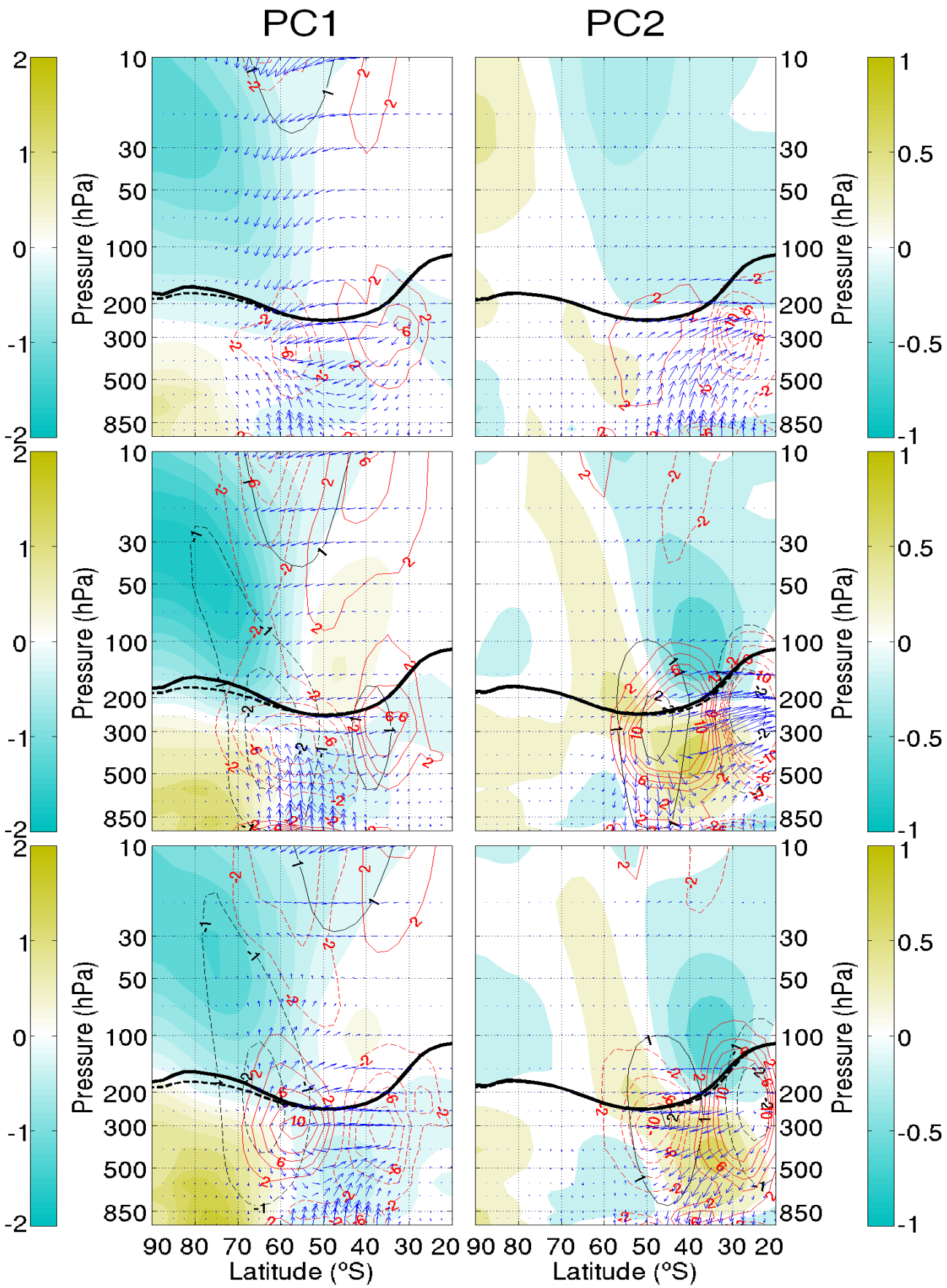

Fig. 6.23: Lagged composite of (left) PC1 and (right) PC2 on anomalous EP flux (arrows) and anomalous EP flux divergence ($3 \cdot 10^{14}$ m^2 s^{-2}; red contours) by all waves, anomalous zonal- mean zonal wind (m s^{-1}; black contours), and anomalous zonal-mean temperature (colors) at lags (top) -4, (middle) -1, and (bottom) +1 days. The climatological (extended winter) and composite tropopause heights are shown with thick dashed and solid lines, respectively. For clarity of representation, the vertical component of the EP vectors has been scaled as a function of pressure using a p^{-3} factor.

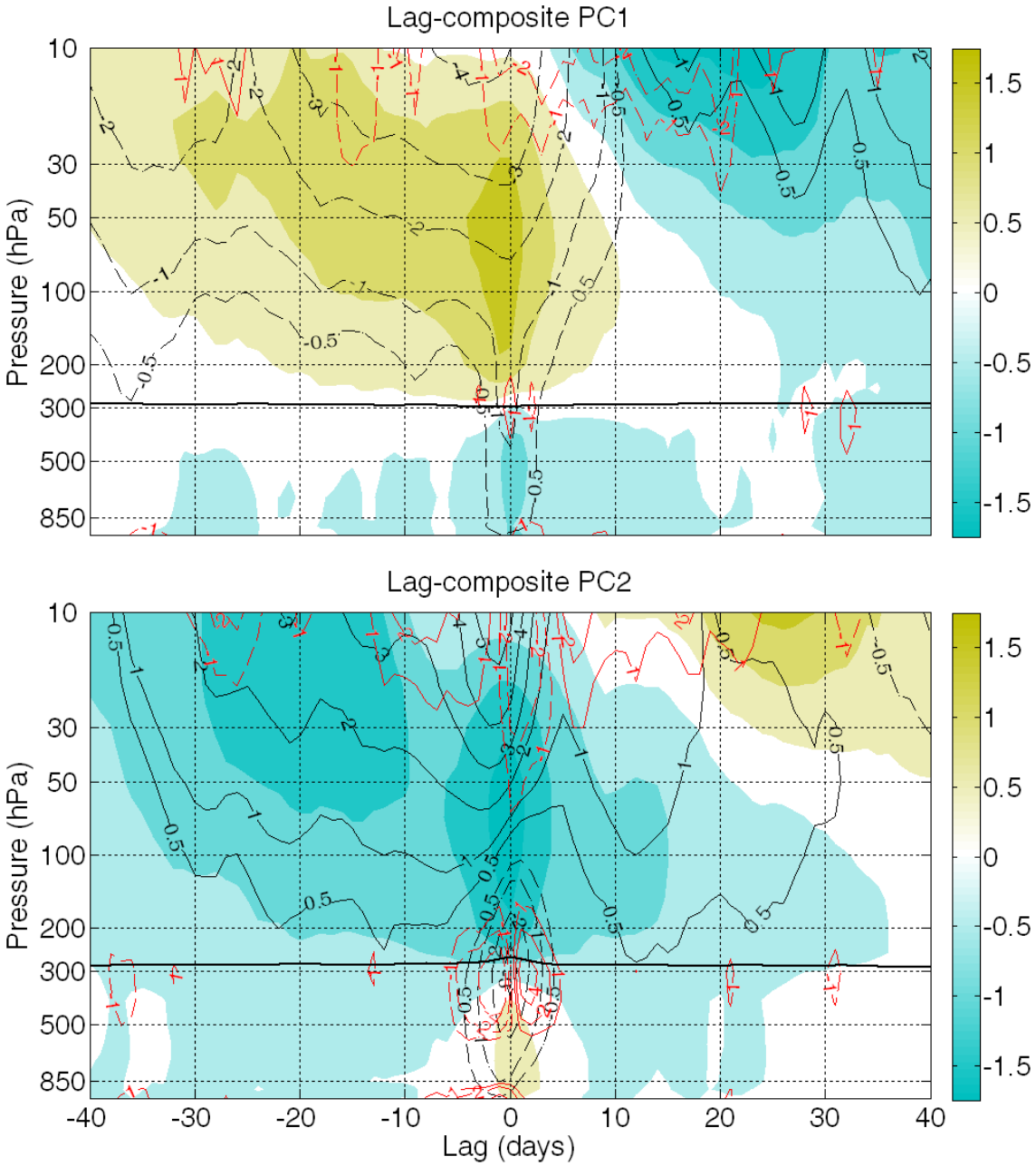

Fig. 6.24: Lagged composite of (top) PC1 and (bottom) PC2 on anomalous zonal-mean temperature (K; colours), anomalous zonal-mean zonal wind (m s^{-1}; black contours), and anomalous planetary EP flux divergence ($3 \cdot 10^{14}$ m^2 s^{-2}; red contours) integrated from 60º to 90ºN. Negative contours are indicated as dashes. The thick black solid line represents the lagged composite on the zonal-mean tropopause pressure averaged from 65º to 90ºN.

6.6 Discussion

This chapter has analysed the structure and dynamics of the leading modes of variability for the Northern Hemisphere extratropical zonal-mean tropopause height in intra-annual time scales. The leading mode has a dipolar structure with a node in the midlatitudes and is strongly correlated with the zonal index. The second mode has a tripolar structure and large amplitude over the polar and subpolar regions. The structure of both modes is robust against changes in the latitudinal and temporal domains of analysis.

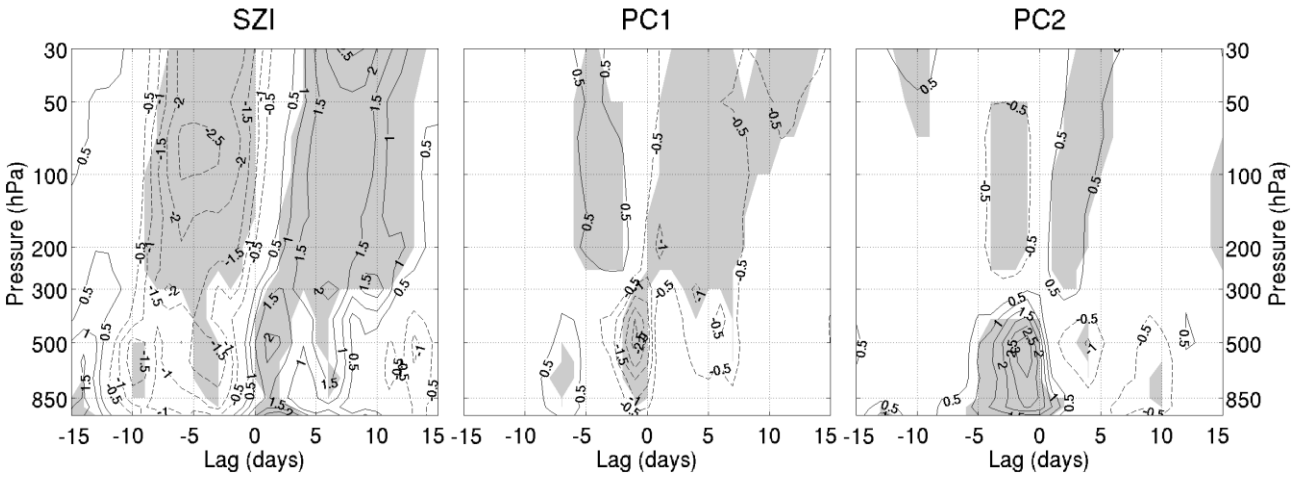

Fig. 6.25: Lagged composite of the vertical component of Eliassen–Palmflux integrated between 50° and 80°N ($3 \cdot 10^{14}$ m^2 s^{-2} Pa) on (left) stratospheric zonal index [SZI; see Limpasuvan *et al.* (2004) for details], (center) leading mode, and (right) second mode of the zonal-mean extratropical tropopause height variability.

Previous observational studies of the intraseasonal tropopause variability (e.g., Dell'Aquila *et al.*, 2006; Son *et al.*, 2007) were motivated by the general circulation problem and by theoretical arguments relating baroclinic equilibration and tropopause rise (Held, 1982; Lindzen, 1993; Schneider, 2004). In idealized models, these ideas have been found to have some relevance for tropopause height adjustment in the initial value problem (Egger, 1995) and for the mean tropopause in forced-dissipative atmospheres (Zurita-Gotor and Vallis, 2011, 2013). In contrast, there is increasing evidence that baroclinic eddy equilibration is quantitatively of little importance for the extratropical internal tropopause variability on intraseasonal time scales. This was already noted by Son *et al.* (2007) who found that (i) strong baroclinic life cycles have a small impact on tropopause height and (ii) intense tropopause height events have a large stratospheric signal. Our analysis is consistent with the findings of Son *et al.* (2007) and provides additional insight on the dynamical forcing of the tropopause variations. In this regard, the first conclusion of our work is that the dominant modes of zonal-mean tropopause variability are characterized by wavelike patterns with opposite-sign anomalies over different latitudinal bands -that is, with tropopause deformations rather than changes in the extratropical-mean tropopause height. Additionally, we found that changes in the extratropical-mean tropopause are typically associated with large local changes in the subtropical and/or polar tropopause, with weak midlatitude changes.

Based on the thermal definition, it is natural to interpret the tropopause deformations from a heat budget perspective. In particular, the anomalous vertical propagation of synoptic and planetary waves in the upper- troposphere/lower-stratosphere region will produce an anomalous dipole in potential temperature associated with the horizontal eddy heat flux convergence (or, equivalently, the residual vertical velocity). The mechanism is well described by Egger (1995) using a baroclinic channel and was also observed by Dell'Aquila *et al.* (2006) in actual data. Because planetary waves can propagate more easily at upper levels and/or into the stratosphere (Charney and Drazin, 1961), they may have a larger impact on tropopause height than synoptic waves as found by Son *et al.* (2007).

Alternatively, one could use a potential vorticity framework to understand the tropopause deformations (Hoskins *et al.*, 1985; Zängl and Wirth, 2002). Despite the well-known limitations of quasigeostrophic theory for dealing with tropopause dynamics [see, e.g., Song and Nakamura (2000)], a clear link was found in this work between the structure of the tropopause changes and the sign of the anomalous quasigeostrophic potential vorticity flux. The modes of tropopause variability obtained here are associated with the enhancement/weakening of wave breaking at tropopause levels, which produces a southward/northward eddy flux of potential vorticity. A negative eddy PV flux is associated with a positive (negative) PV tendency to the south (north) of the enhanced wave breaking and thus with a tropopause drop (rise), while the opposite is true for a positive eddy PV flux/ reduced wave breaking. The quasigeostrophic diagnostics provide a simple conceptual framework for interpreting the changes in wave breaking and associated tropopause deformations in terms of changes in eddy propagation, exploiting the Eliassen–Palm theorem (Edmon *et al.*, 1980). We found that synoptic and planetary waves produce comparable contributions to the Eliassen–Palm divergence for the leading two modes. Additionally, we found that the eddy momentum flux convergence is the dominant term in the anomalous Eliassen–Palm divergence, particularly for the first EOF, which is strongly connected with zonal index variability (Lorenz and Hartmann, 2003).

Both modes of tropopause variability also exhibit a large polar signature. Changes in the polar and subpolar tropopause are associated with changes in the strength of the stratospheric jet that are consistent with the mechanism described by Ambaum and Hoskins (2002). Since isentropic surfaces bend toward cyclonic potential vorticity anomalies (Hoskins

et al. 1985), a strong (weak) polar vortex is associated with a rise (drop) in the polar tropopause. The characteristic time scale of polar vortex changes is much longer than that associated with synoptic and planetary wave breaking at tropopause levels, so that persistent stratospheric wind anomalies can be observed well in advance of the EP-divergence anomalies. We can cleanly separate both influences on tropopause height filtering the data.

Although we have not analysed in this study the source of the pre-existing polar vortex anomalies, these resemble the patterns associated with the polar-jet oscillation (PJO; Kodera *et al*., 2000) and the life cycle of sudden stratospheric warmings (SSW; Limpasuvan *et al*., 2004). In this regard, significant correlations are found for both PC1 and PC2 with the leading mode of variability of the zonal-mean zonal wind at 50hPa (stratospheric zonal index), peaking at lags from -7 to -4 days (0.29 for PC1, -0.34 for PC2). Figure 6.25 shows the downward propagation of stratospheric temperature and wind anomalies as well as the change in phase characteristic of the polar jet vacillations [cf. Fig. 4 of Limpasuvan *et al*. (2004)] during the development and decay of the tropopause modes. In contrast, the tropospheric evolution of the tropopause modes is very different from that of SSWs. Instead of the downward propagation of the temperature anomalies down to the troposphere observed during the mature stages of SSWs (Limpasuvan *et al*., 2004), temperature anomalies reverse sign across the tropopause for our modes. This difference highlights the role of the upper-level EP flux divergence (i.e., vertical changes in meridional eddy heat flux/vertical EP flux) for driving the tropopause anomalies, in contrast with the more vertically uniform EP flux anomalies observed during SSWs (Fig. 6.26). In a similar manner, the convergence of the meridional eddy momentum flux associated with EP flux divergence at tropopause levels causes tropospheric zonal wind perturbations that are not observed during SSWs.

Simulations with the idealized model confirm the picture explained above, as the first mode of variability in the flat simulations is a dipole at midlatitudes while the inclusion of orography increases the amplitude of the variations in the polar tropopause. Note that increasing the baroclinicity in the flat simulations has the effect of increasing the amplitude of the midlatitudinal variations relative to the polar variations –the polar signal is lost in simulation 3 with respect to simulation 1 (see Fig. 6.13), due to the greater wave activity in the former. When mountains are included, it is expected that the enhanced activity of planetary waves impacts the stratospheric polar vortex and thus the polar tropopause, as observed.

Although the variability in simulation 2 is related with warmings in the stratospheric polar vortex, only the inclusion of the tropospheric seasonal cycle in simulation 4 is able to induce SSWs that strongly displace the polar tropopause. As SSWs are produced by the end of the winter in all years in the simulation, it appears that this setup of the idealized model may overestimate the interaction between planetary waves and the stratospheric polar vortex. In spite of this, it might be possible to use the polar tropopause as an indicator of stratospheric polar vortex intensity, or even of its breaking, due to the close relation between the two.

7. Concluding remarks.

The objectives of this thesis have focused on the study of the properties of the tropopause and its variability. In the first part, we studied the applicability of the thermal tropopause definition for differentiating the tropospheric and stratospheric air masses, while in the second part we analyzed tropopause variability based on this definition. Interest on tropopause variability is motivated by its association with stratosphere-troposphere mass exchange and coupling (Holton *et al.*, 1995; Appenzeller, 1996; Gettelman *et al.*, 2011) and by the physical significance of the tropopause as a transport barrier. If the method or definition used to determine this boundary is not appropriate, then the study of its variability loses all significance.

A first conclusion of this thesis is that the thermal tropopause definition works well as long as the stratifications above and below it are not very different from observed stratifications in present-day climate. This is consistent with the similarity between the thermal and dynamical tropopauses noted previously (examples can be found in Hoinka, 1998 or Wong and Wang, 2000), with the exception of strong cyclonic or anticyclonic circulations (Wirth, 2001). However, different climates, for instance glacial climates or simulated climates with very different heating formulations may not necessarily have a tropopause defined by the 2K km^{-1} threshold. Thus, we proposed alternative objective definitions of the tropopause that make use of its characteristic structure but do not rely on any specific threshold. These definitions are based on either the maximum curvature of the potential temperature profile or the

maximum buoyancy frequency at the level where the stratification abruptly changes. The new definitions work reasonably well as long as the contrast between the tropospheric and the stratospheric air masses is well defined -as the transition zone approaches a zero-order discontinuity. In particular, the contrast between the upper-troposphere and lower stratosphere lapse rates with these definitions is similar to that found using the traditional WMO definition, which is not bad given the great variety of situations characterizing this region.

Once the validity of the thermal definition is confirmed in the first part of the thesis, the second part investigates the variability of the zonal-mean tropopause. Two different chapters are focused on the seasonal and the intraseasonal variability. Note, however, that the main drivers of zonal-mean tropopause variability are the same in both cases. On one hand, variations in the strength of the polar vortex are associated with changes in the polar tropopause, whether by the mechanism proposed by Ambaum and Hoskins (2002) or by the downward control principle (Haynes *et al.*, 1991). On the other hand, wave activity may have a direct effect, as anomalous waves breaking is associated with anomalous meridional potential vorticity fluxes that deform the tropopause, and an indirect effect, by altering the strength and position of the residual circulation. The former is characteristic of the intraseasonal variability, while the latter is more associated with the seasonal cycle -although planetary waves propagating upward in the stratosphere may also affect the stratospheric polar vortex. Temperatures above and below the tropopause were used to interpret the driving of tropopause variability during the seasonal cycle as in previous studies (Zängl, 2002). A semi-annual tropopause seasonal cycle is observed in the Arctic in both reanalyses, and can be simulated using an idealized model with realistic polar vortex provided the seasonal cycle of tropospheric heating is also included. Interhemispheric asymmetry in winter is found to be associated with the bigger impact of dynamical heating in the Arctic, as there is compensation between the eddy heat flux and adiabatic heating in the Antarctic. In this region, diabatic heating may play a role in the sinking of the tropopause during the austral summer, while the summer tropopause rising in the Northern Hemisphere may be partly driven by moist processes in the troposphere. Intraseasonal variability is a combination of the variability associated with the variability of the waves in the troposphere, and with changes in the stratospheric polar jet; relations with both the Polar Jet Oscillation and the Zonal Index are thus found for the leading modes of variability. In the model, similar EOFs are found, but Sudden Stratospheric Warmings appear to drive some of the tropopause variations in the presence of strong baro-

clinicity and orography, suggesting a possible role for both in the interactions with the polar vortex.

No hint of baroclinic adjustment impact on tropopause variability was found in this thesis, even when considering extratropical-mean variations, in agreement with previous studies. However, it is still possible that baroclinic adjustment play some role for the determination of the mean state.

Further analyses can be made to strengthen the conclusions reached in this thesis and exploit their implications. In particular, application of the new tropopause definitions to glacial climates (for example, using the simulations of the Last Glacial Maximum given by the Coupled Model Intercomparison Project, CMIP5) may be useful for determining their relevance and possible improvement over the traditional WMO definition. As for the study of tropopause variability, the use of the new databases based on the GPS occultation technique would provide a more detailed structure of the mechanisms driving tropopause variability, as these data have higher vertical resolutions while still being regularly distributed over the world. Apart from this, the idealized model can be exploited much further by performing simulations with different intensities of the polar vortex and a range of mountain heights to analyze the impact on tropopause variability. Likewise, changing the surface meridional temperature gradient may presumably modify the intensity of the residual circulation, thus impacting the variability of the extratropical tropopause. Finally, the association found between the polar tropopause and the stratospheric polar vortex suggests that the former might provide a useful index of polar vortex intensity; in particular, PCA applied to the high-latitude tropopause height might allow us to construct such an index.

References

Ambaum, M. H. P., and B. J. Hoskins, 2002: The NAO troposphere– stratosphere connection. *J. Climate*, **15**, 1969–1978, doi:10.1175/ 1520-0442(2002)015,1969:TNTSC.2.0.CO;2

Andrews, D. G., J. R. Holton, and C. B. Leovy, 1987: Middle Atmosphere Dynamics. *International Geophysics Series*, Vol. **40**, Academic Press, 489 pp.

Añel, J. A., J. C. Antuña, L. de la Torre, R. Nieto and L. Gimeno, 2007: Global statistics of multiple tropopauses from the IGRA database. *Geophys. Res. Lett.*, **34**, 1–5.

Appenzeller, C., J. R. Holton, and K. H. Rosenlof, 1996: Seasonal variation of mass transport across the tropopause. *J. Geophys. Res.*, **101**, 15 071–15 078, doi:10.1029/96JD00821.

Bao, X. and F. Zhang, 2013: Evaluation of NCEP-CFSR, NCEP-NCAR, ERA-Interim, and ERA-40 reanalysis datasets against independent sounding observations over the Tibetan Plateau. *J. Climate,* **26**, 206–214.

Barroso and Zurita-Gotor, 2016: Intraseasonal Variability of the Zonal-Mean Extratropical Tropopause: The Role of Changes in Polar Vortex Strength and Upper-Troposphere Wave Breaking. *J. Climate*, **73**, 1383-1399.

—— and ——, a: Optimal lapse rate threshold for thermal tropopause definition. In preparation.

—— and ——, b: Seasonal cycle of zonal-mean tropopause in reanalyses and in an idealized model. In preparation.

—— and ——, c: Intraseasonal variability of the zonal-mean extratropical tropopause in an idealized model. In preparation.

Berrisford P., D. P. Dee, K. Fielding, M. Fuentes, P. Kallberg, S. Kobayashi, S. M. Uppa-

la, 2009: The ERA-Interim Archive. *ERA Report Series*, No. 1. ECMWF: Reading, UK.

Bethan, S., G. Vaughan, and S. J. Reid, 1996: A comparison of ozone and thermal tropopause heights and the impact of tro- popause definition on quantifying the ozone content of the tro- posphere. *Quart. J. Roy. Meteor. Soc.*, **122**, 929–944, doi:10.1002/ qj.49712253207.

Birner, T., A. Dörnbrack, and U. Schumann, 2002: How sharp is the tropopause at midlatitudes?, *Geophys. Res. Lett.*, **29**(14), 1700, doi:10.1029/2002GL015142.

——, 2006: Fine-scale structure of the extratropical tropopause region. *J. Geophys. Res.*, **111**, D04104, doi:10.1029/ 2005JD006301.

——, 2010: Residual circulation and tropopause structure. *J. Atmos. Sci.*, **67**, 2582–2600, doi:10.1175/2010JAS3287.1.

Bordi, I., A. Dell'Aquila, A. Speranza, and A. Sutera, 2004: On the mid-latitude tropopause height and the orographic–baroclinic adjustment theory. *Tellus*, **56**, 278–286, doi:10.1111/ j.1600-0870.2004.00065.x.

Bretherton, C. S., M. Widmann, V. P. Dymnikov, J. M. Wallace, and I. Bladé, 1999: The effective number of spatial degrees of freedom of a time-varying field. *J. Climate*, **12**, 1990–2009, doi:10.1175/1520-0442(1999)012,1990:TENOSD.2.0.CO;2.

Charney, J. G., and P. G. Drazin, 1961: Propagation of planetary- scale disturbances from the lower into the upper atmosphere. *J. Geophys. Res.*, **66**, 83–109, doi:10.1029/JZ066i001p00083.

——, and M. E. Stern, 1962: On the stability of internal baroclinic jets in a rotating atmosphere. *J. Atmos. Sci.*, **19**, 159– 172.

Cohen, N. Y., E. P. Gerber, and O. Bühler, 2013: Compensation between resolved and unresolved wave driving in the stratosphere: Implications for downward control. *J. Atmos. Sci.*, **70**, 3780–3798, doi:10.1175/JAS-D-12-0346.1

Davis, N. A. and T. Birner, 2013: Seasonal to multidecadal variability of the width of the tropical belt. *J. Geophys. Res.*, **118**, 7783–7787, doi:10.1002/jgrd.50610

Dee, D. P. and Coauthors, 2011: The ERA-Interim reanalysis: Configuration and performance of the data assimilation system. *Q. J. R. Meteorol. Soc.* **137**, 553–597.

Defant, F., H. Taba, 1958: The Break Down of Zonal Circulation during the Period January 8 to 13 , 1956 , the Characteristics of Temperature Field and Tropopause and its Relation to the Atmospheric Field of Motion. *Tellus X*, **4**, 430-350.

Dell'Aquila, A., P. M. Ruti, and A.Sutera, 2006: Effects of the baroclinic adjustment on the tropopause in the NCEP–NCAR reanalysis. *Climate Dyn.*, **28**, 325–332, doi:10.1007/s00382-006-0199-4.

Dines, L. H. G.. 1919: The investigation of the upper air: Introduction. -Reprinted in: Collected papers of W. H. Dines, London, *Roy. Meteorol. Soc.*, 1931, 117-120.

Duchon, C., 1979: Lanczos Filtering in One and Two Dimensions. *J. App. Meteorol.*, **18**, 1016-1022.

Durre, I., R. S. Vose,and D. B. Wuertz, D. B., 2006: Overview of the Integrated Global Radiosonde Archive. *J. Clim.*, **19**, 53–68.

Edmon, H. J., Jr., B. J. Hoskins, and M. E. McIntyre, 1980: Eliassen– Palm cross sections for the troposphere. *J. Atmos. Sci.*, **37**, 2600– 2616, doi:10.1175/1520-0469(1980)037,2600:EPCSFT.2.0.CO;2.

Egger, J., 1995: Tropopause height in baroclinic channel flow. *J.Atmos. Sci.*, **52**, 2232–2241, doi:10.1175/1520-0469(1995)052,2232: THIBCF.2.0.CO;2.

Endlich, R. M., 1954: A note on pressure at the tropopause. *Bull. Amer. Meteorol. Soc.*, **35**, 131-132.

Feldstein, S. B., and S. Lee, 2014: Intraseasonal and interdecadal jet shifts in the Northern Hemisphere: The role of warm pool tropical convection and sea ice. *J. Climate*, **27**, 6497–6518, doi:10.1175/JCLI-D-14-00057.1.

Fueglistaler, S., A. E. Dessler, T. J. Dunkerton, I. Folkins, Q. Fu, and P. W. Mote, 2009: Tropical Tropopause Layer. *Rev. Geophys*. **47**, 1–31.

Gettelman, A., P. Hoor, and L. Pan, 2011: The extratropical upper troposphere and lower stratosphere. *Rev. Geophys.*, **49** (RG3003), 1–31 . doi:10.1029/2011RG000355.1.

Gerber, E. P., and L. M. Polvani (2009), Stratosphere-troposphere coupling in a relatively simple AGCM: The importance of stratospheric variability, *J. Climate*, **22**(8), 1920–1933.

Grise, Kevin M., D. W. J. Thompson, and T. Birner, 2010: A Global Survey of Static Stability in the Stratosphere and Upper Troposphere. *J. Clim.,* **23**, 2275–2292.

Haynes, P. H., M. E. McIntyre, T. G. Shepherd, C. J. Marks, and K. P. Shine, 1991: On the 'Downward Control' of Extratropical Diabatic Circulations by Eddy-Induced Mean Zonal Forces. *J. Atmos. Sci.*, **48**, 651–678.

Haynes, P., J. Scinocca, and M. Greenslade, 2001: Formation and maintenance of the extratropical tropopause by baroclinic eddies. *Geophys. Res. Lett*. **28**, 4179.

Hegglin, M. I., and Coauthors, 2006: Measurements of NO, NOy, N2O, and O3 during SPURT: Implications for transport and chemistry in the lowermost stratosphere. *Atmos. Chem. Phys*., **6**, 1331–1350.

Held, I. M., 1982: On the height of the tropopause and the static stability of the troposphere. *J. Atmos. Sci.*, **39**, 412–417, doi:10.1175/1520-0469(1982)039,0412:OTHOTT.2.0.CO;2.

---, and M. J. Suarez, 1994: A proposal for the Intercomparison of the Dynamical Cores of Atmospheric General Circulation Models. *Bull. Ame. Meteorol. Soc.,* **75**, 1825.1830.

Hess, S. L., 1948: Some new mean meridional cross sections through the atmosphere. *J. Meteor.*, **5**, 293–300.

Highwood, E.J. and B. J. Hoskins, 2000: Properties of the Arctic Tropopause, *Quart. J. Roy. Meteor. Soc.*, **126**, 1515–1532, DOI: 10.1002/qj.49712656515

Hoerling, M. P., T. K. Schaack and A. J. Lenzen, 1991: Global Objective Tropopause Analysis. *Mon. Wea. Rev.*, **119**, 1816–1831.

Hoinka, K. P., 1997: The tropopause: discovery, definition and demarcation. *Meteorol. Zeitschrift*, **6**, 281–303.

Hoinka, K. P., 1998: Statistics of the global tropopause pressure. *Mon. Wea. Rev.*, **126**, 3303–3325, doi:10.1175/ 1520-0493(1998)126,3303:SOTGTP.2.0.CO;2.

Holton, J. R., P. H. Haynes, M. E. McIntyre, A. R. Douglass, R. B. Rood, and L. Pfister, 1995: Stratosphere–troposphere exchange. *Rev. Geophys.*, **33**, 403–439, doi:10.1029/95RG02097.

Hoskins, B. J., M. E. McIntyre, and A. W. Robertson, 1985: On the use and significance of isentropic potential vorticity maps. *Quart. J. Roy. Meteor. Soc.*, **111**, 877–946, doi:10.1002/qj.49711147002.

Houghton, J. T., 1977: The Physics of Atmospheres. *Cambridge University Press*, 203 pp.

Ivanova, A. R., 2013: The tropopause: Variety of definitions and modern approaches to identification. *Russ. Meteorol. Hydrol*. **38**, 808–817.

Jucker, M., S. Fueglistaler, and G. K. Vallis, 2013: Maintenance of the stratospheric structure in an idealized general circulation model, *J. Atmos. Sci.*, **70**(11), 3341–3358, doi:10.1175/JAS-D-12-0305.1.

Jucker, M., S. Fueglistaler, and G. K. Vallis, 2014: Stratospheric sudden warmings in an idealized GCM. *J. Geo- phys. Res. Atmos.,* **119**, 11,054–11,064, doi:10.1002/2014JD022170.

Juckes, M., 1994: Quasigeostrophic dynamics of the tropo- pause. *J. Atmos. Sci.,* **51**, 2756–2768, doi:10.1175/ 1520-0469(1994)051,2756:QDOTT.2.0.CO;2.

——, 2000: The static stability of the midlatitude troposphere: The relevance ofmoisture. *J. Atmos. Sci.*, **57**, 3050–3057, doi:10.1175/ 1520-0469(2000)057,3050:TSSOTM.2.0.CO;2.

Kalnay, and Coauthors, 1996: The NCEP/NCAR 40-Year Reanalysis Project. *Bull. Am. Meteorol.,* **77.**

Kiladis, G. N., K. H. Straub, G. C. Reid, and K. S. Gage, 2001: Aspects of interannual and intraseasonal variability of the tropopause and lower stratosphere. *Quart. J. Roy. Meteor. Soc.*, **127**, 1961–1984.

Kodera, K., Y. Kuroda, and S. Pawson, 2000: Stratospheric sudden warmings and slowly propagating zonal-mean zonal wind anomalies. *J. Geophys. Res.*, **105**, 12 351–12 359, doi:10.1029/ 2000JD900095.

Kushner, P. J., and L. M. Polvani, 2004: Stratosphere-troposphere coupling in a relatively simple AGCM: The role of eddies, *J. Climate*, **17**(3), 629–639, doi:10.1175/1520-0442(2004)017<0629:SCIARS>2.0.CO;2

Limpasuvan, V., D. W. J. Thompson, and D. L. Hartmann, 2004: The life cycle of the Northern Hemisphere sudden stratospheric warmings. *J. Climate*, **17**, 2584–2596, doi:10.1175/ 1520-0442(2004)017,2584:TLCOTN.2.0.CO;2

Lindzen, R. S., 1993: Baroclinic neutrality and the tropopause. *J.Atmos. Sci.*,**50**,1148–1151, doi:10.1175/1520-0469(1993)050,1148: BNATT.2.0.CO;2.

Liu, Y., T. Xu, and J. Liu (2014): Characteristics of the Seasonal Variation of the Global

Tropopause Revealed by COSMIC/GPS Data. *Adv. Sp. Res.,* . doi:10.1016/j.asr.2014.08.020

Lorenz, D. J., and D. L. Hartmann, 2001: Eddy-zonal flow feedback in the Southern Hemisphere. *J. Atmos. Sci.*, **58**, 3312–3327.

——, and ——, 2003: Eddy-zonal flow feedback in the Northern Hemisphere winter. *J. Climate,* 16, 1212–1227.

Möller, F., 1938: Der Jahresgang der Temperatur in der Stratosphäre. *Meteor. Z.*, **55**, 161–170.

Mooney, P. A., F. J. Mulligan and R. Fealy, 2011: Comparison of ERA-40, ERA-Interim and NCEP/NCAR reanalysis data with observed surface air temperatures over Ireland. *Int. J. Climatol*. **31**, 545–557.

North, G. R., F. J. Moeng, T. L. Bell, and R. F. Cahalan, 1982a: The latitude dependence of the variance of zonally averaged quantities. *Mon. Wea. Rev.*, **110**, 319–326.

——, T. L. Bell, R. F. Cahalan, and F. J. Moeng, 1982b: Sampling errors in the estimation of empirical orthogonal functions. *Mon. Wea. Rev*., **110**, 699–706.

Pauluis, O., A. Czaja, and R. Korty, 2010: The global atmospheric circulation in moist isentropic coordinates. *J. Clim*., **23**, 3077–3093.

Pawson, S. and Fiorino, M., 1999: A comparison of reanalyses in the tropical stratosphere. Part 3: inclusion of the pre-satellite data era. *Clim. Dyn*. **15**, 241–250.

Poli, P., S. B. Healy, and D. P. Dee, 2010: Assimilation of Global Positioning System radio occultation data in the ECMWF ERA-Interim reanalysis. *Q. J. R. Meteorol. Soc.,* **136**, 1972–1990.

Polvani, L. M., and P. J. Kushner, 2002: Tropospheric response to stratospheric perturbations in a relatively simple general circulation model, *Geophys. Res. Lett.*, **29**(7), 18-1–18-4,

doi:10.1029/2001GL014284

Randel, W. J., F. Wu, F. and D. Gaffen, 2000: Interannual variability of the tropical tropopause derived from radiosonde data and NCEP reanalyses. *J. Geophys. Res.*, **105**, 15509-15523.

——, R. R. Garcia, and F. Wu, 2002: Time-dependent upwelling in the tropical lower stratosphere estimated from the zonal-mean momentum budget, *J. Atmos. Sci.*, **59**, 2141–2152.

——, F. Wu and P. Forster, 2007: The Extratropical Tropopause Inversion Layer: Global Observations with GPS Data, and a Radiative Forcing Mechanism. *J. Atmos. Sci.*, **64**, 4489–4496.

Reed, R. J., 1955: A study of a characteristic type of upper level frontogenesis. *J. Meteor.*, **12**, 226–237, doi:10.1175/ 1520-0469(1955)012,0226:ASOACT.2.0.CO;2.

Reichler, T., M. Dameris, and R. Sausen, 2003: Determining the tropopause height from gridded data. *Geophys. Res. Lett.*, **30**, 2042, doi:10.1029/2003GL018240.

Ribera, P., C. Peña-Ortiz, J. A. Añel, L. Gimeno, L. de la Torre, and D. Gallego, 2008: Quasi-biennial modulation of the Northern Hemisphere tropopause height and temperature, *J. Geophys. Res.*, **113**, D00B02, doi:10.1029/2007JD009765.

Rosenlof, K. H., 1996: Summer hemisphere differences in temperature and transport in the lower stratosphere, *J. Geophys. Res.*, **101**, 19,129–19,136.

Santer, B. D. and Coauthors, 1999: Uncertainties in observationally based estimates of temperature change in the free atmosphere. *J. Geophys. Res.*, **104**, 6305.

——, and Coauthors, 2003: Behavior of tropopause height and atmospheric temperature in models, reanalyses, and observations: Decadal changes. *J. Geophys. Res,* **108**, 1–22.

Sawyers, J. S., 1954: Day-to-day variations in the tropopause. *Geophys. Mem.*, **92**, 1–40.

Schmauss, A., 1909: Die obere Inversion. *Meteorol. Z.*, **26**, 251-258.

Schneider, T., 2004: The tropopause and the thermal stratification in the extratropics of a dry atmosphere. *J. Atmos. Sci.*, **61**, 1317–1340, doi:10.1175/1520-0469(2004)061,1317:TTATTS.2.0.CO;2.

Seidel, D., and W. Randel, 2006: Variability and trends in the global tropopause estimated from radiosonde data. *J. Geophys. Res.*, **111**, 1–17.

Shepherd, T. G., 2002: Issues in stratosphere–troposphere coupling. *J. Meteor. Soc. Japan*, **80**, 769–792, doi:10.2151/jmsj.80.769.

Simmons, A. J., and D. M. Burridge, 1981: An energy and angular-momentum conserving vertical finite-difference scheme and hybrid vertical-coordinates, *Mon. Wea. Rev.*, **109**, 758–766.

Škerlak, B., M. Sprenger, and H. Wernli, 2014: A global climatology of stratosphere–troposphere exchange using the ERA-Interim data set from 1979 to 2011. *Atmos. Chem. Phys.*, **14**, 913–937.

Son, S., S. Lee, and S. B. Feldstein, 2007: Intraseasonal variability of the zonal-mean extratropical tropopause height. *J. Atmos. Sci.*, **64**, 608–620, doi:10.1175/JAS3855.1.

——, L. M. Polvani, 2007: Dynamical formation of an extra-tropical tropopause inversion layer in a relatively simple general circulation model. Geophys. Res. Lett. 34, L17806 (2007).

——, N. F. Tandon, and L. M. Polvani, 2011: The fine-scale structure of the global tropopause derived from COSMIC GPS radio occultation measurements. *J. Geophys. Res.*, **116**, D20113.

Song, Y., and N. Nakamura, 2000: Eady instability of isolated baroclinic jets with meridionally varying tropopause height. *J. Atmos. Sci.*, **57**, 46–65, doi:10.1175/1520-0469(2000)057,0046: EIOIBJ.2.0.CO;2

Sturaro, G., 2003: A closer look at the climatological discontinuities present in the NCEP/NCAR reanalysis temperature due to the introduction of satellite data, *Cimate Dyn.*, **21** 309-316. doi:10.1007/s00382-003-0334-4

Szczypta, C. and Coauthors, 2011: Verification of the new ECMWF ERA-Interim reanalysis over France. *Hydrol. Earth Syst. Sci.*, **15**, 647–666.

Thépaut J.-N-, P. Courtier, G. Belaud, G. Lemâitre, 1996: Dynamical structure functions in a four-dimensional variational assimilation. *Q. J. R. Meteorol. Soc.,* **122**: 535–561.

Thompson, D.W.J., and J.M. Wallace, 2000: Annular modes in the extratropical circulation. Part I: Month-to-month variability. *J. Climate*, **13**, 1000–1016, doi:10.1175/1520-0442(2000)013,1000: AMITEC.2.0.CO;2.

Thuburn, J., and G. C. Craig, 1997: GCM tests of theories for the height of the tropopause. *J. Atmos. Sci.*, **54**, 869–882, doi:10.1175/ 1520-0469(1997)054,0869:GTOTFT.2.0.CO;2.

——, and G. C. Craig, 2000: Stratospheric influence on tropopause height: The radiative constraint. *J. Atmos. Sci.*, **57**, 17–28, doi:10.1175/1520-0469(2000)057,0017:SIOTHT.2.0.CO;2.

Tiedtke, M., 1988: Parameterization of Cumulus Convection in Large-Scale Models. *Physically-Based Modelling and Simulation of Climate and Climatic Change,* M. Schlesinger, Ed. D. Reidel, 375-431.

Vallis, G. K., 2005: Atmospheric and Oceanic Fluid Dynamics. *Cambridge University Press*. doi:10.1017/CBO9780511790447

Whitaker J. S., G. P. Compo, J.-N. Thépaut, 2009: A comparison of variational and en-

semble-based data assimilation systems for reanalysis of sparse observations. *Mon. Weather Rev.*, **137**: 1991–1999.

Wilcox, L., Hoskins, B. and Shine, K. (2012a) A global blended tropopause based on ERA data, Part I: Climatology. *Quart. J. Roy. Meteorol. Soc.*, **138** (664), 561-575. doi: 10.1002/qj.951

——, ——. and —— (2012b) A global blended tropopause based on ERA data, Part II: trends and tropical broadening. *Quart. J. Roy. Meteorol. Soc.*, **138** (664), 576-584. doi:10.1002/qj.910

Wirth, V., 2000: Thermal versus dynamical tropopause in upper tropospheric balanced flow anomalies. *Quart. J. Roy. Meteor. Soc.*, **126**, 299–317.

——, 2001: Cyclone–Anticyclone Asymmetry Concerning the Height of the Thermal and the Dynamical Tropopause. *J. Atmos. Sci.,* **58**, 26–37.

——, and T. Szabo, 2007: Sharpness of the extratropical tropopause in baroclinic life cycle experiments. *Geophys. Res. Lett.* , **34**, L02809.

Wittman, M. A. H., A. J. Charlton, and L. M. Polvani, 2005: On the Meridional Structure of Annular Modes. *J. Climate,* **18**, 2119–2122.

WMO, 1957: Definition of the tropopause.*WMO Bull.*, **6**, 136.

——, 1986: Atmospheric ozone 1985. *WMO Reports*.

Wong, S. and W.-C. Wang, 2000: Interhemispheric asymmetry in the seasonal variation of the zonal mean tropopause. *J. Geophys. Res.*, **105**, 26645

Wu, Y., and O. Pauluis, 2014: Midlatitude tropopause and low- level moisture. *J. Atmos. Sci.*, **71**, 1187–1200, doi:10.1175/ JAS-D-13-0154.1.

Zahn, A., and C. A. M. Brenninkmeijer, 2003: New directions: A chemical tropopause defined, *Atmos. Env.*, **37**, 439–440.

Zängl, G., and K. P. Hoinka, 2001: The tropopause in the Polar Regions, *J. Climate*, **73**, 1383-1399, DOI: http://dx.doi.org/10.1175/1520-0442(2001)014<3117:TTITPR>2.0.CO;2

——,2002: Dynamical heating in the polar lower stratosphere and its impact on the tropopause. *J. Geophys. Res*. **107**, 5.

——,and V. Wirth, 2002: Synoptic-scale variability of the polar and subpolar tropopause: Data analysis and idealized PV inversions. *Q. J. R. Meteorol. Soc.,* **128**, 2301–2315.

Zurita-Gotor, P., and G. K. Vallis, 2011: Dynamics of midlatitude tropopause height in an idealized model. *J. Atmos. Sci.*, **68**, 823–838, doi:10.1175/2010JAS3631.1.

——, and ——, 2013: Determination of extratropical tropopause height in an idealized gray radiation model. *J. Atmos. Sci.,* **70**, 2272–2292, doi:10.1175/JAS-D-12-0209.1.

List of publications and meeting contributions

Barroso and Zurita-Gotor, 2016: Intraseasonal Variability of the Zonal-Mean Extratropical Tropopause: The Role of Changes in Polar Vortex Strength and Upper-Troposphere Wave Breaking. *J. Climate*, **73**, 1383-1399.

—— and ——, a: Optimal lapse rate threshold for thermal tropopause definition. In preparation.

—— and ——, b: Seasonal cycle of zonal-mean tropopause in reanalyses and in an idealized model. In preparation.

—— and ——, c: Intraseasonal variability of the zonal-mean extratropical tropopause in an idealized model. In preparation.

"Variabilidad de la tropopausa global y extratropical estimada a partir de los datos del reanálisis NCEP/NCAR", J. A. Barroso, P. Zurita-Gotor**. XXXII Jornadas Científicas de la Asociación Meteorológica Española** (2012). Poster.

"Intraseasonal variability of the extratropical tropopause", J. Á. Barroso, P. Zurita-Gotor. **19th Conference on Atmospheric and Oceanic Fluid Dynamics,** Newport, RI, USA (2013). Poster.

"Variability of the extratropical zonal-mean tropopause height", J. Á. Barroso, P. Zurita-Gotor. **EGU General Assembly Conference**, Vienna, Austria (2015). Oral communication.

"Intraseasonal Variability of the Zonal-Mean Extratropical Tropopause Height", J. A. Barroso, P. Zurita-Gotor. **20th Conference on Atmospheric and Oceanic Fluid Dynamics,** Minneapolis, MN, USA (2015). Poster.

"Is 2K/km the optimal threshold for thermal tropopause definition?" J. Á. Barroso, P. Zurita-Gotor. **EGU General Assembly Conference**, Vienna, Austria (2016). Poster.

Other works realized during this thesis but not related with the thesis:

Suárez-Moreno, R., Rodríguez-Fonseca, B., Barroso J.A., Fink, A.H., (2017a): Interdecadal changes in SST-driven teleconnections with Sahel rainfall. Dynamical factors and implications in predictability (submitted)